

THE INTERACTION BETWEEN THE EVH1 DOMAIN OF VASP AND
PROLINE-RICH SEQUENCES: SIGNIFICANCE OF ISOMERIZATION,
PHOSPHORYLATION, AND A SECONDARY BINDING SITE

A Dissertation

Presented to the Faculty of the Graduate School
of Cornell University

In Partial Fulfillment of the Requirements for the Degree of
Doctor of Philosophy

by

Alexander Ian Greenwood

January 2014

© 2014 Alexander Ian Greenwood

THE INTERACTION BETWEEN THE EVH1 DOMAIN OF VASP AND
PROLINE-RICH SEQUENCES: SIGNIFICANCE OF ISOMERIZATION,
PHOSPHORYLATION, AND A SECONDARY BINDING SITE

Alexander Ian Greenwood, Ph.D

Cornell University 2014

Ena/VASP proteins are cytoskeletal rearrangement proteins involved in processes such as phagocytosis, cell migration, and axon guidance in neurons. VASP contains an N-terminal EVH1 domain which localizes it to specific sites in the cell. The VASP-EVH1 domain recognizes the proline-rich motif (F/W)Px ϕ P, which occurs in the immune cell signaling kinase IRAK1 and also as tandem repeats in the focal adhesion protein zyxin. Typically this motif is flanked by negatively charged amino acids that are necessary for a tight ($K_D < 200 \mu\text{M}$) interaction. We have examined the interactions between VASP-EVH1 and the binding sites in IRAK1 and zyxin and describe three novel observations. First, we report that the W₁₆₈-P₁₆₉ peptide bond in the IRAK1 binding site partitions into nearly equal (43% *cis*, 57% *trans*) population of *cis* and *trans* isomers, and that EVH1 binding to this site is specific for the *trans* isomer. We use NMR and tryptophan fluorescence spectroscopy to show that the prolyl isomerase cyclophilin A (CypA) isomerizes this site and accelerates binding of VASP-EVH1 to peptides. Second, we report that phosphorylation of two serines flanking the WPPPP motif in IRAK1 increases the affinity for VASP-EVH1 by a factor of seven. This shows that phosphoserine is an effective substitute for glutamic or aspartic acid in VASP-binding sequences, suggesting that phosphorylation could be a novel mechanism to regulate VASP localization, especially in the case of IRAK1

and lamellipodin, which are known to be phosphorylated. Third, we show that VASP-EVH1 contains a noncanonical second binding site on the face opposite its primary binding site. We show that this site shares some binding specificity with the canonical (F/W)Px ϕ P motif, and that this binding site is employed in the interaction with zyxin to recognize the third and fourth VASP-binding repeats of zyxin. We also show that this binding site is conserved in the homologous Ran-binding domain (RanBD), suggesting that it is widespread in EVH1 homologs. Separately, we report an NMR lineshape analysis-based protocol for dissecting the microscopic rate constants of a prolyl isomerase enzyme.

BIOGRAPHICAL SKETCH

The author was raised in a slightly bohemian household. He grew up with livestock as pets, though his parents were not farmers and they did not eat said pets. His most enduring career plan throughout childhood was to join the ranks of Azimov and Heinlein and become a science fiction writer. This changed in high school when his ability to critique his own writing started outpacing his ability to write. At the same time, he was developing a strong fondness for math and physics and a budding interest in biology. As a freshman physics major at Carnegie Mellon, he was won over by an introductory biology course. This led to him to the field of biophysics, and to his undergraduate mentors John Nagle and Stephanie Tristram-Nagle. He spent two summers in their lipid biophysics laboratory, which resulted in two publications and trip to the CHESS synchrotron source at Cornell. Shortly afterwards, he found himself at Cornell again as a graduate student. It was around that time that the author was extremely fortunate to meet Molly Shook, a graduate student in BMCB whom he married as soon as was possible. At Cornell, his research shifted from lipids to proteins, and he took to the task of becoming proficient at using NMR spectroscopy to understand complex multi-state biomolecular interactions. His research in the Nicholson lab has largely focused on the binding interactions of the EVH1 domain of VASP and on the topic of proline isomerization. His current interests include caring for his 3 ½-month-old daughter Elise.

To Molly.

ACKNOWLEDGMENTS

I would like to thank the people who contributed time and resources to this research: I thank Cynthia Kinsland and the Cornell University Protein Facility for providing us with expression vectors and for her help with preliminary stopped flow experiments. I thank Kun Ping Lu for providing us with the original plasmid used to clone IRAK1-UD, and JeaHoo Kwon for performing the cloning. I thank both the labs of Dyche Mullins and Michael Way for providing us with VASP expression materials. I thank Charalampos Kalodimos for providing us with CypA expression materials. I thank Soumya De for help purifying CypA. I thank Jolita Šečkutė for purifying 3C protease and Monique Rogals for purifying TEV protease. I thank Ross Resnick for performing cell culture experiments. I thank Gerald Feigenson for use of the fluorescence spectrophotometer, and Robin Smith Petruzielo and Lynda Goh for their help in using it. I thank Yi-Pin Lin, Yung-Fu Chang, Greg Finn, and Adrian Tun-Kyi for their guidance in additional research not covered in this dissertation. I would also like to thank the people who have supported me, both intellectually and emotionally. I thank my mentor, Professor Linda Nicholson, my special committee, Professors Robert Oswald and David Wilson, and all of the past and present members of the Nicholson lab for their guidance, patience, and a remarkably steady supply of vegan baked goods. I am especially grateful for the unending love and support of my wife, Molly Shook.

This work was supported by the NSF (award #1157806) and the NIH (R01-AG029385 and a biophysics training grant).

TABLE OF CONTENTS

BIOGRAPHICAL SKETCH	iii.
ACKNOWLEDGEMENTS	v.
TABLE OF CONTENTS	vi.
LIST OF FIGURES	vii.
LIST OF TABLES	x.
LIST OF ABBREVIATIONS	xi.
LIST OF SYMBOLS	xii.
Chapter One: Background and Overview	1
Chapter Two: Isomerase-Catalyzed Binding of IRAK1 to the EVH1 Domain of VASP	29
Chapter Three: The VASP EVH1 Domain Recognizes Phosphorylated Sequences and Contains a Secondary Binding Site	72
Chapter Four: A Noncanonical Binding Site in the EVH1 Domain of VASP is Employed in the Interaction with Zyxin	104
Chapter Five: Complete Determination of the Pin1 Catalytic Domain Thermodynamic Cycle by NMR Lineshape Analysis	136
Chapter Six: Perspectives, Additional Observations, and Future Plans	173
APPENDIX	181

LIST OF FIGURES

Figure 1.1: <i>Cis/trans</i> isomerization and its role in protein interactions and function.	2
Figure 1.2: Domain architectures of the proteins VASP, zyxin, and IRAK1.	9
Figure 1.3: Conserved features of EVH1/RanBD interactions.	12
Figure 2.1: Conformational heterogeneity in the undefined domain of IRAK1.	42
Figure 2.2: The IRAK1-UD/VASP-EVH1 interaction is <i>trans</i> -specific.	45
Figure 2.3: Chemical shift mapping to EVH1 structure.	47
Figure 2.4: Measurement of affinity and kinetics of binding between the VASP-EVH1 domain and IRAK1 ¹⁶²⁻¹⁸⁰ .	49
Figure 2.5: Cyclophilin A catalyzes the isomerization between <i>cis</i> and <i>trans</i> isomers of W168-P169 in IRAK1.	51
Figure 2.6: Tryptophan fluorescence shows cyclophilin A accelerates IRAK1-UD/EVH1 binding and equilibration of IRAK1 isomers.	54
Figure 2.7: Energy diagram describing <i>cis</i> and <i>trans</i> isomers of W168-P169 in IRAK1-UD.	56
Figure 2.8: Tryptophan fluorescence shows CypA accelerates ActA/EVH1 binding.	59
Figure 3.1: Phosphorylation of IRAK1 enhances its affinity for VASP-EVH1.	81
Figure 3.2: Binding kinetics derived from NMR lineshape analysis of ¹⁵ N EVH1 peaks in peptide titrations.	83

Figure 3.3: Suggested basis for EVH1 phosphoserine recognition.	84
Figure 3.4: Alignment and sequence logo of VASP-EVH1 binding sites.	87
Figure 3.5: Phosphorylated IRAK1 can be isomerized by cyclophilin A.	90
Figure 3.6: Evidence for a weak secondary binding site on VASP-EVH1.	91
Figure 3.7: Secondary EVH1 binding site selects phosphorylated IRAK1 peptides.	93
Figure 3.8: Comparison between the binding surfaces of the Ran-binding domain and the VASP-EVH1 domain.	97
Figure 4.1: Sequences of VASP-binding proteins.	107
Figure 4.2: HSQC and ^{15}N -ZZ spectra of the proline-rich region of zyxin.	115
Figure 4.3: Zyxin $^{41-140}$ induces chemical shift changes in the secondary binding site of VASP-EVH1.	118
Figure 4.4: ^{15}N zyxin $^{41-140}$ /EVH1 titration data shows isomer specificity of interaction at motif M2.	119
Figure 4.5: ^{15}N zyxin $^{41-140}$ /EVH1 titration data show multiple populations in slow exchange for zyxin's third and fourth FPxøP motifs.	122
Figure 4.6: Chemical shift perturbation profiles of wt and Y39D EVH1 domain, and example peaks.	124
Figure 4.7: Suggested model of EVH1/ zyxin $^{41-140}$ binding.	126
Figure 4.8: Tyr39 is located centrally in the secondary EVH1 binding site.	129
Figure 5.1: Models used to interpret NMR data.	142
Figure 5.2: Chemical shift perturbation of ^{15}N -labeled Pin1-PPIase upon titration with unlabeled pAPP659-682 peptide.	151
Figure 5.3: Overall binding constant of Pin1 for pAPP659-682 is approximately independent of the presence of the WW domain.	152

Figure 5.4: ^{13}C - ^1H constant-time HSQC spectrum of specifically labeled ^{13}C -pAPP659-682 peptide.	155
Figure 5.5: NMR lineshape fitting of ^{13}C -pAPP659-682 peptide titration data.	157
Figure 5.6: ROESY measurement of Pin1-PPIase isomerization rate.	163
Figure 5.7: Free energy diagram of Pin1-PPIase catalysis.	164
Appendix Figure 2.1: ^1H - ^1H TOCSY showing <i>cis</i> and <i>trans</i> isomers of W168-P169 and S173-P174 peptide bonds in IRAK1 ¹⁶²⁻¹⁸⁰ .	181
Appendix Figure 2.2: Temperature dependence of population of <i>cis</i> isomer of IRAK1-UD.	182
Appendix Figure 2.3: ^1H - ^1H TOCSY showing <i>cis</i> and <i>trans</i> isomers of F335-P336 peptide bond in ActA ³³³⁻³⁴⁴ .	183
Appendix Figure 2.4: Alignment of IRAK1 residues 130-208 in primates shows that W168 is a very recent mutation.	184
Appendix Figure 2.5: Structural model rationalizing isomer specificity of IRAK1-UD/EVH1 interaction.	185
Appendix Figure 3.1: Chemical shift perturbation difference analysis indicates a single binding orientation of EVH1/IRAK1 complex.	186
Appendix Figure 3.2: ^{15}N -EVH1 chemical shift perturbation profiles of IRAK1 ¹⁶²⁻¹⁸⁰ and IRAK1 ^{162-180, W168F} .	187
Appendix Figure 3.3: Temperature dependence of IRAK1 W168 sidechain chemical shift indicates no hydrogen bond with VASP-EVH1.	188
Appendix Figure 4.1: Fitting ^{15}N zyxin ⁴¹⁻¹⁴⁰ /EVH1 binding curves.	189
Appendix Figure 4.2: Fitting ^{15}N EVH1/zyxin peptide titration data.	190
Appendix Figure 6.1: Zinc binding to IRAK1-UD.	198

LIST OF TABLES

Table 2.1: Chemical Shift Assignments of IRAK1 Residues A165-A175 for the <i>Cis</i> and <i>Trans</i> Isomers of W168-P169.	43
Table 2.2: Rates and Equilibrium/Binding Constants for IRAK1 ¹⁶²⁻¹⁸⁰ and ActA ³³³⁻³⁴⁰ .	58
Table 3.1: Binding rates and affinities of IRAK1-derived peptides.	85
Table 4.1: Dissociation constants of EVH1 binding to zyxin constructs.	123
Table 5.1: Summary of fitted and constrained parameters.	158
Appendix Table 4.1: Assignments of zyxin residues 69-126, excluding prolines.	191
Appendix Table 5.1: Impact of variations in constrained parameters on fit.	195
Appendix Table 5.2: Scalar coupling values employed in lineshape simulation.	196

LIST OF ABBREVIATIONS

APP: Amyloid Precursor Protein

CypA: Cyclophilin A

EVH1: Enabled/VASP Homology 1

HSQC: Heteronuclear Single-Quantum Correlation spectroscopy

Hz: Herz (s^{-1})

IL-1R: Interleukin-1 Receptor

IRAK1: Interleukin-1-Receptor Associated Kinase 1

M1-M4: VASP-binding Motifs 1-4 of zyxin

NMR: Nuclear Magnetic Resonance spectroscopy

Pin1: Peptidyl Prolyl *cis/trans* isomerase NIMA-interacting 1

PPII: Polyproline type II helix

PPIase: Peptidyl Prolyl Isomerase enzyme

ppm: parts per million

RanBD: Ran-binding domain

RanBP2: Ran-binding protein 2

ROESY: Rotating-Frame Overhauser Effect Spectroscopy

TLR: Toll-Like Receptor

TOCSY: Total Correlation Spectroscopy

UD: Undefined Domain of IRAK1

VASP: Vasodilator-Stimulated Phosphoprotein

wt: wild-type

LIST OF SYMBOLS

- K_D : Dissociation constant (μM or mM)
- K_D^{trans} : Dissociation constant for the *trans* isomer (μM or mM)
- K_D^{App} : Apparent dissociation constant (μM or mM)
- ω^{Apo} : Chemical shift of free state (Hz)
- ω^{Bound} : Chemical shift of bound state (Hz)
- $\Delta\delta_H$: Chemical shift difference in the ^1H dimension (ppm)
- $\Delta\delta_N$: Chemical shift difference in the ^{15}N dimension (ppm)
- $\Delta\delta^{\max}$: Chemical shift difference between free and bound states (ppm)
- L_{corr} : Correction factor used to scale concentrations
- $R_{2,0}^{Apo}$: Linewidth of free state (Hz)
- $R_{2,0}^{Bound}$: Linewidth of bound state (Hz)
- k_{off} : Off-rate of binding (s^{-1})
- k_{on} : On-rate of binding ($\text{M}^{-1}\text{s}^{-1}$)
- $R_{1,0}^{trans}$: Longitudinal relaxation rate of *trans* isomer peak (s^{-1})
- $R_{1,0}^{cis}$: Longitudinal relaxation rate of *cis* isomer peak (s^{-1})
- $R_{2,0}^{trans}$: Transverse relaxation rate of *trans* isomer peak (s^{-1})
- $R_{2,0}^{cis}$: Transverse relaxation rate of *cis* isomer peak (s^{-1})
- K_{isom} : Ratio of *trans* isomer to *cis* isomer
- $I_{TT,0}$: Initial intensity of *trans* autopeak in ^{15}N -ZZ exchange experiment
- $I_{CC,0}$: Initial intensity of *cis* autopeak in ^{15}N -ZZ exchange experiment
- k_{CT} : *Cis*-to-*trans* rate of isomerization (s^{-1})
- k_{TC} : *Trans*-to-*cis* rate of isomerization (s^{-1})
- k_{ex} : Exchange rate of isomerization, $k_{CT} + k_{TC}$ (s^{-1})
- k_{obs} : Observed isomerization rate (s^{-1})

I_{final} : Equilibrium fluorescence intensity

I_0 : Initial fluorescence intensity

ΔH_{\ddagger}^{ct} : Activation enthalpy of *cis*-to-*trans* isomerization (kJ/mol)

ΔH_{\ddagger}^{tc} : Activation enthalpy of *trans*-to-*cis* isomerization (kJ/mol)

ΔS_{\ddagger}^{ct} : Activation entropy of *cis*-to-*trans* isomerization (kJ/mol/K)

ΔS_{\ddagger}^{tc} : Activation entropy of *trans*-to-*cis* isomerization (kJ/mol/K)

k_{cat}^{cis} : Enzymatic *cis*-to-*trans* rate constant (s^{-1})

k_{cat}^{trans} : Enzymatic *trans*-to-*cis* rate constant (s^{-1})

K_D^{cis} : Dissociation constant for the *cis* isomer (μM or mM)

K_{eq}^{bound} : On-enzyme ratio of *trans* to *cis* isomer

T: Temperature (K)

R: Gas constant ($8.314 J K^{-1} mol^{-1}$)

h: The Planck constant ($6.626 \times 10^{-34} m^2 kg/s$)

k_B : The Boltzmann constant ($1.381 \times 10^{-23} m^2 kg s^{-2} K^{-1}$)

CHAPTER 1

Background and Overview

Conformational Selection of Proline Isomers and the Role of Prolyl Isomerases

The peptide bond that connects amino acids in a protein is planar, as a result of its partial double bond character. This restricts its allowed torsion angles to only 0° (*cis*) or 180° (*trans*). Peptide bonds adopt the *trans* isomer almost exclusively, with the notable exception of those bonds preceding a proline residue. These so-called prolyl peptide bonds, by contrast, partition into an equilibrium of *cis* and *trans* populations in the absence of secondary structure (Fischer, 2000). This equilibrium typically ranges between 5-40% *cis*, depending on the residues immediately preceding and following the proline (Dasgupta et al., 2007; Pahlke et al., 2005; Reimer et al., 1998). Bulky aromatic groups such as tryptophan, tyrosine, and phenylalanine before the proline induce the largest population *cis* (Reimer et al., 1998). In a folded protein on the other hand, one isomer (*trans* more often than not) is usually stabilized over the other (Reimer et al., 1998; Wedemeyer et al., 2002). Likewise, protein-protein interactions are frequently isomer-specific, so that only one isomer participates in binding (De et al., 2012). The energy barrier between prolyl isomers is considerably high (~80 kJ/mol), resulting in very slow (~0.0005-0.003 s⁻¹ at 4° C) interconversion between isomers relative to other torsion angles in proteins (Figure 1.1A) (Fischer, 2000).

In some proteins, such as ribonuclease A, the isomer state of a proline residue is crucial to the protein's fold. In this case, a protein will fail to fold following synthesis on the ribosome until its proline residue is isomerized to the folding-competent isomer (Figure 1.1B). This effect is more pronounced for proteins that require a *cis* isomer to fold, and is compounded when proteins require multiple *cis*

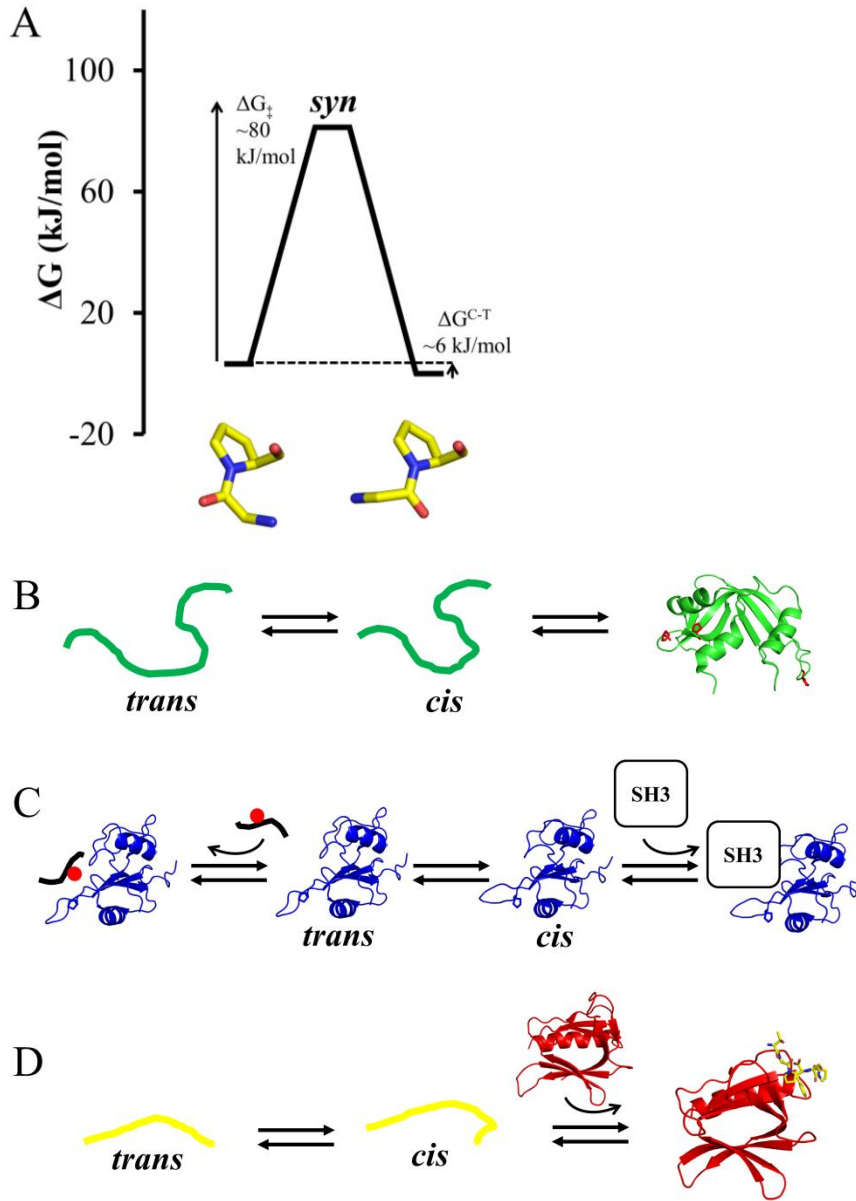


Figure 1.1: *Cis/trans* isomerization and its role in protein interactions and function. (A) Energy diagram portraying a typical free energy difference (ΔG^{C-T}) between the *cis* and *trans* isomers of a prolyl peptide bond, and a typical activation energy (ΔG^\ddagger) of isomerization (based on measurements extrapolated to 25° C from (Reimer et al., 1998)). (B) The native fold of ribonuclease A requires two proline residues to adopt the *cis* isomer and one to adopt the *trans* (simplified in figure), requiring rate-limiting isomerization steps for the protein to fold. (C) The SH2 domain of Itk adopts two conformations, depending on the isomer state of a proline residue. The *cis* isomer binds to the SH3 domain of Itk while the *trans* isomer binds to phosphotyrosine-containing sequences. (D) mGluR1 adopts a *cis*-Pro peptide bond when it binds to the EVH1 domain of Homer, suggesting that binding requires a rate-limiting isomerization step.

isomers (Dodge and Scheraga, 1996; Houry and Scheraga, 1996; Wedemeyer et al., 2002). Multiple families of enzymes have evolved that catalyze this isomerization, collectively called peptidyl-prolyl isomerases (PPIases) (Fischer and Aumuller, 2003).

Conformational heterogeneity and conformational selection are recurring themes in the regulation of protein-protein interactions (Boehr et al., 2009). Prolyl isomers can be thought of as a specific kind of conformational heterogeneity. There are a growing number of examples of proteins that exhibit two conformations which are linked to the isomer state of a key proline residue. For example, the adapter protein Crk adopts an inhibited conformation with a *cis* proline residue in equilibrium with an open, active conformation with this peptide bond adopting the *trans* isomer (Nicholson and Lu, 2007; Sarkar et al., 2011). Likewise, the binding specificity of the IL-2-inducible tyrosine kinase (Itk) SH2 domain is modulated by the isomer state of a proline within the domain (Figure 1.1C) (Colgan et al., 2004). Prolyl isomers have also been found to be linked to functional conformations in the ion channel of the 5-HT₃ receptor (Lummis et al., 2005), the C-type mannose-binding protein (Ng and Weis, 1998), and the *E. coli* protein IscU (Dai et al., 2012).

A simpler but possibly more widespread example of conformational selection of prolyl isomers is the recognition of short motifs by protein domains such as Src-homology 3 (SH3), Enabled/VASP Homology 1 (EVH1), Ubiquitin E2 variant (UEV), GYF, and WW domains (Zarrinpar et al., 2003). Binding motifs rich in proline, so-called proline-rich motifs, are a common target of such domains. Proline-rich motifs typically adopt a left-handed polyproline II helix (PPII) structure, a relatively rigid secondary structure with *trans* peptide bonds. PPII helices are generally solvent exposed, allowing for rapid and reversible binding, with the carbonyl groups of the backbone available to form hydrogen bonds (Siligardi and Drake, 1995).

Furthermore, the rigidity of the PPII helix lowers the loss of conformational entropy upon binding, allowing for tighter interactions than might be achieved by other exposed sequences (Kay et al., 2000). These features help to explain why proline-rich motifs are popular binding targets in cell signaling, which often depends on fast and reversible protein-protein interactions. However, the preponderance of prolines in such motifs presents a potential obstacle to achieving rapid protein interactions due to the presence of slowly-exchanging *cis* and *trans* populations (Reimer et al., 1998), which will not generally both be compatible with binding. In the most striking example of isomer selection of proline-rich motifs, the crystal structure of the EVH1 domain of Homer bound to a peptide from a metabotropic glutamate receptor (mGluR1) suggests that this interaction is specific for the *cis* isomer of the S₁₁₄₉-P₁₁₅₀ peptide bond in mGluR1 (Figure 1.1D) (Beneken et al., 2000). Less dramatically, other structures of proline-rich motifs bound to their binding domains show *trans* peptide bonds (pdb.org).

There are more examples of conformational selection of prolyl isomers that don't involve binding modules that bind proline-rich motifs. A notable example is the conformational specificity of the Ssu72 phosphatase which dephosphorylates specific sites in the RNA polymerase C-terminal domain (CTD) (Krishnamurthy et al., 2004). Ssu72 was originally predicted to be a tyrosine phosphatase (Meinhart et al., 2003), but rather than recognizing phosphotyrosine it has been shown that it actually recognizes the *cis* isomer of pS₅-P₆, which inserts into the deep catalytic pocket of the enzyme the way a tyrosine sidechain would (Xiang et al., 2010; Zhang and Zhang, 2011). The phosphorylation-specific isomerase Pin1 is able to accelerate Ssu72-mediated dephosphorylation of the CTD *in vitro* (Werner-Allen et al., 2010; Xiang et al., 2010) and while mutations of the Pin1 homologue in yeast (Ess1) cause a temperature-sensitive phenotype, Ssu72 overexpression rescues the phenotype

(Krishnamurthy et al., 2009).

Yet another example of proline isomer selection is the conformational specificity of the SCF(TIR1)-mediated degradation of AUX/IAA proteins in auxin signaling in plants. The SCF ubiquitin ligase TIR1 specifically binds to the *cis* isomer of W₅₉-P₆₀ in the GWPPV degron motif in IAA in the presence of the signaling molecule auxin, targeting it for degradation (Tan et al., 2007). In a cell-free auxin response assay a PPIase was necessary for IAA degradation (Dharmasiri et al., 2003). Indeed, isomerases such as cyclophilin A (CypA) are widely involved in signaling in plants (Kumari et al., 2013). Presently, however, the significance of the isomer-specificity of the TIR1 recognition of IAA proteins does not seem to be well-appreciated (Kumari et al., 2013).

While most PPIases (such as the cyclophilins, FKBP, and for the most part, parvulins) exhibit low sequence specificity (Schmidpeter et al., 2011; Zoldak et al., 2009), the parvulin Pin1 is specific for phosphorylated Ser/Thr-Pro sites (Yaffe et al., 1997). Up- and down-regulation of Pin1 activity seems to be connected to multiple human diseases including asthma (Shen et al., 2009), Alzheimer's disease, and many cancers, as well as aging (Lee et al., 2011). Although the role of Pin1 in accelerating *cis*-proline dephosphorylation by Ssu72 seems to be the clearest mechanism of Pin1's function in the cell (Werner-Allen et al., 2010), Pin1 is also known to accelerate dephosphorylation by the *trans* specific phosphatase PP2A (Zhou et al., 2000). In principle, Pin1 may accelerate isomer-specific binding in addition to isomer-specific enzymatic reactions. Phosphorylated Ser/Thr-Pro is a common motif phosphorylated by the so-called proline-directed kinases (Ubersax and Ferrell, 2007), so Pin1 has a long list of potential targets, making it a pleiotropic enzyme.

Cyclophilin A (CypA or Cyp18) is an isomerase most commonly associated with its role in the action of the immunosuppressant drug cyclosporine. Cyclosporine

binds cooperatively to CypA and the phosphatase calcineurin, inhibiting both enzymes (Liu et al., 1991). Inhibition of calcineurin activity then disrupts signaling in T-cells (Clipstone and Crabtree, 1992). However, the isomerase activity-or inhibition of it- is not important for this process because isomerase-dead CypA mutants with wild-type binding for cyclosporine still inhibit calcineurin with wild-type activity (Zydowsky et al., 1992). In a similar example of the versatility of CypA function, CypA can be secreted to the extracellular space where it acts as a chemokine through binding to the CD147 receptor. However, this function is also independent of CypA activity (Song et al., 2011). CypA is involved in the replication of various RNA viruses such as HCV, but its role is not clear as in some cases it also exhibits antiviral activity, such as in the case of HIV (Nagy et al., 2011).

CypA isomerase activity is crucial for its function as a foldase (Wedemeyer et al., 2002), for regulating the conformational states of Crk and Itk as described above (Breheny et al., 2003; Sarkar et al., 2011), and for accelerating phosphorylation by ERK2 (Weiwad et al., 2004). CypA isomerization also seems to be required for progression of cytokinesis in Jurkat cells, though it is not known what its target is in this process (Bannon et al., 2012). Investigations of the roles of CypA isomerase activity are hampered by the existence of many other isomerases with similar activities (Gothel and Marahiel, 1999; Schmidpeter et al., 2011; Zoldak et al., 2009). We have chosen CypA as an isomerase to demonstrate the role of isomerization in VASP (Vasodilator-stimulated phosphoprotein) binding because it is abundant in the cytoplasm. Nevertheless in the cell isomerization of zyxin and IRAK1 (Interleukin-1 receptor associated kinase 1) may well be executed by another enzyme.

Ena/VASP Function and Regulation

Ena/VASP proteins (Mena, VASP, and Evl in mammals) are cytoskeletal

rearrangement proteins that play central roles in cell migration and the control of cell shape (Krause et al., 2003). Ena/VASP proteins control the geometry and dynamics of actin filaments within lamellipodia (Bear et al., 2002), and are crucial for the formation of filopodia in certain contexts (Lebrand et al., 2004; Mejillano et al., 2004). They are also important in the processes of phagocytosis (Coppolino et al., 2001), cell motility (Bear et al., 2000; Bear et al., 2002; Krause et al., 2003), axon guidance in neurons (Goh et al., 2002), and cell-cell interactions (Grevengoed et al., 2001; Vasioukhin et al., 2000). Notably, they are implicated in tumor development by their ability to increase cancer cell invasiveness (Philippart et al., 2008). Like formins, Ena/VASP proteins are processive actin polymerases that recruit monomeric actin to the growing barbed end of actin filaments (Breitsprecher et al., 2011; Hansen and Mullins, 2010). In addition, Ena/VASP proteins protect the barbed end of actin filaments from capping proteins, which otherwise halt actin polymerization upon binding filamentous actin (Barzik et al., 2005; Bear and Gertler, 2009; Bear et al., 2002). This anti-capping function is not observed when VASP is in solution, but only when it is immobilized on beads (Breitsprecher et al., 2011), which mimics its punctate distribution in cells (Bachmann et al., 1999; Vasioukhin et al., 2000). Ena/VASP proteins also display an actin bundling activity which is necessary for formation of filopodia in *Dictyostelium* (Schirenbeck et al., 2006), as well as an anti-branching activity (Bear et al., 2002; Skoble et al., 2001).

There has been some debate on the significance of the processive actin polymerase and anti-capping activities of VASP, because the polymerase activity has been deemed very weak in *in vitro* assays (~1.5 x background spontaneous actin polymerization) (Breitsprecher et al., 2008; Breitsprecher et al., 2011), while the capping protein gelsolin prevented VASP activity in an early report (Boujemaa-Paterski et al., 2001). This first controversy appears to be resolved by the fact that

VASP has a weak affinity for monomeric actin (10.3 μM) (Breitsprecher et al., 2011), while the concentration of actin in the cell is higher than this ($\sim 150 \mu\text{M}$) (Koestler et al., 2009) and the concentration used in *in vitro* assays is lower ($\leq 4 \mu\text{M}$). Likewise weighing the evidence in the literature for the anti-capping activity of VASP against the early report which used a complex mixture including ActA and Arp2/3 (Boujemaa-Paterski et al., 2001), which may have led to difficult-to-interpret results, has led researchers to favor the view that VASP's anti-capping activity is functionally important (Bear and Gertler, 2009).

The domain architecture of VASP is shown in Figure 1.2. VASP contains an N-terminal EVH1 (Ena/VASP Homology 1) domain, a proline-rich region, and an EVH2 (Ena/VASP Homology 2) domain which is comprised of a G-actin binding motif (GAB), a filamentous F-actin binding motif (FAB), and a 15-residue repeat that forms a coiled coil which tetramerizes the protein (Krause et al., 2003). The EVH1 domain contributes to the cellular localization of VASP by binding to the proline-rich (W/F)Px ϕ P motif, where x is any amino acid and ϕ is an aliphatic residue. This motif most commonly occurs as the sequence "FPPPP," and is found in various cytoskeletal proteins such as zyxin, lamellipodin, and vinculin (Ball et al., 2000; Niebuhr et al., 1997). The proline-rich region of Ena/VASP proteins has multiple binding sites for the G-actin-binding protein Profilin (Reinhard et al., 1995), as well as binding sites for multiple SH3 and WW domains of various proteins, such as Abl (Gertler et al., 1996), Src (Gertler et al., 1996), and Fe65 (Ermekova et al., 1997). The SH3 and WW binding sites are generally divergent between the homologues VASP, Mena, and Evl. The G- and F-actin binding motifs are necessary for the actin nucleation (Walders-Harbeck et al., 2002) and actin bundling (Bachmann et al., 1999) activities of VASP, respectively, while tetramerization of VASP enhances these functions (Bachmann et al., 1999; Walders-Harbeck et al., 2002).

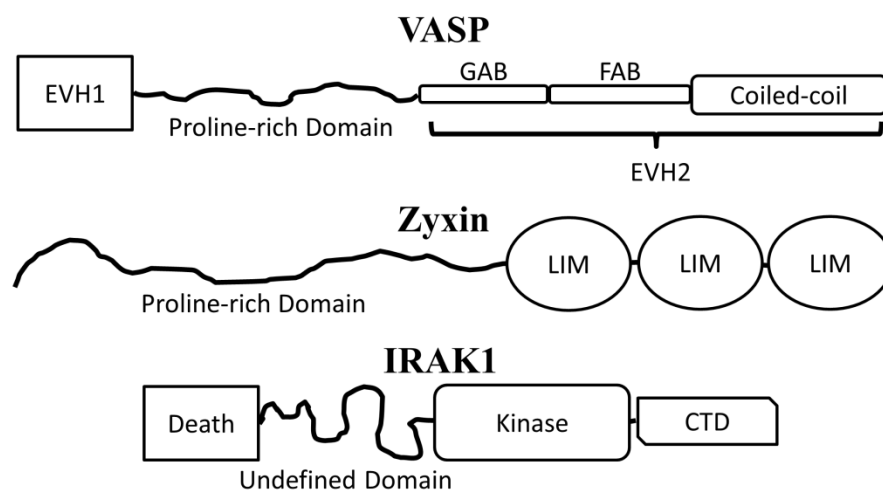


Figure 1.2: Domain architectures of the proteins VASP, zyxin, and IRAK1.

VASP is regulated by phosphorylation at multiple sites. PKA- and PKG-mediated phosphorylation of Ser157, located immediately before the proline-rich region, changes VASP localization from primarily in stress fibers to primarily in focal adhesions in mouse endothelial cells (Benz et al., 2009). This may be related to the decreased affinity of phospho-S157 VASP for zyxin (Moody et al., 2009), which also appears in both stress fibers and focal adhesions (Crawford and Beckerle, 1991). Zyxin can obstruct its FPPPP VASP binding sites by a head-to-tail interaction with one of its own LIM domains, but exposes them in the presence of VASP, most likely because one of its LIM domains also binds VASP's proline-rich region. However, phosphorylation of VASP at S157 prevents this LIM-domain interaction, keeping the VASP-binding sites in zyxin obstructed (Moody et al., 2009). Phosphorylation of VASP in the EVH1 domain at Tyr39 also influences VASP localization. This phosphorylation is performed by Abl tyrosine kinase in Bcr-Abl-transformed leukemic cells, and reduces VASP accumulation in focal adhesions (Maruoka et al., 2012). Remarkably, Tyr39 phosphorylation diminishes VASP binding to zyxin, despite Tyr39's placement on the opposite face of the EVH1 domain from the proline-rich sequence binding site. VASP is also phosphorylated at S239 by both PKA and PKG, and at T278 by AMPK. These two sites are positioned directly after the GAB and FAB sites in the EVH2 domain, respectively. Phosphorylation at either of these sites diminishes VASP-mediated actin filament assembly (Benz et al., 2009).

EVH1 and Ran-Binding Domains

EVH1 domains are found in Ena/VASP proteins, the related actin cytoskeleton-rearrangement protein WASP and its family members, the postsynaptic density protein Homer and its family members, and the recently-discovered related Sprouty and Spred families (Renfranz and Beckerle, 2002). Additionally, EVH1

domains have sequence and structural homology to the Ran-binding domains (RanBD) of the RanBP1 family (Callebaut et al., 1998). EVH1 and Ran-binding domains adopt a fold similar to PH domains, with a 7-strand antiparallel β -sandwich packed against a long C-terminal helix (Fedorov et al., 1999; Vetter et al., 1999). The EVH1 domains of VASP, WASP, and Homer all bind proline-rich motifs, with differing sequence specificities (shown in Figure 1.3), while it is not known what the Sprouty and Spred EVH1 domains bind (Ball et al., 2000; Beneken et al., 2000; Harmer et al., 2005; Niebuhr et al., 1997; Volkman et al., 2002). Ran-binding domains do not bind proline-rich sequences but rather bind the small GTPase Ran (Beddow et al., 1995).

There is now a wealth of crystal and NMR structures available of EVH1 domains bound to peptides, and RanBDs bound to Ran (www.pdb.org). Although the binding specificity differs between domains, there are some conserved features of EVH1/RanBD interactions (Figure 1.3). The binding pocket that makes the most crucial contacts to the bound peptide is conserved throughout EVH1 and Ran-binding domains. Furthermore, EVH1 domains all recognize the same PPII structure despite the fact that the orientation of the WIP peptide bound to WASP-EVH1 is in the opposite orientation compared to Homer and VASP EVH1 domains (Volkman et al., 2002). This can be explained by the rotational pseudosymmetry of the PPII structure, in analogy to the similar flexibility of SH3 domain proline motif recognition (Feng et al., 1994). Lastly, EVH1 domains employ a conserved network of aromatic and polar side-chains (in VASP, residues M14, Y16, W23, F79, and Q81) to directly interact with the carbonyl groups of their proline-rich binding motifs (Volkman et al., 2002).

Some EVH1 domains diverge from this framework. The most extreme example is the EVH1 domain of Mena, which in addition to canonical binding to FPPPP motifs can also bind the third LIM domain of Tes, a feature unique to

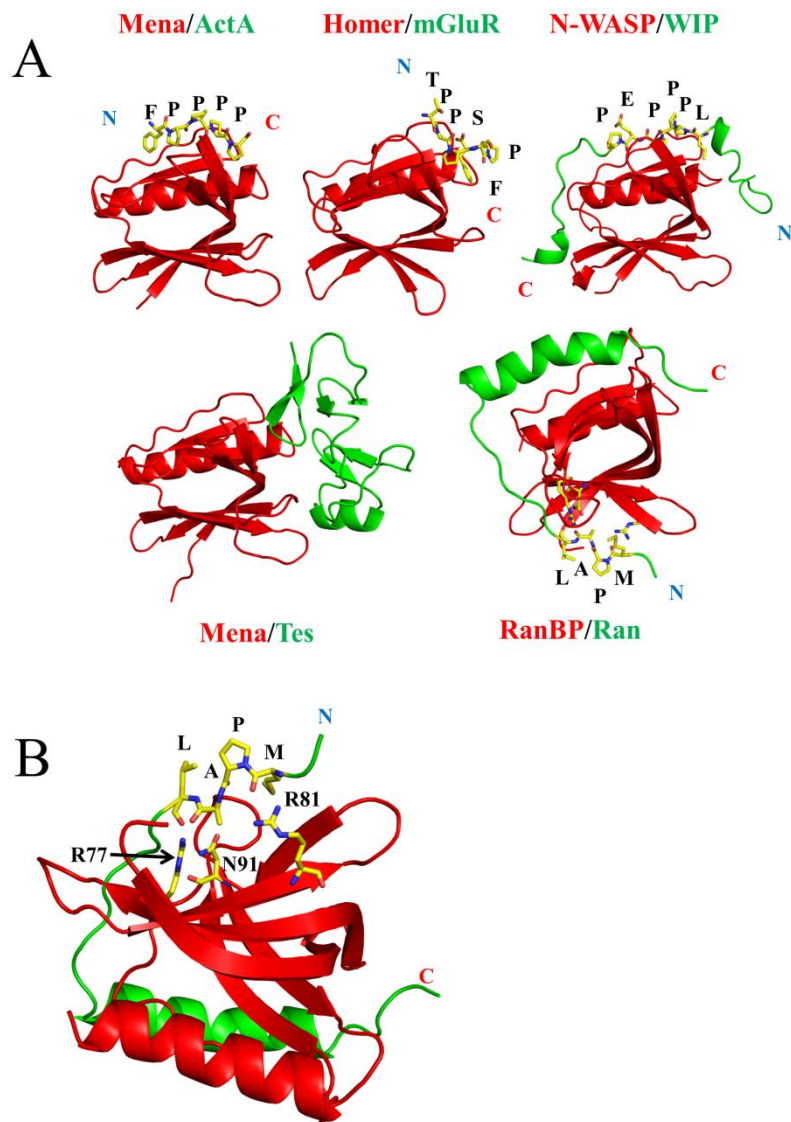


Figure 1.3: Conserved features of EVH1/RanBD interactions. (A) The EVH1 domains of Mena, Homer, and N-WASP all bind proline-rich sequences (specified) in a conserved concave groove. Mena also binds the LIM domain of Tes at an overlapping site. (B) The first Ran-binding domain of RanBP2 binds a helical segment of Ran in this concave surface, while binding an extended sequence of Ran in a second binding site on the opposite face. RanBP2 residues R77, R88, and N91 participate in this second interaction. (Figure adapted from (Volkman et al., 2002))

Mena (Boeda et al., 2007). Less extreme is the interaction between WASP-EVH1 and WIP, which wraps around the EVH1 domain to make additional contacts above and below the canonical binding site, utilizing residues in three distinct conserved WIP epitopes (Peterson et al., 2007; Volkman et al., 2002). The interaction between the RanBD1 of RanBP2 and Ran differs from EVH1 domain interactions in three main ways. First of all, the conserved binding site of RanBD1 binds a Ran sequence that adopts an α -helix followed by an acidic DEDDDL motif, as opposed to the proline-rich sequences bound by WASP, VASP, and Homer. Secondly, the N-terminal sequence of RanBD1 extends to make significant contacts with Ran. Third, the N-terminal sequence of Ran extends to make significant contacts with the face opposite the primary binding site of RanBD1, which is not contacted analogously in any EVH1 domain architectures. Specifically, the sidechains of RanBP2 residues R77, R81, and N91 hydrogen bond with the carbonyl groups of the backbone of Ran residues M179, A181, and L182 (Vetter et al., 1999). Notably, this Ran sequence adopts a PPII helix, and its interaction with RanBD1 is distinctly reminiscent of the canonical mechanism of PPII recognition by these domains, in which sidechains hydrogen bond with the carbonyl groups of the PPII helix.

Zyxin Function, Regulation, and Interaction with VASP

Zyxin is a LIM domain protein that localizes primarily to focal adhesions, stress fibers, and adherens junctions (Beckerle, 1986; Crawford and Beckerle, 1991). In response to cellular mechanical stress, zyxin is phosphorylated at residue S142, which induces it to dissociate from focal adhesions and bind to damaged stress fibers (Hirata et al., 2008; Hoffman et al., 2012; Yoshigi et al., 2005). This may work by disrupting an inhibitory head-to-tail interaction which occurs between the proline-rich

region of zyxin and its LIM domains (Moody et al., 2009), which target it to cellular locations (Nix et al., 2001). Recruitment of VASP and the actin cross-linking protein α -actinin by zyxin then serves to repair and reinforce actin stress fibers (Hoffman et al., 2012).

In addition to directly participating in the mechanical stress response, zyxin is also translocated to the nucleus in response to cyclic stretch in endothelial cells where it regulates transcription of a large number of stretch-sensitive genes (Nix et al., 2001; Wojtowicz et al., 2010). Additionally, mislocalization of zyxin by disrupting its interaction with α -actinin impacts cell migration and spreading (Drees et al., 1999).

The domain architecture of zyxin is shown in Figure 1.2. Zyxin contains an N-terminal region of undetermined structure which binds to α -actinin (Drees et al., 1999) as well as the cytoskeletal proteins LASP-1 and LIM-nebulette (Li et al., 2004). Following this sequence is a long sequence highly enriched in prolines and acidic residues, which contains four (W/F)Px ϕ P VASP-binding motifs (Drees et al., 2000; Niebuhr et al., 1997). Lastly, zyxin has three LIM domains on its C-terminus which are involved in both localizing zyxin (Nix et al., 2001) and regulating its interaction with VASP (Moody et al., 2009).

The appearance of four VASP binding sites in the proline-rich region of zyxin is reminiscent of several other VASP-binding proteins including lamellipodin, which contains five such sites, ActA, which contains four, and vinculin and palladin, which each contain two. This trend has been suggested to serve to strengthen the interaction with the tetrameric VASP, which in principle should bind a protein with four binding sites considerably tighter by the principle of avidity. Notably, in short peptide form none of the (W/F)Px ϕ P motifs bind VASP-EVH1 with especially tight affinity ($K_D > 60 \mu\text{M}$) and the fourth motif has not shown any binding at all. Alternatively, four binding sites may instead bring together four VASP tetramers, which may function

differently than an individual VASP tetramer (Ball et al., 2000). As mentioned earlier, it has been shown that VASP only exhibits its anti-capping activity when clustered on beads and not in solution (Breitsprecher et al., 2011). Lastly, the proximity of the second, third, and fourth binding sites in zyxin raise the question of whether or not these sites can all be simultaneously bound by separate EVH1 domains.

Finally, it is interesting to note that VASP binds not just to the proline-rich region of zyxin but also to the LIM domain region (Moody et al., 2009). This not only allows for regulation of the interaction by either phosphorylation of VASP (Moody et al., 2009) or phosphorylation of zyxin by Akt (Call et al., 2011), but also changes the actin polymerase activity of VASP. When full-length zyxin, but not either of the individual regions, binds to VASP, the bundling and actin polymerase activity of VASP is greatly reduced (Grange et al., 2012).

IRAK1 Function and Interaction with VASP

The IRAK (Interleukin-1 receptor associated kinase) family kinases play central roles in the innate immune response by participating in TLR and IL-1R signaling pathways (Flannery and Bowie, 2010). These signaling pathways coordinate such processes as the antiviral response, inflammation, and activation of the adaptive immune response (Martin and Wesche, 2002). Toll-like receptors recognize PAMPs which are common to certain pathogens but not the host, such as double stranded RNA (Alexopoulou et al., 2001), unmethylated CpG DNA sites (Hemmi et al., 2000), lipopolysaccharide (Hoshino et al., 1999), and flagellin (Hayashi et al., 2001). IL-1 receptors on the other hand recognize cytokines such as IL-1 β and IL-18, which are expressed in response to TLR signaling. IL-1R and TLR signaling pathways share common downstream components, including the adapter MyD88, Tollip, and the members of the IRAK family of kinases (O'Neill, 2008).

The IRAK kinases, IRAK1, IRAK2, IRAK3 (IRAKM), and IRAK4 in mammals, play related but distinct roles in innate immunity. Although all four proteins contain a kinase domain, IRAKM lacks kinase activity (Flannery and Bowie, 2010). IRAK1, a focus of this dissertation, is implicated in numerous autoimmune and inflammatory diseases including experimental autoimmune encephalomyelitis (an animal model of multiple sclerosis) (Deng et al., 2003), endotoxemia (Singh and Li, 2012), atherosclerosis (Lakoski et al., 2007), and systemic lupus erythematosus (Jacob et al., 2009; Kaufman et al., 2013). On a cellular level, IRAK1 is important for production of IL-6 in response to stimulation of fibroblasts with IL-1 (Kanakaraj et al., 1998), production of IFN- γ in response to stimulation of Th1 cells with IL-18 (Kanakaraj et al., 1999), and production of IFN- α in response to TLR7 or TLR9 activation (Uematsu et al., 2005).

The domain architecture of IRAK1 is shown in Figure 1.2. IRAK1 consists of an N-terminal death domain which is required for recruitment to TLR and IL-1R signaling complexes (Lin et al., 2010; Wesche et al., 1997). This is followed by the undefined domain (IRAK1-UD), a proline- and serine-rich region which is involved in binding to various proteins including Pin1 (Tun-Kyi et al., 2011), Pellino (Lin et al., 2008), NEMO (Conze et al., 2008), and VASP (Gan and Li, 2010). Following this region is a kinase domain, which is thought to autophosphorylate the proline-rich domain as well as additional targets (Kollewe et al., 2004; Uematsu et al., 2005). Finally, IRAK1 contains C-terminal domain which contains multiple TRAF6 binding sites (Jiang et al., 2002), and is thought to regulate IRAK1 activity by associating with the death domain (Nguyen et al., 2009).

IRAK1, complexed with Tollip in the cytosol (Burns et al., 2000), is recruited to signaling complexes at the plasma membrane or the cytoplasmic face of endosomes following Toll-like or IL-1 receptor stimulation (Gottipati et al., 2008). The death

domain of IRAK1 participates in a helical array of the death domains of the adapter MyD88, IRAK4, and IRAK1 (or the partially-redundant IRAK2), the so-called Myddosome (Lin et al., 2010). IRAK4 next phosphorylates IRAK1 on residues T209 and T387. This leads to activation of the kinase activity of IRAK1 and extensive autophosphorylation of the UD (Kollewe et al., 2004). This phosphorylation causes dissociation of IRAK1 from the Myddosome as well as Tollip from IRAK1 (Gottipati et al., 2008; Wesche et al., 1997). Depending on the signaling pathway, IRAK1 can then perform various functions, including phosphorylating IRF7 (Uematsu et al., 2005), becoming sumoylated and translocated to the nucleus (Su et al., 2007), or forming a complex with TRAF6, IRAK4, and Pellino leading to TAK1 activation (Qian et al., 2001).

IRAK1 was recently shown to co-immunoprecipitate with VASP in human THP1 and MAT-2 cells. Furthermore, in murine bone marrow-derived macrophages (BMDM), IRAK1 is necessary for sustained PKC-induced phosphorylation of VASP at S157 in response to treatment with PMA, a PKC activator. This was suggested to influence cell migration, as IRAK1-deficient murine BMDMs migrated slower than wt cells in response to PMA treatment (Gan and Li, 2010). The connection between these two observations is not clear, however, because while human IRAK1 contains a VASP-binding site with the sequence LWPPPP in the proline-rich domain, mouse IRAK1 does not appear to contain a VASP-binding site.

The interaction between IRAK1 and VASP is notable in that it is the only known VASP-EVH1-binding motif to contain a tryptophan instead of phenylalanine, though tryptophan-containing sequences have been shown to bind tighter (Ball et al., 2000; Niebuhr et al., 1997; Zimmermann et al., 2003). Furthermore, this motif does not contain flanking negatively charged residues, which have been shown to be important for tight interactions with VASP-EVH1 (Ball et al., 2000; Carl et al., 1999).

Rather, the VASP-binding motif in IRAK1 is flanked by serines, one of which (S173) is known to be phosphorylated (Tun-Kyi et al., 2011), and the other of which (S166) may be as well given the extensive autophosphorylation of the IRAK1-UD upon IRAK1 activation (Kollewe et al., 2004).

Experimental Approach

This dissertation describes, for the most part, studies of protein-protein and protein-peptide interactions, with a focus on proline-rich domains and sequences, which have relied heavily on NMR spectroscopy. This has been a successful approach for a few reasons. Proline isomerization, a key topic in this dissertation, occurs on the timescale of minutes or longer, resulting in distinct *cis* and *trans* peaks for each isomer in an NMR spectrum (Grathwohl and Wuthrich, 1976). Isomerization can be accelerated into the NMR-sensitive timescale of seconds with an isomerase enzyme such as CypA or Pin1, allowing for identification of pairs of isomers (Farrow et al., 1994). Therefore, NMR provides more information about *cis-trans* equilibria than the static structures produced by X-ray crystallography. Secondly, these experiments have taken advantage of the utility of NMR spectroscopy to precisely measure moderate-to-weak binding affinities ($K_D > 10 \mu\text{M}$) with atomic-level information, even when the binding scheme being studied is significantly more complex than a simple one-to-one interaction (Kovrigin, 2012). We have mostly relied on protein titrations using routine ^{15}N - ^1H HSQC spectra, and have aimed to extract as much information as possible from these experiments by paying close attention to minor details in the binding curves as well as to lineshapes. Lastly, we have benefitted from the sensitivity of NMR spectra to chemical exchange (both inter- and intramolecular) on the timescale of microseconds to seconds, allowing for measurements of binding rates and enzymatic rate constants by the analysis of lineshapes (Kovrigin, 2012; Palmer, 2004).

Our experiments have been limited to *in vitro* analysis of protein and peptide interactions—as such it has been important to maintain our focus on interactions that are deemed both biologically relevant and likely to return additional insights upon scrutiny of NMR data. We have largely focused on the intrinsically disordered proline-rich domains of IRAK1 and zyxin, and the interactions between VASP-EVH1 and its binding site(s) in these domains. This seems an odd choice for NMR spectroscopy, as unstructured proline-rich regions tend to yield difficult, overlapped spectra, but we have benefitted from key details of the sequences of these domains. Firstly, the VASP binding site in IRAK1 features a tryptophan, which yields a sidechain indole amide peak well-resolved from the rest of the spectrum. Secondly, the zyxin sequence used was short enough and enriched so much in proline (which does not produce a peak in an ^{15}N - ^1H HSQC) that overlap was not a major issue and assignments for non-proline residues were easily achievable. Finally, both sequences are very soluble and produce very sharp peaks due to their extreme flexibility and relatively fast tumbling rates.

REFERENCES

- Alexopoulou, L., Holt, A.C., Medzhitov, R., and Flavell, R.A. (2001). Recognition of double-stranded RNA and activation of NF-kappaB by Toll-like receptor 3. *Nature* *413*, 732-738.
- Bachmann, C., Fischer, L., Walter, U., and Reinhard, M. (1999). The EVH2 domain of the vasodilator-stimulated phosphoprotein mediates tetramerization, F-actin binding, and actin bundle formation. *J Biol Chem* *274*, 23549-23557.
- Ball, L.J., Kuhne, R., Hoffmann, B., Hafner, A., Schmieder, P., Volkmer-Engert, R., Hof, M., Wahl, M., Schneider-Mergener, J., Walter, U., *et al.* (2000). Dual epitope recognition by the VASP EVH1 domain modulates polyproline ligand specificity and binding affinity. *EMBO J* *19*, 4903-4914.
- Bannon, J.H., O'Donovan, D.S., Kennelly, S.M., and Mc Gee, M.M. (2012). The peptidyl prolyl isomerase cyclophilin A localizes at the centrosome and the midbody and is required for cytokinesis. *Cell Cycle* *11*, 1340-1353.
- Barzik, M., Kotova, T.I., Higgs, H.N., Hazelwood, L., Hanein, D., Gertler, F.B., and Schafer, D.A. (2005). Ena/VASP proteins enhance actin polymerization in the presence of barbed end capping proteins. *J Biol Chem* *280*, 28653-28662.
- Bear, J.E., and Gertler, F.B. (2009). Ena/VASP: towards resolving a pointed controversy at the barbed end. *J Cell Sci* *122*, 1947-1953.
- Bear, J.E., Loureiro, J.J., Libova, I., Fassler, R., Wehland, J., and Gertler, F.B. (2000). Negative regulation of fibroblast motility by Ena/VASP proteins. *Cell* *101*, 717-728.
- Bear, J.E., Svitkina, T.M., Krause, M., Schafer, D.A., Loureiro, J.J., Strasser, G.A., Maly, I.V., Chaga, O.Y., Cooper, J.A., Borisy, G.G., and Gertler, F.B. (2002). Antagonism between Ena/VASP proteins and actin filament capping regulates fibroblast motility. *Cell* *109*, 509-521.
- Beckerle, M.C. (1986). Identification of a new protein localized at sites of cell-substrate adhesion. *J Cell Biol* *103*, 1679-1687.
- Beddow, A.L., Richards, S.A., Orem, N.R., and Macara, I.G. (1995). The Ran/TC4 GTPase-binding domain: identification by expression cloning and characterization of a conserved sequence motif. *Proc Natl Acad Sci U S A* *92*, 3328-3332.
- Beneken, J., Tu, J.C., Xiao, B., Nuriya, M., Yuan, J.P., Worley, P.F., and Leahy, D.J. (2000). Structure of the Homer EVH1 domain-peptide complex reveals a new twist in polyproline recognition. *Neuron* *26*, 143-154.
- Benz, P.M., Blume, C., Seifert, S., Wilhelm, S., Waschke, J., Schuh, K., Gertler, F., Munzel, T., and Renne, T. (2009). Differential VASP phosphorylation controls remodeling of the actin cytoskeleton. *J Cell Sci* *122*, 3954-3965.
- Boeda, B., Briggs, D.C., Higgins, T., Garvalov, B.K., Fadden, A.J., McDonald, N.Q., and Way, M. (2007). Tes, a specific Mena interacting partner, breaks the rules for EVH1 binding. *Mol Cell* *28*, 1071-1082.
- Boehr, D.D., Nussinov, R., and Wright, P.E. (2009). The role of dynamic conformational ensembles in biomolecular recognition. *Nat Chem Biol* *5*, 789-796.
- Boujemaa-Paterski, R., Gouin, E., Hansen, G., Samarin, S., Le Clainche, C., Didry, D., Dehoux, P., Cossart, P., Kocks, C., Carlier, M.F., and Pantaloni, D. (2001). *Listeria* protein ActA mimics WASp family proteins: it activates filament barbed end branching by Arp2/3 complex. *Biochemistry* *40*, 11390-11404.

Breheny, P.J., Laederach, A., Fulton, D.B., and Andreotti, A.H. (2003). Ligand specificity modulated by prolyl imide bond Cis/Trans isomerization in the Itk SH2 domain: a quantitative NMR study. *J Am Chem Soc* 125, 15706-15707.

Breitsprecher, D., Kiesewetter, A.K., Linkner, J., Urbanke, C., Resch, G.P., Small, J.V., and Faix, J. (2008). Clustering of VASP actively drives processive, WH2 domain-mediated actin filament elongation. *EMBO J* 27, 2943-2954.

Breitsprecher, D., Kiesewetter, A.K., Linkner, J., Vinzenz, M., Stradal, T.E., Small, J.V., Curth, U., Dickinson, R.B., and Faix, J. (2011). Molecular mechanism of Ena/VASP-mediated actin-filament elongation. *EMBO J* 30, 456-467.

Burns, K., Clatworthy, J., Martin, L., Martinon, F., Plumpton, C., Maschera, B., Lewis, A., Ray, K., Tschopp, J., and Volpe, F. (2000). Tollip, a new component of the IL-1RI pathway, links IRAK to the IL-1 receptor. *Nat Cell Biol* 2, 346-351.

Call, G.S., Chung, J.Y., Davis, J.A., Price, B.D., Primavera, T.S., Thomson, N.C., Wagner, M.V., and Hansen, M.D. (2011). Zyxin phosphorylation at serine 142 modulates the zyxin head-tail interaction to alter cell-cell adhesion. *Biochem Biophys Res Commun* 404, 780-784.

Callebaut, I., Cossart, P., and Dehoux, P. (1998). EVH1/WH1 domains of VASP and WASP proteins belong to a large family including Ran-binding domains of the RanBP1 family. *FEBS Lett* 441, 181-185.

Carl, U.D., Pollmann, M., Orr, E., Gertler, F.B., Chakraborty, T., and Wehland, J. (1999). Aromatic and basic residues within the EVH1 domain of VASP specify its interaction with proline-rich ligands. *Curr Biol* 9, 715-718.

Clipstone, N.A., and Crabtree, G.R. (1992). Identification of calcineurin as a key signalling enzyme in T-lymphocyte activation. *Nature* 357, 695-697.

Colgan, J., Asmal, M., Neagu, M., Yu, B., Schneidkraut, J., Lee, Y., Sokolskaja, E., Andreotti, A., and Luban, J. (2004). Cyclophilin A regulates TCR signal strength in CD4+ T cells via a proline-directed conformational switch in Itk. *Immunity* 21, 189-201.

Conze, D.B., Wu, C.J., Thomas, J.A., Landstrom, A., and Ashwell, J.D. (2008). Lys63-linked polyubiquitination of IRAK-1 is required for interleukin-1 receptor- and toll-like receptor-mediated NF-kappaB activation. *Mol Cell Biol* 28, 3538-3547.

Coppolino, M.G., Krause, M., Hagendorff, P., Monner, D.A., Trimble, W., Grinstein, S., Wehland, J., and Sechi, A.S. (2001). Evidence for a molecular complex consisting of Fyb/SLAP, SLP-76, Nck, VASP and WASP that links the actin cytoskeleton to Fcgamma receptor signalling during phagocytosis. *J Cell Sci* 114, 4307-4318.

Crawford, A.W., and Beckerle, M.C. (1991). Purification and characterization of zyxin, an 82,000-dalton component of adherens junctions. *J Biol Chem* 266, 5847-5853.

Dai, Z., Tonelli, M., and Markley, J.L. (2012). Metamorphic protein IscU changes conformation by cis-trans isomerizations of two peptidyl-prolyl peptide bonds. *Biochemistry* 51, 9595-9602.

Dasgupta, B., Chakrabarti, P., and Basu, G. (2007). Enhanced stability of cis Pro-Pro peptide bond in Pro-Pro-Phe sequence motif. *FEBS Lett* 581, 4529-4532.

De, S., Greenwood, A.I., Rogals, M.J., Kovrigin, E.L., Lu, K.P., and Nicholson, L.K. (2012). Complete thermodynamic and kinetic characterization of the isomer-specific interaction between Pin1-WW domain and the amyloid precursor protein cytoplasmic tail phosphorylated at Thr668. *Biochemistry* 51, 8583-8596.

Deng, C., Radu, C., Diab, A., Tsen, M.F., Hussain, R., Cowdery, J.S., Racke, M.K., and Thomas, J.A. (2003). IL-1 receptor-associated kinase 1 regulates susceptibility to organ-specific autoimmunity. *J Immunol* 170, 2833-2842.

Dharmasiri, N., Dharmasiri, S., Jones, A.M., and Estelle, M. (2003). Auxin action in a cell-free system. *Curr Biol* 13, 1418-1422.

Dodge, R.W., and Scheraga, H.A. (1996). Folding and unfolding kinetics of the proline-to-alanine mutants of bovine pancreatic ribonuclease A. *Biochemistry* 35, 1548-1559.

Drees, B., Friederich, E., Fradelizi, J., Louvard, D., Beckerle, M.C., and Golsteyn, R.M. (2000). Characterization of the interaction between zyxin and members of the Ena/vasodilator-stimulated phosphoprotein family of proteins. *J Biol Chem* 275, 22503-22511.

Drees, B.E., Andrews, K.M., and Beckerle, M.C. (1999). Molecular dissection of zyxin function reveals its involvement in cell motility. *J Cell Biol* 147, 1549-1560.

Ermekova, K.S., Zambrano, N., Linn, H., Minopoli, G., Gertler, F., Russo, T., and Sudol, M. (1997). The WW domain of neural protein FE65 interacts with proline-rich motifs in Mena, the mammalian homolog of *Drosophila* Enabled. *J Biol Chem* 272, 32869-32877.

Farrow, N.A., Zhang, O., Forman-Kay, J.D., and Kay, L.E. (1994). A heteronuclear correlation experiment for simultaneous determination of ¹⁵N longitudinal decay and chemical exchange rates of systems in slow equilibrium. *J Biomol NMR* 4, 727-734.

Fedorov, A.A., Fedorov, E., Gertler, F., and Almo, S.C. (1999). Structure of EVH1, a novel proline-rich ligand-binding module involved in cytoskeletal dynamics and neural function. *Nat Struct Biol* 6, 661-665.

Feng, S., Chen, J.K., Yu, H., Simon, J.A., and Schreiber, S.L. (1994). Two binding orientations for peptides to the Src SH3 domain: development of a general model for SH3-ligand interactions. *Science* 266, 1241-1247.

Fischer, G. (2000). Chemical aspects of peptide bond isomerisation. *Chemical Society Reviews* 29, 119-127.

Fischer, G., and Aumuller, T. (2003). Regulation of peptide bond cis/trans isomerization by enzyme catalysis and its implication in physiological processes. *Rev Physiol Biochem Pharmacol* 148, 105-150.

Flannery, S., and Bowie, A.G. (2010). The interleukin-1 receptor-associated kinases: critical regulators of innate immune signalling. *Biochem Pharmacol* 80, 1981-1991.

Gan, L., and Li, L. (2010). Interleukin-1 Receptor-Associated Kinase-1 (IRAK-1) functionally associates with PKCepsilon and VASP in the regulation of macrophage migration. *Mol Immunol* 47, 1278-1282.

Gertler, F.B., Niebuhr, K., Reinhard, M., Wehland, J., and Soriano, P. (1996). Mena, a relative of VASP and *Drosophila* Enabled, is implicated in the control of microfilament dynamics. *Cell* 87, 227-239.

Goh, K.L., Cai, L., Cepko, C.L., and Gertler, F.B. (2002). Ena/VASP proteins regulate cortical neuronal positioning. *Curr Biol* 12, 565-569.

Gothel, S.F., and Marahiel, M.A. (1999). Peptidyl-prolyl cis-trans isomerases, a superfamily of ubiquitous folding catalysts. *Cell Mol Life Sci* 55, 423-436.

Gottipati, S., Rao, N.L., and Fung-Leung, W.P. (2008). IRAK1: a critical signaling mediator of innate immunity. *Cell Signal* 20, 269-276.

Grange, J., Moody, J.D., Ascione, M.P., and Hansen, M.D. (2012). Zyxin-VASP

interactions alter actin regulatory activity in zyxin-VASP complexes. *Cell Mol Biol Lett* 18, 1-10.

Grathwohl, C., and Wuthrich, K. (1976). The X-Pro peptide bond as an nmr probe for conformational studies of flexible linear peptides. *Biopolymers* 15, 2025-2041.

Grevenkoed, E.E., Loureiro, J.J., Jesse, T.L., and Peifer, M. (2001). Abelson kinase regulates epithelial morphogenesis in *Drosophila*. *J Cell Biol* 155, 1185-1198.

Hansen, S.D., and Mullins, R.D. (2010). VASP is a processive actin polymerase that requires monomeric actin for barbed end association. *J Cell Biol* 191, 571-584.

Harmer, N.J., Sivak, J.M., Amaya, E., and Blundell, T.L. (2005). 1.15 Å crystal structure of the *X. tropicalis* Spred1 EVH1 domain suggests a fourth distinct peptide-binding mechanism within the EVH1 family. *FEBS Lett* 579, 1161-1166.

Hayashi, F., Smith, K.D., Ozinsky, A., Hawn, T.R., Yi, E.C., Goodlett, D.R., Eng, J.K., Akira, S., Underhill, D.M., and Aderem, A. (2001). The innate immune response to bacterial flagellin is mediated by Toll-like receptor 5. *Nature* 410, 1099-1103.

Hemmi, H., Takeuchi, O., Kawai, T., Kaisho, T., Sato, S., Sanjo, H., Matsumoto, M., Hoshino, K., Wagner, H., Takeda, K., and Akira, S. (2000). A Toll-like receptor recognizes bacterial DNA. *Nature* 408, 740-745.

Hirata, H., Tatsumi, H., and Sokabe, M. (2008). Zyxin emerges as a key player in the mechanotransduction at cell adhesive structures. *Commun Integr Biol* 1, 192-195.

Hoffman, L.M., Jensen, C.C., Chaturvedi, A., Yoshigi, M., and Beckerle, M.C. (2012). Stretch-induced actin remodeling requires targeting of zyxin to stress fibers and recruitment of actin regulators. *Mol Biol Cell* 23, 1846-1859.

Hoshino, K., Takeuchi, O., Kawai, T., Sanjo, H., Ogawa, T., Takeda, Y., Takeda, K., and Akira, S. (1999). Cutting edge: Toll-like receptor 4 (TLR4)-deficient mice are hyporesponsive to lipopolysaccharide: evidence for TLR4 as the Lps gene product. *J Immunol* 162, 3749-3752.

Houry, W.A., and Scheraga, H.A. (1996). Nature of the unfolded state of ribonuclease A: effect of cis-trans X-Pro peptide bond isomerization. *Biochemistry* 35, 11719-11733.

Jacob, C.O., Zhu, J., Armstrong, D.L., Yan, M., Han, J., Zhou, X.J., Thomas, J.A., Reiff, A., Myones, B.L., Ojwang, J.O., *et al.* (2009). Identification of IRAK1 as a risk gene with critical role in the pathogenesis of systemic lupus erythematosus. *Proc Natl Acad Sci U S A* 106, 6256-6261.

Jiang, Z., Ninomiya-Tsuji, J., Qian, Y., Matsumoto, K., and Li, X. (2002). Interleukin-1 (IL-1) receptor-associated kinase-dependent IL-1-induced signaling complexes phosphorylate TAK1 and TAB2 at the plasma membrane and activate TAK1 in the cytosol. *Mol Cell Biol* 22, 7158-7167.

Kanakaraj, P., Ngo, K., Wu, Y., Angulo, A., Ghazal, P., Harris, C.A., Siekierka, J.J., Peterson, P.A., and Fung-Leung, W.P. (1999). Defective interleukin (IL)-18-mediated natural killer and T helper cell type 1 responses in IL-1 receptor-associated kinase (IRAK)-deficient mice. *J Exp Med* 189, 1129-1138.

Kanakaraj, P., Schafer, P.H., Cavender, D.E., Wu, Y., Ngo, K., Grealish, P.F., Wadsworth, S.A., Peterson, P.A., Siekierka, J.J., Harris, C.A., and Fung-Leung, W.P. (1998). Interleukin (IL)-1 receptor-associated kinase (IRAK) requirement for optimal induction of multiple IL-1 signaling pathways and IL-6 production. *J Exp Med* 187, 2073-2079.

Kaufman, K.M., Zhao, J., Kelly, J.A., Hughes, T., Adler, A., Sanchez, E., Ojwang,

J.O., Langefeld, C.D., Ziegler, J.T., Williams, A.H., *et al.* (2013). Fine mapping of Xq28: both MECP2 and IRAK1 contribute to risk for systemic lupus erythematosus in multiple ancestral groups. *Ann Rheum Dis* 72, 437-444.

Kay, B.K., Williamson, M.P., and Sudol, M. (2000). The importance of being proline: the interaction of proline-rich motifs in signaling proteins with their cognate domains. *FASEB J* 14, 231-241.

Koestler, S.A., Rottner, K., Lai, F., Block, J., Vinzenz, M., and Small, J.V. (2009). F- and G-actin concentrations in lamellipodia of moving cells. *PLoS One* 4, e4810.

Kollewe, C., Mackensen, A.C., Neumann, D., Knop, J., Cao, P., Li, S., Wesche, H., and Martin, M.U. (2004). Sequential autophosphorylation steps in the interleukin-1 receptor-associated kinase-1 regulate its availability as an adapter in interleukin-1 signaling. *J Biol Chem* 279, 5227-5236.

Kovrigin, E.L. (2012). NMR line shapes and multi-state binding equilibria. *J Biomol NMR* 53, 257-270.

Krause, M., Dent, E.W., Bear, J.E., Loureiro, J.J., and Gertler, F.B. (2003). Ena/VASP proteins: regulators of the actin cytoskeleton and cell migration. *Annu Rev Cell Dev Biol* 19, 541-564.

Krishnamurthy, S., Ghazy, M.A., Moore, C., and Hampsey, M. (2009). Functional interaction of the Ess1 prolyl isomerase with components of the RNA polymerase II initiation and termination machineries. *Mol Cell Biol* 29, 2925-2934.

Krishnamurthy, S., He, X., Reyes-Reyes, M., Moore, C., and Hampsey, M. (2004). Ssu72 Is an RNA polymerase II CTD phosphatase. *Mol Cell* 14, 387-394.

Kumari, S., Roy, S., Singh, P., Singla-Pareek, S.L., and Pareek, A. (2013). Cyclophilins: Proteins in search of function. *Plant Signal Behav* 8.

Lakoski, S.G., Li, L., Langefeld, C.D., Liu, Y., Howard, T.D., Brosnihan, K.B., Xu, J., Bowden, D.W., and Herrington, D.M. (2007). The association between innate immunity gene (IRAK1) and C-reactive protein in the Diabetes Heart Study. *Exp Mol Pathol* 82, 280-283.

Lebrand, C., Dent, E.W., Strasser, G.A., Lanier, L.M., Krause, M., Svitkina, T.M., Borisy, G.G., and Gertler, F.B. (2004). Critical role of Ena/VASP proteins for filopodia formation in neurons and in function downstream of netrin-1. *Neuron* 42, 37-49.

Lee, T.H., Pastorino, L., and Lu, K.P. (2011). Peptidyl-prolyl cis-trans isomerase Pin1 in ageing, cancer and Alzheimer disease. *Expert Rev Mol Med* 13, e21.

Li, B., Zhuang, L., and Trueb, B. (2004). Zyxin interacts with the SH3 domains of the cytoskeletal proteins LIM-nebulette and Lasp-1. *J Biol Chem* 279, 20401-20410.

Lin, C.C., Huoh, Y.S., Schmitz, K.R., Jensen, L.E., and Ferguson, K.M. (2008). Pellino proteins contain a cryptic FHA domain that mediates interaction with phosphorylated IRAK1. *Structure* 16, 1806-1816.

Lin, S.C., Lo, Y.C., and Wu, H. (2010). Helical assembly in the MyD88-IRAK4-IRAK2 complex in TLR/IL-1R signalling. *Nature* 465, 885-890.

Liu, J., Farmer, J.D., Jr., Lane, W.S., Friedman, J., Weissman, I., and Schreiber, S.L. (1991). Calcineurin is a common target of cyclophilin-cyclosporin A and FKBP-FK506 complexes. *Cell* 66, 807-815.

Lummis, S.C., Beene, D.L., Lee, L.W., Lester, H.A., Broadhurst, R.W., and Dougherty, D.A. (2005). Cis-trans isomerization at a proline opens the pore of a neurotransmitter-gated ion channel. *Nature* 438, 248-252.

Martin, M.U., and Wesche, H. (2002). Summary and comparison of the signaling mechanisms of the Toll/interleukin-1 receptor family. *Biochim Biophys Acta* 1592, 265-280.

Maruoka, M., Sato, M., Yuan, Y., Ichiba, M., Fujii, R., Ogawa, T., Ishida-Kitagawa, N., Takeya, T., and Watanabe, N. (2012). Abl-1-bridged tyrosine phosphorylation of VASP by Abelson kinase impairs association of VASP to focal adhesions and regulates leukaemic cell adhesion. *Biochem J* 441, 889-899.

Meinhart, A., Silberzahn, T., and Cramer, P. (2003). The mRNA transcription/processing factor Ssu72 is a potential tyrosine phosphatase. *J Biol Chem* 278, 15917-15921.

Mejillano, M.R., Kojima, S., Applewhite, D.A., Gertler, F.B., Svitkina, T.M., and Borisy, G.G. (2004). Lamellipodial versus filopodial mode of the actin nanomachinery: pivotal role of the filament barbed end. *Cell* 118, 363-373.

Moody, J.D., Grange, J., Ascione, M.P., Boothe, D., Bushnell, E., and Hansen, M.D. (2009). A zyxin head-tail interaction regulates zyxin-VASP complex formation. *Biochem Biophys Res Commun* 378, 625-628.

Nagy, P.D., Wang, R.Y., Pogany, J., Hafren, A., and Makinen, K. (2011). Emerging picture of host chaperone and cyclophilin roles in RNA virus replication. *Virology* 411, 374-382.

Ng, K.K., and Weis, W.I. (1998). Coupling of prolyl peptide bond isomerization and Ca²⁺ binding in a C-type mannose-binding protein. *Biochemistry* 37, 17977-17989.

Nguyen, T., De Nardo, D., Masendycz, P., Hamilton, J.A., and Scholz, G.M. (2009). Regulation of IRAK-1 activation by its C-terminal domain. *Cell Signal* 21, 719-726.

Nicholson, L.K., and Lu, K.P. (2007). Prolyl cis-trans Isomerization as a molecular timer in Crk signaling. *Mol Cell* 25, 483-485.

Niebuhr, K., Ebel, F., Frank, R., Reinhard, M., Domann, E., Carl, U.D., Walter, U., Gertler, F.B., Wehland, J., and Chakraborty, T. (1997). A novel proline-rich motif present in ActA of *Listeria monocytogenes* and cytoskeletal proteins is the ligand for the EVH1 domain, a protein module present in the Ena/VASP family. *EMBO J* 16, 5433-5444.

Nix, D.A., Fradelizi, J., Bockholt, S., Menichi, B., Louvard, D., Friederich, E., and Beckerle, M.C. (2001). Targeting of zyxin to sites of actin membrane interaction and to the nucleus. *J Biol Chem* 276, 34759-34767.

O'Neill, L.A. (2008). The interleukin-1 receptor/Toll-like receptor superfamily: 10 years of progress. *Immunol Rev* 226, 10-18.

Pahlke, D., Freund, C., Leitner, D., and Labudde, D. (2005). Statistically significant dependence of the Xaa-Pro peptide bond conformation on secondary structure and amino acid sequence. *BMC Struct Biol* 5, 8.

Palmer, A.G., 3rd (2004). NMR characterization of the dynamics of biomacromolecules. *Chem Rev* 104, 3623-3640.

Peterson, F.C., Deng, Q., Zettl, M., Prehoda, K.E., Lim, W.A., Way, M., and Volkman, B.F. (2007). Multiple WASP-interacting protein recognition motifs are required for a functional interaction with N-WASP. *J Biol Chem* 282, 8446-8453.

Philippar, U., Roussos, E.T., Oser, M., Yamaguchi, H., Kim, H.D., Giampieri, S., Wang, Y., Goswami, S., Wyckoff, J.B., Lauffenburger, D.A., *et al.* (2008). A Mena invasion isoform potentiates EGF-induced carcinoma cell invasion and metastasis. *Dev Cell* 15, 813-828.

Qian, Y., Commane, M., Ninomiya-Tsuji, J., Matsumoto, K., and Li, X. (2001). IRAK-mediated translocation of TRAF6 and TAB2 in the interleukin-1-induced activation of NF κ B. *J Biol Chem* 276, 41661-41667.

Reimer, U., Scherer, G., Drewello, M., Kruber, S., Schutkowski, M., and Fischer, G. (1998). Side-chain effects on peptidyl-prolyl cis/trans isomerisation. *J Mol Biol* 279, 449-460.

Reinhard, M., Giehl, K., Abel, K., Haffner, C., Jarchau, T., Hoppe, V., Jockusch, B.M., and Walter, U. (1995). The proline-rich focal adhesion and microfilament protein VASP is a ligand for profilins. *EMBO J* 14, 1583-1589.

Renfranz, P.J., and Beckerle, M.C. (2002). Doing (F/L)PPPPs: EVH1 domains and their proline-rich partners in cell polarity and migration. *Curr Opin Cell Biol* 14, 88-103.

Sarkar, P., Saleh, T., Tzeng, S.R., Birge, R.B., and Kalodimos, C.G. (2011). Structural basis for regulation of the Crk signaling protein by a proline switch. *Nat Chem Biol* 7, 51-57.

Schirenbeck, A., Arasada, R., Bretschneider, T., Stradal, T.E., Schleicher, M., and Faix, J. (2006). The bundling activity of vasodilator-stimulated phosphoprotein is required for filopodium formation. *Proc Natl Acad Sci U S A* 103, 7694-7699.

Schmidpeter, P.A., Jahreis, G., Geitner, A.J., and Schmid, F.X. (2011). Prolyl isomerases show low sequence specificity toward the residue following the proline. *Biochemistry* 50, 4796-4803.

Shen, Z.J., Esnault, S., Schinzel, A., Borner, C., and Malter, J.S. (2009). The peptidyl-prolyl isomerase Pin1 facilitates cytokine-induced survival of eosinophils by suppressing Bax activation. *Nat Immunol* 10, 257-265.

Siligardi, G., and Drake, A.F. (1995). The importance of extended conformations and, in particular, the PII conformation for the molecular recognition of peptides. *Biopolymers* 37, 281-292.

Singh, N., and Li, L. (2012). Reduced oxidative tissue damage during endotoxemia in IRAK-1 deficient mice. *Mol Immunol* 50, 244-252.

Skoble, J., Auerbuch, V., Goley, E.D., Welch, M.D., and Portnoy, D.A. (2001). Pivotal role of VASP in Arp2/3 complex-mediated actin nucleation, actin branch-formation, and *Listeria monocytogenes* motility. *J Cell Biol* 155, 89-100.

Song, F., Zhang, X., Ren, X.B., Zhu, P., Xu, J., Wang, L., Li, Y.F., Zhong, N., Ru, Q., Zhang, D.W., *et al.* (2011). Cyclophilin A (CyPA) induces chemotaxis independent of its peptidylprolyl cis-trans isomerase activity: direct binding between CyPA and the ectodomain of CD147. *J Biol Chem* 286, 8197-8203.

Su, J., Richter, K., Zhang, C., Gu, Q., and Li, L. (2007). Differential regulation of interleukin-1 receptor associated kinase 1 (IRAK1) splice variants. *Mol Immunol* 44, 900-905.

Tan, X., Calderon-Villalobos, L.I., Sharon, M., Zheng, C., Robinson, C.V., Estelle, M., and Zheng, N. (2007). Mechanism of auxin perception by the TIR1 ubiquitin ligase. *Nature* 446, 640-645.

Tun-Kyi, A., Finn, G., Greenwood, A., Nowak, M., Lee, T.H., Asara, J.M., Tsokos, G.C., Fitzgerald, K., Israel, E., Li, X., *et al.* (2011). Essential role for the prolyl isomerase Pin1 in Toll-like receptor signaling and type I interferon-mediated immunity. *Nat Immunol* 12, 733-741.

Ubersax, J.A., and Ferrell, J.E., Jr. (2007). Mechanisms of specificity in protein

phosphorylation. *Nat Rev Mol Cell Biol* 8, 530-541.

Uematsu, S., Sato, S., Yamamoto, M., Hirotani, T., Kato, H., Takeshita, F., Matsuda, M., Coban, C., Ishii, K.J., Kawai, T., *et al.* (2005). Interleukin-1 receptor-associated kinase-1 plays an essential role for Toll-like receptor (TLR)7- and TLR9-mediated interferon- α induction. *J Exp Med* 201, 915-923.

Vasioukhin, V., Bauer, C., Yin, M., and Fuchs, E. (2000). Directed actin polymerization is the driving force for epithelial cell-cell adhesion. *Cell* 100, 209-219.

Vetter, I.R., Nowak, C., Nishimoto, T., Kuhlmann, J., and Wittinghofer, A. (1999). Structure of a Ran-binding domain complexed with Ran bound to a GTP analogue: implications for nuclear transport. *Nature* 398, 39-46.

Volkman, B.F., Prehoda, K.E., Scott, J.A., Peterson, F.C., and Lim, W.A. (2002). Structure of the N-WASP EVH1 domain-WIP complex: insight into the molecular basis of Wiskott-Aldrich Syndrome. *Cell* 111, 565-576.

Walders-Harbeck, B., Khaitlina, S.Y., Hinssen, H., Jockusch, B.M., and Illenberger, S. (2002). The vasodilator-stimulated phosphoprotein promotes actin polymerisation through direct binding to monomeric actin. *FEBS Lett* 529, 275-280.

Wedemeyer, W.J., Welker, E., and Scheraga, H.A. (2002). Proline cis-trans isomerization and protein folding. *Biochemistry* 41, 14637-14644.

Weiward, M., Werner, A., Rucknagel, P., Schierhorn, A., Kullertz, G., and Fischer, G. (2004). Catalysis of proline-directed protein phosphorylation by peptidyl-prolyl cis/trans isomerases. *J Mol Biol* 339, 635-646.

Werner-Allen, J.W., Lee, C.J., Liu, P., Nicely, N.I., Wang, S., Greenleaf, A.L., and Zhou, P. (2010). cis-Proline-mediated Ser(P)5 dephosphorylation by the RNA polymerase II C-terminal domain phosphatase Ssu72. *J Biol Chem* 286, 5717-5726.

Wesche, H., Henzel, W.J., Shillinglaw, W., Li, S., and Cao, Z. (1997). MyD88: an adapter that recruits IRAK to the IL-1 receptor complex. *Immunity* 7, 837-847.

Wojtowicz, A., Babu, S.S., Li, L., Gretz, N., Hecker, M., and Cattaruzza, M. (2010). Zyxin mediation of stretch-induced gene expression in human endothelial cells. *Circ Res* 107, 898-902.

Xiang, K., Nagaike, T., Xiang, S., Kilic, T., Beh, M.M., Manley, J.L., and Tong, L. (2010). Crystal structure of the human symplekin-Ssu72-CTD phosphopeptide complex. *Nature* 467, 729-733.

Yaffe, M.B., Schutkowski, M., Shen, M., Zhou, X.Z., Stukenberg, P.T., Rahfeld, J.U., Xu, J., Kuang, J., Kirschner, M.W., Fischer, G., *et al.* (1997). Sequence-specific and phosphorylation-dependent proline isomerization: a potential mitotic regulatory mechanism. *Science* 278, 1957-1960.

Yoshigi, M., Hoffman, L.M., Jensen, C.C., Yost, H.J., and Beckerle, M.C. (2005). Mechanical force mobilizes zyxin from focal adhesions to actin filaments and regulates cytoskeletal reinforcement. *J Cell Biol* 171, 209-215.

Zarrinpar, A., Bhattacharyya, R.P., and Lim, W.A. (2003). The structure and function of proline recognition domains. *Sci STKE* 2003, RE8.

Zhang, Y., and Zhang, M. (2011). Crystal structure of Ssu72, an essential eukaryotic phosphatase specific for the C-terminal domain of RNA polymerase II, in complex with a transition state analogue. *Biochem J* 434, 435-444.

Zhou, X.Z., Kops, O., Werner, A., Lu, P.J., Shen, M., Stoller, G., Kullertz, G., Stark, M., Fischer, G., and Lu, K.P. (2000). Pin1-dependent prolyl isomerization regulates dephosphorylation of Cdc25C and tau proteins. *Mol Cell* 6, 873-883.

Zimmermann, J., Kuhne, R., Volkmer-Engert, R., Jarchau, T., Walter, U., Oschkinat, H., and Ball, L.J. (2003). Design of N-substituted peptomer ligands for EVH1 domains. *J Biol Chem* 278, 36810-36818.

Zoldak, G., Aumuller, T., Lucke, C., Hritz, J., Oostenbrink, C., Fischer, G., and Schmid, F.X. (2009). A library of fluorescent peptides for exploring the substrate specificities of prolyl isomerases. *Biochemistry* 48, 10423-10436.

Zydowsky, L.D., Etzkorn, F.A., Chang, H.Y., Ferguson, S.B., Stolz, L.A., Ho, S.I., and Walsh, C.T. (1992). Active site mutants of human cyclophilin A separate peptidyl-prolyl isomerase activity from cyclosporin A binding and calcineurin inhibition. *Protein Sci* 1, 1092-1099.

CHAPTER 2

Isomerase-Catalyzed Binding of IRAK1 to the EVH1 Domain of VASP¹

Abstract

Interleukin-1 receptor-associated kinase 1 (IRAK1) is a crucial signaling kinase in the immune system, involved in Toll-like receptor (TLR) signaling. Vasodilator-stimulated phosphoprotein (VASP) is a central player in cell migration that regulates actin polymerization and connects signaling events to cytoskeletal remodeling. A VASP/IRAK1 interaction is thought to be important in controlling macrophage migration in response to PKC ϵ activation. We show that the monomeric VASP-EVH1 domain directly binds to the ₁₆₈WPPPP₁₇₂ motif in the IRAK1 undefined domain (IRAK1-UD) with moderate ($K_D^{trans} = 116 \pm 2 \mu\text{M}$) affinity. We further show that this motif adopts distinct *cis* and *trans* isomers for the Trp168 – Pro169 peptide bond with nearly equal populations, and that binding to VASP-EVH1 is specific for the *trans* isomer, linking isomerization to binding. NMR lineshape analysis and tryptophan fluorescence experiments reveal the complete kinetics and thermodynamics of the binding reaction, showing diffusion-limited binding to the *trans* isomer followed by slow, isomerization-dependent binding. We further demonstrate that the peptidyl-prolyl isomerase (PPIase) cyclophilin A (CypA) catalyzes isomerization of the Trp168 – Pro169 peptide bond and accelerates IRAK1-UD binding to VASP-EVH1. We propose that binding of IRAK1 to tetrameric VASP is regulated by avidity through assembly of IRAK1 onto receptor-anchored signaling complexes, and that an isomerase such as CypA may modulate IRAK1 signaling *in vivo*. These studies demonstrate a direct interaction between IRAK1 and VASP, and

¹ Chapter 2 is based on a manuscript to be submitted at *Biochemistry*.

suggest a potential mechanism for how this interaction might be regulated by both assembly of IRAK1 onto an activated signaling complex and by PPIase enzymes.

Introduction

Toll-like receptors (TLRs) provide the first line of defense against viral, bacterial and fungal invaders (Moresco et al., 2011). These receptors recognize specific pathogen-associated molecular patterns (PAMPs) that are not normally present in the host, such as flagellin, double-stranded RNA, and lipopolysaccharides (LPS) (Carpenter and O'Neill, 2009; McGettrick and O'Neill, 2010; Uematsu and Akira, 2007). To date, at least 10 distinct human TLRs have been identified, some of which reside in the plasma membrane to detect extracellular PAMPs, while others localize to intracellular compartments where they detect endocytosed PAMPs (Casanova et al., 2011; Moresco et al., 2011). PAMP detection by TLRs triggers signaling cascades that upregulate the expression of type I interferons (IFNs) and proinflammatory cytokines to orchestrate innate and adaptive immunity. Such cytokines include interleukin-1 β (IL-1 β) and the related IL-18, which are recognized by the interleukin-1 receptor (IL-1R) family of receptors. TLRs and IL-1Rs share a homologous cytoplasmic Toll/IL-1 receptor (TIR) domain and are therefore classified together as members of the Toll/Interleukin-1 family of receptors (Martin and Wesche, 2002).

While TLRs and IL-1Rs and their ligands are diverse, the signaling pathways of several of these receptors share specific components, such as the adaptor MyD88 and the interleukin-1-receptor associated kinase 1 (IRAK1) (Martin and Wesche, 2002). The activation of both TLR and IL-1R family members induces their dimerization (Qin et al., 2005; Watters et al., 2007). In mammals, the subsequent intracellular signaling steps include the assembly of a multi-protein complex (the

Myddosome) nucleated by the receptor TIR domains. A recent crystal structure suggests that, minimally, four MyD88 molecules bind the clustered receptor TIR domains and initiate a helical array onto which the death domains (DDs) of four IRAK4 molecules, then four IRAK1 (or IRAK2) molecules assemble (Lin et al., 2010). Although the kinase activity of IRAK1 is involved in its subsequent dissociation from this receptor-initiated complex (Cao et al., 1996; Gottipati et al., 2008), much of IRAK1 signaling function is accomplished as an adaptor protein through its interactions with downstream binding partners. Interactions with IRAK1 are typically mediated through its DD, C-terminal domain, or undefined domain (Gottipati et al., 2008).

The IRAK1 undefined domain (IRAK1-UD) is a 95-residue proline-rich region containing 27 Pro residues. To date, only a few proteins have been implicated as specific binding partners for this domain, namely Pin1 (Tun-Kyi et al., 2011), NEMO (Conze et al., 2008), and Pellino (Haghighyeghi et al., 2010; Kim et al., 2011; Lin et al., 2008). Additionally, the vasodilator-stimulated phosphoprotein (VASP) has recently been shown to co-immunoprecipitate and functionally interact with IRAK1 in the regulation of macrophage migration (Gan and Li, 2010). Cellular localization of VASP is mediated by an N-terminal Ena–VASP homology 1 (EVH1) domain, a binding module that recognizes the proline-rich motif (W/F)P \times ϕ P (Niebuhr et al., 1997; Pistor et al., 1995; Ball et al., 2000) where x is any amino acid and ϕ is an aliphatic residue, and x and ϕ are frequently proline. This motif is present in the focal adhesion proteins Zyxin and Vinculin and the *Listeria monocytogenes* surface protein ActA, as well as in IRAK1 (Ball et al., 2002; Gan and Li, 2010). The interaction between VASP and IRAK1 is predicted to be mediated by the EVH1 domain of VASP, since the IRAK1-UD contains an EVH1 binding motif (₁₆₈WPPPP₁₇₂) and mutation of IRAK1 in this site (L167A, W168A) prevents co-immunoprecipitation

(co-IP) of IRAK1 and VASP (Gan and Li, 2010). However, since co-IP can be mediated by additional factors, a direct interaction between VASP-EVH1 and IRAK1-UD was not demonstrated.

The proline content of the IRAK1-UD imparts special conformational and kinetic properties to this domain. In addition to disrupting secondary structure (Levitt, 1978), proline residues tend to induce a considerable population of the *cis* isomer in their preceding peptide bond, between 5% and 40% depending mostly on the sequence of residues immediately preceding and following the proline (Reimer et al., 1998). Inter-conversion between prolyl isomers is a slow process with a time constant of between 100-1000 s, but prolyl isomerase enzymes have evolved that accelerate this isomerization (Fischer et al., 1984). One such isomerase is cyclophilin A (CypA), a cytosolic enzyme with specific roles in viral infectivity (Towers, 2007) and signaling in immune cells (Bannon et al., 2012; Colgan et al., 2004; Nicholson and Lu, 2007; Sarkar et al., 2011; Song et al., 2011).

Here, we demonstrate and quantify the direct interaction between the VASP-EVH1 domain and the $_{168}\text{WPPPP}_{172}$ region of IRAK1-UD and show that binding is specific for the *trans* isomer of the $\text{W}_{168}\text{-P}_{169}$ peptide bond. Strikingly, at equilibrium the $\text{W}_{168}\text{-P}_{169}$ peptide bond is 43% *cis* and 57% *trans*, with nearly half of the protein in the *cis* conformation incapable of binding to VASP-EVH1. We speculate that this relatively weak interaction ($K_D^{\text{trans}} = 116 \pm 2 \mu\text{M}$) could act as a molecular switch whereby this affinity of IRAK1 for VASP (a constitutive tetramer) is dramatically enhanced by avidity when multiple IRAK1 molecules assemble onto the activated Myddosome. IRAK1 could thereby recruit VASP to the plasma membrane in response to TLR or IL-1 receptor signaling. In a particularly novel finding, we show that the peptidyl-prolyl isomerase CypA accelerates the completion of the IRAK1-UD/VASP-EVH1 binding reaction, effectively catalyzing binding through its isomerization of the

W₁₆₈-P₁₆₉ peptide bond. These studies provide the first demonstration of a direct interaction between IRAK1 and VASP, and suggest a potential mechanism for how this interaction might be regulated by both assembly of IRAK1 onto an activated Myddosome and by peptidyl-prolyl isomerase enzymes.

Materials and Methods

Protein and Peptide Preparation.

All proteins were expressed as N-terminal 6X-His tagged fusion proteins in BL21-DE3 *Escherichia coli* cells. Human IRAK1-UD (IRAK1 residues 101-222) was encoded in a pET vector (kanamycin resistance) with a TEV protease cleavage site between the 6X-His tag and the protein. Human VASP-EVH1 (VASP residues 1-115) was encoded in a pMW172 vector (ampicillin resistance, a gift from M. Way, London Research Institute) with a 3Cpro protease cleavage site between the 6X-His tag and protein as described (Boeda et al., 2007). Human CypA (full length) was encoded in a pTFT74 vector (ampicillin resistance, gift from C. Kalodimos, Rutgers University) without a cleavage site as described (Piotukh et al., 2005). Cells were grown in 1 L M9 medium with 19 mM ¹⁵NH₄Cl (or ¹⁴NH₄Cl to produce unlabeled protein) and antibiotic at 37 °C until they reached an OD₆₀₀ of ~ 0.8. Protein expression was then induced with 1 mM IPTG for ~ 4 hours at 37 °C (IRAK1-UD) or ~ 16 hours at 18 °C (VASP-EVH1 and CypA), after which cells were harvested and resuspended in 20 ml wash buffer (50 mM NaH₂PO₄, 300 mM NaCl, 20 mM imidazole, 0.1 mM TCEP, pH 8.0) with 100 µl protease inhibitor cocktail and 1 mM TCEP added. Cells were lysed by freezing and thawing, adding 20 mg lysozyme, and sonicating on ice for 10 cycles. Cell debris was removed by centrifuging at 23,000 g followed by filtering the supernatant with a 0.8-µm syringe filter. The filtrate was passed through a nickel-NTA column which was then washed with 20 bed volumes of wash buffer. Protein was

eluted with 10 ml of elution buffer (50 mM Na_2HPO_4 , 300 mM KCl, 100 mM imidazole, pH 8.0) and dialyzed into cleavage buffer (50 mM Tris-HCl, 1 mM TCEP, pH 8.0) or NMR buffer (20 mM KH_2PO_4 , 50 mM KCl, 1 mM TCEP, pH 6.7) in the case of CypA. After dialysis, recombinant His-tagged 3C protease or TEV protease was added to the protein sample and the cleavage reaction was performed overnight at 4 °C. The His tag and His-tagged protease were then removed by passing the cleavage reaction back through a nickel-NTA column. The flow-through was dialyzed into NMR buffer, and concentrated with 5000 MWC centrifugal concentrators as necessary. NMR samples also contained 5 mM NaN_3 and 7% D_2O . The NMR sample in the ^{15}N -ZZ experiment had 10 mM TCEP to prevent oxidation of the especially concentrated sample. Protein concentration was measured by UV absorbance using the theoretical extinction coefficients at 280 nm of $23,500 \text{ cm}^{-1}\text{M}^{-1}$ for wild-type IRAK1-UD, $21,000 \text{ cm}^{-1}\text{M}^{-1}$ for VASP-EVH1, and $8,500 \text{ cm}^{-1}\text{M}^{-1}$ for CypA. Plasmids encoding the IRAK1-UD mutants W102G/W130G/W200G and W102F/W130F/W168F were generated by three sequential rounds of site-directed mutagenesis using the Quikchange protocol (Stratagene), mutant IRAK1-UD proteins were produced as above, and protein concentrations were determined using the adjusted theoretical extinction coefficient ($5,500 \text{ cm}^{-1}\text{M}^{-1}$).

A synthetic peptide encompassing IRAK1 residues P₁₆₂-K₁₈₀ (IRAK1¹⁶²⁻¹⁸⁰) was purchased and received as a lyophilized powder (Tufts Core Facility, Boston, MA). Likewise, a peptide encompassing ActA residues 333-344 (ActA³³³⁻³⁴⁴) was purchased from Genscript (Piscataway, NJ). Peptides were dissolved in NMR buffer. Peptide concentrations were determined by UV absorbance, using the theoretical extinction coefficient of $5500 \text{ cm}^{-1}\text{M}^{-1}$ at 280 nm for IRAK1¹⁶²⁻¹⁸⁰ and $390 \text{ cm}^{-1}\text{M}^{-1}$ at 257 nm for ActA³³³⁻³⁴⁴. Sample pH was adjusted using NaOH and HCl before use.

NMR Data Collection/Processing.

All NMR experiments were performed on a Varian Inova 600 MHz spectrometer equipped with a {H, C, N} Z-axis gradient probe. Unless otherwise stated, NMR experiments were performed at 25 °C. All NMR spectra were processed and analyzed with the software nmrPipe (Delaglio et al., 1995), nmrDraw (Delaglio et al., 1995), and Sparky (Goddard TD, 2008). Either an exponential or phase-shifted sine bell window function was applied to free induction decays prior to Fourier transformation. The Sparky peak detection function was used to measure peak positions and heights.

NMR Titration Experiments.

Altogether, four titration experiments were carried out. Three titrations of ^{15}N EVH1 domain (with unlabeled IRAK1-UD, IRAK1¹⁶²⁻¹⁸⁰, and ActA³³³⁻³⁴⁴) were performed, as well as a titration of ^{15}N IRAK1-UD with unlabeled EVH1 domain. In each titration, the most saturated sample was prepared first and the subsequent titration samples were prepared by mixing a portion of the previous sample with a stock of labeled protein, thus keeping the concentration of labeled protein constant while varying the titrant concentration. All titrations were performed in NMR buffer with 5 mM NaN_3 and 7% D_2O . In the titration of ^{15}N EVH1 domain with IRAK1-UD, the concentration of EVH1 was held at 0.51 mM and the IRAK1-UD concentrations were 0, 0.07, 0.11, 0.17, 0.25, 0.38, 0.56, 0.84, and 1.27 mM. In the titration of ^{15}N EVH1 domain with IRAK1¹⁶²⁻¹⁸⁰, the concentration of ^{15}N EVH1 was held between 0.35-0.38 mM and the peptide concentrations were 0, 0.03, 0.06, 0.12, 0.24, 0.48, 0.95, 1.9, and 3.8 mM. In the titration of ^{15}N EVH1 domain with ActA³³³⁻³⁴⁴, the concentration of ^{15}N EVH1 was held at 0.37 mM and the peptide concentrations were 0, 0.04, 0.08, 0.15, 0.30, 0.61, 1.21, 2.43, and 4.86 mM. In the titration of ^{15}N IRAK1-UD with EVH1 domain, the concentration of ^{15}N IRAK1-UD was held at 0.34 mM and the EVH1 concentrations were 0, 0.18, 0.35, and 0.70 mM. For each titration condition, a

^{15}N - ^1H fast-HSQC (Mori et al., 1995) spectrum was recorded with a spectral width of 8 kHz in the proton dimension (total of 2048 complex data points) and 1.7 kHz (^{15}N UD-perspective titration and ^{15}N EVH1-perspective IRAK1-UD titration) or 1.8 kHz (^{15}N EVH1 peptide titrations) in the nitrogen dimension (total of 256 complex data points).

Quantification of Binding and NMR Lineshape Analysis.

The peak trajectories of resolved residues in NMR titrations were used to determine binding constants. For a given peak, the change in chemical shift between the apo spectrum and a titration point spectrum for the proton and nitrogen dimensions, $\Delta\delta_H$ and $\Delta\delta_N$, were fit as a function of the apparent dissociation constant, K_D^{App} , and the protein/peptide molar concentrations. For given total concentrations of EVH1, $[\text{EVH1}^{tot}]$, and IRAK1, $[\text{IRAK1}^{tot}]$, the concentration of bound complex, $[\text{EVH1:IRAK1}]$, is given by

$$[\text{EVH1:IRAK1}] = \frac{1}{2} \left\{ K_D^{App} + [\text{EVH1}^{tot}] + [\text{IRAK1}^{tot}] - \sqrt{(K_D^{App} + [\text{EVH1}^{tot}] + [\text{IRAK1}^{tot}])^2 - 4[\text{EVH1}^{tot}][\text{IRAK1}^{tot}]} \right\} \quad (2.1)$$

Using chemical shift changes of ^{15}N EVH1 peaks, K_D^{App} was determined from the titrations of ^{15}N EVH1 with IRAK1-UD and IRAK1¹⁶²⁻¹⁸⁰ using the equation

$$[\text{EVH1:IRAK1}] = \frac{\Delta\delta_i}{\Delta\delta^{\max}} [\text{EVH1}^{tot}] \quad (2.2)$$

where i is H or N, and $\Delta\delta^{\max}$ is the chemical shift difference between free and bound (a fitted parameter). To account for inaccuracies in the calculation of the extinction coefficient, the concentrations of peptide in the ActA³³³⁻³⁴⁴ titration were scaled by a fitted correction factor, L_{corr} using the equation

$$[\text{ActA}^{333-344}]_{corrected} = [\text{ActA}^{333-344}]_{measured} \cdot L_{corr} \quad (2.3)$$

This was warranted given the sharp binding curves, which were very sensitive to stoichiometry. For each titration set, the reported K_D^{App} value and its error were determined by fitting each of 21 ^1H and 21 ^{15}N chemical shift datasets independently,

and taking the mean and standard error of the resulting fitted values. Fits were performed by least-squares minimization using the Solver function in Microsoft Excel.

Lineshape analysis of the ^{15}N EVH1 peptide titrations was carried out as described (De et al., 2012), using the *BiophysicsLab* Matlab package (Kovrigin, 2012). Lineshapes were extracted as 1D slices in each dimension (^1H , ^{15}N) using the *BiophysicsLab* Sparky extension. To eliminate any titration-dependent variation in signal intensity, the area under each peak slice was normalized. The software calculates the populations of free and bound EVH1 domain using equation 2.1 and simulates lineshape data using the two-state solution to the Bloch-McConnell equations (McConnell, 1958) (Cavanagh J, 2007). The dissociation constant, K_D^{App} , apo chemical shift, ω^{Apo} , and linewidth of the apo state, $R_{2,0}^{Apo}$, previously determined by peak positions and the spectrum of apo ^{15}N EVH1, were constrained while the dissociation rate, k_{off} , bound chemical shift, ω^{Bound} , and linewidth of the bound state, $R_{2,0}^{Bound}$, were determined by least squares fitting. We report the average and standard error of the fitted parameters k_{off} and k_{on} from individual fits of four lineshape datasets. A global fit which yielded statistically equivalent values of these parameters was also performed.

Modeling the IRAK1/EVH1 complex.

The model of VASP-EVH1 bound to IRAK1¹⁶²⁻¹⁸⁰ was built using a solution structure of the VASP EVH1 domain (PDB ID code 1EGX (Ball et al., 2000)) and a crystal structure of the complex between the Mena EVH1 domain and an ActA-derived peptide (PDB ID code 1EVH (Prehoda et al., 1999)) with the sequence FPPPPT. The Mena and VASP EVH1 structures were overlaid using the “magic fit” function in the program Swiss-Pdb viewer (Guex and Peitsch, 1997). The IRAK1 sequence A165-A175 was introduced into the binding site by changing the ActA peptide (chain B) in the complex crystal structure to the IRAK1 sequence using the

“mutate” and “add residue” functions in Swiss-Pdb viewer. The torsion angles of W168 in the IRAK1 peptide were adjusted to align the indole ring with the phenylalanine side chain in the ActA peptide sequence, and the torsion angles of R83 in the EVH1 domain were adjusted slightly to accommodate the bound peptide. Energy minimization was performed using the GROMOS96 implementation within Swiss-Pdb viewer.

Demonstration of Isomerization by Nzz Exchange Spectroscopy.

^{15}N -ZZ exchange spectroscopy (Farrow et al., 1994) was performed on a 0.8 mM ^{15}N -IRAK1-UD sample, with or without 8 μM CypA in NMR buffer. Mixing times were 0, 0.01101, 0.02202, 0.03303, 0.04404, 0.05505, 0.082575, and 0.1101 s. For each spectrum, a spectral width of 8 kHz (total of 2048 complex data points) was used in the proton dimension, and 1.7 kHz (total of 256 data points) in the nitrogen dimension, with 40 transients per FID and a recycle delay of 1.0 s. To assist in identifying crosspeaks, the spectra with nonzero mixing time were added together using the NMRPipe command addNMR. To determine the rate of W168-P169 isomerization, peak heights for autopeaks and crosspeaks corresponding to the sidechain of W168 were obtained using Sparky. The heights of these four peaks as a function of mixing time were fit to the two-state solution of the Bloch-McConnell equations (Cavanagh J, 2007; McConnell, 1958) by least-squares minimization with Microsoft Excel (Solver function). The longitudinal relaxation constants for the *cis* and *trans* isomers, $R_{1,0}^{trans}$ and $R_{1,0}^{cis}$, (determined by running the ^{15}N -ZZ exchange experiment without CypA present) and the ratio of *trans* to *cis* isomer, K_{isom} (determined from homonuclear TOCSY peak volumes corresponding to the *cis* and *trans* isomers of the W₁₆₈-P₁₆₉ peptide bond), were treated as fixed parameters. Fitted parameters included the initial intensities of autopeaks, $I_{TT,0}$ and $I_{CC,0}$, and the exchange rate of isomerization, k_{ex} . The mixing time dependences of all four peaks

were fit simultaneously.

Tryptophan Fluorescence Experiments.

All tryptophan fluorescence experiments were carried out using a F-7000 fluorescence spectrophotometer (Hitachi High Technologies America, Schaumburg, IL). In mixing experiments, 2 ml of 100 μM (IRAK1¹⁶²⁻¹⁸⁰ experiment) or 77 μM (ActA³³³⁻³⁴⁴ experiment) EVH1 domain, with or without 62 nM of CypA, was equilibrated in a quartz cuvette, gently stirred and temperature controlled at 25 °C. Peptide was then diluted from a concentrated stock into the cuvette for a final concentration of 53 μM (IRAK1¹⁶²⁻¹⁸⁰ experiment) or 50 μM (ActA³³³⁻³⁴⁴ experiment) and a time course was recorded (2 s interval, 40 minutes, or 0.5 s interval, 20 minutes). The fluorescence signal was measured by exciting at 294 nm and collecting at 360 nm (2.5 nm bandpass for excitation, 20 nm bandpass for emission) for the IRAK1¹⁶²⁻¹⁸⁰ experiment, and exciting at 290 nm and collecting at 334 nm (2.5 nm bandpass for excitation, 20 nm bandpass for emission) for the ActA³³³⁻³⁴⁴ experiment. In the dilution experiments, 4 μl of an equilibrated stock containing 1 mM EVH1 domain and 1 mM IRAK1¹⁶²⁻¹⁸⁰ was diluted into 2 ml of NMR buffer (or NMR buffer with a catalytic quantity of CypA) in a stirred and temperature controlled ($T = 20, 25, 30^\circ\text{C}$) quartz cuvette. A time course was then recorded (1 s or 0.5 s interval, 15-50 minutes). The fluorescence signal was measured by exciting at 280 nm and collecting at 360 nm (1.0 nm bandpass for excitation, 20 nm bandpass for emission). Fluorescence data was fit following subtraction of a baseline, which was determined either from taking data of the EVH1 domain prior to adding peptide, or, for the dilution experiments, using the data from long after the exponential signal had stabilized. Data was fit to the exponential function,

$$I(t) = I_{final} + (I_0 - I_{final})e^{-tk_{obs}} \quad (2.4)$$

where I_{final} and I_0 are the equilibrium and initial fluorescence intensities,

respectively, and k_{obs} is the rate constant given by (De et al., 2012; Hagerman and Baldwin, 1976; Ng and Weis, 1998)

$$k_{obs} = k_{CT} + k_{TC} / (1 + \frac{[EVH1^{free}]}{K_D^{App}}) \quad (2.5)$$

where k_{CT} and k_{TC} are the *cis*-to-*trans* and *trans*-to-*cis* rates of isomerization. The rates k_{CT} and k_{TC} reflect the intrinsic isomerization rates when the experiment is performed in the absence of CypA, but increase linearly with the concentration of CypA. Equation 2.5 is an approximation that requires that the kinetics of binding be fast compared to the kinetics of isomerization, and that $[EVH1^{free}]$ can be treated as a time-independent parameter. In the dilution experiment, $[EVH1^{free}] / K_D^{App}$ approximates to 0 and the equation reduces to $k_{obs} = k_{CT} + k_{TC} = k_{CT}(1 + 1/K_{isom})$.

To measure the affinity of EVH1 binding to ActA³³³⁻³⁴⁴ using tryptophan fluorescence, 50 μ M EVH1 with 1 μ M CypA was incubated in the quartz cuvette at 25 °C and ActA³³³⁻³⁴⁴ was titrated in 7 μ M increments. Data was collected as a time course to monitor stability of signal. For each titration point, a time course was collected (10 s, 0.1 s interval) and the average fluorescence signal at each peptide concentration was fit to a standard bimolecular binding curve in analogy to equations 1 and 2. As in the NMR titration, the peptide concentration was scaled by a fitted correction factor to account for inaccuracies in the extinction coefficient calculation. All fitting of fluorescence data was performed by least squares minimization using the Solver function in Microsoft Excel.

Results

The undefined domain of IRAK1 is conformationally heterogeneous

As a first step toward characterizing the IRAK1/VASP interaction, ¹⁵N-labeled human IRAK1-UD (residues 101-222, Figure 2.1A) was examined by two-dimensional NMR spectroscopy. The ¹⁵N-IRAK1-UD yields a ¹⁵N-¹H HSQC

spectrum with very narrow peak dispersion, characteristic of a disordered polypeptide (Figure 2.1B). Furthermore, it displays a number of minor peaks at low contour level, which, given the 27 proline residues in this sequence, could be attributed to the *cis* isomers of the various X-Pro peptide bonds (demonstrated below). Because *cis-trans* isomerization is a slow process with an exchange time constant (τ) on the order of minutes in the absence of isomerase activity (Reimer et al., 1998), an equilibrium between *cis* and *trans* isomers generally results in two distinct NMR peaks for residues whose chemical environment differs for the two isomers. The four Trp indole NHs in this sequence give rise to six peaks (Figure 2.1C), with the two W-P motifs (W₁₆₈-P₁₆₉ and W₂₀₀-P₂₀₁) each giving rise to two peaks corresponding to their comparable *cis* and *trans* populations. Unique resonance assignments of the W₁₆₈ and W₂₀₀ indole NH peaks were obtained via mutagenesis (Figure 2.1C). Based on peak volumes, the equilibrium *cis* and *trans* populations of the W₁₆₈-P₁₆₉ peptide bond are nearly equal (43% *cis* and 57% *trans* by TOCSY spectra, 45% *cis* and 55% *trans* by HSQC), yielding an equilibrium constant of $K_{isom} = [trans]/[cis] = 1.33$. Similarly, the populations of W₂₀₀-P₂₀₁ are 35% *cis* and 65% *trans*. This is consistent with the intrinsic tendency of the bulky tryptophan side chain to induce a large *cis* population when preceding a proline (Reimer et al., 1998).

By employing 3D TOCSY and NOESY experiments on the ¹⁵N-IRAK1-UD, and aided by homonuclear TOCSY and NOESY spectra of an IRAK1-derived peptide encompassing residues P₁₆₂-K₁₈₀ (IRAK1¹⁶²⁻¹⁸⁰) it was possible to determine peak assignments for several residues in and around the ₁₆₈WPPPP₁₇₂ motif (Table 2.1). Several residues within the A165-S173 region exhibited distinct chemical shifts for the two isomers of the W₁₆₈-P₁₆₉ peptide bond, and distinct *cis* (25%) and *trans* (75%) peaks were also observed for the isomers of the S₁₇₃-P₁₇₄ peptide bond (Appendix Figure 2.1). Assignments of the prolyl isomers of the W₁₆₈-P₁₆₉ peptide bond were

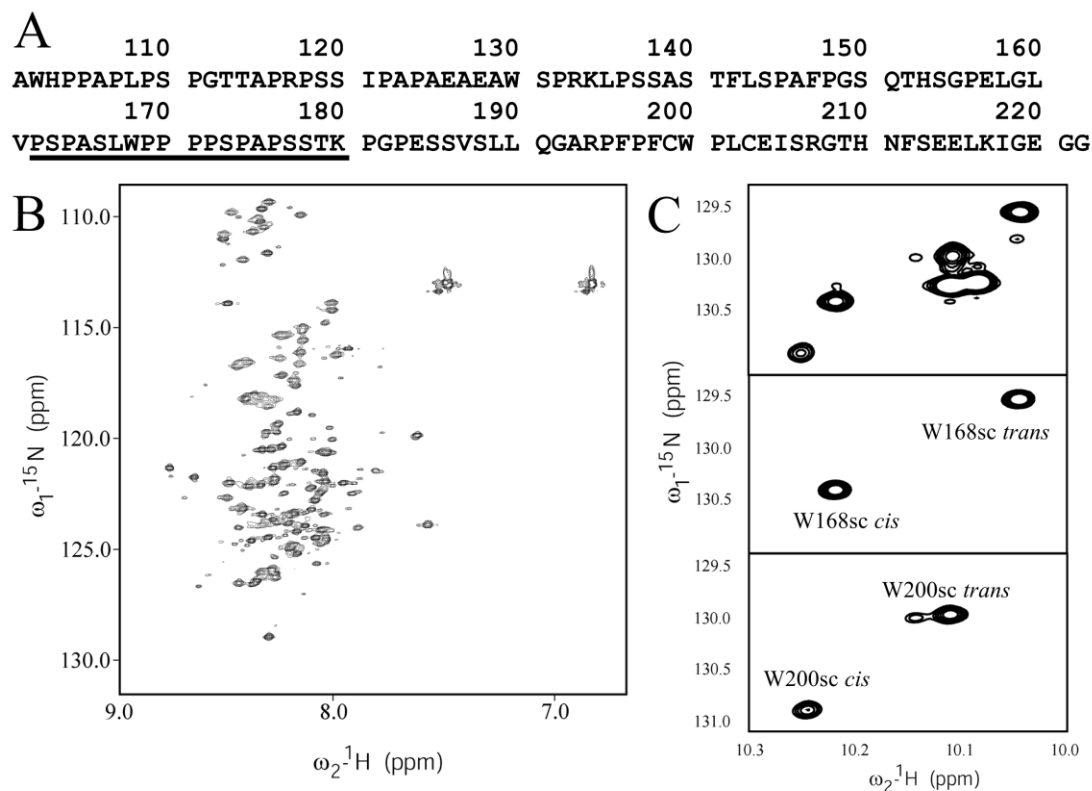


Figure 2.1: Conformational heterogeneity in the undefined domain of IRAK1. (A) Sequence of the IRAK1-UD construct used (IRAK1 residues 101-222). The backbone NH region of the ^{15}N - ^1H HSQC spectrum of IRAK1-UD (B) shows very narrow chemical shift dispersion, indicating that the UD does not adopt a stable fold. The tryptophan sidechain indole peaks, located downfield (C) display six peaks for the four tryptophans in the sequence (top). The two W-P motifs in this sequence, W168 and W200, were identified (middle and bottom) by mutating the other tryptophans (using the W102G/W130G/W200G and W102F/W130F/W168F IRAK1-UD mutants, respectively), and the *cis* and *trans* isomers of each are labeled.

accomplished both by identification of characteristic through-space NOEs to proline protons from the preceding residue's alpha proton ($d_{\alpha\delta}$ for the *trans* isomer and $d_{\alpha\alpha}$ for the *cis* isomer), and by exchange cross peaks in the ^{15}N -ZZ exchange experiment in the presence of the isomerase CypA, as described below.

Table 2.1: Chemical Shift Assignments of IRAK1 Residues A165-A175 for the *Cis* and *Trans* Isomers of W168-P169

Residue	N	NH	H α	H β	other
W168-P169 trans					
A165	124.306	8.261	4.131	1.301	
S166	115.062	8.066	4.299	3.769, 3.722	
L167	124.392	7.934	4.14	1.23, 1.278	δCH_2 0.785, 0.725
W168	122.59	7.918	4.942	3.039, 3.275	ϵNH 10.026
P169	-	-	4.72	*	δCH_2 3.76, 3.57
P170	-	-	*	*	*
P171	-	-	*	*	*
P172	-	-	*	*	*
S173	118.216	8.353	4.654	3.765, 3.836	
P174	-	-	*	*	*
A175	126.655	8.359	4.541	1.327	
W168-P169 cis					
A165	124.537	8.31	4.283	1.376	
S166	115.425	8.168	4.42	3.855	
L167	125.01	8.098	4.344	1.556	δCH_2 0.888, 0.832
W168	123.538	8.037	4.477	3.111	ϵNH 10.201
P169	-	-	3.26	*	δCH_2 3.37, 3.27
P170	-	-	*	*	*
P171	-	-	*	*	*
P172	-	-	*	*	*
S173	118.228	8.326	4.669	3.829, 3.747	
P174	-	-	*	*	*
A175	126.655	8.359	4.541	1.327	

(-) indicates proline residues that do not have amide protons or routinely-observed nitrogen chemical shifts.

(*) indicates chemical shifts that were not assignable due to overlap.

These results, which represent the first structural information on the proline-

rich IRAK1 undefined domain, show that this domain is conformationally heterogeneous. While the narrow chemical shift dispersion in the ^{15}N - ^1H HSQC spectrum indicates rapid exchange between allowed regions of backbone conformational space, the additional peaks arising from *cis-trans* isomerization demonstrate that multiple sites undergo slow two-state exchange, adding to the conformational richness of this domain.

Determination of the IRAK1-UD recognition sequence and isomer-specificity of interaction with VASP-EVH1

When ^{15}N -IRAK1-UD was titrated with VASP-EVH1, six backbone peaks and one tryptophan sidechain peak move substantially. These peaks correspond to the NH groups of A165-A175 (proline residues in the sequence do not yield ^{15}N - ^1H HSQC peaks) (Figure 2.2A, B). This demonstrates that binding is specific for the $_{168}\text{WPPPP}_{172}$ motif in IRAK1-UD and that the interaction is in fast exchange on the NMR timescale (Cavanagh J, 2007) ($\sim 4000\text{ s}^{-1}$ in this case). As described above, this region of the IRAK1-UD sequence exhibits distinct peaks corresponding to the *cis* and *trans* states of the $\text{W}_{168}\text{-P}_{169}$ peptide bond. While the peaks corresponding to the *trans* isomer of $\text{W}_{168}\text{-P}_{169}$ move significantly upon binding, the *cis* isomer peaks simply decrease in intensity as EVH1 is added, indicating that the interaction is specific for the *trans* isomer (Figure 2.2A, B). Therefore, a coupled equilibrium model that includes both *cis-trans* isomerization and binding (Figure 2.2C) is indicated for this system. This result is consistent with the crystal structures of both the EVH1 domain of Mena (Prehoda et al., 1999) and Evl (Fedorov et al., 1999) bound to ActA peptides, which show a *trans* peptide bond between the phenylalanine and the first proline of the bound FPPPP sequence.

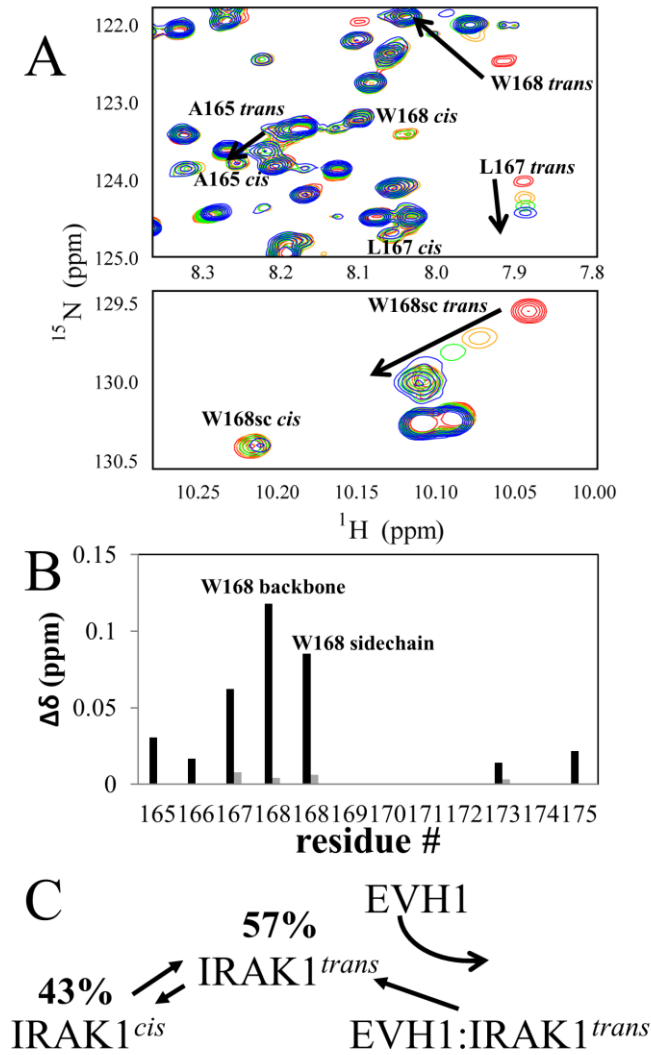


Figure 2.2: The IRAK1-UD/VASP-EVH1 interaction is *trans*-specific. (A) When ^{15}N -labeled IRAK1-UD is titrated with unlabeled VASP-EVH1 domain in a series of ^{15}N - ^1H HSQC spectra, peaks corresponding to the backbone and side-chain amides of IRAK1 residues 165-175 (excluding prolines) display different behaviors depending on the isomer state of W168-P169. Colors represent progression of [EVH1] with red being apo IRAK1-UD and blue being highest [EVH1]. Top shows a portion of the backbone amide region of the ^{15}N - ^1H HSQC series, and bottom shows the tryptophan indole region of the spectra. (B) Composite chemical shift changes, $\Delta\delta = \sqrt{(\delta_H - \delta_H^{Apo})^2 + (0.154 \cdot (\delta_N - \delta_N^{Apo}))^2}$, of backbone and side chain amides of IRAK1 residues 165-175 between the apo and final spectra of the EVH1/ ^{15}N IRAK1-UD titration. Black bars represent peaks corresponding to the *trans* isomer of W168-P169, and grey bars represent peaks for the *cis* isomer, for peaks that were discernible in the final spectrum. (C) The coupled equilibrium model, including isomerization in the IRAK1 protein and *trans*-specific binding, used to interpret and fit binding data.

Determination of the thermodynamics and kinetics of the interaction between IRAK1-UD and VASP-EVH1

In order to measure the affinity and kinetics of binding between IRAK1-UD and VASP-EVH1, ^{15}N -EVH1 was titrated with unlabeled IRAK1¹⁶²⁻¹⁸⁰. Use of IRAK1¹⁶²⁻¹⁸⁰ rather than the full IRAK1-UD was preferred due to its solubility (allowing saturation of ^{15}N -EVH1 to be approached) and its negligible contribution to the molecular weight of the bound complex. This titration yielded several resolved peak trajectories (Figure 2.3A), indicating fast exchange on the NMR timescale as was observed from the ^{15}N -labeled IRAK1-UD perspective (Figure 2.2). Using the peak assignments for VASP-EVH1 (BioMagResBank accession number 18569 (Ball et al., 2000)), we observed that the pattern of chemical shift perturbations across the EVH1 sequence upon adding IRAK1¹⁶²⁻¹⁸⁰ closely matches that observed for the FPPPP motifs in ActA binding to VASP-EVH1 (Ball et al., 2000). This was confirmed by titrating ^{15}N -EVH1 with an ActA-derived peptide ActA³³³³⁻³⁴⁴ (333FEFPPPPTEDEL₃₄₄) and comparing chemical shift perturbations (Figure 2.3B). This suggests that IRAK1¹⁶²⁻¹⁸⁰ binds in the same orientation as displayed by published structures of Ena/VASP EVH1 domain peptide complexes (Fedorov et al., 1999; Prehoda et al., 1999). The largest perturbations arose from residues (e.g. W23 sidechain, K71, Y72, N73 sidechain, A75, Q81 sidechain, R83) in the binding surface defined by the crystal structure of the Mena EVH1/ActA complex (Prehoda et al., 1999), as illustrated by mapping chemical shift perturbations to the EVH1 solution structure (Ball et al., 2000) (Figure 2.3C). Analysis of 21 ^1H and 21 ^{15}N chemical shift datasets yielded an apparent dissociation constant K_D^{App} of 0.203 ± 0.003 mM (example fits are shown in Figure 2.4A). This apparent affinity corresponds to a K_D^{trans} of 0.116 ± 0.002 mM, adjusted for coupling to the *cis-trans* equilibrium (Figure 2.2D) by the equation

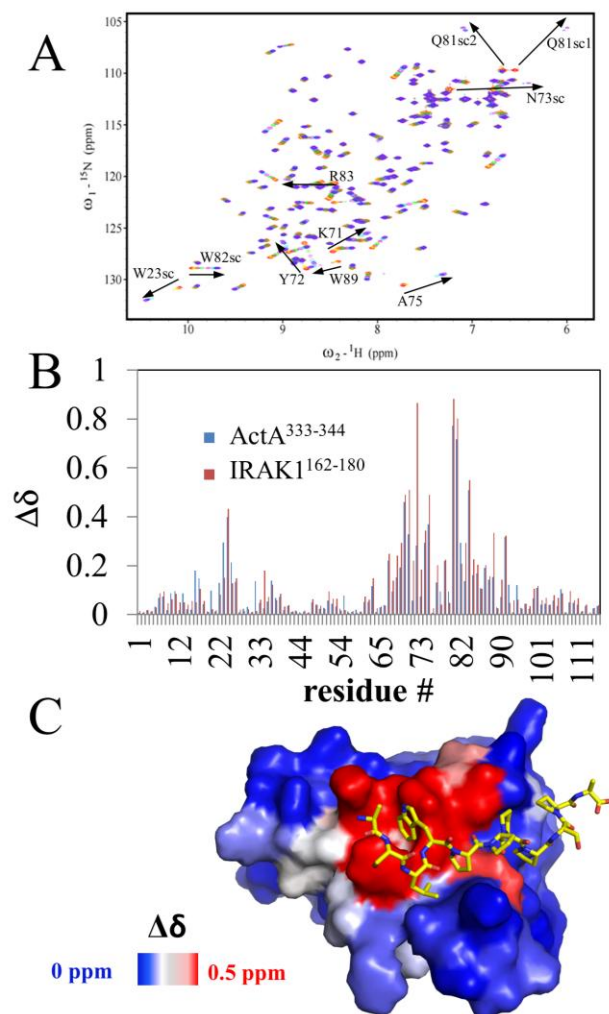


Figure 2.3: Chemical shift mapping to EVH1 structure. ^{15}N EVH1 domain was titrated with the IRAK1-derived peptide IRAK1¹⁶²⁻¹⁸⁰ and a series of ^{15}N - ^1H HSQC spectra (A) were taken. Colors indicate peptide concentration, transitioning between free (red) and bound (purple) EVH1. (B) Composite chemical shift changes for ^{15}N EVH1 peaks between apo and peptide bound positions. Chemical shift changes for IRAK1¹⁶²⁻¹⁸⁰ titration are shown in red and changes for ActA³³³⁻³⁴⁴ titration are shown in blue. (C) Representation of the solution structure of the VASP EVH1 domain (PDB ID code 1EGX (Ball et al., 2000)) with the IRAK1 peptide-induced chemical shift perturbations mapped to it. For each residue, the surface representation is colored according to the greater of the chemical shift changes of the backbone and sidechain amide. Images were generated using the surface view representation and colored according to chemical shift perturbation using the data2bfactor.py and color_b.py scripts from Dr. Robert L. Campbell's PyMol script repository at Queen's University, Ontario, Canada (<http://pldserver1.biochem.queensu.ca/~rlc/work/pymol/>) in PyMOL (Delano, 2002). The peptide was modeled into the binding site by homology with the crystal structure of the Mena EVH1 domain bound to an ActA-derived peptide (PDB ID code 1EVH (Prehoda et al., 1999)).

$$K_D^{App} = K_D^{trans} (1 + 1 / K_{isom}) \quad (2.6)$$

where K_D^{trans} is the dissociation constant of the *trans* isomer of IRAK1 binding to the EVH1 domain, and K_{isom} is the ratio of *trans* to *cis* for the free W₁₆₈-P₁₆₉ peptide bond as determined above. Titration of ¹⁵N EVH1 with full-length IRAK1-UD yielded $K_D^{App} = 0.28 \pm 0.02$ mM (data not shown). This reasonable agreement further validated the use of the peptide.

Lineshape analysis of the above titration data was employed to determine the on- and off-rates of the VASP-EVH1/IRAK1-UD interaction, as described previously (De et al., 2012) and in Materials and Methods. The ¹⁵N-EVH1 peaks that move the most in response to IRAK1¹⁶²⁻¹⁸⁰ binding all display a similar pattern of broadening at intermediate titration points before narrowing as saturation is reached (Figure 2.4B). This exchange broadening is dependent on the difference in chemical shift and the timescale of exchange between the free and bound states. Each peak that is resolved throughout the titration therefore potentially provides two independent measures of the binding kinetics via the peak lineshapes, one in the ¹H and one in the ¹⁵N dimension. Analysis of four lineshape datasets (A75-¹H, W23sc-¹H, W82sc-¹H, Q81sc-¹⁵N) yielded a k_{off} of $4,000 \pm 200$ s⁻¹ and a k_{on} of $3.5 \pm 0.1 \cdot 10^7$ M⁻¹s⁻¹ (Figure 2.4B). This on-rate is near the diffusion limit, as is common for interactions with proline-rich sequences (Kay et al., 2000). Repeating this analysis with the ¹⁵N EVH1/ActA³³³⁻³⁴⁴ data (data not shown) yielded a substantially faster on-rate ($k_{on} = 1.2 \pm 0.1 \cdot 10^8$ M⁻¹s⁻¹, $k_{off} = 1,800 \pm 200$ s⁻¹), however, suggesting that electrostatic steering by the negative charges in this ActA sequence can contribute to the binding rate.

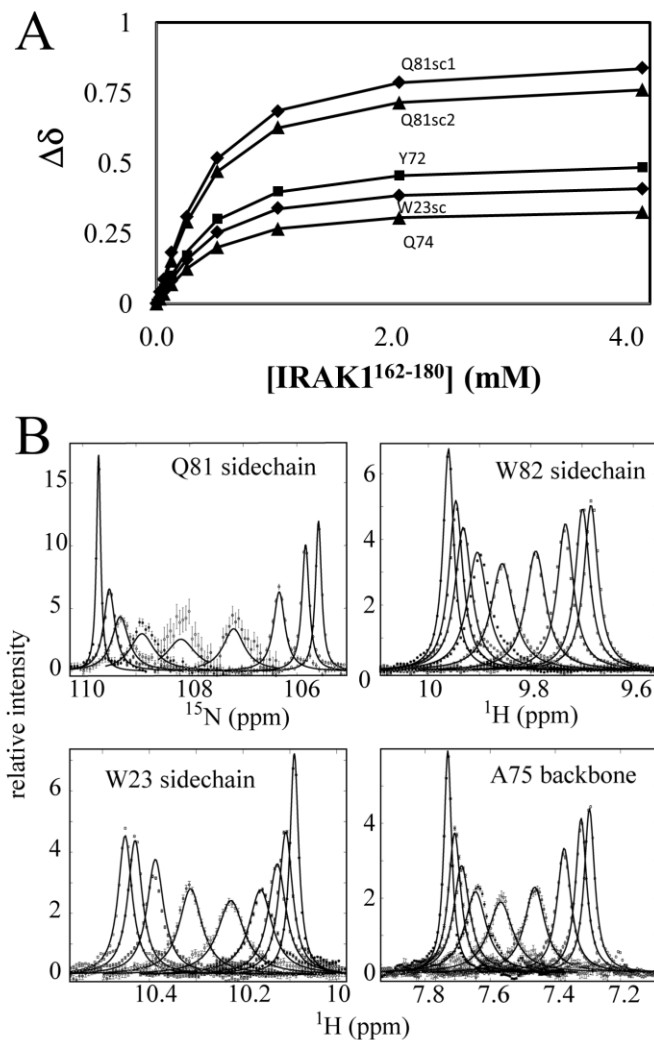


Figure 2.4: Measurement of affinity and kinetics of binding between the VASP-EVH1 domain and $\text{IRAK1}^{162-180}$. (A) Composite chemical shift changes between free and bound states for selected EVH1 peaks as a function of peptide concentration (symbols). The data were fit (solid lines) to obtain the apparent dissociation constant (K_D^{App}) of the interaction of 0.203 ± 0.003 mM. (B) NMR lineshape analysis of selected EVH1 peaks in the peptide titration series. 1D slices through the centers of ^{15}N EVH1 peaks were extracted along the ^{15}N or ^1H dimensions, and the data (symbols) were fit (solid lines) to yield on and off rates. The obtained rates were $k_{\text{on}} = 3.5 \pm 0.1 \cdot 10^7 \text{ M}^{-1}\text{s}^{-1}$ and $k_{\text{off}} = 4,000 \pm 200 \text{ s}^{-1}$.

Demonstration of cyclophilin A catalysis of W₁₆₈-P₁₆₉ isomerization by NMR spectroscopy

To test whether CypA catalyzes isomerization of the W₁₆₈-P₁₆₉ peptide bond in IRAK1, we applied 2D ¹⁵N-ZZ NMR exchange experiments to 0.8 mM ¹⁵N-IRAK1-UD in the presence of 8 μM CypA (Figure 2.5A). ¹⁵N-ZZ spectroscopy allows for the identification and measurement of conformational exchange in the range between about 0.1 and 10 s⁻¹ (Farrow et al., 1994). Since the lower limit of this rate regime is approximately one to two orders of magnitude faster than typical uncatalyzed *cis-trans* isomerization rates (Reimer et al., 1998), intrinsic (uncatalyzed) *cis-trans* isomerization exchange is not detected in this experiment. If two peaks display mutual cross-peaks in an ¹⁵N-ZZ spectrum, it indicates that the same nucleus exchanges between two distinct states, and monitoring the cross-peak intensity as a function of mixing time allows for measurement of the exchange rate (Farrow et al., 1994). In the ¹⁵N-ZZ spectra of ¹⁵N-IRAK1-UD, exchange cross peaks between many pairs of *cis* and *trans* isomers of X-Pro motifs throughout the sequence were observed in the presence of but not in the absence of CypA, indicating both the general lack of sequence specificity of CypA activity (Schmidpeter et al., 2011; Zoldak et al., 2009) and the high conformational heterogeneity of the proline-rich IRAK1-UD (Figure 2.5A). CypA-catalyzed isomerization of the ₁₆₈WPPPP₁₇₂ motif was quantified using the resolved W₁₆₈ indole NH *cis* and *trans* peaks that show unambiguous exchange cross peaks (Figure 2.5A). Analysis of these W₁₆₈ indole NH exchange cross peaks and auto peaks yielded the catalyzed *cis*-to-*trans* and *trans*-to-*cis* isomerization rates, $k_{CT} = 0.89$ and $k_{TC} = 0.72$ s⁻¹ (Figure 2.5B), respectively. The enzyme concentration in this experiment (8 μM) was chosen so that isomerization would be in this range, as cross peaks are too small to resolve at lower isomerization rates and the peaks would begin to broaden at higher rates, complicating analysis.

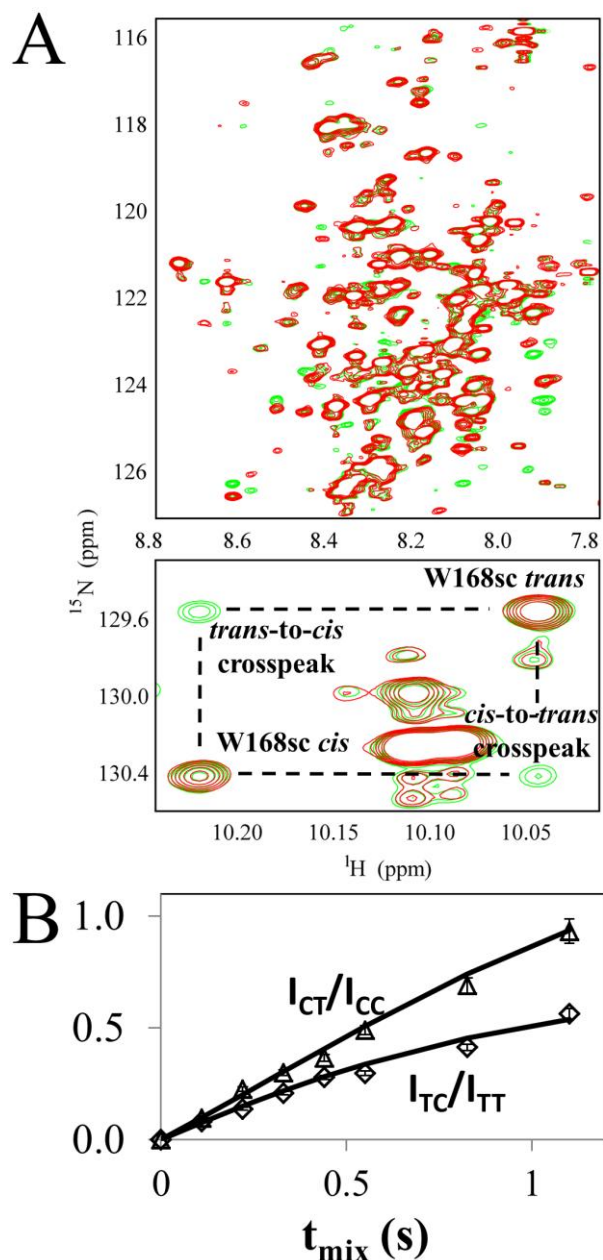


Figure 2.5: Cyclophilin A catalyzes the isomerization between *cis* and *trans* isomers of W168-P169 in IRAK1. (A) ^{15}N ZZ-exchange spectra of ^{15}N IRAK1 UD with a catalytic (8 μM) concentration of cyclophilin A (CypA). The red spectrum is taken with a mixing time of 0, while the green spectrum is a summation of multiple spectra with mixing times of 0.11, 0.22, 0.33, 0.44, 0.55, 0.83, and 1.10 s. The green spectrum shows cross peaks between pairs of peaks of *cis*/*trans* isomers in the sequence. Top shows a section of the backbone amide region and bottom shows the tryptophan indole region, featuring the W168 sidechain peaks. (B) Plot of normalized W168sc crosspeak intensities from the ^{15}N -ZZ experiment as a function of mixing time. Data points are shown as symbols and fits are shown as lines.

Tryptophan fluorescence enables measurement of uncatalyzed prolyl isomerization and activation enthalpy of W_{168} - P_{169} peptide bond

In contrast to ^{15}N -ZZ spectroscopy, fluorescence spectroscopy can be used to measure slow ($\tau > 10$ s) processes like uncatalyzed prolyl isomerization (De et al., 2012; Ng and Weis, 1998; Thies et al., 1999). Tryptophan fluorescence was employed to measure the kinetics of equilibration over the isomerization timescale, since both VASP-EVH1 and IRAK1¹⁶²⁻¹⁸⁰ contain tryptophan residues in or near the interaction interface. The exquisite sensitivity of tryptophan fluorescence to local environment provides the potential for measuring differences not just between free and bound states, but also between the *cis* and *trans* isomers of the W_{168} - P_{169} peptide bond in free IRAK1¹⁶²⁻¹⁸⁰. Observation of the *cis-trans* isomerization kinetics is possible if the *cis* and *trans* populations can be significantly perturbed from their equilibrium values, and their return to equilibrium can be monitored. The strict specificity of the VASP-EVH1/IRAK1-UD interaction for the *trans* isomer of the W_{168} - P_{169} peptide bond provides a mechanism for perturbing this equilibrium, allowing either enrichment of the free *cis* isomer by rapid mixing of the two binding partners at high concentration ($[\text{IRAK1}^{162-180}]$ and $[\text{VASP-EVH1}] \geq K_D^{\text{App}}$), or enrichment of the free *trans* isomer by rapid dilution of the complex to a low concentration ($[\text{IRAK1}^{162-180}]$ and $[\text{VASP-EVH1}] < K_D^{\text{App}}$). In either case, the temporal separation of the fast binding reaction and slow prolyl isomerization allows detection and quantification of the slow, rate-limiting isomerization process.

Upon mixing IRAK1¹⁶²⁻¹⁸⁰ peptide with excess VASP-EVH1, the 57% population of *trans* conformation rapidly reaches its binding equilibrium with the EVH1 domain, and the free *trans* is depleted relative to the free *cis*. Subsequent conversion of *cis* to *trans* (toward equilibrium) provides additional *trans* that binds, generating a time-dependent fluorescence signal that can reflect both equilibration of

isomer populations of free peptide and the additional isomerization-dependent binding. The initial binding phase (to the initial 57% *trans*) is not observable because it is too fast (4000 s^{-1} as determined by NMR above) to be resolved under the experimental conditions, even in stopped-flow experiments (data not shown). To implement the mixing experiment, 2 μl of 53 mM IRAK1¹⁶²⁻¹⁸⁰ peptide was added to 2 ml (final concentration of 53 μM IRAK1¹⁶²⁻¹⁸⁰) containing a high concentration of EVH1 domain (100 μM) in a quartz cuvette and a fluorescence signal time course of the mixture was recorded. The observed slow increase in tryptophan fluorescence was well fit by a single exponential with a rate constant of 0.0025 s^{-1} (Figure 2.6A, B). Notably, the observed change in fluorescence signal could reflect time-dependent binding (rate-limited by prolyl isomerization), the isomerization of the free peptide itself, or a combination of both.

Direct observation of changes in fluorescence signal due to isomerization of the free peptide was achieved using a dilution approach. When pre-formed VASP-EVH1/ IRAK1¹⁶²⁻¹⁸⁰ complex is diluted to a concentration below K_D^{App} , the complex will rapidly dissociate and peptide (in the *trans* isomer state) will be released. The released peptide is far from the *cis-trans* equilibrium, with high *trans* and low *cis* populations. The return of these populations to their equilibrium values can be monitored by tryptophan fluorescence if the *cis* and *trans* isomers elicit different fluorescence signals. This approach unambiguously detects the prolyl isomerization kinetics independent of the binding reaction kinetics, since isomerization is temporally well separated from the rapid initial dissociation of the diluted complex, and subsequent binding is negligible in such a dilute condition.

To implement this approach, a concentrated mixture of 1 mM VASP-EVH1 and 1 mM IRAK1¹⁶²⁻¹⁸⁰ was allowed to fully equilibrate (≥ 1 hour), then 4 μl of this mixture was diluted into the cuvette for a final concentration of 2 μM EVH1 and

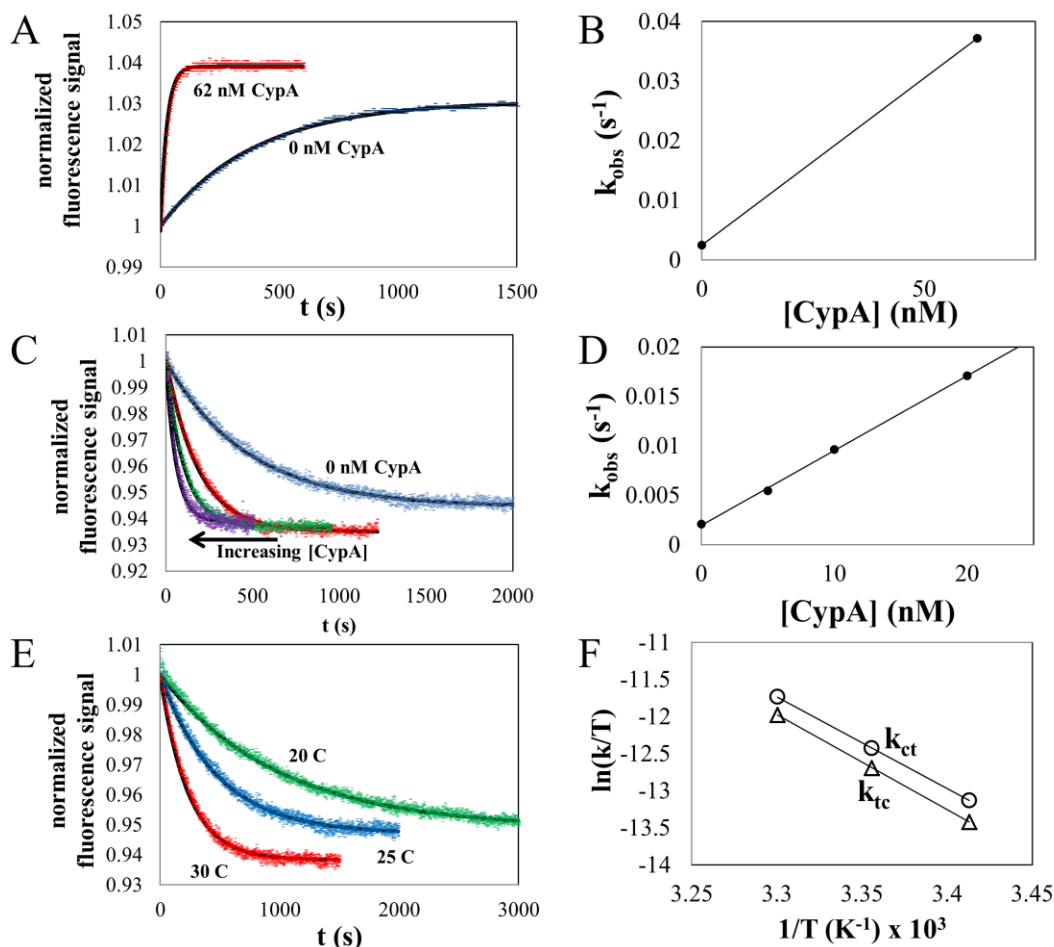


Figure 2.6: Tryptophan fluorescence shows cyclophilin A accelerates IRAK1-UD/EVH1 binding and equilibration of IRAK1 isomers. (A) Mixing the peptide IRAK1¹⁶²⁻¹⁸⁰ with an excess of VASP-EVH1 domain yields a slow increase in tryptophan fluorescence signal that reflects both binding and isomerization. Including CypA in the mixture accelerates this equilibration. (B) Dependence of the rate constant of equilibration in the mixing experiment, k_{obs} , on CypA concentration. (C) Diluting a concentrated stock of IRAK1¹⁶²⁻¹⁸⁰ mixed with VASP-EVH1 to below the K_D^{App} of the interaction results in a slow decrease in fluorescence signal that simply reflects isomerization of the unbound peptide. As in the mixing experiment, CypA accelerates the equilibration of isomers. (D) Dependence of the rate constant of equilibration in the dilution experiment, k_{obs} , on CypA concentration. (E) Performing the dilution experiment at different temperatures shows a strong dependence of k_{obs} on temperature. (F) Eyring plots for the *cis*-to-*trans* and *trans*-to-*cis* rates (k_{CT} and k_{TC}), used to obtain the activation enthalpy and entropy of IRAK1¹⁶²⁻¹⁸⁰ isomerization.

peptide, well below the K_D^{App} . Fast dissociation of the bound *trans* peptide occurred in the dead time of the instrument, while slow equilibration of the *cis* and *trans* isomers of the free peptide was observed as a gradual decrease in tryptophan fluorescence signal over the course of an hour at 25 °C. This demonstrates that the *trans* isomer of the free peptide indeed produces a higher fluorescence intensity than the *cis* isomer, allowing direct detection of the isomerization kinetics. The data was well fit by a single exponential, yielding $k_{obs} = 0.00211 \text{ s}^{-1}$ (in good agreement with the mixing experiment). The corresponding intrinsic *cis*-to-*trans* and *trans*-to-*cis* rates of isomerization are $k_{CT} = 0.0012 \text{ s}^{-1}$ and $k_{TC} = 0.00091 \text{ s}^{-1}$, calculated as described in Materials and Methods. Inclusion of 5, 10, and 20 nM cyclophilin A in the dilution experiment accelerated the rate constant by 2, 4 and 8-fold, displaying a linear dependence on CypA concentration as expected (Figure 2.6C, D). In addition to the ability to directly observe the isomerization process, this experiment has the important advantages of using ~50-fold less material than the mixing experiment, and avoiding the inner-filter effect (which the mixing experiment is susceptible to).

To measure the activation enthalpy of W₁₆₈-P₁₆₉ isomerization, the dilution fluorescence experiment was performed at different temperatures (Figure 2.6E, F). The extraction of individual isomerization rates k_{CT} and k_{TC} from the measured k_{ex} was accomplished using the temperature dependence of K_{isom} determined from homonuclear TOCSY spectra of IRAK1¹⁶²⁻¹⁸⁰ (Appendix Figure 2.2). These rates were fit to the linear form of the Eyring-Polanyi equation (Connors, 1990):

$$\ln(k_{CT,TC}/T) = -\Delta H_{\ddagger}^{CT,TC}/(R \cdot T) + \ln(k_B/h) + \Delta S_{\ddagger}^{CT,TC}/R \quad (2.7)$$

where T is temperature, R is the gas constant, k_B is the Boltzmann constant, h is Planck's constant, and $\Delta H_{\ddagger}^{CT,TC}$ and $\Delta S_{\ddagger}^{CT,TC}$ are the activation enthalpy and entropies of *cis*-to-*trans* (CT) and *trans*-to-*cis* (TC) isomerization. Fitting to this equation yields

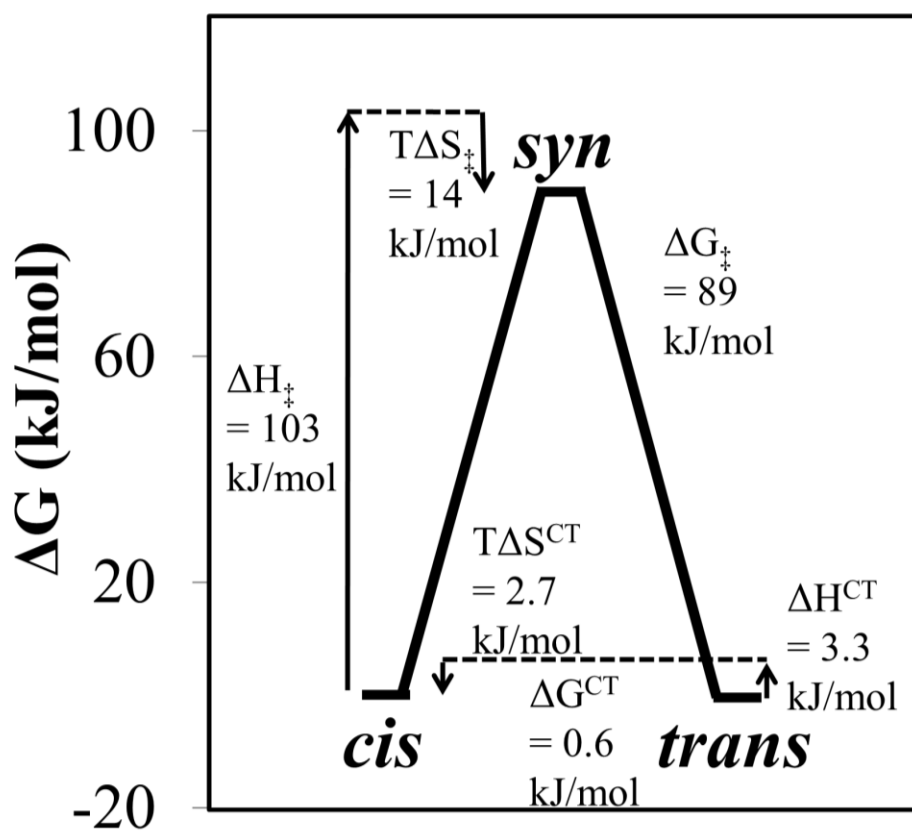


Figure 2.7: Energy diagram describing *cis* and *trans* isomers of W168-P169 in IRAK1-UD. The activation enthalpy and entropy for the *cis*-to-*trans* transition, the difference in enthalpy and entropy between the *cis* and *trans* isomers, and the free energy difference for each are specified.

slopes that correspond to activation enthalpies of 103 and 106 kJ/mol, respectively (Figure 2.6F, Figure 2.7). Extrapolation to physiological temperature (37 °C) yields the population of *trans* (55%) and the uncatalyzed isomerization rate ($k_{ex} = 0.011 \text{ s}^{-1}$). The activation enthalpies and entropies of the *cis*-to-*trans* transition and the differences in enthalpies and entropies between the *cis* and *trans* isomers are illustrated in an energy diagram (Figure 2.7).

Tryptophan fluorescence shows that cyclophilin A “catalyzes” VASP-EVH1 interactions

Inclusion of CypA in the mixing experiment described earlier can be expected to accelerate completion of the *trans*-specific VASP-EVH1/IRAK1¹⁶²⁻¹⁸⁰ binding reaction, after the initial binding of the pre-existing *trans* isomer. In fact, inclusion of 62 nM cyclophilin A in this mixing experiment accelerated the reaction approximately 15-fold (Figure 2.6A, B). However, since changes in the *cis* and *trans* populations give rise to changes in the fluorescence signal, it is difficult to distinguish between fluorescence signal due solely to isomerization of free peptide (which would dominate if binding did not give rise to substantial differences in fluorescence signal, or if VASP-EVH1 is not in excess) and fluorescence signal representing CypA-accelerated binding to VASP-EVH1. Thus, while in principle the mixing experiment should provide the opportunity to observe “CypA-catalyzed binding” of this *trans*-specific interaction, the contribution of isomerization of free peptide to the observed fluorescence signal precludes detection of a signal dependent solely on binding.

In order to directly observe CypA acceleration of binding of VASP-EVH1 to a binding partner, the mixing experiment described above was performed using the peptide ActA³³³⁻³⁴⁴, which also partitions into *cis* (25%) and *trans* (75%) isomers (Appendix Figure 2.3). This sequence contains a phenylalanine instead of tryptophan in the binding motif, and therefore tryptophan fluorescence experiments are not

sensitive to prolyl isomerization of the free peptide. By contrast, Trp23 in the EVH1 domain binding surface is shielded in the complex relative to the apo domain, so fluorescence experiments with this peptide are still sensitive to binding. Titrating EVH1 domain with this peptide shows that the tryptophan fluorescence signal of EVH1 increases over 34% upon binding (Figure 2.8A). Mixing ActA³³³⁻³⁴⁴ with an excess of EVH1 domain produced a slow increase in tryptophan fluorescence, following an exponential expression with a rate of 0.0038 s⁻¹ (Figure 2.7B). This can be unambiguously interpreted as prolyl isomerization-limited binding, because the only tryptophan fluorescence signal arises from the EVH1 domain in this case. This measured rate corresponds to the intrinsic *trans*-to-*cis* (0.0012 s⁻¹) and *cis*-to-*trans* (0.0035 s⁻¹) isomerization rates according to equation 2.5. Equation 2.5 accounts for coupling between isomerization and binding by scaling the intrinsic *trans*-to-*cis* rate by the fraction of free peptide. Inclusion of cyclophilin A in the mixture accelerated the reaction as expected, by 10-fold (Figure 2.8B). This provides a direct example of a prolyl isomerase, cyclophilin A, accelerating an interaction between VASP-EVH1 and one of its binding partners.

Table 2.2: Rates and Equilibrium/Binding Constants for IRAK1¹⁶²⁻¹⁸⁰ and ActA³³³⁻³⁴⁰

	IRAK1¹⁶²⁻¹⁸⁰	ActA³³³⁻³⁴⁴
k_{CT}	0.0012 s ⁻¹	0.0035 s ⁻¹
k_{TC}	0.00091 s ⁻¹	0.0012 s ⁻¹
[<i>trans</i>]/[<i>cis</i>]	1.33	3.0
k_{off}	4,000 ± 200 s ⁻¹	1,800 ± 200 s ⁻¹
k_{on}	3.5 ± 0.1 x 10 ⁷ M ⁻¹ s ⁻¹	1.2 ± 0.1 x 10 ⁸ M ⁻¹ s ⁻¹
K_D^{trans}	116 ± 2 μM	14 ± 1 μM

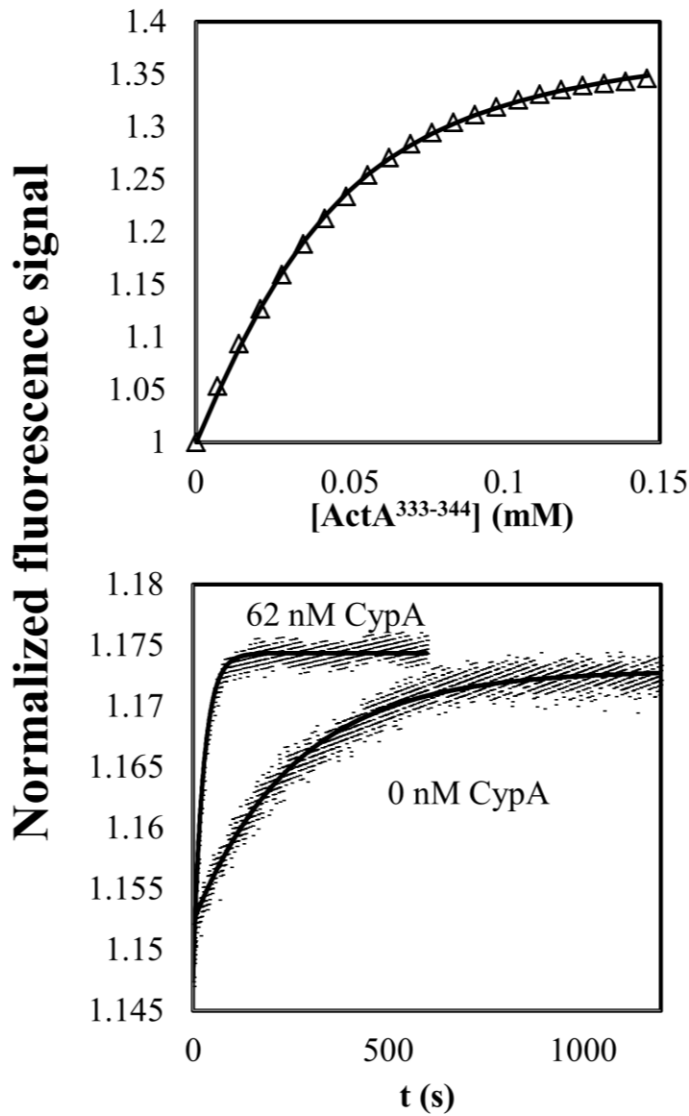


Figure 2.8: Tryptophan fluorescence shows CypA accelerates ActA/EVH1 binding. (A) The tryptophan fluorescence signal of the VASP-EVH1 domain increases upon binding $\text{ActA}^{333-344}$, allowing independent measurement of the binding constant. Data is shown as symbols and a fit is shown as a solid line. (B) Mixing an excess of EVH1 domain with $\text{ActA}^{333-344}$ results in a slow binding phase which can be accelerated with a catalytic quantity (62 nM) of CypA.

Discussion

Here, we have applied biophysical methods to investigate and quantify binding between the EVH1 domain of VASP and the undefined domain of IRAK1. Using purified components, we have demonstrated that the VASP-EVH1 domain binds to the $^{168}\text{WPPPP}_{172}$ motif in IRAK1-UD, with specificity for the *trans* isomer of the $\text{W}_{168}\text{-P}_{169}$ peptide bond. Our studies provide a quantitative thermodynamic and kinetic description of the coupled equilibrium between $\text{W}_{168}\text{-P}_{169}$ *cis-trans* isomerization and IRAK1-UD/VASP-EVH1 binding, and demonstrate how acceleration of isomerization by CypA effectively catalyzes binding. Using a combination of approaches we are able to report both the kinetics of isomerization and binding to the peptides IRAK1¹⁶²⁻¹⁸⁰ and ActA³³³⁻³⁴⁴ (Table 2.2). Catalysis of the rate-limiting isomerization step in an isomer-specific binding reaction represents a largely overlooked function for peptidyl prolyl isomerase enzymes. These results offer important insights into the role of *cis-trans* isomerization in innate immunity signaling, and present a physical mechanism for connecting IRAK1-mediated signaling pathways to VASP-mediated regulation of actin cytoskeletal dynamics.

A logical mechanism of regulation of VASP binding is control of the oligomeric state of its binding partners, since VASP functions as a constitutive tetramer (Bachmann et al., 1999). Receptor oligomerization has long been understood to be an important mechanism in signal transduction (Lemmon and Schlessinger, 1994; Weiss and Schlessinger, 1998), especially in the context of the immune system (McCulloch et al., 2006; Wilson et al., 2009). The driving force in oligomerization as a signal transduction mechanism is avidity, the enhancement in affinity from a relatively weak 1:1 interaction to an exponentially enhanced multimer/multimer interaction (Roitt, 2001). In some cases signal-induced oligomerization of downstream partners is important for transducing a signal, in a kind of “oligomerization cascade”

in which oligomerization of one protein induces oligomerization in a downstream binding partner and so on (Dong et al., 2006; Sun et al., 2004). The IRAK1:VASP monomer-monomer interaction quantified here is relatively weak (116 μ M). IRAK-1 tetramerizes in IL-1R and TLR signaling in response to binding to the oligomeric Myddosome, which may significantly increase the interaction with the tetrameric VASP. Interestingly, since the theoretically tightest interaction is between two tetramers, the fact that the WPPPP binding site partitions into 43% *cis* and 57% *trans* isomers means the tightest interaction would only initially arise for $(0.57)^4 = 11\%$ of the total available IRAK1 tetramers. This principle can be generalized to other isomer-specific interactions between oligomers (even a more modest 25% *cis* corresponds to $(0.75)^4 = 32\%$ of tetramers). An analogy can be drawn to protein folding, in which the isomerization of multiple proline residues in the fold of a protein can collectively contribute to folding kinetics (Wedemeyer et al., 2002). The Ena/VASP proteins are important actin-binding proteins that regulate the actin cytoskeleton by increasing actin filament length. This may be achieved through an anti-capping mechanism, in which Ena/VASP proteins supply monomeric actin to the barbed ends of actin filaments while preventing access of capping proteins that can terminate elongation (Bear and Gertler, 2009). Alternatively, this may be through the processive filament elongation activity Ena/VASP proteins exhibit upon clustering (Breitsprecher et al., 2011; Hansen and Mullins, 2010). Ena/VASP proteins tend to localize at sites with high actin cytoskeleton dynamics, such as filopodial tips and the periphery and ruffles of lamellae (Rottner et al., 1999), which extend during cell spreading. Ena/VASP proteins are also components of the adherens junctions (Reinhard et al., 1996; Vasioukhin et al., 2000) and focal adhesions (Gertler et al., 1996), multi-protein complexes that anchor the actin cytoskeleton to neighboring cells or to the extracellular matrix and therefore must disassemble and reassemble dynamically in

migrating cells, requiring concerted regulation of actin polymerization (Wehrle-Haller and Imhof, 2003). Ena/VASP proteins are central to cellular processes involving cytoskeletal remodeling, such as axon guidance (Goh et al., 2002), migration (Bear et al., 2000; Krause et al., 2003), and cell-cell interaction (Grevengoed et al., 2001; Vasioukhin et al., 2000), warranting detailed characterization of the interactions that localize them to specific sites.

It was recently reported that VASP and IRAK1 co-immunoprecipitate in human THP1 and MAT-2 cells (Gan and Li, 2010). The same researchers also investigated IRAK1's involvement in phosphorylation of VASP by PKC. They found that activation of PKC by PMA-stimulation of IRAK1-deficient murine bone-marrow derived macrophages (BMDMs) resulted in less sustained VASP phosphorylation than in wild-type cells, as well as impaired migration (Gan and Li, 2010). These results seem to collectively suggest a role for the VASP/IRAK1 interaction in macrophage migration. However, while human IRAK1 contains the WPPPP VASP binding motif we describe here, mouse IRAK1 does not contain any such motif. In fact, the appearance of the WPPPP binding motif in human IRAK1 is due to an Arg-to-Trp point mutation that occurred very recently on an evolutionary timescale (Appendix Figure 2.4). It is possible that this is a result of selective pressure, and indeed genes in the immune system tend to evolve more rapidly due to coevolution with pathogens (McTaggart et al., 2012). At any rate, it is not currently clear what function the direct interaction between VASP and IRAK1 plays.

The localization of Ena/VASP proteins can occur in response to signals that trigger cytoskeletal remodeling, and this regulated spatial targeting is a critical aspect of directing cytoskeletal dynamics to the right place at the right time (Krause et al., 2003). In one example, the actin cytoskeleton of helper T cells is polarized towards antigen-presenting cells upon T cell receptor (TCR) stimulation. This rearrangement

of the actin cytoskeleton is dependent on recruitment of Ena/VASP proteins to the TCR signaling complex via a FPPPP motif in the protein Fyb/SLAP (Krause et al., 2000). In another example, phagocytosis relies on precisely coordinated spatiotemporal reorganization of the actin cytoskeleton, often initiated by stimulation of Fc-receptors (May and Machesky, 2001). As in T cells, Fyb/SLAP recruits Ena/VASP proteins to signaling complexes downstream of Fc-receptors in macrophages. This process was shown to be necessary for formation of the actin-based phagocytic cup and phagocytosis of opsonised red blood cells (Coppolino et al., 2001). In both cases, the interaction between Ena/VASP proteins and Fyb/SLAP is crucial to linking receptor activation to cytoskeletal remodeling. The interaction between VASP and IRAK1 appears to be another example of receptor activation leading to the recruitment of VASP to an activated signaling complex in order to initiate cytoskeletal remodeling.

Patients with autosomal recessive deficiency of IRAK4, which acts directly upstream of IRAK1, show defects in neutrophil migration and phagocytosis (Bouma et al., 2009). TLR signaling is thought to modulate phagosome maturation, in which phagosomes fuse with endosomes and lysosomes to degrade engulfed pathogens, although reports differ on whether the effect is to enhance or impair maturation (Blander and Medzhitov, 2004; Yates et al., 2007). Furthermore, TLR signaling through MyD88 dependent and independent processes can impact gene expression to enhance phagocytosis (Doyle et al., 2004; Kong and Ge, 2008). Given the important role of VASP in the process of phagocytosis (Coppolino et al., 2001), the direct interaction between TLR machinery (IRAK1) and VASP as characterized here may serve as yet another mechanism to link TLR signaling and the reorganization of the actin cytoskeleton as occurs in phagocytosis.

Our results showing that the W₁₆₈-P₁₆₉ peptide bond in the IRAK1-UD

partitions into populations of 43% *cis* and 57% *trans* and that only the *trans* isomer participates in binding to VASP provide a compelling example of the relevance of isomerization in the dynamics of protein-protein interactions. Our measurements of the binding kinetics ($k_{on} = 3.5 \pm 0.1 \cdot 10^7 \text{ M}^{-1}\text{s}^{-1}$, $k_{off} = 4,000 \pm 200 \text{ s}^{-1}$) and uncatalyzed isomerization ($k_{ex} = 0.0021 \text{ s}^{-1}$) of this scheme affirm that these processes occur on disparate timescales and that isomerization is a rate-limiting step for binding. A cytoplasmic prolyl isomerase such as CypA may therefore play a role in proper function of VASP by “catalyzing binding” to its partners. Indeed, there is growing evidence that the prolyl isomerase activity of cyclophilins has specific functions in cell signaling, particularly in immune cells. CypA regulates a conformational switch in Interleukin-2 tyrosine kinase (Itk) by isomerizing a proline in the Itk SH2 domain, allowing inter-conversion between active and inactive states (Colgan et al., 2004). In another example, CypA isomerizes a conformational switch in the adaptor protein Crk, also accelerating conversion between inactive and active conformations (Nicholson and Lu, 2007; Sarkar et al., 2011). The isomerase activity of CypA has also been found to be required for cytokinesis in Jurkat cells (Bannon et al., 2012). CypA is required for efficient replication of both human immunodeficiency virus type 1 (HIV-1) and hepatitis C virus (HCV), although it is not yet clear why (Towers, 2007). Interestingly, extracellular CypA is a potent chemokine through its binding to the receptor CD147, but this function is independent of its PPIase activity (Song et al., 2011).

We have employed tryptophan fluorescence to measure the intrinsic rate of isomerization of the W₁₆₈-P₁₆₉ site in IRAK1. To our knowledge this is the first example of an experiment that takes advantage of the intrinsic difference in tryptophan fluorescence intensities of the *cis* and *trans* isomers of the W-P dipeptide sequence to measure the kinetics of isomerization of an unstructured peptide. We have shown both

that the isomerase CypA can accelerate isomerization of IRAK1¹⁶²⁻¹⁸⁰, but also (using the tryptophan fluorescence of the EVH1 domain) that CypA isomerization of the related sequence in ActA can accelerate binding of ActA to EVH1. This represents a direct demonstration of an underappreciated role of prolyl isomerases, the acceleration of isomer-specific protein-protein interactions.

Structurally, VASP recognition of the motif (W/F)Px ϕ P is mediated by a hydrophobic groove in the EVH1 domain which accommodates the PPII helix adopted by the motif. Two sidechains, Gln81 and Trp23, are positioned to hydrogen bond with the carbonyl oxygens of the first proline and third residue (x) in the motif, respectively. Lastly, a hydrophobic pocket defined by the side chain methylenes K71, N73, Q81, and R83 accommodates a hydrophobic aromatic like tryptophan or phenylalanine, or to a smaller degree, the aliphatic leucine (Ball et al., 2000; Fedorov et al., 1999; Prehoda et al., 1999). Flipping the W/F-P peptide bond to the *cis* isomer while constraining the two hydrogen bonds causes the side chain of the first residue to flip away from the binding surface (Appendix Figure 2.5). Thus, the fact that optimal binding requires both that the side chain of the first residue insert into this pocket and the carbonyls of the second and third residues hydrogen bond to sidechains in the EVH1 domain can explain our result that binding is specific for the *trans* isomer of the (W/F)-P peptide bond.

The WPPPP motif in IRAK1 is the only established biological VASP binding site that features a tryptophan instead of a phenylalanine. However, multiple peptide binding studies have demonstrated a preference of VASP-EVH1 for WPx ϕ P over FPx ϕ P motifs (Ball et al., 2000; Niebuhr et al., 1997). It should be noted that phenylalanine is only lower than tryptophan and tyrosine in its tendency to stabilize the *cis* isomer when preceding a proline residue (Reimer et al., 1998). Therefore, the principle of *cis-trans* isomerization as an important consideration for EVH1 binding is

relevant for FPx ϕ P motifs as well as the WPx ϕ P motif described here.

Conclusions

The VASP/IRAK1 interaction provides an intriguing example of how, in a binding interaction with a proline motif, the binding kinetics can be substantially dependent on *cis-trans* isomerization. Binding between tetrameric VASP and a multivalent binding partner such as IRAK1 assembled onto the Myddosome may be especially dependent on isomerization because the probability of a multivalent protein being all-*trans* ($[\% \text{ trans}]^4$) is lower than for a single binding site. Notably, this can be applied to other known VASP interaction partners such as zyxin (Reinhard et al., 1995), lamellipodin (Krause et al., 2004), and ActA (Domann et al., 1992) which have four to five FPx ϕ P motifs in tandem repeat, or vinculin (Reinhard et al., 1996), which oligomerizes. Given the relatively weak affinity of the monomeric VASP-EVH1 for its substrates (19-200 μ M), as well as the tendency of VASP binding sites to exist as tandem repeats, it seems likely that avidity is a driving force for VASP interactions. Therefore, we suggest that a cytoplasmic isomerase such as CypA may be necessary for proper function of VASP-mediated signaling processes. However, future studies are needed to experimentally test this prediction.

REFERENCES

- Bachmann, C., Fischer, L., Walter, U., and Reinhard, M. (1999). The EVH2 domain of the vasodilator-stimulated phosphoprotein mediates tetramerization, F-actin binding, and actin bundle formation. *J Biol Chem* 274, 23549-23557.
- Ball, L.J., Jarchau, T., Oshkinat, H., and Walter, U. (2002). EVH1 domains: structure, function and interactions. *FEBS Lett* 513, 45-52.
- Ball, L.J., Kuhne, R., Hoffmann, B., Hafner, A., Schmieder, P., Volkmer-Engert, R., Hof, M., Wahl, M., Schneider-Mergener, J., Walter, U., *et al.* (2000). Dual epitope recognition by the VASP EVH1 domain modulates polyproline ligand specificity and binding affinity. *EMBO J* 19, 4903-4914.
- Bannon, J.H., O'Donovan, D.S., Kennelly, S.M., and Mc Gee, M.M. (2012). The peptidyl prolyl isomerase cyclophilin A localizes at the centrosome and the midbody and is required for cytokinesis. *Cell Cycle* 11, 1340-1353.
- Bear, J.E., and Gertler, F.B. (2009). Ena/VASP: towards resolving a pointed controversy at the barbed end. *J Cell Sci* 122, 1947-1953.
- Bear, J.E., Loureiro, J.J., Libova, I., Fassler, R., Wehland, J., and Gertler, F.B. (2000). Negative regulation of fibroblast motility by Ena/VASP proteins. *Cell* 101, 717-728.
- Blander, J.M., and Medzhitov, R. (2004). Regulation of phagosome maturation by signals from toll-like receptors. *Science* 304, 1014-1018.
- Boeda, B., Briggs, D.C., Higgins, T., Garvalov, B.K., Fadden, A.J., McDonald, N.Q., and Way, M. (2007). Tes, a specific Mena interacting partner, breaks the rules for EVH1 binding. *Mol Cell* 28, 1071-1082.
- Bouma, G., Doffinger, R., Patel, S.Y., Peskett, E., Sinclair, J.C., Barcenas-Morales, G., Cerron-Gutierrez, L., Kumararatne, D.S., Davies, E.G., Thrasher, A.J., and Burns, S.O. (2009). Impaired neutrophil migration and phagocytosis in IRAK-4 deficiency. *Br J Haematol* 147, 153-156.
- Breitsprecher, D., Kieseewetter, A.K., Linkner, J., Vinzenz, M., Stradal, T.E., Small, J.V., Curth, U., Dickinson, R.B., and Faix, J. (2011). Molecular mechanism of Ena/VASP-mediated actin-filament elongation. *EMBO J* 30, 456-467.
- Cao, Z., Henzel, W.J., and Gao, X. (1996). IRAK: a kinase associated with the interleukin-1 receptor. *Science* 271, 1128-1131.
- Carpenter, S., and O'Neill, L.A. (2009). Recent insights into the structure of Toll-like receptors and post-translational modifications of their associated signalling proteins. *Biochem J* 422, 1-10.
- Casanova, J.L., Abel, L., and Quintana-Murci, L. (2011). Human TLRs and IL-1Rs in host defense: natural insights from evolutionary, epidemiological, and clinical genetics. *Annu Rev Immunol* 29, 447-491.
- Cavanagh J, F.W., Palmer AG, Rance M, Skelton NJ (2007). Protein NMR spectroscopy: principles and practice, 2nd edn (London: Academic Press).
- Colgan, J., Asmal, M., Neagu, M., Yu, B., Schneidkraut, J., Lee, Y., Sokolskaja, E., Andreotti, A., and Luban, J. (2004). Cyclophilin A regulates TCR signal strength in CD4+ T cells via a proline-directed conformational switch in Itk. *Immunity* 21, 189-201.
- Connors, K.A. (1990). Chemical Kinetics (New York: VCH).
- Conze, D.B., Wu, C.J., Thomas, J.A., Landstrom, A., and Ashwell, J.D. (2008). Lys63-linked polyubiquitination of IRAK-1 is required for interleukin-1 receptor- and

toll-like receptor-mediated NF-kappaB activation. *Mol Cell Biol* 28, 3538-3547.

Coppolino, M.G., Krause, M., Hagendorff, P., Monner, D.A., Trimble, W., Grinstein, S., Wehland, J., and Sechi, A.S. (2001). Evidence for a molecular complex consisting of Fyb/SLAP, SLP-76, Nck, VASP and WASP that links the actin cytoskeleton to Fcgamma receptor signalling during phagocytosis. *J Cell Sci* 114, 4307-4318.

De, S., Greenwood, A.I., Rogals, M.J., Kovrigin, E.L., Lu, K.P., and Nicholson, L.K. (2012). Complete thermodynamic and kinetic characterization of the isomer-specific interaction between Pin1-WW domain and the amyloid precursor protein cytoplasmic tail phosphorylated at Thr668. *Biochemistry* 51, 8583-8596.

Delaglio, F., Grzesiek, S., Vuister, G.W., Zhu, G., Pfeifer, J., and Bax, A. (1995). NMRPipe: a multidimensional spectral processing system based on UNIX pipes. *J Biomol NMR* 6, 277-293.

Delano, W.L. (2002). The PyMOL Molecular Graphics System, Version 1.3. (Schrödinger, LLC.).

Domann, E., Wehland, J., Rohde, M., Pistor, S., Hartl, M., Goebel, W., Leimeister-Wachter, M., Wuenscher, M., and Chakraborty, T. (1992). A novel bacterial virulence gene in *Listeria monocytogenes* required for host cell microfilament interaction with homology to the proline-rich region of vinculin. *EMBO J* 11, 1981-1990.

Dong, W., Liu, Y., Peng, J., Chen, L., Zou, T., Xiao, H., Liu, Z., Li, W., Bu, Y., and Qi, Y. (2006). The IRAK-1-BCL10-MALT1-TRAF6-TAK1 cascade mediates signaling to NF-kappaB from Toll-like receptor 4. *J Biol Chem* 281, 26029-26040.

Doyle, S.E., O'Connell, R.M., Miranda, G.A., Vaidya, S.A., Chow, E.K., Liu, P.T., Suzuki, S., Suzuki, N., Modlin, R.L., Yeh, W.C., *et al.* (2004). Toll-like receptors induce a phagocytic gene program through p38. *J Exp Med* 199, 81-90.

Farrow, N.A., Zhang, O., Forman-Kay, J.D., and Kay, L.E. (1994). A heteronuclear correlation experiment for simultaneous determination of ¹⁵N longitudinal decay and chemical exchange rates of systems in slow equilibrium. *J Biomol NMR* 4, 727-734.

Fedorov, A.A., Fedorov, E., Gertler, F., and Almo, S.C. (1999). Structure of EVH1, a novel proline-rich ligand-binding module involved in cytoskeletal dynamics and neural function. *Nat Struct Biol* 6, 661-665.

Fischer, G., Bang, H., and Mech, C. (1984). [Determination of enzymatic catalysis for the cis-trans-isomerization of peptide binding in proline-containing peptides]. *Biomed Biochim Acta* 43, 1101-1111.

Gan, L., and Li, L. (2010). Interleukin-1 Receptor-Associated Kinase-1 (IRAK-1) functionally associates with PKCepsilon and VASP in the regulation of macrophage migration. *Mol Immunol* 47, 1278-1282.

Gertler, F.B., Niebuhr, K., Reinhard, M., Wehland, J., and Soriano, P. (1996). Mena, a relative of VASP and *Drosophila* Enabled, is implicated in the control of microfilament dynamics. *Cell* 87, 227-239.

Goddard TD, K.D. (2008). Sparky 3. (University of California, San Francisco).

Goh, K.L., Cai, L., Cepko, C.L., and Gertler, F.B. (2002). Ena/VASP proteins regulate cortical neuronal positioning. *Curr Biol* 12, 565-569.

Gottipati, S., Rao, N.L., and Fung-Leung, W.P. (2008). IRAK1: a critical signaling mediator of innate immunity. *Cell Signal* 20, 269-276.

Grevengoed, E.E., Loureiro, J.J., Jesse, T.L., and Peifer, M. (2001). Abelson kinase regulates epithelial morphogenesis in *Drosophila*. *J Cell Biol* 155, 1185-1198.

Guex, N., and Peitsch, M.C. (1997). SWISS-MODEL and the Swiss-PdbViewer: an

environment for comparative protein modeling. *Electrophoresis* *18*, 2714-2723.

Hagerman, P.J., and Baldwin, R.L. (1976). A quantitative treatment of the kinetics of the folding transition of ribonuclease A. *Biochemistry* *15*, 1462-1473.

Haghighyeghi, A., Sarac, A., Czerniecki, S., Grosshans, J., and Schock, F. (2010). Pellino enhances innate immunity in *Drosophila*. *Mech Dev* *127*, 301-307.

Hansen, S.D., and Mullins, R.D. (2010). VASP is a processive actin polymerase that requires monomeric actin for barbed end association. *J Cell Biol* *191*, 571-584.

Kay, B.K., Williamson, M.P., and Sudol, M. (2000). The importance of being proline: the interaction of proline-rich motifs in signaling proteins with their cognate domains. *FASEB J* *14*, 231-241.

Kim, J.H., Sung, K.S., Jung, S.M., Lee, Y.S., Kwon, J.Y., Choi, C.Y., and Park, S.H. (2011). Pellino-1, an adaptor protein of interleukin-1 receptor/toll-like receptor signaling, is sumoylated by Ubc9. *Mol Cells*.

Kong, L., and Ge, B.X. (2008). MyD88-independent activation of a novel actin-Cdc42/Rac pathway is required for Toll-like receptor-stimulated phagocytosis. *Cell Res* *18*, 745-755.

Kovrigina, E.L. (2012). NMR line shapes and multi-state binding equilibria. *J Biomol NMR* *53*, 257-270.

Krause, M., Dent, E.W., Bear, J.E., Loureiro, J.J., and Gertler, F.B. (2003). Ena/VASP proteins: regulators of the actin cytoskeleton and cell migration. *Annu Rev Cell Dev Biol* *19*, 541-564.

Krause, M., Leslie, J.D., Stewart, M., Lafuente, E.M., Valderrama, F., Jagannathan, R., Strasser, G.A., Robinson, D.A., Liu, H., Way, M., *et al.* (2004). Lamellipodin, an Ena/VASP ligand, is implicated in the regulation of lamellipodial dynamics. *Dev Cell* *7*, 571-583.

Krause, M., Sechi, A.S., Konradt, M., Monner, D., Gertler, F.B., and Wehland, J. (2000). Fyn-binding protein (Fyb)/SLP-76-associated protein (SLAP), Ena/vasodilator-stimulated phosphoprotein (VASP) proteins and the Arp2/3 complex link T cell receptor (TCR) signaling to the actin cytoskeleton. *J Cell Biol* *149*, 181-194.

Lemmon, M.A., and Schlessinger, J. (1994). Regulation of signal transduction and signal diversity by receptor oligomerization. *Trends Biochem Sci* *19*, 459-463.

Levitt, M. (1978). Conformational preferences of amino acids in globular proteins. *Biochemistry* *17*, 4277-4285.

Lin, C.C., Huoh, Y.S., Schmitz, K.R., Jensen, L.E., and Ferguson, K.M. (2008). Pellino proteins contain a cryptic FHA domain that mediates interaction with phosphorylated IRAK1. *Structure* *16*, 1806-1816.

Lin, S.C., Lo, Y.C., and Wu, H. (2010). Helical assembly in the MyD88-IRAK4-IRAK2 complex in TLR/IL-1R signalling. *Nature* *465*, 885-890.

Martin, M.U., and Wesche, H. (2002). Summary and comparison of the signaling mechanisms of the Toll/interleukin-1 receptor family. *Biochim Biophys Acta* *1592*, 265-280.

May, R.C., and Machesky, L.M. (2001). Phagocytosis and the actin cytoskeleton. *J Cell Sci* *114*, 1061-1077.

McConnell, H.M. (1958). Reaction rates by nuclear magnetic resonance. *J. Chem. Phys.* *28*, 430-431.

McCulloch, C.A., Downey, G.P., and El-Gabalawy, H. (2006). Signalling platforms

that modulate the inflammatory response: new targets for drug development. *Nat Rev Drug Discov* 5, 864-876.

McGettrick, A.F., and O'Neill, L.A. (2010). Regulators of TLR4 signaling by endotoxins. *Subcell Biochem* 53, 153-171.

McTaggart, S.J., Obbard, D.J., Conlon, C., and Little, T.J. (2012). Immune genes undergo more adaptive evolution than non-immune system genes in *Daphnia pulex*. *BMC Evol Biol* 12, 63.

Moresco, E.M., LaVine, D., and Beutler, B. (2011). Toll-like receptors. *Curr Biol* 21, R488-493.

Mori, S., Abeygunawardana, C., Johnson, M.O., and van Zijl, P.C. (1995). Improved sensitivity of HSQC spectra of exchanging protons at short interscan delays using a new fast HSQC (FHSQC) detection scheme that avoids water saturation. *J Magn Reson B* 108, 94-98.

Ng, K.K., and Weis, W.I. (1998). Coupling of prolyl peptide bond isomerization and Ca²⁺ binding in a C-type mannose-binding protein. *Biochemistry* 37, 17977-17989.

Nicholson, L.K., and Lu, K.P. (2007). Prolyl cis-trans Isomerization as a molecular timer in Crk signaling. *Mol Cell* 25, 483-485.

Niebuhr, K., Ebel, F., Frank, R., Reinhard, M., Domann, E., Carl, U.D., Walter, U., Gertler, F.B., Wehland, J., and Chakraborty, T. (1997). A novel proline-rich motif present in ActA of *Listeria monocytogenes* and cytoskeletal proteins is the ligand for the EVH1 domain, a protein module present in the Ena/VASP family. *EMBO J* 16, 5433-5444.

Piotukh, K., Gu, W., Kofler, M., Labudde, D., Helms, V., and Freund, C. (2005). Cyclophilin A binds to linear peptide motifs containing a consensus that is present in many human proteins. *J Biol Chem* 280, 23668-23674.

Pistor, S., Chakraborty, T., Walter, U., and Wehland, J. (1995). The bacterial actin nucleator protein ActA of *Listeria monocytogenes* contains multiple binding sites for host microfilament proteins. *Curr Biol* 5, 517-525.

Prehoda, K.E., Lee, D.J., and Lim, W.A. (1999). Structure of the enabled/VASP homology 1 domain-peptide complex: a key component in the spatial control of actin assembly. *Cell* 97, 471-480.

Qin, J., Qian, Y., Yao, J., Grace, C., and Li, X. (2005). SIGIRR inhibits interleukin-1 receptor- and toll-like receptor 4-mediated signaling through different mechanisms. *J Biol Chem* 280, 25233-25241.

Reimer, U., Scherer, G., Drewello, M., Kruber, S., Schutkowski, M., and Fischer, G. (1998). Side-chain effects on peptidyl-prolyl cis/trans isomerisation. *J Mol Biol* 279, 449-460.

Reinhard, M., Jouvenal, K., Tripier, D., and Walter, U. (1995). Identification, purification, and characterization of a zyxin-related protein that binds the focal adhesion and microfilament protein VASP (vasodilator-stimulated phosphoprotein). *Proc Natl Acad Sci U S A* 92, 7956-7960.

Reinhard, M., Rudiger, M., Jockusch, B.M., and Walter, U. (1996). VASP interaction with vinculin: a recurring theme of interactions with proline-rich motifs. *FEBS Lett* 399, 103-107.

Roitt, I.M., Brostoff, J., and Male, D.K. (2001). *Immunology*, 6th edn (Edinburgh; New York: Mosby).

Rottner, K., Behrendt, B., Small, J.V., and Wehland, J. (1999). VASP dynamics

during lamellipodia protrusion. *Nat Cell Biol* 1, 321-322.

Sarkar, P., Saleh, T., Tzeng, S.R., Birge, R.B., and Kalodimos, C.G. (2011). Structural basis for regulation of the Crk signaling protein by a proline switch. *Nat Chem Biol* 7, 51-57.

Schmidpeter, P.A., Jahreis, G., Geitner, A.J., and Schmid, F.X. (2011). Prolyl isomerases show low sequence specificity toward the residue following the proline. *Biochemistry* 50, 4796-4803.

Song, F., Zhang, X., Ren, X.B., Zhu, P., Xu, J., Wang, L., Li, Y.F., Zhong, N., Ru, Q., Zhang, D.W., *et al.* (2011). Cyclophilin A (CyPA) induces chemotaxis independent of its peptidylprolyl cis-trans isomerase activity: direct binding between CyPA and the ectodomain of CD147. *J Biol Chem* 286, 8197-8203.

Sun, L., Deng, L., Ea, C.K., Xia, Z.P., and Chen, Z.J. (2004). The TRAF6 ubiquitin ligase and TAK1 kinase mediate IKK activation by BCL10 and MAL1 in T lymphocytes. *Mol Cell* 14, 289-301.

Thies, M.J., Mayer, J., Augustine, J.G., Frederick, C.A., Lilie, H., and Buchner, J. (1999). Folding and association of the antibody domain CH3: prolyl isomerization precedes dimerization. *J Mol Biol* 293, 67-79.

Towers, G.J. (2007). The control of viral infection by tripartite motif proteins and cyclophilin A. *Retrovirology* 4, 40.

Tun-Kyi, A., Finn, G., Greenwood, A., Nowak, M., Lee, T.H., Asara, J.M., Tsokos, G.C., Fitzgerald, K., Israel, E., Li, X., *et al.* (2011). Essential role for the prolyl isomerase Pin1 in Toll-like receptor signaling and type I interferon-mediated immunity. *Nat Immunol* 12, 733-741.

Uematsu, S., and Akira, S. (2007). Toll-like receptors and Type I interferons. *J Biol Chem* 282, 15319-15323.

Vasioukhin, V., Bauer, C., Yin, M., and Fuchs, E. (2000). Directed actin polymerization is the driving force for epithelial cell-cell adhesion. *Cell* 100, 209-219.

Watters, T.M., Kenny, E.F., and O'Neill, L.A. (2007). Structure, function and regulation of the Toll/IL-1 receptor adaptor proteins. *Immunol Cell Biol* 85, 411-419.

Wedemeyer, W.J., Welker, E., and Scheraga, H.A. (2002). Proline cis-trans isomerization and protein folding. *Biochemistry* 41, 14637-14644.

Wehrle-Haller, B., and Imhof, B.A. (2003). Actin, microtubules and focal adhesion dynamics during cell migration. *Int J Biochem Cell Biol* 35, 39-50.

Weiss, A., and Schlessinger, J. (1998). Switching signals on or off by receptor dimerization. *Cell* 94, 277-280.

Wilson, N.S., Dixit, V., and Ashkenazi, A. (2009). Death receptor signal transducers: nodes of coordination in immune signaling networks. *Nat Immunol* 10, 348-355.

Yates, R.M., Hermetter, A., Taylor, G.A., and Russell, D.G. (2007). Macrophage activation downregulates the degradative capacity of the phagosome. *Traffic* 8, 241-250.

Zoldak, G., Aumuller, T., Lucke, C., Hritz, J., Oostenbrink, C., Fischer, G., and Schmid, F.X. (2009). A library of fluorescent peptides for exploring the substrate specificities of prolyl isomerases. *Biochemistry* 48, 10423-10436.

CHAPTER 3

The VASP EVH1 Domain Recognizes Phosphorylated Sequences and Contains a Secondary Binding Site

Abstract

Protein domains that recognize phosphorylated serine or threonine residues include FHA, MH2, FF, 14-3-3, polo box, BRCT, WD40, and WW domains. These domains generally bind phosphorylated sequences with affinities many orders of magnitude greater than their unphosphorylated analogs. The VASP EVH1 domain is not considered a phosphorylation-binding domain, but rather binds the proline rich (F/W)Px ϕ P motif. This motif appears in the cytoskeletal proteins zyxin, vinculin, and lamellipodin as well as the proteins Fyb/SLAP and IRAK1 which are involved in immune cell signaling. However, this core motif is generally flanked by negatively charged amino acids that contribute to the affinity of the interaction with VASP. We show that the VASP binding site in IRAK1, a relatively weakly binding site that does not contain negatively charged amino acids, binds VASP-EVH1 with sevenfold increased affinity upon phosphorylation of two flanking serine residues. We report the binding affinities, binding kinetics, and chemical shift perturbation profiles of a series of IRAK1-derived peptides, providing insights into the contacts and forces that determine VASP-EVH1 binding specificity. We also demonstrate that, as previously shown for the unphosphorylated sequence, phosphorylated IRAK1 partitions into nearly equally populated *cis* and *trans* isomers. Based on these results we propose that the VASP/IRAK1 interaction is regulated by IRAK1 autophosphorylation. Given that IRAK1 autophosphorylates in response to TLR/IL-1R signaling, this could serve to link those signaling pathways with VASP-mediated cytoskeletal rearrangement without requiring VASP to constitutively bind to IRAK1. We further note that serine

residues are enriched in VASP binding sites and propose that other VASP interactions may likewise be regulated by phosphorylation. Lastly, we report the observation of a noncanonical binding site on the opposite face of the EVH1 domain which may recognize a variation on the canonical (F/W)Px ϕ P binding sequence. We propose that this secondary site may bind the tandem repeats of VASP interaction proteins such as zyxin and lamellipodin.

Introduction

IRAK1 is a Ser/Thr kinase which is activated by phosphorylation by the related IRAK4 upon either toll-like receptor (TLR) or interleukin-1 receptor (IL-1R) stimulation (Li et al., 2002; O'Neill, 2008). This is achieved by the formation of a helical array of the death domains of IRAK4, IRAK1 (or IRAK2), and the adapter protein MyD88 on the intracellular TIR (toll/IL-1 receptor) domains of the receptors, collectively known as the Myddosome (Lin et al., 2010). This leads to further, extensive phosphorylation, probably via IRAK1 itself, of the Ser/Pro rich undefined domain (UD) of IRAK1 (Kollewe et al., 2004). This phosphorylation is necessary for dissociation of IRAK1 from the Myddosome (Cao et al., 1996), as well as interactions with downstream binding partners including Pin1 (Tun-Kyi et al., 2011) and Pellino (Lin et al., 2008).

We have previously shown that a proline-rich sequence in the IRAK1-UD binds to the EVH1 domain of the actin cytoskeletal rearrangement protein VASP (Chapter 2). The VASP-EVH1 domain binds the proline rich (F/W)Px ϕ P motif where ϕ is an aliphatic amino acid and x is any amino acid (Ball et al., 2000; Niebuhr et al., 1997; Pistor et al., 1995). Most commonly in actual confirmed VASP-binding proteins, the binding site sequence is FPPPP. Furthermore, negatively charged amino acids usually flank this core motif at one or more of the five positions C-terminal to

the motif as well as one or more of the four N-terminal to it. These negative charges contribute significantly to the affinity of the interaction (Ball et al., 2000; Carl et al., 1999). In this paper, we demonstrate that the interaction between the VASP-EVH1 domain and the $_{167}\text{LWPPPP}_{172}$ region of IRAK1-UD is significantly strengthened by phosphorylation of two serine residues (S166, S173) flanking the $_{167}\text{LWPPPP}_{172}$ sequence ($K_D = 25 \pm 2 \mu\text{M}$ vs. $203 \pm 3 \mu\text{M}$ unphosphorylated). This suggests that the interaction is regulated by autophosphorylation of IRAK1, which can occur in response to TLR or IL-1 receptor signaling (Cao et al., 1996; Kollwe et al., 2004). Binding of IRAK1 to the constitutive tetramer (Haffner et al., 1995) VASP could be further enhanced by IRAK1 tetramerization, which is triggered by assembly of the Myddosome during TLR or IL-1 receptor signaling (Lin et al., 2010). These observations suggest a novel mechanism for how IRAK1 autophosphorylation might play an important role in regulating the connection between innate immunity signaling and cytoskeletal remodeling. More broadly, they suggest that localization of Ena/VASP proteins may be regulated by phosphorylation of serine/threonine residues in their binding partners, especially lamellipodin, which is involved in the formation of lamellipodia.

Despite the fact that IRAK1 harbors the only WPPPP motif known to interact with VASP, multiple studies report that VASP-EVH1 has a significant preference for WPPPP over FPPPP motifs (Ball et al., 2000; Niebuhr et al., 1997; Zimmermann et al., 2003). We investigate the structural origin of this preference by assessing the differences in hydrogen bond formation and binding kinetics between WPPPP and FPPPP motifs. We further show that isomerization of the $\text{W}_{168}\text{-P}_{169}$ peptide bond by cyclophilin A, which has shown to facilitate binding to VASP-EVH1 (Chapter 2), is not hampered by phosphorylation of S166 and S173. Lastly, we report the observation of a weak secondary peptide-binding surface on the EVH1 domain, featuring an

arginine residue strictly conserved in the EVH1 domains of WASP, RanBP1, and Homer protein families.

Materials and Methods

Protein Purification and Peptide Preparation.

Proteins were purified as previously described (Chapter 2). Briefly, proteins were bacterially expressed as N-terminally tagged 6X-histidine fusion proteins and purified using nickel-NTA columns. ¹⁵N-labeled Human VASP-EVH1 (VASP residues 1-115) (Boeda et al., 2007) was purified with the histidine tag removed using a protease cut site, while full-length human CypA was purified with the histidine tag intact (Piotukh et al., 2005). After purification proteins were dialyzed into NMR buffer (20 mM KH₂PO₄, 50 mM KCl, 1 mM TCEP, pH 6.7) and 5 mM NaN₃ and 7% D₂O were added. Protein concentration was measured by UV absorbance using theoretical extinction coefficients.

Peptides encompassing IRAK1 residues P₁₆₂-K₁₈₀ either with the natural sequence (IRAK1¹⁶²⁻¹⁸⁰), with a phosphate group on Ser166 (IRAK1^{162-180, pS166}), with phosphate groups on both Ser166 and Ser173 (IRAK1^{162-180, pS166, pS173}), or a tryptophan-to-phenylalanine mutation (IRAK1^{162-180, W168F}) were purchased and delivered as a lyophilized powder. Slightly longer peptides encompassing IRAK1 residues E₁₅₇-K₁₈₀ with phosphorylation either at Ser163 (IRAK1^{157-180, pS163}) or Ser173 (IRAK1^{157-180, pS173}) were similarly purchased. IRAK1¹⁶²⁻¹⁸⁰, IRAK1^{162-180, W168F}, IRAK1^{157-180, pS163}, IRAK1^{157-180, pS173}, and IRAK1^{162-180, pS166, pS173} were purchased from the Tufts University Core Facility (Boston, MA), while IRAK1^{162-180, pS166} was purchased from Genscript (Piscataway, NJ). Peptides were dissolved in NMR buffer plus 5 mM NaN₃ and 7% D₂O. Peptide concentration was determined by UV absorbance, using the theoretical extinction coefficient of 195 cm⁻¹M⁻¹ at 257 nm

for IRAK1^{162-180, W168F}, and 5500 cm⁻¹M⁻¹ at 280 nm for the other peptides. NaOH and HCl were used to adjust sample pH.

NMR Data Collection and Processing.

NMR experiments were carried out at 25 °C (unless otherwise stated) on a Varian Inova 600 MHz spectrometer with a {H, C, N} Z-axis gradient probe. NMR data processing was performed using nmrPipe, apodizing with either a phase-shifted sine bell or exponential window function. Data analysis was performed using the software nmrDraw (Delaglio et al., 1995) and Sparky (Goddard TD, 2008), using the Sparky peak detection function to measure peak heights and positions.

NMR Titrations.

Five titrations of ¹⁵N EVH1 domain (with the peptides IRAK1^{157-180, pS163}, IRAK1^{162-180, pS166}, IRAK1^{157-180, pS173}, IRAK1^{160-180, pS166, pS173}, and IRAK1^{162-180, W168F}) were performed. NMR titrations were carried out by preparing the most saturated sample first and producing subsequent samples by diluting with a stock of labeled EVH1 domain, as described (Chapter 2). In the titration of ¹⁵N EVH1 domain with IRAK1^{162-180, W168F}, the concentration of EVH1 was held between 0.33-0.37 mM and the peptide concentrations were 0, 0.11, 0.22, 0.43, 0.87, 1.73, 3.46, and 6.92 mM. In the titration of ¹⁵N EVH1 domain with IRAK1^{157-180, pS163}, the concentration of EVH1 was held between 0.36-0.37 mM and the peptide concentrations were 0, 0.02, 0.05, 0.09, 0.19, 0.37, 0.75, and 1.49 mM. In the titration of ¹⁵N EVH1 domain with IRAK1^{162-180, pS166}, the concentration of EVH1 was held between 0.36-0.37 mM and the peptide concentrations were 0, 0.03, 0.05, 0.11, 0.22, 0.44, 0.87, 1.75, and 3.49 mM. In the titration of ¹⁵N EVH1 domain with IRAK1^{157-180, pS173}, the concentration of EVH1 was held at 0.37 mM and the peptide concentrations were 0, 0.01, 0.03, 0.06, 0.11, 0.23, 0.46, 0.92, and 1.83 mM. In the titration of ¹⁵N EVH1 domain with IRAK1^{162-180, pS166, pS173}, the concentration of EVH1 was held at 0.37 mM and the

peptide concentrations were 0, 0.02, 0.04, 0.08, 0.16, 0.31, 0.63, 1.25, 2.50, and 5.01 mM. In the proton dimension, a spectral width of 8 kHz (2048 complex data points) was used and in the nitrogen dimension a width of 1.8 kHz (256 complex data points) was used. Resonance assignments for the ^{15}N EVH1 domain were obtained from the BioMagResBank (accession number 18569 (Ball et al., 2000)).

Measurement of Amide Proton Temperature Coefficients.

Two IRAK1¹⁶²⁻¹⁸⁰ ^1H - ^1H TOCSY temperature series were taken (of 4 mM IRAK1¹⁶²⁻¹⁸⁰ and 0.5 mM IRAK1¹⁶²⁻¹⁸⁰ with 1.5 mM EVH1 domain, at temperatures 20, 24, 28, 32, and 36 and 20, 25, and 30 °C respectively. Temperature coefficients were obtained by linear fitting of the proton chemical shift of each peak, after proper referencing of the spectra (Wishart et al., 1995).

Quantification of Binding Affinities and NMR Lineshape Analysis.

NMR lineshape analysis was carried out as described (De et al., 2012) (Chapter 2). The dissociation constant K_D was first measured by fitting chemical shift perturbation data from the ^{15}N EVH1 titrations. For given concentrations of IRAK1 peptide, $[\text{IRAK1}^{\text{tot}}]$, and EVH1, $[\text{EVH1}^{\text{tot}}]$, the change in chemical shift for each dimension ($\Delta\delta_{\text{H}}$ and $\Delta\delta_{\text{N}}$) for a given titration point is proportional to the percentage of bound EVH1 domain,

$$\Delta\delta = \Delta\delta^{\text{max}} \cdot (K_D + [\text{EVH1}^{\text{tot}}] + [\text{IRAK1}^{\text{tot}}] - \sqrt{(K_D + [\text{EVH1}^{\text{tot}}] + [\text{IRAK1}^{\text{tot}}])^2 - 4 \cdot [\text{EVH1}^{\text{tot}}][\text{IRAK1}^{\text{tot}}]}) / (2[\text{EVH1}^{\text{tot}}]) \quad (3.1)$$

Fitted parameters included the chemical shift difference between free and bound $\Delta\delta^{\text{max}}$, the dissociation constant K_D , and for binding curves with a sharp enough shape ($K_D < 100 \mu\text{M}$), a scaling factor to correct for small inaccuracies in the peptide concentration measurement, as described in Chapter 2. 21 ^1H and 21 ^{15}N chemical shift datasets were independently fit using the Solver function in Excel, yielding a

mean and standard error which we report as K_D and its error. We also report the K_D^{trans} , the dissociation constant specifically for the *trans* isomer of the (W/F)-P peptide bond for each peptide, given by

$$K_D^{trans} = K_D \cdot K_{isom} / (1 + K_{isom}) \quad (3.2)$$

where K_{isom} is the ratio of *trans* to *cis*, determined from peak volumes in ^1H - ^1H TOCSY spectra.

NMR Lineshape analysis was carried out as described (De et al., 2012; Greenwood et al., 2011) using the *BiophysicsLab* Matlab package (Kovrigin, 2012). Briefly, the dependence of ^{15}N EVH1 ^1H and ^{15}N lineshapes on peptide concentration were fit to the two-state solution to the Bloch-McConnell equations (Cavanagh J, 2007; McConnell, 1958) to extract the dissociation rate, k_{off} of the interaction. Constrained parameters included the dissociation constant, K_D , apo chemical shift, ω^{Apo} , linewidth of apo state, $R_{2,0}^{free}$, and ratio of *trans* to *cis*, K_{isom} , while the dissociation rate k_{off} and chemical shift and linewidth of the bound state, ω^{Bound} and $R_{2,0}^{bound}$, were all fitted. We report as error the standard error of multiple fits of independent lineshape datasets.

To measure the affinity of peptide binding to the weak secondary binding site, the ^{15}N EVH1 titration ^{15}N and ^1H chemical shift data from the tightest-binding peptide, IRAK1^{162-180, pS166, pS173}, were fit to a three-state model. This was carried out similarly with *BiophysicsLab*, but without application of the lineshape analysis component. Eight binding curves from residues in the primary binding site and 21 binding curves sensitive to the secondary binding event were simultaneously fit. ^{15}N chemical shift data was scaled by a factor of 0.154 so that ^{15}N and ^1H data would roughly contribute equally to the fit. Fitted parameters included the dissociation constants for the primary and secondary sites, a single set of bound chemical shifts for the primary site datasets, and two sets of bound chemical shifts for the secondary-site

binding curves. The apo chemical shifts for all residues were determined from the apo spectrum and constrained in the fit.

Electrostatic Potential Map.

The electrostatic potential map was generated using the Adaptive Poisson-Boltzmann Solver (APBS) plugin in Pymol (Baker et al., 2001). Dielectrics of 78 and 2 were used for the solution and protein, respectively, and a concentration of 150 mM monovalent ion was used.

Modeling the IRAK-1/EVH1 complex.

The model of VASP-EVH1 bound to IRAK1¹⁶⁵⁻¹⁷⁵ was built as described (Chapter 2), using the solution structure of the VASP EVH1 domain (PDB ID code 1EGX (Ball et al., 2000)) and the crystal structure of the Mena EVH1 domain/ActA complex (PDB ID code 1EVH (Prehoda et al., 1999)). Briefly, the VASP solution structure was aligned with the Mena crystal structure and the IRAK1 sequence was built in using the ActA peptide structure as a guide. Modeling was performed using Swiss-Pdb viewer (Guex and Peitsch, 1997) and the model was colored by chemical shift perturbation using the scripts “data2bfactor.py” and “color_b.py” from Dr. Robert L. Campbell’s PyMol script repository at Queen’s University, Ontario, Canada (<http://pldserver1.biochem.queensu.ca/~rlc/work/pymol/>) in PyMOL (Delano, 2002).

Demonstration of Isomerization by ROESY Spectroscopy.

¹H-¹H ROESY spectra (mixing times of 0.04, 0.06, 0.08, 0.10, 0.15, 0.20 s) were acquired for a sample of 3.64 mM IRAK1^{162-180, pS166, pS173} with 10 μ M CypA. Spectral widths of 8 kHz were used in both dimensions, with 2048 (256) directly (indirectly) detected data points. The heights of the W168 sidechain crosspeaks and *cis* and *trans* autopeaks were measured and fit to the two-state solution of the Bloch-McConnell equations (Cavanagh J, 2007; McConnell, 1958) using the Solver function

in Microsoft Excel. Fixed parameters included the ratio of *trans* to *cis* isomer, K_{isom} , determined from peak volumes from a ^1H - ^1H TOCSY spectrum. The initial intensity of the *cis* and *trans* autopeaks, $I_{CC,0}$ and $I_{TT,0}$, and the isomerization rate k_{ex} were fitted.

Results

The IRAK1 VASP-EVH1 interaction is enhanced by phosphorylation of IRAK1

The VASP binding sites in ActA, Zyxin, Vinculin, and Lamellipodin all contain flanking negatively charged amino acid residues that contribute to EVH1 domain binding (Ball et al., 2000; Carl et al., 1999). However, the $_{167}\text{LWPPPP}_{172}$ motif in IRAK1 is instead flanked by serine residues (Ser166 and Ser173). The UD of IRAK1 is known to be hyperphosphorylated upon receptor stimulation (Kollewe et al., 2004), suggesting that flanking phosphoserine residues might contribute to the VASP-EVH1 interaction with the $_{167}\text{LWPPPP}_{172}$ motif in activated IRAK1. Ser173 has been shown to be phosphorylated in response to TLR7 stimulation (Tun-Kyi et al., 2011) but phosphorylation of Ser166 has not been investigated.

To investigate whether potential phosphorylation of the IRAK1-UD influences EVH1 binding, we employed two-dimensional NMR spectroscopy with ^{15}N -labeled VASP-EVH1 domain. We titrated ^{15}N -EVH1 with a series of peptides encompassing residues E157-K180 or P162-K180 but with various serine residues phosphorylated in order to determine the impact of phosphorylation on the affinity and kinetics of binding (peptides are defined in Figure 3.1A). Fitting peak positions as a function of peptide concentration allowed for determination of the dissociation constant, K_D , for each peptide, summarized in Table 1 (Figure 3.1B). Furthermore, we calculated the K_D^{trans} , the dissociation constant specifically for the *trans* isomer of the (W/F)-P peptide bond which the EVH1 domain specifically selects. K_D^{trans} is proportional to

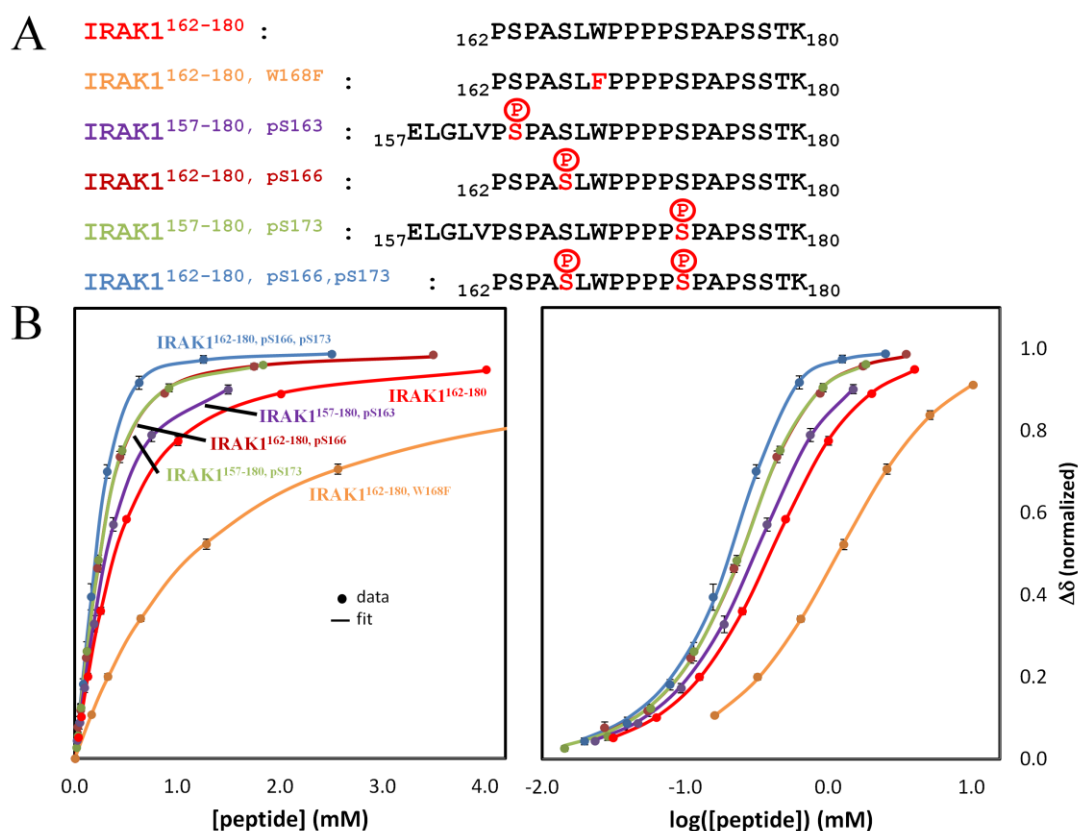


Figure 3.1: Phosphorylation of IRAK1 enhances its affinity for VASP-EVH1. (A) IRAK1-derived peptides used in this study. Phosphate groups are displayed above the sequences. (B) Comparison of the binding curves from six ¹⁵N EVH1 titrations, with the peptides defined in panel A. The data and fit for each peptide are averages of 42 normalized individual binding curves and their fits. Binding curves are shown on both linear (left) and log (right) scales. Depending on the identity of the aromatic residue (phenylalanine vs. tryptophan) and the phosphorylation status of serines 166 and 173, the binding affinity of this sequence for VASP-EVH1 can vary over an order of magnitude.

K_D and defined by Equation 3.2. Phosphorylation of either Ser166 or Ser173 increases the affinity more than threefold, while phosphorylation of both serines increases the affinity more than sevenfold. By contrast, phosphorylation of the more distant Ser163 resulted in a measurable but smaller increase in the binding affinity. In each titration, the peaks that moved the farthest upon addition of peptide broadened at intermediate peptide concentrations and sharpened again upon saturation (Figure 3.2.) This line-broadening is sensitive to the kinetics of binding, allowing determination of the on- and off-rates of the interaction using NMR lineshape analysis. In each case, phosphorylation increased the k_{on} rate and decreased the k_{off} rate, though the effect on the k_{off} rate was generally greater (Table 3.1). This suggests a combination of electrostatic steering (increasing k_{on}) and electrostatic stabilization of the complex (decreasing k_{off}).

In order to identify EVH1 residues interacting with the phosphate groups on Ser166 and Ser173, a model of the complex was built using a solution structure (PDB ID 1EGX (Ball et al., 2000)) of the VASP EVH1 domain and the crystal structure of the Mena EVH1 domain bound to an ActA-derived peptide (PDB ID 1EVH (Prehoda et al., 1999)), as described (Chapter 2). The differences in bound ^{15}N EVH1 chemical shift between the titrations with phosphopeptides and the unphosphorylated IRAK1¹⁶²⁻¹⁸⁰, given by

$$\Delta\Delta\delta = \sqrt{(\delta_{H,bound}^{IRAK1-162-180} - \delta_{H,bound}^{peptide})^2 + (0.154 \cdot (\delta_{N,bound}^{IRAK1-162-180} - \delta_{N,bound}^{peptide}))^2} \quad 3.3$$

were then mapped to the model (Figure 3.3A). The 10 peaks with the largest $\Delta\Delta\delta$ between IRAK1¹⁶²⁻¹⁸⁰ and IRAK1^{162-180, pS166} included the sidechain of W82 and the backbone amides of D84-V88 and K71. This implicates the sidechains of R83, R86 and K71, all of which seem positioned in the model to interact with a phosphate group on Ser166. Likewise, peaks representing the backbone amides of residues N20, R22, and W23 were among the five peaks with the highest difference in bound

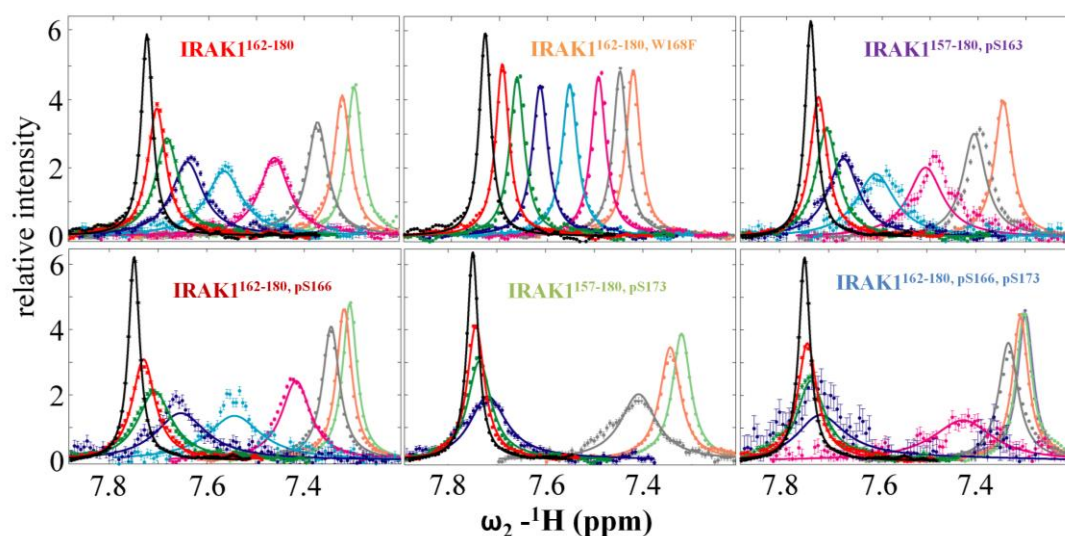


Figure 3.2: Binding kinetics derived from NMR lineshape analysis of ^{15}N EVH1 peaks in peptide titrations. 1D peak slices either along the ^{15}N or ^1H dimension were derived from 2D ^{15}N EVH1 spectra and fit to obtain the kinetics of binding. Displayed are the data (symbols) and fits (solid lines) of the A75 ^1H dimension peak slices for the peptides IRAK1¹⁶²⁻¹⁸⁰, IRAK1^{162-180, W168F}, IRAK1^{157-180, pS163}, IRAK1^{162-180, pS166}, IRAK1^{157-180, pS173}, and IRAK1^{162-180, pS166, pS173}.

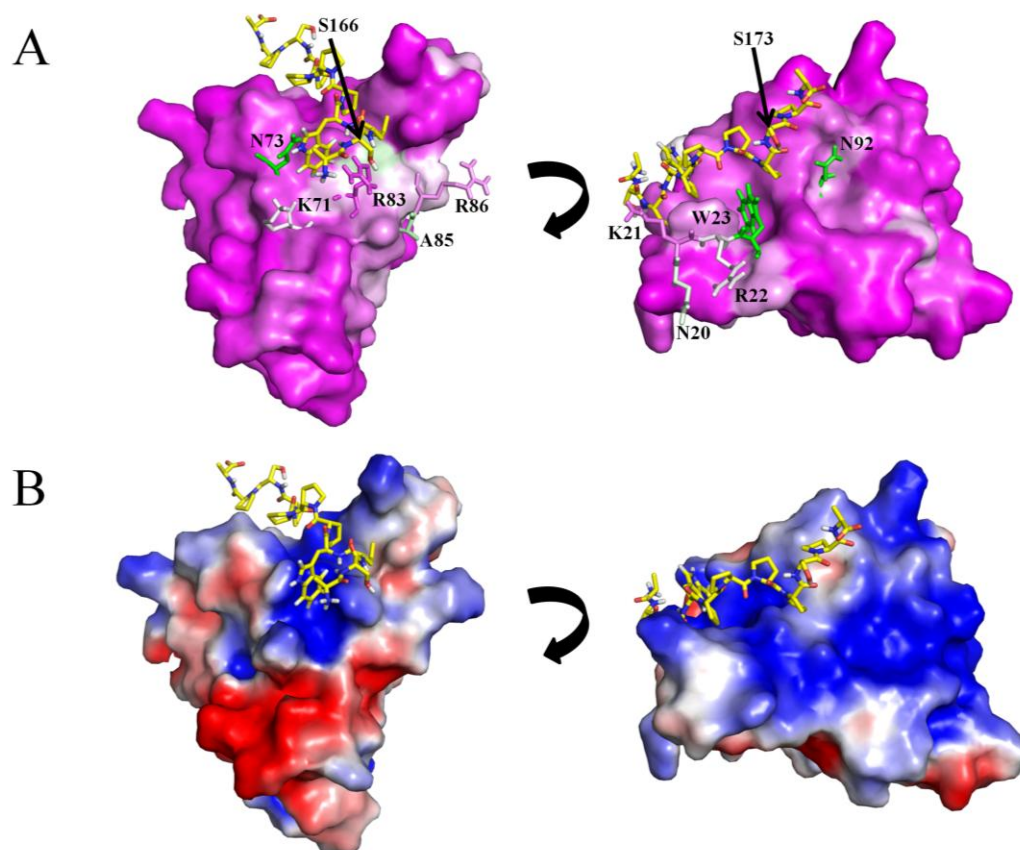


Figure 3.3: Suggested basis for EVH1 phosphoserine recognition. (A) Model of EVH1/IRAK1 complex colored by chemical shift perturbation differences. Left, the surface representation of the EVH1 domain is colored by the chemical shift difference between the complexes with the IRAK1¹⁶²⁻¹⁸⁰ and IRAK1^{162-180, pS166} peptides, and on the right by the difference between the IRAK1¹⁶²⁻¹⁸⁰ and IRAK1^{157-180, pS173} peptides (magenta=no difference, green=highest difference). Select side chains are shown as sticks and similarly colored. (B) Electrostatic surface potential of the EVH1 domain. The peptide-binding groove as well as the surface interacting with the C-terminal residues of the peptide both show strong positive surface potentials (blue=positive, red=negative).

chemical shift between IRAK1¹⁶²⁻¹⁸⁰ and IRAK1^{162-180, pS173}, suggesting that a phosphate group on Ser173 could participate in a salt bridge with the sidechains of K21, R22, or both, when bound to the EVH1 domain. Additionally, mapping the $\Delta\Delta\delta$ of each peptide in Figure 3.1A to the EVH1 structure allows for a rough visualization of the position of each modified peptide residue in the complex (Appendix Figure 3.1).

Table 3.1: Binding rates and affinities of IRAK1-derived peptides

	k_{off} (s ⁻¹)	k_{on} (M ⁻¹ s ⁻¹)	K_D (μM)	K_D^{trans} (μM)
IRAK1^{162-180,‡}	4,000 ± 200	3.5 ± 0.1 x 10⁷	203 ± 3	116 ± 2
IRAK1^{162-180, W168F}	16,000 ± 2000	3.0 ± 0.4 x 10⁷	720 ± 12	550 ± 9
IRAK1^{162-180-pS163}	3,200 ± 100	4.4 ± 0.2 x 10⁷	127 ± 5	72 ± 3
IRAK1^{162-180-pS166}	2,100 ± 200	6.2 ± 0.6 x 10⁷	60 ± 3	34 ± 1
IRAK1^{162-180-pS173}	1,500 ± 200	4.4 ± 0.5 x 10⁷	60 ± 2	34 ± 1
IRAK1^{162-180-pS166, pS173}	900 ± 60	6.3 ± 0.4 x 10⁷	25 ± 2	14 ± 1

‡ previously reported in Chapter 2

We note that although phosphorylation of S166 and S173 significantly improves binding, chemical shifts are only marginally perturbed (at greatest, $\Delta\Delta\delta < 0.12$ ppm). This may indicate enhancement of binding by phosphorylation is driven by longer-range electrostatic forces rather than specific close contacts between the phosphate groups and EVH1 side-chains. Lending some support to this interpretation is the electrostatic surface potential map (Figure 3.3B), calculated using the Adaptive Poisson-Boltzmann Solver program in Pymol (Baker et al., 2001). This calculation shows firstly that the peptide-binding groove actually possesses a positive surface potential. Secondly, there is an extensive positive patch poised to interact with residues C-terminal to the primary motif, potentially well beyond the five positions we have considered here. Also supporting this interpretation is the fact that, although there is a clear bias for negatively charged amino acids in the ~4 positions preceding

and ~5 following the primary VASP-EVH1 binding motif in its binding partners, there does not seem to be a strong bias for any individual position over the others.

We generated a sequence logo from an alignment of the VASP-EVH1 binding sites in ActA, Lamellipodin, Fyb/SLAP, Zyxin, Vinculin, LPP, palladin and IRAK1 (Figure 3.4) using WebLogo 3.3 (<http://weblogo.berkeley.edu/>) (Crooks et al., 2004). This identified positions 13, 11, 4, and 12 (numbering as in Figure 3.4) as the sites with the highest frequency of aspartate or glutamate residues, 59%, 41%, 35%, and 29% respectively. Interestingly, these are the positions of the negatively charged residues in the ActA binding sites, which are the tightest known natural binding sequences of VASP-EVH1 (Ball et al., 2000).

Lastly, this sequence logo spotlights the enrichment of serine residues within VASP-EVH1 binding sites at positions 1, 2, 7, and 10. This may suggest that phosphorylation at VASP binding sites may serve as a mechanism to regulate actin polymerization. Of particular note are the first, third, and fourth motifs of lamellipodin and the first motif of palladin, which are known to be phosphorylated (<http://www.phosphosite.org/>) (Asano et al., 2011; Carlson et al., 2011; Hornbeck et al., 2004; Olsen et al., 2010).

Examining the specificity of VASP-EVH1 for tryptophan vs. phenylalanine motifs

IRAK1 represents the only so-far established WPxφP-containing binding partner of Ena/VASP family EVH1 domains, as opposed to the FPxφP motifs found in vinculin, zyxin, lamellipodin, and ActA. However, multiple studies have reported that substitution of tryptophan in place of phenylalanine in the ActA-derived motif ³³²SFEFPPPPTEDEL₃₄₄ enhances binding significantly (Ball et al., 2000; Niebuhr et al., 1997; Zimmermann et al., 2003). To investigate with atomic resolution the differences between WPxφP and FPxφP recognition by VASP-EVH1, we repeated the above NMR analysis with a peptide with Trp168 mutated to Phe (IRAK1¹⁶²⁻¹⁸⁰, W168F)

to compare with the previously reported experiment using the wt sequence (Chapter 2). Titrating ^{15}N -EVH1 with IRAK1^{162-180, W168F} yielded peak trajectories very similar to the IRAK1¹⁶²⁻¹⁸⁰ titration, with a few exceptions. The binding curves generated from the titration yielded a weaker affinity than for the wild-type sequence ($K_D = 0.72 \pm 0.012$ mM, vs. 0.203 ± 0.003 mM for wt, Figure 3.1B). The extent of line broadening was greatly reduced, indicating faster binding kinetics (Figure 3.2, top center). Indeed, fitting lineshapes as above yielded $k_{off} = 16,000 \pm 2,000 \text{ s}^{-1}$, corresponding to $k_{on} = 3.0 \pm 0.4 \cdot 10^7 \text{ M}^{-1}\text{s}^{-1}$.

The strong ring currents of the tryptophan side chain can have large effects on the chemical shift of nearby nuclei. As expected, then, substituting phenylalanine for tryptophan in the sequence of IRAK1^{162-180, W168F} led to significant differences in the bound chemical shifts of ^{15}N EVH1. The peaks arising from the side chains of Trp23, Asn73 ($^1\text{H}^{\delta 21}$ and $^1\text{H}^{\delta 22}$), Gln81 ($^1\text{H}^{\epsilon 21}$), Trp82, and the backbone amides of residues Tyr72 and Trp89 all showed $\Delta\Delta\delta > 0.15$ ppm (Appendix Figure 3.2). Most notably, the side chain of Asn73 ($^1\text{H}^{\delta 22}$) showed $\Delta\Delta\delta = 0.62$ ppm. We examined the possibility that this large $\Delta\Delta\delta$ reflected a hydrogen bond with the Trp168 sidechain amide, which could explain the nearly 5-fold increase in affinity (by K_D^{trans} , corresponding to a difference in the free energy of binding of 3.85 kJ/mol) for IRAK1¹⁶²⁻¹⁸⁰ over IRAK1^{162-180, W168F}. To test this theory, we measured the temperature dependence of the chemical shift of the Trp168 indole amide peak in the presence and absence of excess EVH1 domain. The temperature dependence of backbone amide proton chemical shifts, $\Delta\delta/\Delta T$, is a well-established indicator of hydrogen bonding (Cierpicki and Otlewski, 2001), leading us to presume that tryptophan indole amides follow a similar trend. Generally, backbone amides with a temperature gradient more positive than -4.6 ppb/K have an 85% or greater likelihood of being in a hydrogen bond. However, sidechains amides have a moderately more positive temperature gradient

than backbone amides in the absence of any hydrogen bonds. We found that the indole peak of Trp168 in both bound and free IRAK1¹⁶²⁻¹⁸⁰ had almost identical temperature dependence, (-4.1 and -4.0 ppb/K, Appendix Figure 3.3) very close to that reported for a short unstructured (not hydrogen bonded) peptide (-4.03 ppb/K) (Merutka et al., 1995). This led us to conclude that the Trp168 side chain does not form a hydrogen bond in the complex between EVH1 and IRAK1¹⁶²⁻¹⁸⁰.

Cyclophilin A catalysis of W₁₆₈-P₁₆₉ isomerization is not prevented by phosphorylation

We have previously observed that the W₁₆₈-P₁₆₉ peptide bond in IRAK1 is in equilibrium between cis (43%) and trans (57%) isomers, and that binding to VASP-EVH1 is specific for the trans isomer (Chapter 2). We had shown that the prolyl isomerase enzyme cyclophilin A (CypA) catalyzes isomerization of this bond and thus facilitates binding to VASP. However, phosphorylation of the residue directly preceding proline is known to hamper CypA activity (Yaffe et al., 1997). To test whether phosphorylation of the flanking Ser residues S166 and S173 prevents CypA catalysis of isomerization of the W₁₆₈-P₁₆₉ peptide bond in IRAK1, we measured the isomerization rate of 3.64 mM IRAK1^{162-180, pS166, pS173} in the presence of 10 μ M CypA using the ¹H-¹H ROESY experiment (Figure 3.5) as previously described (De et al., 2012; Greenwood et al., 2011). This experiment produced cross peaks which were fit to yield an isomerization rate of 3.7 s⁻¹, confirming that CypA can isomerize this motif. This is not surprising given that S166 is two residues from P169 rather than preceding it, which would likely prevent catalysis.

Identification of a highly conserved secondary binding site on VASP-EVH1

Interpretation of the ¹⁵N EVH1 phosphopeptide titration data was complicated by the divergence of a subset of peaks from the predominant binding behavior. Some peaks, most prominently corresponding to the backbones amides of S2, R48, A85, and the side-chains of Q37, Q58, and N63 remained relatively stationary at low

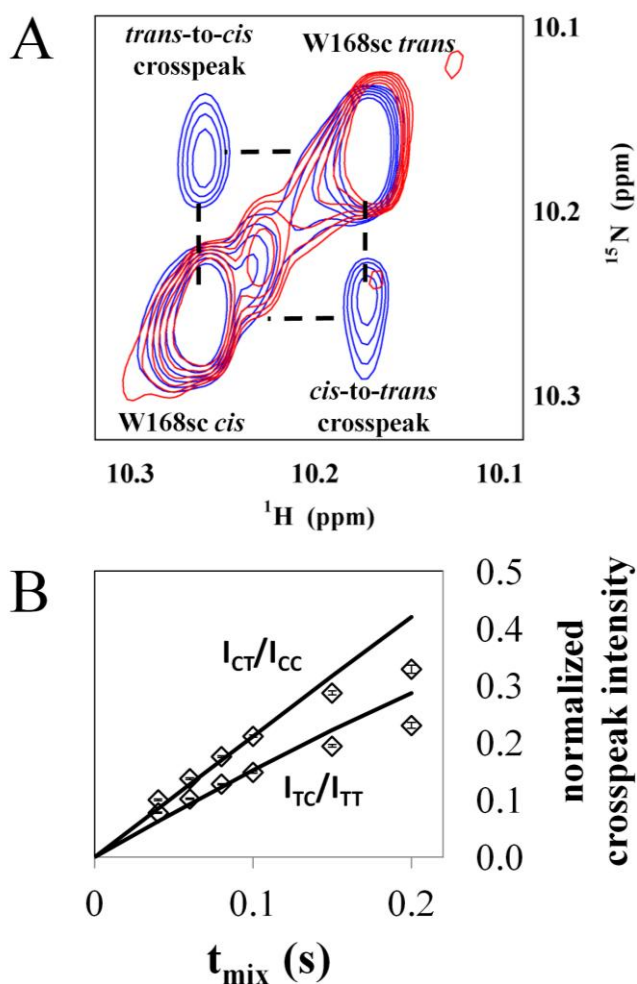


Figure 3.5: Phosphorylated IRAK1 can be isomerized by cyclophilin A. (A) The ^1H - ^1H ROESY spectrum of IRAK1^{162-180, pS166, pS173} (mixing time of 100 ms) shows that the *cis* and *trans* isomers of W168-P169 interconvert in the presence (blue) but not in the absence (red) of 10 μM cyclophilin A. (B) Normalized crosspeak intensities as a function of mixing time are fit to obtain the isomerization rate.

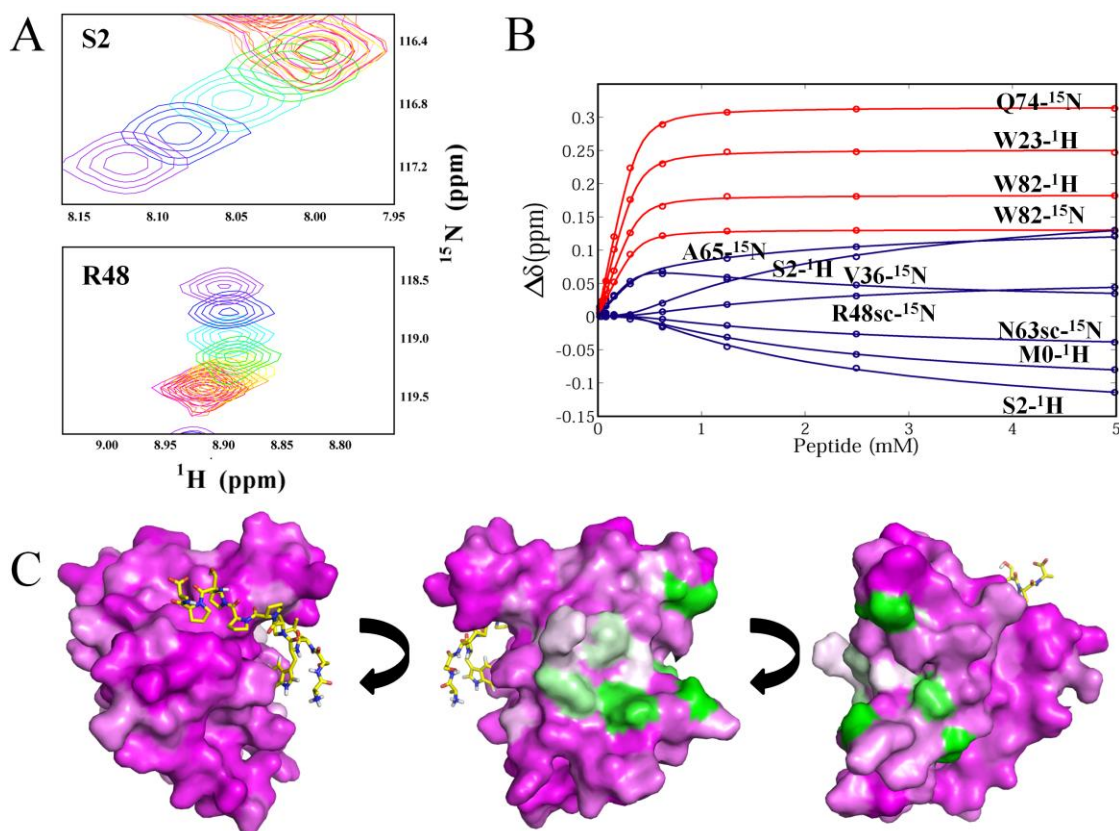


Figure 3.6: Evidence for a weak secondary binding site on VASP-EVH1. (A) Examples of peaks that sense a secondary binding event in the ^{15}N EVH1/IRAK1^{162-180, pS166, pS173} titration. This is distinguished by either peaks displaying three-state behavior (such as R48) or by peaks remaining stationary at substoichiometric peptide concentrations and moving once the primary binding site is nearly saturated (such as S2). (B) Representative binding curves from the ^{15}N EVH1/IRAK1^{162-180, pS166, pS173} titration, fit to a three-state model. Shown in red are proton or nitrogen (scaled by the scaling factor 0.154) chemical shifts of residues in the primary binding site, and shown in blue are chemical shifts of residues sensitive to the secondary binding event or both. Symbols represent titration data and lines represent a global fit. (C) The secondary binding site mapped to the solution structure of VASP-EVH1 (Ball et al., 2000). The coloration of the surface view reflects the chemical shift differences between the last two titration points of the ^{15}N EVH1/IRAK1^{162-180, pS166, pS173} titration in which only the occupancy of the secondary binding site significantly changes (magenta=no change, green=highest change). The yellow stick representation shows the position of the IRAK1 peptide in the primary site.

concentrations of peptide and began to move at the highest concentrations of peptide, suggesting a secondary, weak binding interaction with the peptide (Figure 3.6A). This necessitated careful selection of peaks that did not display this behavior for our main analysis. Remarkably, the extent of this secondary behavior seemed to correspond well with the affinity of the peptide for the primary binding site (Figure 3.7), as the tighter-binding peptides induced larger chemical shift changes for these residues at any given concentration and the tightest-binding peptide yielded saturation binding curves. The side-chains of Q37 and Q58 showed very small chemical shift changes for the titrations with unphosphorylated peptides, suggesting that these residues may interact with the phosphate groups.

The titration that induced the largest chemical shift perturbations of these residues, with the peptide IRAK1^{162-180, pS166, pS173}, produced binding curves that were deemed tight enough to fit to obtain the dissociation constant for the secondary binding site. This was performed by globally fitting 22 binding curves from peaks displaying three-state behavior simultaneously with eight binding curves from residues within the primary binding site (Figure 3.6B). This yielded a K_D of 2.15 mM for the secondary site and a K_D of 20 μ M for the primary site, in close agreement with the earlier fit that simply ignored the secondary site. Because of the vastly different binding affinities for the primary and secondary sites, it is easy to separately determine the chemical shift perturbation profiles of the tight and weak binding sites by analyzing chemical shift differences between spectra and low concentrations and high concentrations of peptide, respectively. Mapping the difference in chemical shift perturbations between the two final IRAK1^{162-180, pS166, pS173} titration points (highest concentration peptide) to the structural model described above shows a unique binding surface on the face opposite to the primary binding site of the VASP-EVH1 domain, supporting the existence of a distinct, weak binding site (Figure 3.6C). This binding

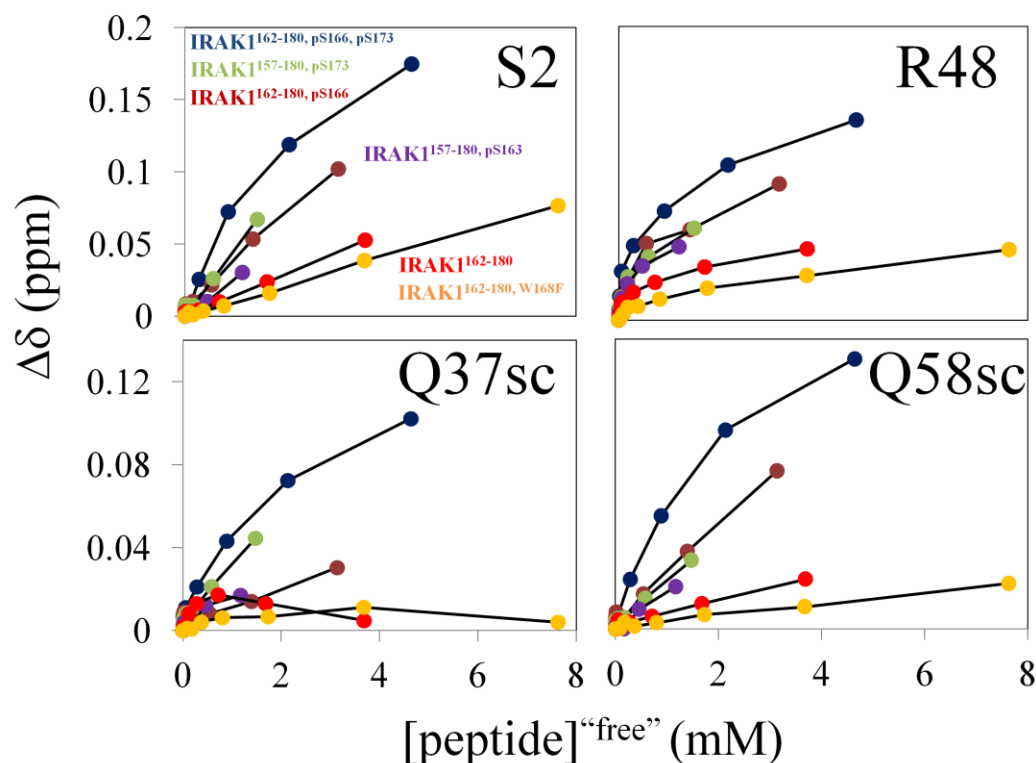


Figure 3.7: Secondary EVH1 binding site selects phosphorylated IRAK1 peptides. Binding curves of residues in the secondary binding site as a function of “free” peptide concentration (defined as the concentration of peptide not bound to the primary binding site, obtained from fits) for the peptides IRAK1^{162-180, W168F}, IRAK1¹⁶²⁻¹⁸⁰, IRAK1^{157-180, pS163}, IRAK1^{162-180, pS166}, IRAK1^{157-180, pS173}, and IRAK1^{162-180, pS166, pS173}. Data are solid symbols with lines to guide the eye. The side-chains of Q37 and Q58 show very small chemical shift changes for the non-phosphorylated peptides, suggesting that they may interact with the phosphate groups.

surface comprises strands 1, 2, 3, and 4, which form a concave surface similar to the canonical binding site on the opposite face. The large chemical shift changes for the sidechains peaks of R48, Q37, N63 and Q58 as well as the backbone peak of S2 may indicate hydrogen bonding between the peptide and these side chains. Notably, R48 and N63 are well-conserved residues that are involved in binding of Ran to the homologous Ran-binding domain of RanBP2, as described in the discussion.

Discussion

Ena/VASP proteins are actin-binding proteins that serve to remodel the actin cytoskeleton, specifically in the processes of axon guidance (Goh et al., 2002), phagocytosis (Coppolino et al., 2001), cell migration (Bear et al., 2000; Krause et al., 2003), and cell-cell interactions (Grevengoed et al., 2001; Vasioukhin et al., 2000). They function by increasing the length of actin filaments, either by an anti-capping mechanism (Bear and Gertler, 2009) or by their processive filament elongation activity (Breitsprecher et al., 2011; Hansen and Mullins, 2010). VASP tends to be localized to focal adhesions (Gertler et al., 1996), adherens junctions (Reinhard et al., 1996; Vasioukhin et al., 2000), filapodial tips (Rottner et al., 1999), and the leading edge of lamellipodia (Rottner et al., 1999). This localization of VASP is mediated by its N-terminal EVH1 domain, a small domain with a PH fold that recognizes the proline-rich motif (F/W)Px ϕ P (Ball et al., 2000; Niebuhr et al., 1997; Pistor et al., 1995). This motif, most commonly occurring simply as the sequence FPPPP, is present in the focal adhesion proteins zyxin and vinculin as well as the lamellipodial protein lamellipodin. Most of the VASP binding sites in the proteins ActA, Zyxin, Vinculin, Fyb/SLAP and Lamellipodin contain two or more acidic residues flanking the core binding motif (Figure 3.4). Generally, 1-2 acidic amino acids are present in the three positions preceding the core motif, and 1-3 are present in the four positions

following the motif. Point mutants of the acidic residues in the ActA sequence have reduced binding affinity for VASP, and the positively charged EVH1 residues K21 and R22 are implicated in recognition of the C-terminal amino acids (Carl et al., 1999). We have shown here for the first time that phosphorylation of serine residues within these positions can have a similar contribution (~3 kJ/mol for each phosphoserine) to VASP binding. The impact of phosphorylation on VASP binding is a novel finding suggesting a new mechanism of regulation of VASP interactions by phosphorylation of its binding partners. There may be other examples of this in nature, as some other VASP binding sites also contain phosphorylatable residues in these positions (Figure 3.4). In particular, lamellipodin, a protein required for formation of lamellipodia, contains a C-terminal threonine and a C-terminal serine in its first and third FPPPP motifs. It is known that these residues can be phosphorylated during mitosis or through the ERK2 signaling pathway (<http://www.phosphosite.org/>) (Carlson et al., 2011; Hornbeck et al., 2004; Olsen et al., 2010).

IRAK1 autophosphorylates multiple serine residues in its UD upon receptor stimulation, and *in vitro* kinase assays have suggested that this autophosphorylation is very extensive, resulting in phosphorylation of nearly all of the serines in the UD (Kollewe et al., 2004). Specifically Ser173 is thought to be phosphorylated in response to TLR7 stimulation (Tun-Kyi et al., 2011). We propose that phosphorylation of the IRAK1-UD in response to TLR or IL-1R stimulation may contribute to recruitment of VASP to the site of stimulation at the plasma membrane. Thus, the effect of phosphorylation on VASP-IRAK1 binding provides evidence of a potential novel regulatory mechanism for VASP function in cell signaling.

Although the consensus binding motif for Mena/VASP/Evl EVH1 domains is frequently given by FPxφP rather than (W/F)PxφP, in agreement with other studies (Ball et al., 2000; Niebuhr et al., 1997; Zimmermann et al., 2003) we have shown here

that substitution of the larger aromatic tryptophan for the aromatic phenylalanine actually increases the affinity of the interaction. Our chemical shift temperature coefficient analysis is not consistent with a hydrogen bond between the EVH1 Asn73 side chain carbonyl and the indole amide proton of Trp168 in IRAK1. More likely, tryptophan may pack more favorably than phenylalanine in the hydrophobic binding pocket, and/or the torsion angle strain in the conformation that allows the side chain to insert into the pocket may be lower for tryptophan than phenylalanine. Importantly, the preference for tryptophan may indicate that additional VASP binding partners remain to be identified, since FPx ϕ P is widely used as the consensus sequence.

We have shown that the VASP-EVH1 domain contains a secondary binding surface on the face opposite its primary binding site which weakly binds the phosphorylated peptide IRAK1^{162-180, pS166, pS173} with a dissociation constant of ~2.15 mM. The large chemical shift perturbations of the R48 and N63 sidechain peaks provide insight into the evolutionary origins of this binding surface. The EVH1 domain of VASP shares structural and sequence homology with the Ran-binding domains of Ran-binding proteins 1 and 2 (Callebaut et al., 1998; Vetter et al., 1999), small proteins that bind to the Ran GTPase and inhibit guanine nucleotide exchange. Crystal structures show that RanBD binds the C-terminal helix of Ran in a peptide-binding groove (Vetter et al., 1999) formed by beta strands 1, 2, 5, 6, and 7, which is analogous to the primary binding site of the EVH1 domains of Ena/VASP proteins that bind proline rich sequences (Prehoda et al., 1999), as well as Homer (Beneken et al., 2000) and WASP (Gan and Li, 2010; Volkman et al., 2002) EVH1 domains (Figure 3.8). However, Ran also wraps almost all the way around the RanBD to make significant contacts with the opposite face of the domain. Notably, the backbone carbonyls of Ran residues A181 and L182 hydrogen bond to R77 in the first RanBD

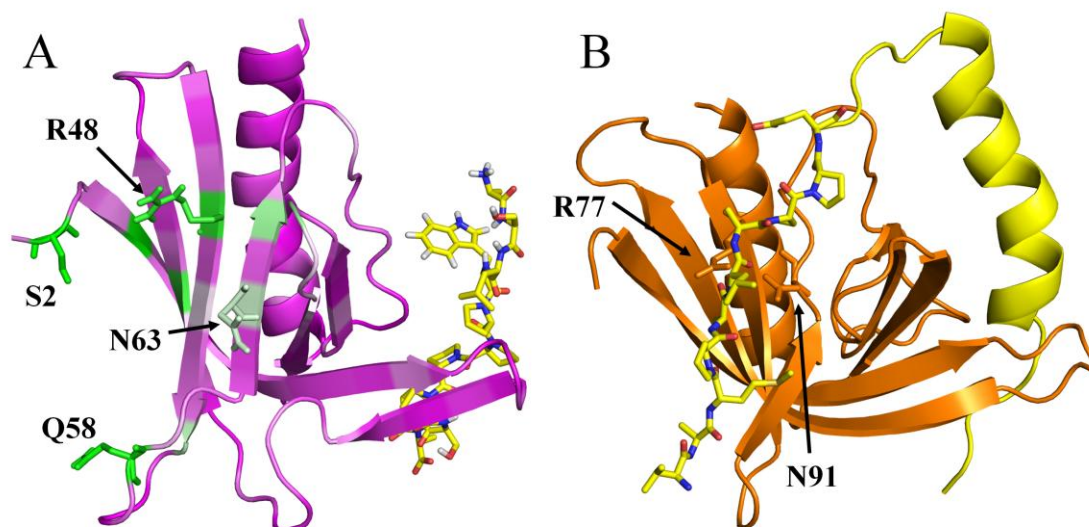


Figure 3.8: Comparison between the binding surfaces of the Ran-binding domain and the VASP-EVH1 domain. (A) Cartoon representation of the VASP-EVH1 solution structure (Ball et al., 2000) with the secondary binding site chemical shift changes mapped to it (magenta=no change, green=highest change). Residues that show the largest chemical shift changes are shown as sticks. The primary binding site is identified by the stick representation of the bound IRAK1 peptide. (B) Cartoon representation of the core of the structure of the first Ran-binding domain of RanBP2 (orange), bound to residues 177-211 of Ran (yellow) (PDB ID 1RRP) (Vetter et al., 1999). The helix-binding site is analogous to the primary binding site on VASP-EVH1, while the extended Ran sequence is bound on the opposite face, analogous to the secondary binding site on VASP-EVH1. RanBP2 residues R77 and N91, homologous to R48 and N63 in VASP, are shown as sticks.

of RanBP2, which corresponds to R48 in VASP-EVH1 and is one of the most conserved residues (Callebaut et al., 1998) throughout the families of WASP and Homer EVH1 domains as well as Ran-binding domains. Likewise, the similarly well-conserved N91 of RanBP2, which corresponds to N63 in VASP, hydrogen bonds to the backbone carbonyl of Ran residue L182. Given this strict conservation, it may be possible the functional significance of this binding surface is also conserved.

Remarkably, the extent of peptide binding for this surface appears to correlate with the affinity for the primary site, suggesting that the sequence specificity of the secondary binding site has some similarities to the primary site. Specifically, it appears to be sensitive to the identity of the residue in position 5, selecting tryptophan over phenylalanine, and appears to recognize the negative charges of phosphate groups on either side of the (F/W)-PPPP motif. It also seems likely that the polyproline II helix adopted by this proline-rich sequence is an important feature of recognition, given that the Ran sequence P180-E186 also adopts this structure (Vetter et al., 1999). Given this information, it seems feasible that this binding surface may bind a similar motif as the canonical binding site.

Although it is uncertain whether the weak binding surface described here has biological significance, the similarity between the sequence specificities of this and the canonical site offers an intriguing hypothesis. Many VASP-binding proteins such as lamellipodin and zyxin contain multiple tandem repeats of VASP-binding sites. Given these results it seems very plausible that such tandem repeats could be bound by both faces of the EVH1 domain rather than each motif being bound by a separate VASP molecule. Possibly depending on clustering of VASP or the binding partner VASP could alternate between binding stoichiometries. Further experiments in our lab are in progress to test this hypothesis. Interestingly, it has recently been shown that Abl kinase can phosphorylate VASP residue Y39, which resides within this binding

surface, and that this phosphorylation disrupts the interaction between VASP and zyxin (Maruoka et al., 2012).

In summary, we have described two previously unreported features of the VASP-EVH1 domain's interactions with its target proteins: a preference for phosphorylated sequences, and a secondary peptide binding site. The phosphorylation dependence of the VASP/IRAK1 interaction described here suggests a novel mechanism by which VASP function can be regulated. In response to TLR or IL-1R stimulation, IRAK1 may autophosphorylate at the Ser166 and Ser173 residues flanking the VASP binding site, recruiting VASP to the periphery of the cell, which has been proposed to contribute to cell migration (Gan and Li, 2010). Future work, however, is needed to test whether TLR/IL-1R signaling and phosphorylation control the VASP/IRAK1 interaction in the context of the cell. The described secondary binding site on the domain face opposite the primary site may bind a variation on the canonical (F/W)-PPPP motif, and may interact with the tandem repeats of zyxin and lamellipodin. Future work is also needed to investigate this hypothesis.

REFERENCES

- Asano, E., Maeda, M., Hasegawa, H., Ito, S., Hyodo, T., Yuan, H., Takahashi, M., Hamaguchi, M., and Senga, T. (2011). Role of palladin phosphorylation by extracellular signal-regulated kinase in cell migration. *PLoS One* 6, e29338.
- Baker, N.A., Sept, D., Joseph, S., Holst, M.J., and McCammon, J.A. (2001). Electrostatics of nanosystems: application to microtubules and the ribosome. *Proc Natl Acad Sci U S A* 98, 10037-10041.
- Ball, L.J., Kuhne, R., Hoffmann, B., Hafner, A., Schmieder, P., Volkmer-Engert, R., Hof, M., Wahl, M., Schneider-Mergener, J., Walter, U., *et al.* (2000). Dual epitope recognition by the VASP EVH1 domain modulates polyproline ligand specificity and binding affinity. *EMBO J* 19, 4903-4914.
- Bear, J.E., and Gertler, F.B. (2009). Ena/VASP: towards resolving a pointed controversy at the barbed end. *J Cell Sci* 122, 1947-1953.
- Bear, J.E., Loureiro, J.J., Libova, I., Fassler, R., Wehland, J., and Gertler, F.B. (2000). Negative regulation of fibroblast motility by Ena/VASP proteins. *Cell* 101, 717-728.
- Beneken, J., Tu, J.C., Xiao, B., Nuriya, M., Yuan, J.P., Worley, P.F., and Leahy, D.J. (2000). Structure of the Homer EVH1 domain-peptide complex reveals a new twist in polyproline recognition. *Neuron* 26, 143-154.
- Boeda, B., Briggs, D.C., Higgins, T., Garvalov, B.K., Fadden, A.J., McDonald, N.Q., and Way, M. (2007). Tes, a specific Mena interacting partner, breaks the rules for EVH1 binding. *Mol Cell* 28, 1071-1082.
- Breitsprecher, D., Kiesewetter, A.K., Linkner, J., Vinzenz, M., Stradal, T.E., Small, J.V., Curth, U., Dickinson, R.B., and Faix, J. (2011). Molecular mechanism of Ena/VASP-mediated actin-filament elongation. *EMBO J* 30, 456-467.
- Callebaut, I., Cossart, P., and Dehoux, P. (1998). EVH1/WH1 domains of VASP and WASP proteins belong to a large family including Ran-binding domains of the RanBP1 family. *FEBS Lett* 441, 181-185.
- Cao, Z., Henzel, W.J., and Gao, X. (1996). IRAK: a kinase associated with the interleukin-1 receptor. *Science* 271, 1128-1131.
- Carl, U.D., Pollmann, M., Orr, E., Gertler, F.B., Chakraborty, T., and Wehland, J. (1999). Aromatic and basic residues within the EVH1 domain of VASP specify its interaction with proline-rich ligands. *Curr Biol* 9, 715-718.
- Carlson, S.M., Chouinard, C.R., Labadorf, A., Lam, C.J., Schmelzle, K., Fraenkel, E., and White, F.M. (2011). Large-scale discovery of ERK2 substrates identifies ERK-mediated transcriptional regulation by ETV3. *Sci Signal* 4, rs11.
- Cavanagh J, F.W., Palmer AG, Rance M, Skelton NJ (2007). Protein NMR spectroscopy: principles and practice, 2nd edn (London: Academic Press).
- Cierpicki, T., and Otlewski, J. (2001). Amide proton temperature coefficients as hydrogen bond indicators in proteins. *J Biomol NMR* 21, 249-261.
- Coppolino, M.G., Krause, M., Hagendorff, P., Monner, D.A., Trimble, W., Grinstein, S., Wehland, J., and Sechi, A.S. (2001). Evidence for a molecular complex consisting of Fyb/SLAP, SLP-76, Nck, VASP and WASP that links the actin cytoskeleton to Fcγ receptor signalling during phagocytosis. *J Cell Sci* 114, 4307-4318.
- Crooks, G.E., Hon, G., Chandonia, J.M., and Brenner, S.E. (2004). WebLogo: a sequence logo generator. *Genome Res* 14, 1188-1190.

De, S., Greenwood, A.I., Rogals, M.J., Kovrigin, E.L., Lu, K.P., and Nicholson, L.K. (2012). Complete thermodynamic and kinetic characterization of the isomer-specific interaction between Pin1-WW domain and the amyloid precursor protein cytoplasmic tail phosphorylated at Thr668. *Biochemistry* 51, 8583-8596.

Delaglio, F., Grzesiek, S., Vuister, G.W., Zhu, G., Pfeifer, J., and Bax, A. (1995). NMRPipe: a multidimensional spectral processing system based on UNIX pipes. *J Biomol NMR* 6, 277-293.

Delano, W.L. (2002). The PyMOL Molecular Graphics System, Version 1.3. (Schrödinger, LLC).

Gan, L., and Li, L. (2010). Interleukin-1 Receptor-Associated Kinase-1 (IRAK-1) functionally associates with PKCepsilon and VASP in the regulation of macrophage migration. *Mol Immunol* 47, 1278-1282.

Gertler, F.B., Niebuhr, K., Reinhard, M., Wehland, J., and Soriano, P. (1996). Mena, a relative of VASP and Drosophila Enabled, is implicated in the control of microfilament dynamics. *Cell* 87, 227-239.

Goddard TD, K.D. (2008). Sparky 3. (University of California, San Francisco).

Goh, K.L., Cai, L., Cepko, C.L., and Gertler, F.B. (2002). Ena/VASP proteins regulate cortical neuronal positioning. *Curr Biol* 12, 565-569.

Greenwood, A.I., Rogals, M.J., De, S., Lu, K.P., Kovrigin, E.L., and Nicholson, L.K. (2011). Complete determination of the Pin1 catalytic cycle by NMR lineshape analysis. *J. Biomol. NMR* *in press*.

Grevengoed, E.E., Loureiro, J.J., Jesse, T.L., and Peifer, M. (2001). Abelson kinase regulates epithelial morphogenesis in Drosophila. *J Cell Biol* 155, 1185-1198.

Guex, N., and Peitsch, M.C. (1997). SWISS-MODEL and the Swiss-PdbViewer: an environment for comparative protein modeling. *Electrophoresis* 18, 2714-2723.

Haffner, C., Jarchau, T., Reinhard, M., Hoppe, J., Lohmann, S.M., and Walter, U. (1995). Molecular cloning, structural analysis and functional expression of the proline-rich focal adhesion and microfilament-associated protein VASP. *EMBO J* 14, 19-27.

Hansen, S.D., and Mullins, R.D. (2010). VASP is a processive actin polymerase that requires monomeric actin for barbed end association. *J Cell Biol* 191, 571-584.

Hornbeck, P.V., Chabra, I., Kornhauser, J.M., Skrzypek, E., and Zhang, B. (2004). PhosphoSite: A bioinformatics resource dedicated to physiological protein phosphorylation. *Proteomics* 4, 1551-1561.

Kollewe, C., Mackensen, A.C., Neumann, D., Knop, J., Cao, P., Li, S., Wesche, H., and Martin, M.U. (2004). Sequential autophosphorylation steps in the interleukin-1 receptor-associated kinase-1 regulate its availability as an adapter in interleukin-1 signaling. *J Biol Chem* 279, 5227-5236.

Kovrigin, E.L. (2012). NMR line shapes and multi-state binding equilibria. *J Biomol NMR* 53, 257-270.

Krause, M., Dent, E.W., Bear, J.E., Loureiro, J.J., and Gertler, F.B. (2003). Ena/VASP proteins: regulators of the actin cytoskeleton and cell migration. *Annu Rev Cell Dev Biol* 19, 541-564.

Li, S., Strelow, A., Fontana, E.J., and Wesche, H. (2002). IRAK-4: a novel member of the IRAK family with the properties of an IRAK-kinase. *Proc Natl Acad Sci U S A* 99, 5567-5572.

Lin, C.C., Huoh, Y.S., Schmitz, K.R., Jensen, L.E., and Ferguson, K.M. (2008). Pellino proteins contain a cryptic FHA domain that mediates interaction with

phosphorylated IRAK1. *Structure* 16, 1806-1816.

Lin, S.C., Lo, Y.C., and Wu, H. (2010). Helical assembly in the MyD88-IRAK4-IRAK2 complex in TLR/IL-1R signalling. *Nature* 465, 885-890.

Maruoka, M., Sato, M., Yuan, Y., Ichiba, M., Fujii, R., Ogawa, T., Ishida-Kitagawa, N., Takeya, T., and Watanabe, N. (2012). Abl-1-bridged tyrosine phosphorylation of VASP by Abelson kinase impairs association of VASP to focal adhesions and regulates leukaemic cell adhesion. *Biochem J* 441, 889-899.

McConnell, H.M. (1958). Reaction rates by nuclear magnetic resonance. *J. Chem. Phys.* 28, 430-431.

Merutka, G., Dyson, H.J., and Wright, P.E. (1995). 'Random coil' ¹H chemical shifts obtained as a function of temperature and trifluoroethanol concentration for the peptide series GGXGG. *J Biomol NMR* 5, 14-24.

Niebuhr, K., Ebel, F., Frank, R., Reinhard, M., Domann, E., Carl, U.D., Walter, U., Gertler, F.B., Wehland, J., and Chakraborty, T. (1997). A novel proline-rich motif present in ActA of *Listeria monocytogenes* and cytoskeletal proteins is the ligand for the EVH1 domain, a protein module present in the Ena/VASP family. *EMBO J* 16, 5433-5444.

O'Neill, L.A. (2008). The interleukin-1 receptor/Toll-like receptor superfamily: 10 years of progress. *Immunol Rev* 226, 10-18.

Olsen, J.V., Vermeulen, M., Santamaria, A., Kumar, C., Miller, M.L., Jensen, L.J., Gnad, F., Cox, J., Jensen, T.S., Nigg, E.A., *et al.* (2010). Quantitative phosphoproteomics reveals widespread full phosphorylation site occupancy during mitosis. *Sci Signal* 3, ra3.

Piotukh, K., Gu, W., Kofler, M., Labudde, D., Helms, V., and Freund, C. (2005). Cyclophilin A binds to linear peptide motifs containing a consensus that is present in many human proteins. *J Biol Chem* 280, 23668-23674.

Pistor, S., Chakraborty, T., Walter, U., and Wehland, J. (1995). The bacterial actin nucleator protein ActA of *Listeria monocytogenes* contains multiple binding sites for host microfilament proteins. *Curr Biol* 5, 517-525.

Prehoda, K.E., Lee, D.J., and Lim, W.A. (1999). Structure of the enabled/VASP homology 1 domain-peptide complex: a key component in the spatial control of actin assembly. *Cell* 97, 471-480.

Reinhard, M., Rudiger, M., Jockusch, B.M., and Walter, U. (1996). VASP interaction with vinculin: a recurring theme of interactions with proline-rich motifs. *FEBS Lett* 399, 103-107.

Rottner, K., Behrendt, B., Small, J.V., and Wehland, J. (1999). VASP dynamics during lamellipodia protrusion. *Nat Cell Biol* 1, 321-322.

Tun-Kyi, A., Finn, G., Greenwood, A., Nowak, M., Lee, T.H., Asara, J.M., Tsokos, G.C., Fitzgerald, K., Israel, E., Li, X., *et al.* (2011). Essential role for the prolyl isomerase Pin1 in Toll-like receptor signaling and type I interferon-mediated immunity. *Nat Immunol* 12, 733-741.

Vasioukhin, V., Bauer, C., Yin, M., and Fuchs, E. (2000). Directed actin polymerization is the driving force for epithelial cell-cell adhesion. *Cell* 100, 209-219.

Vetter, I.R., Nowak, C., Nishimoto, T., Kuhlmann, J., and Wittinghofer, A. (1999). Structure of a Ran-binding domain complexed with Ran bound to a GTP analogue: implications for nuclear transport. *Nature* 398, 39-46.

Volkman, B.F., Prehoda, K.E., Scott, J.A., Peterson, F.C., and Lim, W.A. (2002).

Structure of the N-WASP EVH1 domain-WIP complex: insight into the molecular basis of Wiskott-Aldrich Syndrome. *Cell* 111, 565-576.

Wishart, D.S., Bigam, C.G., Yao, J., Abildgaard, F., Dyson, H.J., Oldfield, E., Markley, J.L., and Sykes, B.D. (1995). ¹H, ¹³C and ¹⁵N chemical shift referencing in biomolecular NMR. *J Biomol NMR* 6, 135-140.

Yaffe, M.B., Schutkowski, M., Shen, M., Zhou, X.Z., Stukenberg, P.T., Rahfeld, J.U., Xu, J., Kuang, J., Kirschner, M.W., Fischer, G., *et al.* (1997). Sequence-specific and phosphorylation-dependent proline isomerization: a potential mitotic regulatory mechanism. *Science* 278, 1957-1960.

Zimmermann, J., Kuhne, R., Volkmer-Engert, R., Jarchau, T., Walter, U., Oschkinat, H., and Ball, L.J. (2003). Design of N-substituted peptomer ligands for EVH1 domains. *J Biol Chem* 278, 36810-36818.

CHAPTER 4

A Noncanonical Binding Site in the EVH1 Domain of VASP is Employed in the Interaction with Zyxin

Abstract

VASP is a processive actin polymerase with roles in the control of cell shape and cell migration. Through its interaction with the cytoskeletal adaptor protein zyxin, VASP can localize to damaged stress fibers which it serves to repair and reinforce with the aid of the actin-binding protein α -actinin. VASP localization is mediated by its N-terminal Ena/VASP Homology domain (EVH1), which binds to the motif (W/F)Px ϕ P (most commonly occurring as FPPPP) found in cytoskeletal proteins such as vinculin, lamellipodin, and zyxin. These FPPPP motifs very frequently occur in tandem repeats of four or five, and zyxin contains four such sites. This may allow the tetrameric VASP to bind very tightly through avidity. Motivated by the observation of an additional non-canonical and distinct binding surface on VASP-EVH1, we asked whether tandem repeat sequences can also bind this second site. The sequence containing the EVH1-binding sites of zyxin's proline-rich domain, zyxin⁴¹⁻¹⁴⁰ was purified as an ¹⁵N-labeled 100-residue protein and assignments of most non-proline residues were obtained exclusively by ¹⁵N-separated TOCSY and NOESY experiments and site-directed mutagenesis. Additionally, the *cis* and *trans* isomers of many F-P sites were also identified using ¹⁵N-ZZ exchange spectroscopy in the presence of the prolyl isomerase cyclophilin A. Dissection of the complex binding scheme between zyxin⁴¹⁻¹⁴⁰ and VASP-EVH1 was accomplished by performing multiple binding titrations with different Phe-to-Ala zyxin⁴¹⁻¹⁴⁰ mutants. Small peaks and shoulders representing the *cis* isomer of F93-P94 enabled us to make inferences about the binding orientation. We show here that when the VASP EVH1 domain binds

the second (tightest binding) zyxin motif, it makes significant contacts with the third and fourth motifs utilizing a noncanonical binding site on the face opposite the primary binding site, reminiscent of the homologous Ran-binding domain's interaction with Ran. We further show that this secondary-site binding is specifically reduced or possibly eliminated for the Y39D EVH1 mutant, which mimics Abl-induced phosphorylation of this secondary site in VASP-EVH1. We propose that these observations may account for the reported reduced binding of Y39D VASP to zyxin, and may aid in understanding the role of tyrosine phosphorylation of VASP in the regulation of cell adhesion.

Introduction

The processive actin polymerase (Breitsprecher et al., 2008; Breitsprecher et al., 2011) VASP (Vasodilator-Stimulated Phosphoprotein) is an important regulator of the organization of the actin cytoskeleton (Krause et al., 2003). VASP and its homologs Mena and Evl are involved in the formation of lamellipodia (Bear et al., 2002) and filopodia (Lebrand et al., 2004; Mejillano et al., 2004), as well as the cellular processes of phagocytosis (Coppolino et al., 2001), cell migration (Bear et al., 2000; Bear et al., 2002; Krause et al., 2003), and neuron axon guidance (Goh et al., 2002). VASP functions both as an actin polymerase and as an anti-capping protein (Barzik et al., 2005; Bear and Gertler, 2009; Bear et al., 2002), by protecting the barbed end of actin filaments from capping proteins. VASP and its homologs localize to specific sites in the cell such as lamellipodia and filopodia as well as focal adhesions and sites of stress fiber damage (Hoffman et al., 2012; Reinhard et al., 1992; Rottner et al., 1999; Smith et al., 2010; Tokuo and Ikebe, 2004) through binding to proline-rich sequences with its EVH1 (Ena/VASP homology 1) domain (Ball et al., 2000; Niebuhr et al., 1997).

In response to cell mechanical stress, VASP is recruited to actin stress fibers, which it serves to reinforce and repair. This is mediated by an interaction with zyxin, a cytoskeletal protein involved in the mechanical stress response (Hoffman et al., 2012; Smith et al., 2010). Zyxin is phosphorylated at S142 in response to mechanical stimulation, which disrupts an inhibitory head-tail intramolecular interaction (Call et al., 2011; Moody et al., 2009). Zyxin is then recruited to damaged stress fibers through an interaction between its LIM domains and unknown factors (Smith et al., 2013). Simultaneously, phosphorylated zyxin binds the proteins VASP and α -actinin with multiple binding motifs in its disordered N-terminus.

The interaction between VASP and zyxin is mediated by both interactions between the proline-rich region zyxin and the EVH1 domain of VASP and an interaction between the LIM domain region of zyxin and the proline-rich region of VASP (Moody et al., 2009). This allows the interaction to be regulated by phosphorylation at several sites. First of all, zyxin can adopt an inhibited conformation in which its LIM domains obstruct its proline-rich region, which can be destabilized by phosphorylation of S142 by Akt (Call et al., 2011; Chan et al., 2007; Moody et al., 2009). Secondly, although the LIM/VASP interaction can overcome this inhibitory conformation, phosphorylation of VASP at S157 by PKA prevents this (Moody et al., 2009). Thirdly, phosphorylation of Y39 in the EVH1 domain of VASP by Abl inhibits its interaction with zyxin (Maruoka et al., 2012), though it is not clear why given the placement of Y39 far from the EVH1 binding site.

The VASP-EVH1 domain binds the motif (W/F)Px ϕ P, where x is any amino acid and ϕ is aliphatic (Ball et al., 2000; Niebuhr et al., 1997). This motif most frequently occurs as FPPPP, and very often occurs in groups of four or five, as in the cytoskeletal proteins lamellipodin and zyxin, and the *Listeria monocytogenes* protein ActA (Figure 4.1). This is speculated to be a mechanism to increase binding between

ActA

270	280	290	300	310	320
NASD <u>FPPPT</u>	DEELRLALPE	TPMLLGFNAP	ATSEPSSF <u>E</u> <u>PPPP</u>	TDEELR	LALPETPMLL
330	340	350	360	370	380
GFNAPATSEP	SSFE <u>FPPPT</u>	EDELEIIRET	ASSLDSSFTR	GDLASLRNAI	NRHSQNFSD <u>F</u>
390					
<u>PPIF</u>	TEEELN				

Lamellipodin

870	880	890	900	910	920
VVKQIASQ <u>F</u> <u>PP</u>	TPPAMES	QPLKVPANV	APQSPPAVKA	KPKWQPSSIP	VPSPD <u>FPPPP</u>
930	940	950	960	970	980
PESSLV <u>FPPPP</u>	<u>P</u> SPVPAPPP	PPPPTASPTP	DKSGSPGKKT	SKTSSPGGKK	PPPTPQRNSS
990	1000	1010	1020	1030	1040
IKSSSGAEHP	EPKRPSVDSL	VSKFTPPAES	GSPSKETLPP	PAAPPKPGKL	NLSGVNLPGV
1050	1060	1070	1080	1090	
LQQGCVSAKA	PVLSGRGKDS	VVE <u>FPSPP</u>	SD <u>FPPPP</u>	PET	ELPLPPIEIP

Zyxin

70	80	90	100	110	120
GEIPPPPPED	<u>FPLPP</u> PLAG	DGDDAEGALG	GA <u>FPPPP</u>	PPI	EES <u>FPPAP</u>
130					
PEEEGGPEAP					

Figure 4.1: Sequences of VASP-binding proteins. The proteins ActA, Lamellipodin, and zyxin all contain between four and five FP χ P motifs (red, underlined) which bind the EVH1 domain of VASP.

VASP and its binding partners, by combining the individual affinities of each of the four EVH1 domains in a VASP tetramer (Zimmermann et al., 2002). Indeed, deletions of VASP's C-terminal tetramerization domain (EVH2, or Ena-VASP Homology 2 domain) impair its ability to bind zyxin in cell lysates (Ahern-Djamali et al., 1998) and to localize to focal adhesions (Haffner et al., 1995). Inconsistent with this, however are the facts that the EVH2 domain is dispensable for *Listeria* motility (Geese et al., 2002) and that there seems to be a linear dependence of the rate of *Listeria* movement on the number of VASP-binding sites in ActA (Smith et al., 1996). It has been proposed alternatively that multiple FPPPP sites can be bound by multiple VASP tetramers, which would allow VASP to cross-link its binding partners (Zimmermann et al., 2002).

We have previously observed that VASP-EVH1 contains a secondary binding site that binds peptides with the core motif "LWPPPP." Interestingly, the primary and secondary binding sites seem to share some sequence specificity, recognizing both flanking negative charges and the aromatic tryptophan/phenylalanine. However, this was a very weak interaction, with the tightest-binding peptide binding with a K_D of 2.15 mM (Chapter 3). The question arose whether under certain conditions the tandem repeat motifs of zyxin, lamellipodin, and ActA might bind this secondary site rather than the primary site, by wrapping around the EVH1 domain in analogy to the structures of the homologous WASP-EVH1/WIP (Peterson et al., 2007; Volkman et al., 2002) and RanBP2-RanBD1/Ran (Vetter et al., 1999) complexes.

Here, we provide evidence that the third and fourth VASP-binding motifs in the proline-rich region of zyxin bind to the secondary site of EVH1 domain in the context of the full proline-rich sequence of zyxin (zyxin⁴¹⁻¹⁴⁰), but only weakly in a short peptide. Furthermore, we show that the phosphomimetic EVH1 mutant Y39D

demonstrates reduced or abolished binding at this secondary site. This secondary site may contribute to the overall affinity between zyxin and VASP, which could explain the effect of Y39 phosphorylation on cellular localization of VASP.

Materials and Methods

Protein purification

Human VASP-EVH1 domain (residues 1-115) and full-length human CypA were produced as described (Chapter 2), as bacterially-expressed 6X-His fusion proteins. The Y39D EVH1 mutant was similarly produced using site-directed mutagenesis. A pDEST17 plasmid (ampicillin resistance) encoding human zyxin residues 41-140, plus an N-terminal 6X-His fusion and a TEV cleavage site, was produced using the GATEWAY cloning system. The zyxin⁴¹⁻¹⁴⁰ sequence was amplified from a RFP-zyxin expression vector purchased from Addgene (Addgene plasmid 26720 (Bhatt et al., 2002)). Various Phe-to-Ala mutations (F71A/F104A , F71A/F104A/F114A , and F71A/F104A/F93A) were introduced by site-directed mutagenesis. Zyxin⁴¹⁻¹⁴⁰ was grown in BL21-DE3 *E. coli* cells in 1 L M9 minimal media with 19 mM ¹⁵NH₄Cl (or ¹⁴NH₄Cl to produce unlabeled protein). Cells were grown to an OD₆₀₀ of ~0.8 at 37 °C, the temperature was reduced to 17 °C, and protein expression was induced overnight with 1 mM IPTG. Cells were spun down and resuspended in 20 ml denaturing buffer (20 mM NaH₂PO₄, 500 mM NaCl, 6 M GuHCl, pH 8.0). Cells were then lysed by sonicating for 15 cycles (10 s on, 20 s off). The sonicate was centrifuged at 23,000 g and the supernatant was filtered with a 0.8 µM syringe filter to remove cell debris. The filtrate was then passed through a nickel-NTA column and the beads were washed with 40 ml of pH 8 wash buffer (20 mM NaH₂PO₄, 500 mM NaCl, 8 M urea, pH 8.0) and 20 ml of wash buffer at pH 6.0. Protein was then eluted with wash buffer at pH 4.0 and dialyzed into TEV cleavage buffer (50 mM Tris, 0.1 mM TCEP, pH 8) or

NMR buffer (20 mM KH_2PO_4 , 50 mM KCl, 1 mM TCEP, pH 6.7). To cleave the 6X-His tag, TEV protease was added and the protein was allowed to cleave at 4 °C for 1-2 days. The His tag was then removed with nickel resin as described (Chapter 2) and protein was dialyzed into NMR buffer. The other proteins were purified using native preps as described (Chapter 2), and dialyzed into NMR buffer following cleavage and removal of His tag. NMR samples also contained 5 mM NaN_3 , 0.05% protease inhibitor cocktail (EDTA-free, Sigma), and 7% D_2O . Unlabeled zyxin⁴¹⁻¹⁴⁰ proteins used in the ¹⁵N-EVH1 titrations had the His tag intact in order to measure protein concentration by absorbance (using tyrosine residues between the tag and cleavage site), and CypA had the His tag intact due to the absence of a cleavage site. NMR samples were concentrated with 3000 MWC centrifugal concentrators. Protein concentration was determined by UV absorption at 280 nm, using the theoretical extinction coefficients of 21,000 $\text{cm}^{-1}\text{M}^{-1}$ for VASP-EVH1, 8,500 $\text{cm}^{-1}\text{M}^{-1}$ for CypA, and 5.96 $\text{cm}^{-1}\text{M}^{-1}$ for uncleaved zyxin⁴¹⁻¹⁴⁰. The concentration of cleaved ¹⁵N zyxin⁴¹⁻¹⁴⁰, which does not have any UV absorbance, was determined by including a fitted correction factor in the binding curve fitting procedure.

Peptide production

Synthetic peptides encompassing the third and fourth binding motifs of zyxin, zyxin⁹⁹⁻¹²³ and zyxin^{99-123, F104A} were purchased from Genscript (Piscataway, NJ). Peptides were dissolved in NMR buffer and their pHs were adjusted using NaOH. Peptide concentration was determined using the theoretical extinction coefficients of 390 and 195 $\text{cm}^{-1}\text{M}^{-1}$ at 257 nm.

NMR data collection and processing

NMR experiments were carried out at 25 °C using a Varian Inova 600 MHz spectrometer with a {H, C, N} Z-axis gradient probe. Spectra were processed with nmrPipe and analyzed with Sparky. Prior to Fourier transformation, ¹⁵N zyxin⁴¹⁻¹⁴⁰ -

perspective data were processed with a phase-shifted sine bell window function and ^{15}N EVH1 data were processed with an exponential window function. Peak positions and volumes were measured using the Sparky peak detection function.

Resonance assignments

^{15}N -separated 3D TOCSY and NOESY spectra were taken on ^{15}N zyxin⁴¹⁻¹⁴⁰ using mixing times of 70 and 100 ms, respectively. Sequential assignments for residues 69-126, excluding prolines, were obtained from $\text{H}^{\text{N}}(\text{i})\text{-H}^{\alpha}(\text{i}-1)$ NOESY connectivities and additional insights from site-directed mutagenesis and binding titrations. Assignments for the *cis* isomers of various X-Pro sites in the sequence were obtained by the ^{15}N -ZZ exchange experiment described below. Resonance assignments for the EVH1 domain were obtained from the BioMagResBank, accession number 18569 (Ball et al., 2000), and incongruent assignments or residues near the N-terminus were clarified by 3D TOCSY and NOESY spectra of ^{15}N EVH1.

^{15}N -ZZ exchange experiments

^{15}N -ZZ exchange spectra were taken of ^{15}N zyxin⁴¹⁻¹⁴⁰ in the presence of 5 μM CypA. Mixing times of 0, 22, 44, 110, 220, and 440 ms were taken. Comparison of spectra with longer mixing times to the 0 ms spectrum allowed for identification of exchange cross peaks, which identify pairs of peaks representing *cis* and *trans* isomers of the F71-P72, F93-P94, F104-P105, and F113-P114 peptide bonds.

NMR titration experiments

Three ^{15}N EVH1-perspective HSQC titration experiments were performed. In each experiment the sample with the highest concentration of zyxin construct was produced first, and subsequent samples were produced by mixing part of the previous sample with a part of a stock of ^{15}N EVH1. The experiments were: EVH1 domain titrated with wt zyxin⁴¹⁻¹⁴⁰, zyxin⁹⁹⁻¹²³, and zyxin^{99-123, F104A}. In the wt zyxin⁴¹⁻¹⁴⁰ titration, the concentration of ^{15}N EVH1 was held at 0.37 mM and the zyxin⁴¹⁻¹⁴⁰ concentrations

were 0, 0.101, 0.201, 0.403, and 0.805. In the zyxin⁹⁹⁻¹²³ titration the concentration of ¹⁵N EVH1 was held at 0.3 mM and the zyxin⁹⁹⁻¹²³ concentrations were 0.13, 0.27, 0.54, 1.08, 2.17, 4.33, and 8.67 mM. In the zyxin^{99-123, F104A} titration the concentration of ¹⁵N EVH1 was held at 0.18 mM and the zyxin^{99-123, F104A} concentrations were 0, 0.12, 0.24, 0.49, 0.97, 1.95, 3.90, and 7.79 mM. Four ¹⁵N zyxin⁴¹⁻¹⁴⁰-perspective HSQC titration experiments were performed, with the mutants F71A/F104A , F71A/F104A/F114A , and F71A/F104A/F93A and wt zyxin⁴¹⁻¹⁴⁰ . In the wt zyxin⁴¹⁻¹⁴⁰ titration EVH1 domain was continually added from a stock to the NMR sample, diluting the ¹⁵N zyxin⁴¹⁻¹⁴⁰ further for each sample. In the other titrations, the most concentrated sample was produced first and subsequent samples were produced by mixing with a more concentrated stock of ¹⁵N zyxin⁴¹⁻¹⁴⁰, so that the concentration of ¹⁵N zyxin⁴¹⁻¹⁴⁰ increased as the concentration of EVH1 decreased. For the wt zyxin⁴¹⁻¹⁴⁰ titration the concentrations of EVH1 were 0, 0.02, 0.03, 0.05, 0.13, 0.22, 0.47, and 0.79 mM. For the F71A/F104A zyxin⁴¹⁻¹⁴⁰ titration the concentrations of EVH1 were 0.09, 0.18, 0.35, and 0.71 mM. For the F71A/F104A/F114A zyxin⁴¹⁻¹⁴⁰ titration the concentrations of EVH1 were 0.08, 0.16, 0.32, and 0.64 mM. For the F71A/F104A/F93A zyxin⁴¹⁻¹⁴⁰ titration the concentrations of EVH1 were 0.08, 0.16, 0.32, and 0.64 mM. Four spectra were taken of ¹⁵N zyxin⁴¹⁻¹⁴⁰ constructs with either 54 μ M EVH1 Y39D (wt zyxin⁴¹⁻¹⁴⁰) or 94 μ M EVH1 Y39D (zyxin⁴¹⁻¹⁴⁰ F71A/F104A, F71A/F104A/F114A, and F71A/F104A/F93A). Additionally, four spectra with equivalent concentrations of zyxin and wt EVH1 domain were taken. The ¹⁵N-EVH1 perspective spectra were taken with spectral widths of 8 kHz in the proton dimension (2048 complex data points) and 1.8 kHz in the nitrogen dimension (256 complex data points). The ¹⁵N- zyxin⁴¹⁻¹⁴⁰ perspective spectra were taken with spectral widths of 6 kHz in the proton dimension (2048 complex data points) and 1.4 kHz in the nitrogen dimension (256 complex data points).

Quantification of binding

^{15}N and ^1H chemical shift perturbation datasets were globally fit to either two- or three-state models. ^{15}N EVH1/ zyxin⁹⁹⁻¹²³ titration data was fit to a three state model allowing for the zyxin⁹⁹⁻¹²³ peptide to bind either at the primary or secondary site, with distinct chemical shifts for each case. However, key primary-site residues such as Q81sc were deemed to only be sensitive to binding at the primary site and thus only had chemical shift parameters for the free and primary-site-bound states. Fitted parameters included the chemical shifts of the bound states and dissociation constants for the two sites, K_D^{primary} and $K_D^{\text{secondary}}$. From the ^{15}N EVH1/ zyxin⁹⁹⁻¹²³ dataset, three binding curves for the primary binding site and 20 binding curves for the secondary site were globally fit. From the ^{15}N EVH1/ zyxin^{99-123, F104A} dataset, five primary site binding curves and 27 secondary site binding curves were fit. F71A/F104A and F71A/F104A/F114A ^{15}N zyxin⁴¹⁻¹⁴⁰/EVH1 titration datasets were fit to a three state model allowing for EVH1 to bind with either 1:1 or 1:2 stoichiometries. F71A/F104A/F93A ^{15}N zyxin⁴¹⁻¹⁴⁰ was modeled to only bind EVH1 domain in a 1:1 complex. Peaks of residues near the third and fourth motifs were modeled to have distinct chemical shifts in the 1:1 and 1:2 complexes, while peaks of residues near the second motif were modeled to be insensitive to this. Fitted parameters included the chemical shifts of the bound states and dissociation constants for the 1:1 and 1:2 complexes, K_D^1 and K_D^2 . Fitting was accomplished by minimizing the sum of squares of the residuals using the *BiophysicsLab* Matlab package.

Results

Assignment and characterization of the proline-rich region of zyxin

In order to investigate whether VASP uses the secondary site in its EVH1 domain to interact with its binding partners, we chose to study its interaction with the

proline-rich domain of zyxin. Residues 41-140 of zyxin (Figure 4.2A), which contain all four of its FPxøP motifs (M1, M2, M3, M4), was cloned and bacterially expressed and purified as an ^{15}N -labeled protein. The ^{15}N - ^1H HSQC of zyxin⁴¹⁻¹⁴⁰ (Figure 4.2B) shows very narrow peak dispersion characteristic of a disordered sequence undergoing rapid sampling of conformational space. Thanks to the relatively small number of residues that give rise to peaks (66, excluding prolines and the N-terminal residue), however, nearly all the peaks in the spectrum are resolved from each other.

It was possible to assign residues 69-126 (excluding prolines) with primarily 3D TOCSY and NOESY spectra, using $\text{H}^{\text{N}}(\text{i})$ - $\text{H}^{\alpha}(\text{i}-1)$ NOESY connectivities (Appendix Table 4.1). For residues isolated by proline residues which do not have NH protons, assignments were aided by site-directed mutagenesis and process-of-elimination. Comparisons of HSQCs of the mutants F71A/F104A , F71A/F104A/F114A , and F71A/F104A/F93A (described below) and wt zyxin⁴¹⁻¹⁴⁰ allowed for identification of peaks that responded to these mutations, likely to correspond to residues near the site of mutation. Furthermore, assignments were carried out after titration data and ^{15}N -ZZ exchange experiments (described below) were underway, allowing for attention to be focused on peaks that responded to EVH1 binding or isomerization, and were thus likely to be near EVH1 binding sites.

A small subset of peaks in the zyxin⁴¹⁻¹⁴⁰ HSQC had much smaller ($\sim 1/4\text{X}$) peak volumes, suggesting that they represented the slowly-exchanging *cis* isomers of the various X-Pro sites in the sequence. To further understand this, the ^{15}N -ZZ exchange experiment was performed on ^{15}N zyxin⁴¹⁻¹⁴⁰ in the presence of 5 μM cyclophilin A (CypA), a prolyl isomerase that can accelerate proline isomerization into the NMR-sensitive timescale of seconds (Figure 4.2C). Indeed, this experiment produced exchange cross peaks between the minor peaks and other, larger peaks, which, remarkably, in every case corresponded to residues close to one of the four

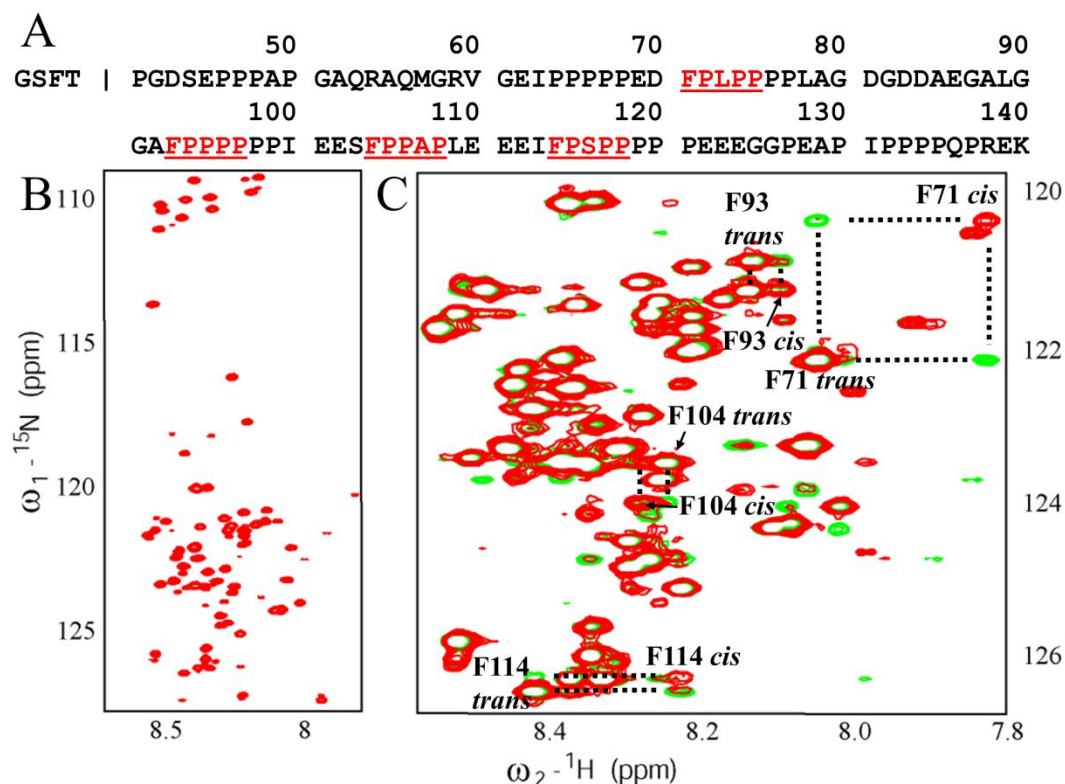


Figure 4.2: HSQC and ^{15}N -ZZ spectra of the proline-rich region of zyxin. (A) The sequence of zyxin⁴¹⁻¹⁴⁰ contains many prolines and four VASP-binding sites (red, underlined). The four amino acids to the left of residue P41 are a consequence of cloning. (B) The ^{15}N - ^1H HSQC spectrum of ^{15}N zyxin⁴¹⁻¹⁴⁰ shows narrow peak dispersion but nearly all peaks are resolved. (C) The ^{15}N -ZZ experiment performed on ^{15}N zyxin⁴¹⁻¹⁴⁰ in the presence of 5 μM CypA allows for identification of *cis* and *trans* isomers of each of the four Phe-Pro sites in the sequence. Mixing times of 0 ms (red) and 220 ms (green) are shown.

Phe-Pro motifs in the sequence. This can be attributed to the tendency of phenylalanine to induce a relatively large population of *cis* when preceding a proline residue (Reimer et al., 1998). Thus, assignments for the minor *cis* isomers were possible by observing cross peaks in the ^{15}N -ZZ exchange spectra, and confirming their identities by observing $\text{H}^{\text{N}}(\text{i})\text{-H}^{\alpha}(\text{i}-1)$ NOESY connectivities when possible (Appendix Table 4.1). The dominance of Phe-Pro motifs in producing *cis* populations can be explained by the intrinsic tendency of bulky amino acids such as phenylalanine to induce a large percentage of *cis* isomer. Because we have previously shown that the interaction between VASP-EVH1 and its (W/F)PX ϕ P binding motifs is specific for the *trans* isomer of the (W/F)-P peptide bond (Chapter 2), it was of particular importance to account for the *cis/trans* equilibria of these sites.

Zyxin induces chemical shift changes at a unique binding interface on VASP-EVH1.

Having purified and characterized the proline-rich region of zyxin that harbors its VASP-binding sites, we next attempted to characterize its interaction with VASP-EVH1. As a first step, ^{15}N EVH1 domain was titrated with unlabeled zyxin⁴¹⁻¹⁴⁰ and a series of HSQC spectra were taken. Remarkably, zyxin⁴¹⁻¹⁴⁰ induced severe broadening in all EVH1 peaks so much that below a ratio of 1:4 zyxin⁴¹⁻¹⁴⁰ to EVH1, only two peaks corresponding to glycines in the flexible tail preceding Met1 of EVH1 were discernible. This may be a result of formation of an ensemble of high molecular-weight complexes where multiple EVH1 domains bind to the four motifs in zyxin⁴¹⁻¹⁴⁰ and potentially the primary and secondary binding sites in EVH1 are similarly occupied by multiple zyxin⁴¹⁻¹⁴⁰ molecules. This prevented in-depth analysis, but it was still possible to analyze the chemical shift perturbation pattern induced by zyxin⁴¹⁻¹⁴⁰. The composite chemical shift perturbations at a ratio of 1:4 zyxin⁴¹⁻¹⁴⁰ to EVH1 were extrapolated based on the binding curve of Gly-2 (not shown). Although this analysis assumes a simple 1:1 complex, which later experiments show is not an

appropriate assumption, it nevertheless produced a chemical shift perturbation profile that matched the previously reported (Chapter 2) profile of ActA³³³⁻³⁴⁴-induced chemical shift changes quite well (Figure 4.3A). The primary difference between these profiles is that a number of key residues are sensitive to binding to zyxin⁴¹⁻¹⁴⁰ but not ActA³³³⁻³⁴⁴. These residues, which include S2, R48, N63 and A65, map to the previously-characterized (Chapter 3) secondary site (Figure 4.3B).

EVH1 binding to zyxin motif M4 is sensitive to sequence and isomer state at motif M2

In order to identify the residues in zyxin that contact the secondary binding site in the EVH1 domain, ¹⁵N zyxin⁴¹⁻¹⁴⁰ was titrated with unlabeled EVH1 domain. As opposed to the ¹⁵N EVH1 perspective titration, line-broadening only incrementally affected the spectra, and most peaks remained resolved throughout the titration. Peaks corresponding to residues within the first, second, and fourth binding motifs all moved significantly at early titration points, while peaks of residues in the third binding motif only started to move at very high concentrations of EVH1 (Figure 4.4A, left). This was unexpected, as it has previously been reported that a peptide containing only the fourth binding motif did not demonstrate detectable binding to EVH1 domain, while the third motif binds with moderate (197 μM) affinity (Ball et al., 2000).

Interestingly, the very different shapes of binding curves corresponding to each motif seem to suggest that it is possible for four EVH1 domains to bind each of the four FPPPP motifs in zyxin at once, overcoming any steric clash (Figure 4.4A). However, the unexpected preference of the EVH1 domain for motif M4 over motif M3 suggested that the fourth binding motif is bound very differently in the context of the full sequence and focused our attention on it. Specifically, we asked whether binding of motifs M1, M2, or M3 at the EVH1 domain's primary site allowed motif M4 to bind at the EVH1 domain's secondary site. We selected motif M2 as the motif most likely to participate in this kind of interaction, based on the number of residues

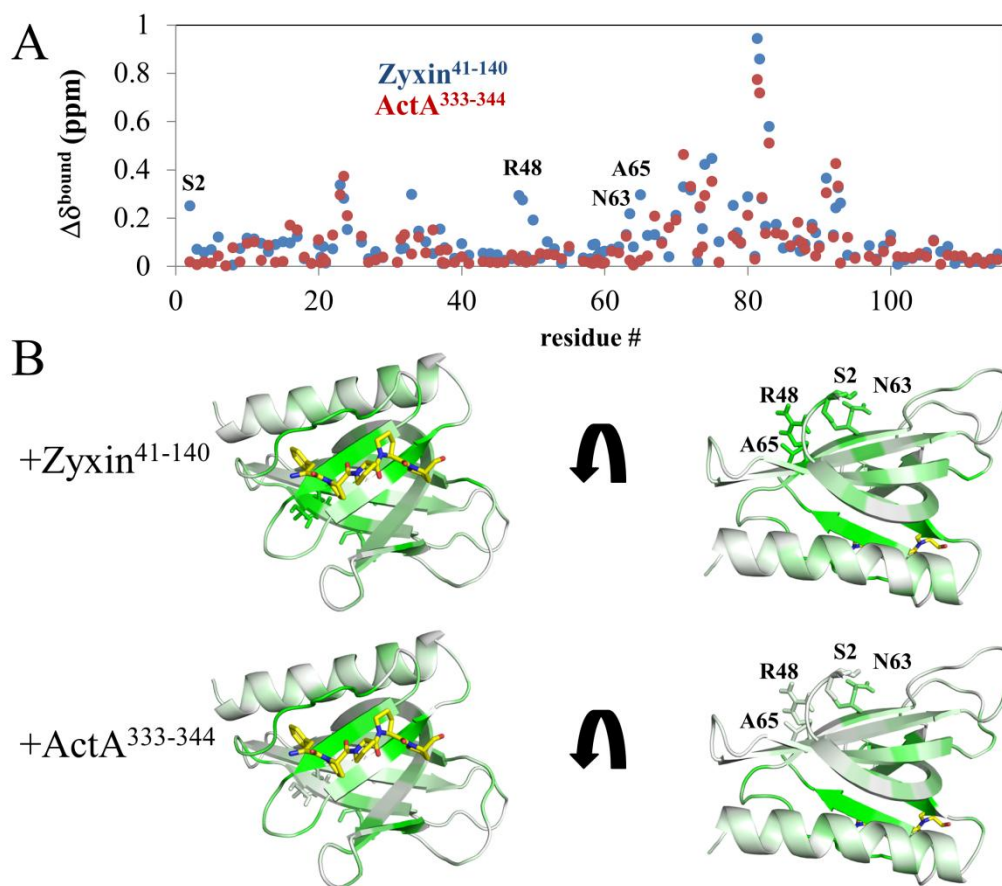


Figure 4.3: Zyxin⁴¹⁻¹⁴⁰ induces chemical shift changes in the secondary binding site of VASP-EVH1. (A) Composite chemical shift changes of ¹⁵N EVH1 residues upon binding zyxin⁴¹⁻¹⁴⁰ (blue) or the peptide ActA³³³⁻³⁴⁴ (red). Certain EVH1 residues, such as S2, R48, N63, and A65, are only sensitive to binding to zyxin⁴¹⁻¹⁴⁰. (B) Mapping chemical shift changes to the structure of VASP-EVH1 shows that zyxin⁴¹⁻¹⁴⁰ induces chemical shift perturbations for residues in the primary binding site but also for residues on the opposite face of the EVH1 domain. ActA³³³⁻³⁴⁴ by contrast only influences residues in the primary binding site (Data from Chapter 2). Green = highest chemical shift perturbation, white = no perturbation.

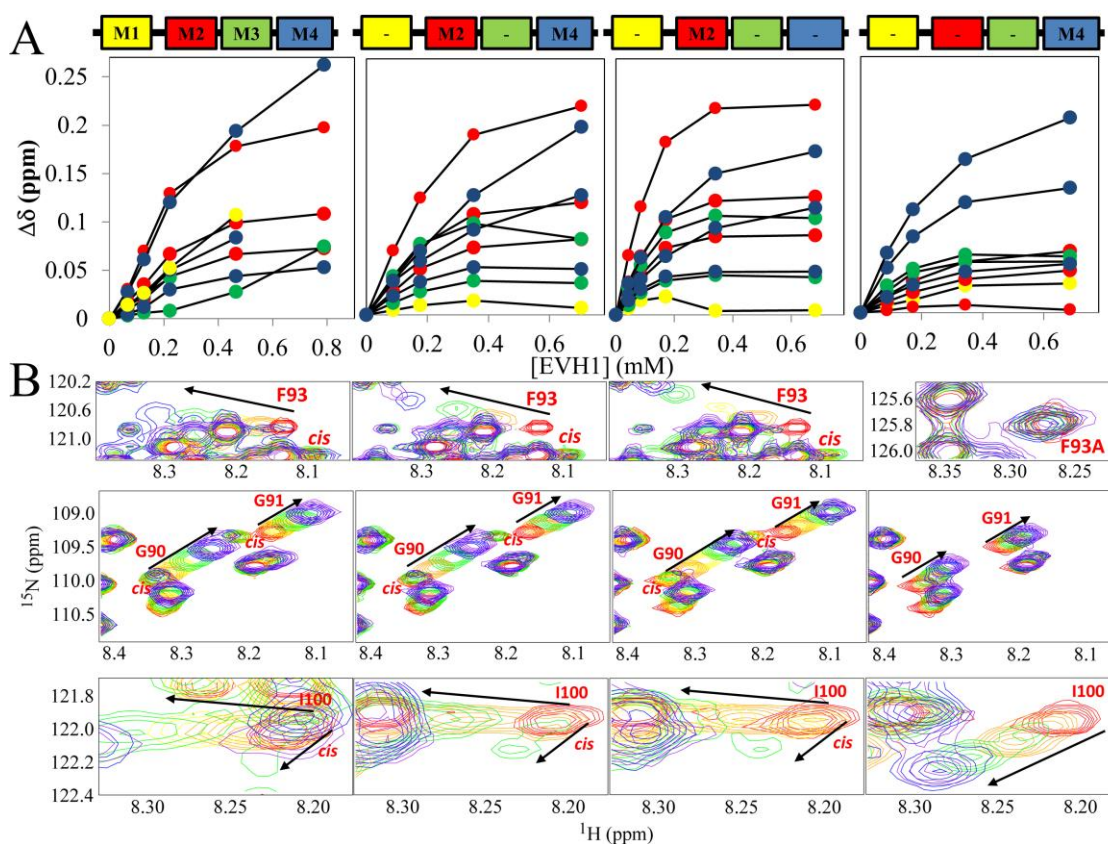


Figure 4.4: ^{15}N zyxin⁴¹⁻¹⁴⁰/EVH1 titration data shows isomer specificity of interaction at motif M2. (A) Above, various zyxin⁴¹⁻¹⁴⁰ mutants are represented by either “M1-M4” for motifs 1-4, or “-” for a Phe-to-Ala mutant at a given motif. Binding curves for (left to right) wt, F71A/F104A, F71A/F104A/F114A, and F71A/F93A/F104A ^{15}N zyxin⁴¹⁻¹⁴⁰ titrated with EVH1 domain are shown. Motifs M1-M4 are represented by yellow, red, green and blue symbols, respectively, in the binding plots. Binding at the third and fourth motifs persists when these motifs are mutated. (B) Features of binding titration data for residues at motif M2. Peaks for the *trans* isomers of F93, G90 and G91 all move with increasing [EVH1] while the *cis* isomers remain stationary and decrease in intensity. For the I100 peak on the other side of motif M2, the *cis* isomer moves in a very distinct trajectory. Mutating F93 to alanine (rightmost column) does not abolish binding entirely, and the *cis* isomer is no longer observable. The I100 peak moves along a similar trajectory as the *cis* isomer in the other titrations for this mutant.

between motifs M2 and M4 (19). Therefore, in an effort to simplify the complex binding interaction between these proteins, the ^{15}N zyxin⁴¹⁻¹⁴⁰/EVH1 titration was repeated with the zyxin mutants F71A/F104A , F71A/F104A/F114A , and F71A/F104A/F93A. These titrations did not suffer significantly from line-broadening and the F71A/F104A mutant showed peak trajectories for residues near motifs M2 and M4 that were on the whole very similar to the wt titration.

Binding curves for all four zyxin⁴¹⁻¹⁴⁰ titrations are shown in Figure 4.4A. Interestingly, while mutation of motif M1 (F71A) seems to prevent binding at this motif, significant chemical shift changes for residues at the other three motifs persist when they are mutated. The most drastic mutation, F93A, resulted in weaker binding curves and reduced chemical shift perturbations for residues in motif M2, while mutating motif M4 (F114A) does not substantially change the binding curves or chemical shift changes.

Small features of these titrations lend insight into the binding orientation of these proteins (Figure 4.4B). The previously-demonstrated (Chapter 2) *trans* isomer-specificity of binding at the EVH1 domain primary site resulted in very different behavior for the peaks corresponding to the *cis* and *trans* isomers of F93-P94. While the *trans* peaks moved substantially, the *cis* peaks of G90, G91, and F93 only decreased in intensity upon addition of EVH1 domain. In contrast, the peak corresponding to I100 showed a minor population, most likely corresponding to the *cis* isomer, that moved in a very different direction rather than remain stationary. Meanwhile, residues in the third and fourth motifs showed minor population peaks that became resolved upon titration of EVH1 and lagged behind, and in some cases moved in slightly different (such as I113), or substantially different (such as S116) directions (Figure 4.5). This “lagging” behavior was most pronounced for residues in

the third motif, and most pronounced in the triple mutant F71A/F104A/F114A. Importantly, these minor population peaks were distinct from the peaks of the *cis* isomer of F114-P115, which unexpectedly moved comparably to the *trans* peaks. Remarkably, when motif M2 was mutated (F93A), the peaks for these M3 and M4 residues followed these minor-peak trajectories rather than the trajectories of the previous major populations, and there was no longer evidence of a minor population, with a few small exceptions. Thus, the binding trajectories of residues in motifs M3 and M4 are surprisingly sensitive to factors that influence EVH1 binding (the sequence and the isomer state of F93-P94) at motif M2. Furthermore, motif M2 seems to have some affinity for EVH1 even when F93 is mutated to alanine or when the F93-P94 peptide bond is *cis*, but it seems to bind in a distinct orientation, based on the behavior of the I100 peak.

In order to quantitatively interpret the binding curves obtained from these titrations, we noted that peaks for residues in motifs M3 and M4 displayed clear three-state behavior, in which they shift trajectories or even begin moving back towards the Apo chemical shift as the EVH1 domain concentration is increased. This was not observed for residues in motif M2, and the extent of this was nearly completely abolished in the F71A/F104A/F93A mutant. We interpreted this as evidence that the EVH1 domain can bind in multiple stoichiometries, which is not surprising given the multiplicity of binding motifs. Fitting the binding curves to models (Appendix Figure 4.1) allowing 1:1 and 1:2 complexes yielded good fits, and the binding constants listed in Table 4.1. Fitting the binding curves from the wt zyxin titration was not attempted due to the complexity of the binding scheme.

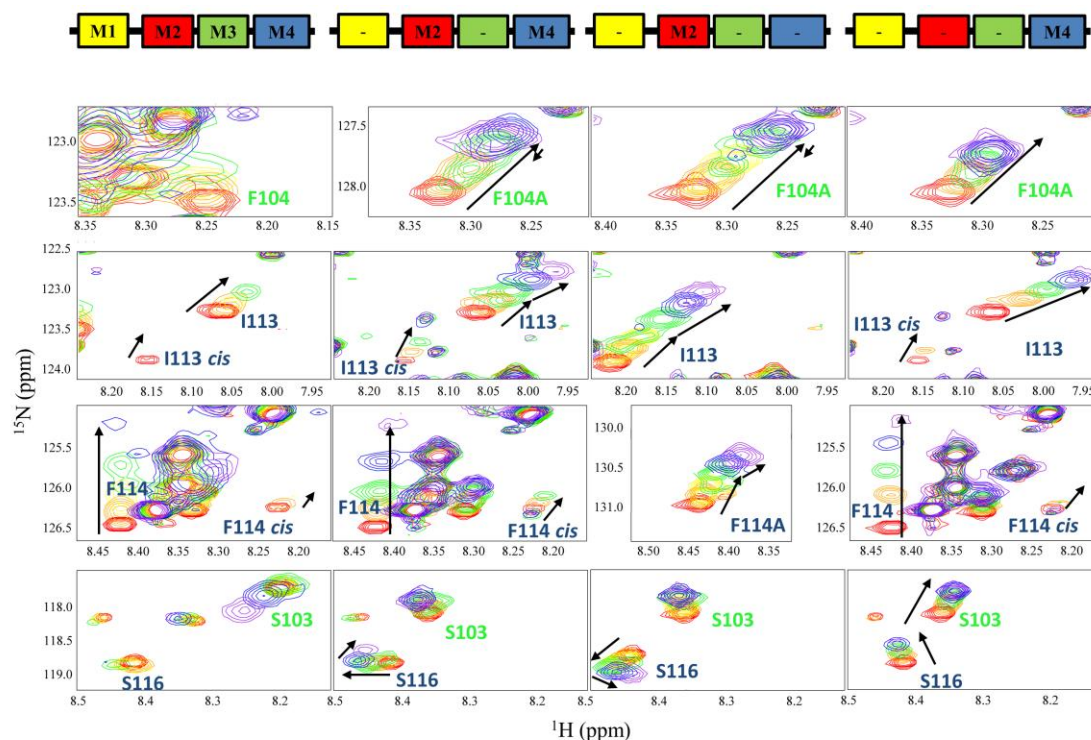


Figure 4.5: ^{15}N zyxin⁴¹⁻¹⁴⁰/EVH1 titration data show multiple populations in slow exchange for zyxin's third and fourth FPx ϕ P motifs. Each column represents a different zyxin⁴¹⁻¹⁴⁰ construct (wt, F71A/F104A, F71A/F104A/F114A, and F71A/F93A/F104A as represented by colored boxes above). The F104, I113, and F114 peaks (top three rows) show a trailing minor population that is not present for the F71A/F104A/F93A mutant (fourth column). Both *cis* and *trans* peaks of F114 and I113 (middle two rows) move upon addition of EVH1 domain. Finally, both S103 and S116 (bottom row) show clear three-state behavior that is abolished in the F71A/F104A/F93A titration.

Table 4.1: Dissociation constants of EVH1 binding to zyxin constructs

construct	$K_D^{primary}$	$K_D^{secondary}$
zyxin ⁹⁹⁻¹²³	141 μ M	4.2 mM
zyxin ^{99-123, F104A}	125 μ M	2.5 mM
	K_D^1	K_D^2
zyxin F71A/F104A	33 μ M	226 μ M
zyxin F71A/F104A/F114A	14 μ M	135 μ M
zyxin F71A/F104A/F93A	93 μ M	-

The phosphomimetic Y39D EVH1 mutant is impaired in binding at the secondary site

It has been reported that phosphorylation of Y39 by Abl reduces VASP accumulation in focal adhesions, and that mutation of Y39 to aspartic acid reduced VASP binding to zyxin. Because Y39 is located within the secondary binding site we have described, we wondered whether Y39 phosphorylation inhibits binding at the EVH1 secondary site. Furthermore, we reasoned that adding EVH1 Y39D to ¹⁵N-labeled zyxin⁴¹⁻¹⁴⁰ would help to map the zyxin residues that interact with the secondary site.

The phosphomimetic Y39D EVH1 mutant was produced as an unlabeled protein and added to zyxin⁴¹⁻¹⁴⁰ as before. Because of low protein yield, only one spectrum was taken for each ¹⁵N- zyxin⁴¹⁻¹⁴⁰ construct: wt zyxin⁴¹⁻¹⁴⁰ with 54 μ M EVH1-Y39D, and the mutants F71A/F104A , F71A/F104A/F114A , and F71A/F104A/F93A with 94 μ M EVH1-Y39D. Plots of the chemical shift perturbation profiles of these spectra compared to the analogous wt-EVH1 profiles are shown in Figure 4.6A. The largest differences between the wt-EVH1 and EVH1-Y39D perturbation profiles are seen for the triple mutants F71A/F104A/F114A, and F71A/F104A/F93A. In these cases, EVH1 Y39D induces significantly smaller chemical shift perturbations for residues spanning motifs M2, M3, and M4. The largest differences are seen for residues near mutated motifs, i.e. M4 for the

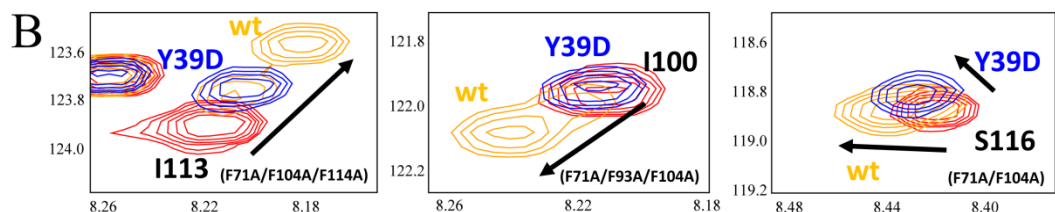
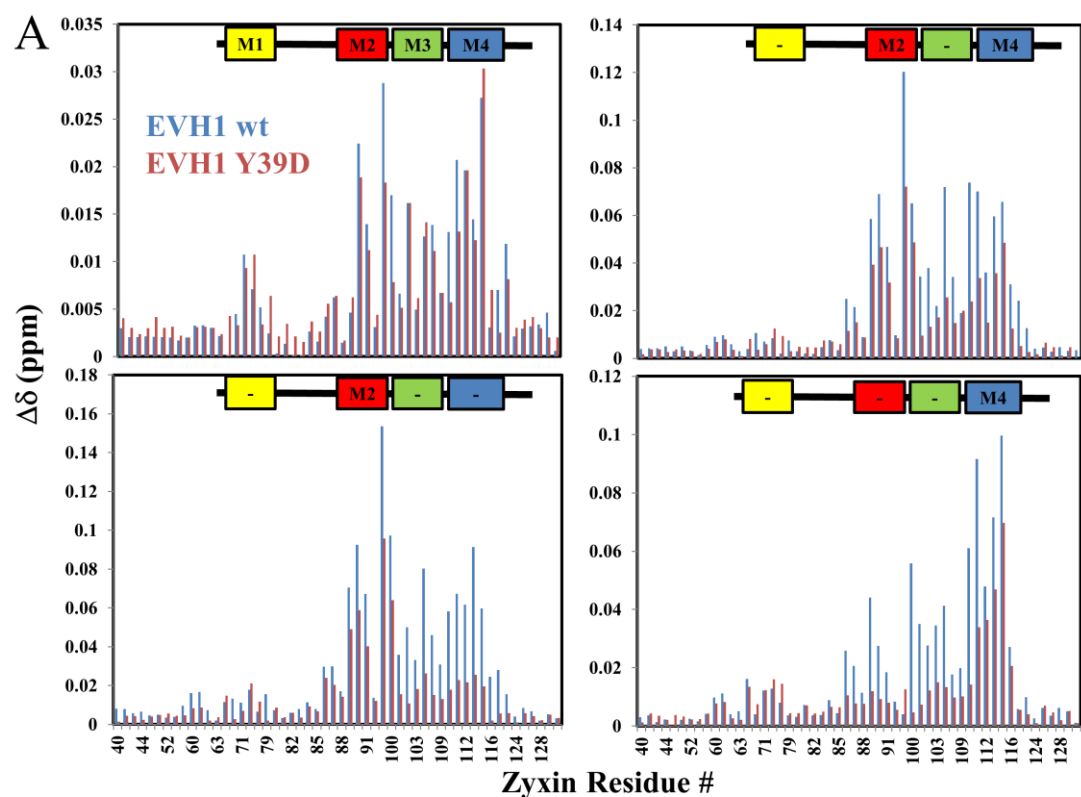


Figure 4.6: Chemical shift perturbation profiles of wt and Y39D EVH1 domain, and example peaks. (A) Bar charts representing the composite chemical shift perturbations ($\Delta\delta$) induced by adding either wt (blue bars) or Y39D (red bars) EVH1 domain to the four zyxin⁴¹⁻¹⁴⁰ constructs (wt, F71A/F104A, F71A/F104A/F114A, and F71A/F93A/F104A) represented by colored boxes above each charts. The position of the colored boxes reflects the position of each motif in the sequence. In the triple mutants, there is a significant decrease in chemical shift perturbation values for residues 100-123 for Y39D relative to wt EVH1 domain. (B) The Y39D EVH1 mutant induces chemical shifts that often correspond to the minor, slowly-exchanging population seen previously (left, I113 peak as example). The I100 peak, which exhibited a strikingly different peak trajectory for the F71A/F93A/F104A mutant, simply does not move when EVH1-Y39D is added to this mutant (center). The S116 peak, which previously displayed three-state behavior, moves in the direction of the final chemical shift when EVH1-Y39D is added.

F71A/F104A/F114A data and M2 for the F71A/F104A/F93A data, and M3 for both. Remarkably, in almost all cases peaks that had shown a lagging population in the wt-EVH1 spectra adopted the chemical shift of that lagging population at the corresponding EVH1 concentration. The I100 peak no longer moved at all in the F71A/F104A/F93A/EVH1-Y39D spectrum, indicating that the alternative orientation for that residue could not be adopted for Y39D EVH1. Lastly the S116 peak, which had shown three-state behavior in the wt EVH1 titration, moved towards its final, 1:2 peak position for this Y39D mutant (Figure 4.6B).

Collectively, these data suggest strongly that the Y39D mutation disrupts binding at a distinct secondary EVH1 site, which is employed primarily at a stoichiometry of 1:1. This distinct site seems to bind residues 100-123, and seems to compete with the primary site, as the effects of the Y39D mutation are most pronounced at mutated motifs that can no longer bind the primary site. Figure 4.7 suggests a model of the multi-state binding scheme for VASP-EVH1 and the three zyxin⁴¹⁻¹⁴⁰ mutants used in this study (F71A/F104A, F71A/F104A/F114A, and F71A/F93A/F104A) that accounts for most of our observations. This model defines two 1:1 complexes between the EVH1 domain and zyxin⁴¹⁻¹⁴⁰, either with the primary EVH1 site bound to motif M2 and the secondary EVH1 site bound to motif M4, or visa-versa, with the first binding orientation dominating. When the F93-P94 peptide bond adopts the *cis* conformation, or when F93 is mutated to alanine, the equilibrium is shifted towards this second orientation. As EVH1 domain concentration is increased, the equilibrium is shifted towards a 1:2 zyxin:EVH1 complex, where motifs M2 and M4 are both bound in the primary EVH1 domain site. The Y39D mutation in the EVH1 domain disrupts the secondary binding site interaction, causing the chemical shifts of the two possible 1:1 complexes to collectively resemble those of the 1:2

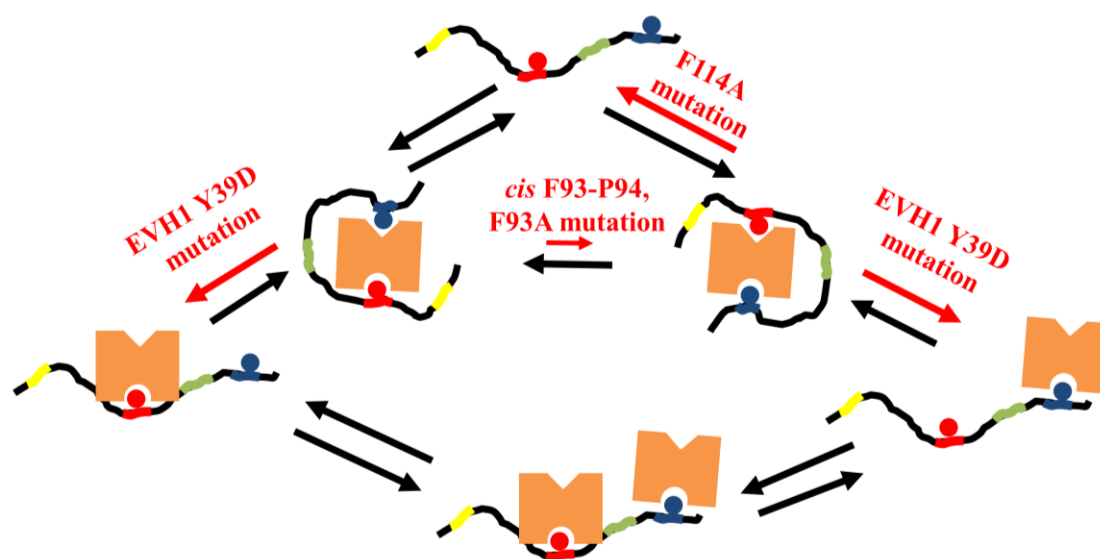


Figure 4.7: Suggested model of EVH1/ zyxin⁴¹⁻¹⁴⁰ binding. This model describes the binding scheme between EVH1 and the three mutant zyxin⁴¹⁻¹⁴⁰ constructs used in this study (F71A/F104A, F71A/F104A/F114A, and F71A/ F93A/F104A). The EVH1 domain is shown as an orange box with primary (rounded) and secondary (triangular) binding sites on opposite faces. Zyxin⁴¹⁻¹⁴⁰ is shown a flexible black line with four binding motifs (M1-M4, yellow, red, green, blue). This model defines two 1:1 complexes in equilibrium, and a 1:2 complex where both M2 and M4 are bound by the primary EVH1 binding site. The impacts of various mutations in both the EVH1 domain and zyxin⁴¹⁻¹⁴⁰ on the equilibrium of binding orientations are specified. Additionally, the impact of the isomer state of F93-P94 on the binding orientation is shown.

complex.

Zyxin motifs M3-M4 as a short peptide only bind the secondary EVH1 site with low affinity

In order to examine the specificity of zyxin motifs M3 and M4 for the secondary vs. primary binding sites in the EVH1 domain, we titrated ^{15}N EVH1 domain with a peptide corresponding to residues 99-123 of zyxin (zyxin⁹⁹⁻¹²³) or a mutant that abolished binding at the third motif (zyxin^{99-123, F104A}). The long sequence was used because these were the residues that seemed to respond to the Y39D mutation in the earlier analysis. Fitting the data from both titrations to a three-state model (Appendix Figure 4.2) yielded the dissociation constant for the secondary and primary sites for each peptide (Table 4.1). Strangely, the F104A mutant peptide bound to the primary site with identical affinity as the wild-type peptide and slightly higher affinity to the secondary site. This experiment helped to better map the secondary site, since peaks sensitive to weak secondary binding continue to move at EVH1 concentrations where the primary site is saturated (Figure 4.8). This experiment showed only very weak binding to the secondary site (2.5-4.2 mM), and tighter binding to the primary site than reported in (Ball et al., 2000) (~125-141 μM). Therefore, we concluded that binding at motif M2 is an important prerequisite for binding in the secondary site of the EVH1 domain.

Discussion

This work highlights the utility of NMR titration analysis for the study of complex protein-protein interactions involving several binding sites. The ^{15}N - ^1H HSQC of the intrinsically disordered proline-rich sequence zyxin⁴¹⁻¹⁴⁰ yields residue-specific data that can be used to simultaneously track four distinct binding events. This provides the opportunity to address the question of whether four EVH1 domains can

simultaneously bind the four binding motifs in zyxin. Furthermore, measurement of binding in the context of the full-length sequence allows for detection of secondary contacts with residues very far in sequence from a primary binding motif. Lastly, the site specificity of NMR analysis allows unambiguous decoupling of primary and secondary binding events.

Additionally, this work provides an example of the usefulness of identification and interpretation of *cis/trans* equilibria. The *trans*-specificity of the EVH1/FPPPP interaction made it possible to interpret the minor lagging population seen for peaks of motif M3 and M4 residues as a *cis* population. This in turn provided evidence that binding of motif M2 in the primary EVH1 domain site is important for a secondary interaction involving motifs M3 and M4.

EVH1 domains consist of two antiparallel β -sheets which share two strands (1 and 2), forming a sandwich, packed against a long C-terminal helix. The canonical (primary) binding site is a concave surface formed by one of the sheets (Figure 4.8). The secondary binding site we define here, on the other hand, is a rather similar concave surface formed by the other sheet, on the opposite side of the domain. The residues most sensitive to the secondary interaction include the very N-terminal sequence of the protein (M0-C7) as well as the side-chains of R48, and N63, which are all in close proximity to each other.

EVH1 domains all share a conserved primary binding site which binds proline rich sequences adopting a polyproline type II (PPII) structure. However, secondary interactions with additional epitopes have been reported, including for the VASP-EVH1 domain itself. The WASP-EVH1 domain binds the protein WIP making contacts in its conserved canonical binding site, but also additional sites both above and below (Volkman et al., 2002). Similarly, the VASP-EVH1 domain recognizes the epitope ₃₄₃EL₃₄₄ in ActA using residues Q31 and A32, relatively far from the primary

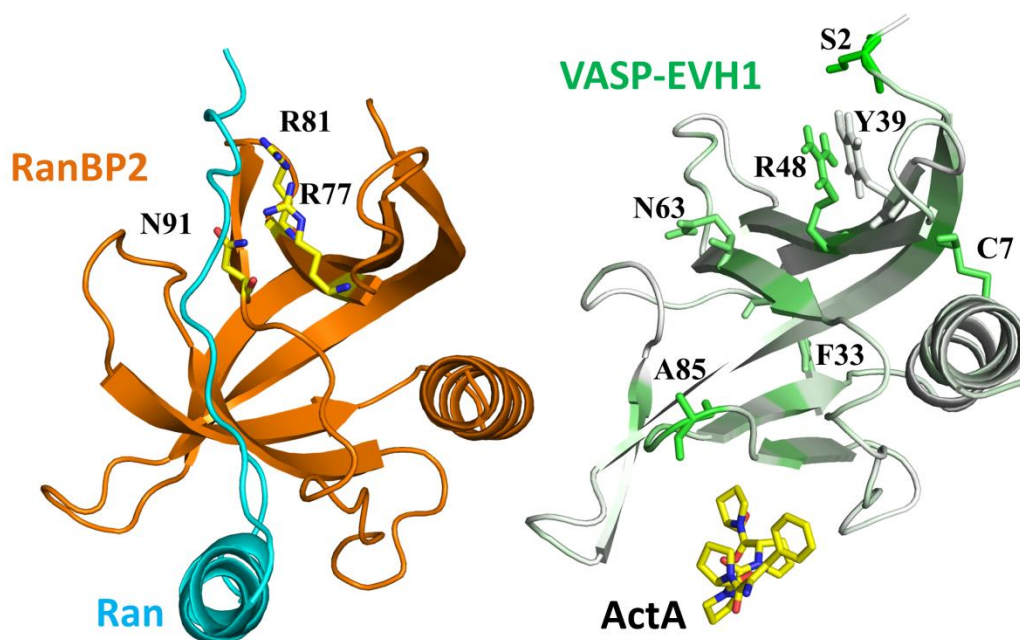


Figure 4.8: Tyr39 is located centrally in the secondary EVH1 binding site. (left) The first Ran-binding domain of RanBP2 (orange) binds Ran (cyan) using a similar secondary binding surface as the site we describe, employing residues R77, R81, and N91 which correspond to R48, R52, and N63 in VASP-EVH1. (right) VASP-EVH1 residue Y39 is located centrally in the secondary binding site. EVH1 is colored according to chemical shift perturbations induced at high concentrations of the zyxin⁹⁹⁻¹²³ peptide (white = no perturbation, green = highest perturbation). Key residues are shown as sticks. The ActA sequence FPPPP (yellow) is shown bound in the primary site. (Model produced as in Chapter2).

binding site (Ball et al., 2000). While none of these secondary EVH1 sites are quite as distant as the binding surface described here, the homologous Ran-binding domain (RanBD) does seem to utilize this site.

EVH1 domains share structure and sequence homology with RanBDs (Callebaut et al., 1998). The crystal structure of the first RanBD of RanBP2 bound to the nuclear transport protein Ran demonstrates that key features of the secondary binding interaction of VASP -EVH1 are conserved for Ran-binding domains (Vetter et al., 1999). In this structure, there are multiple significant contacts between RanBD1 and Ran besides contacts to the “primary” site, which binds an α -helical segment of Ran rather than the PPII structure that EVH1 domains bind. In particular, the N-terminal sequence of Ran binds to the face of RanBD1 that corresponds to the secondary binding site we have described (Figure 4.8). The sidechains of RanBP2 residues R77, R81, and N91 (corresponding to VASP-EVH1 residues R48, R52, and N63) hydrogen bond with the backbone carbonyl groups of residues M179, A181, and L182 in Ran. Interestingly, these Ran residues adopt a PPII structure, and the recognition of their backbone carbonyl groups by RanBP2 is very reminiscent of the conserved mechanism by which EVH1 domains recognize their proline-rich motifs in the primary binding site.

In an alignment of EVH1 and Ran-binding domains, the residues R48 and N63 are very well-conserved (Callebaut et al., 1998). Given the degree of conservation of these residues, it is tempting to speculate that this secondary binding site is utilized by proteins such as WASP and Homer as well. On the other hand, R48 may play a structural role, as it forms a salt bridge with E3 in VASP, possibly contributing to the stability of the β sheet. This and the very weak binding affinity of the secondary site for motifs M3 and M4 in isolation (zyxin⁹⁹⁻¹²³) suggest that it is also possible that this

binding site in VASP is only vestigial.

Some support for the biological relevance of the secondary binding interaction described here comes from the recently reported impact of phosphorylation of VASP-EVH1 by Abl tyrosine kinase (Maruoka et al., 2012). In Bcr-Abl-positive leukemic cells, Abl phosphorylates Y39 of VASP, which is centrally located in the binding site we describe (Figure 4.8). This may regulate the interaction between VASP and zyxin, since the phosphomimetic mutant Y39D has a reduced ability to bind zyxin in cell lysates. Furthermore, overexpression of either the Y39D or Y39F mutants, but not wt VASP, impairs adhesion of K562 cells to fibronectin, implying a cycle of phosphorylation and dephosphorylation is important for proper regulation of VASP. We have provided evidence that the Y39D mutant of VASP-EVH1 retains wt binding affinity for its primary site but that it is incapable of binding in the secondary site. Taken together, this data suggests that the secondary binding site is crucial for the interaction with zyxin in the cellular context.

Because we have focused our attention on motifs M2 and M4, it may be quite possible that motif M1 may similarly recruit other sites in zyxin to the secondary EVH1 site, or that it itself might interact with the secondary site. Indeed, when we produced a truncated version of zyxin that did not contain the fourth binding motif, (zyxin^{41-108, F104A}) and added it to ¹⁵N-labeled EVH1 domain, the secondary site responded similarly to the longer zyxin⁴¹⁻¹⁴⁰ construct (data not shown). This suggests that either motif M3 is more central to the secondary interaction, or alternatively that additional binding orientations involving motif M1 remain to be characterized. Future work should also be done to assign the EVH1 Y39D mutant in order to confirm that it is impaired for binding in the secondary site as the data suggests.

In conclusion, we have identified and characterized a noncanonical binding site on the VASP-EVH1 domain and shown that it binds the third and fourth VASP-

binding motifs of zyxin. We show that this interaction occurs in the context of the full VASP-binding region (zyxin⁴¹⁻¹⁴⁰) but only very weakly for a shorter sequence (zyxin⁹⁹⁻¹²³), suggesting that binding of zyxin's motif M2 at the primary site of the EVH1 domain is important for this secondary interaction. We further show that the Y39D mutant, which mimics the effect of Abl-mediated phosphorylation of Y39 (Maruoka et al., 2012), shows impaired or abolished capacity to participate in this secondary interaction. However, we have not shown whether or not disruption of this secondary binding interaction is enough to significantly decrease the overall affinity of VASP-EVH1/zyxin binding *in vitro*, which could help explain the reported cellular impact of Y39 phosphorylation. Future work should address this question.

REFERENCES

- Ahern-Djamali, S.M., Comer, A.R., Bachmann, C., Kastenmeier, A.S., Reddy, S.K., Beckerle, M.C., Walter, U., and Hoffmann, F.M. (1998). Mutations in *Drosophila* enabled and rescue by human vasodilator-stimulated phosphoprotein (VASP) indicate important functional roles for Ena/VASP homology domain 1 (EVH1) and EVH2 domains. *Mol Biol Cell* *9*, 2157-2171.
- Ball, L.J., Kuhne, R., Hoffmann, B., Hafner, A., Schmieder, P., Volkmer-Engert, R., Hof, M., Wahl, M., Schneider-Mergener, J., Walter, U., *et al.* (2000). Dual epitope recognition by the VASP EVH1 domain modulates polyproline ligand specificity and binding affinity. *EMBO J* *19*, 4903-4914.
- Barzik, M., Kotova, T.I., Higgs, H.N., Hazelwood, L., Hanein, D., Gertler, F.B., and Schafer, D.A. (2005). Ena/VASP proteins enhance actin polymerization in the presence of barbed end capping proteins. *J Biol Chem* *280*, 28653-28662.
- Bear, J.E., and Gertler, F.B. (2009). Ena/VASP: towards resolving a pointed controversy at the barbed end. *J Cell Sci* *122*, 1947-1953.
- Bear, J.E., Loureiro, J.J., Libova, I., Fassler, R., Wehland, J., and Gertler, F.B. (2000). Negative regulation of fibroblast motility by Ena/VASP proteins. *Cell* *101*, 717-728.
- Bear, J.E., Svitkina, T.M., Krause, M., Schafer, D.A., Loureiro, J.J., Strasser, G.A., Maly, I.V., Chaga, O.Y., Cooper, J.A., Borisy, G.G., and Gertler, F.B. (2002). Antagonism between Ena/VASP proteins and actin filament capping regulates fibroblast motility. *Cell* *109*, 509-521.
- Bhatt, A., Kaverina, I., Otey, C., and Huttenlocher, A. (2002). Regulation of focal complex composition and disassembly by the calcium-dependent protease calpain. *J Cell Sci* *115*, 3415-3425.
- Breitsprecher, D., Kieseewetter, A.K., Linkner, J., Urbanke, C., Resch, G.P., Small, J.V., and Faix, J. (2008). Clustering of VASP actively drives processive, WH2 domain-mediated actin filament elongation. *EMBO J* *27*, 2943-2954.
- Breitsprecher, D., Kieseewetter, A.K., Linkner, J., Vinzenz, M., Stradal, T.E., Small, J.V., Curth, U., Dickinson, R.B., and Faix, J. (2011). Molecular mechanism of Ena/VASP-mediated actin-filament elongation. *EMBO J* *30*, 456-467.
- Call, G.S., Chung, J.Y., Davis, J.A., Price, B.D., Primavera, T.S., Thomson, N.C., Wagner, M.V., and Hansen, M.D. (2011). Zyxin phosphorylation at serine 142 modulates the zyxin head-tail interaction to alter cell-cell adhesion. *Biochem Biophys Res Commun* *404*, 780-784.
- Callebaut, I., Cossart, P., and Dehoux, P. (1998). EVH1/WH1 domains of VASP and WASP proteins belong to a large family including Ran-binding domains of the RanBP1 family. *FEBS Lett* *441*, 181-185.
- Chan, C.B., Liu, X., Tang, X., Fu, H., and Ye, K. (2007). Akt phosphorylation of zyxin mediates its interaction with acinus-S and prevents acinus-triggered chromatin condensation. *Cell Death Differ* *14*, 1688-1699.
- Coppolino, M.G., Krause, M., Hagendorff, P., Monner, D.A., Trimble, W., Grinstein, S., Wehland, J., and Sechi, A.S. (2001). Evidence for a molecular complex consisting of Fyb/SLAP, SLP-76, Nck, VASP and WASP that links the actin cytoskeleton to Fcgamma receptor signalling during phagocytosis. *J Cell Sci* *114*, 4307-4318.
- Geese, M., Loureiro, J.J., Bear, J.E., Wehland, J., Gertler, F.B., and Sechi, A.S.

(2002). Contribution of Ena/VASP proteins to intracellular motility of listeria requires phosphorylation and proline-rich core but not F-actin binding or multimerization. *Mol Biol Cell* *13*, 2383-2396.

Goh, K.L., Cai, L., Cepko, C.L., and Gertler, F.B. (2002). Ena/VASP proteins regulate cortical neuronal positioning. *Curr Biol* *12*, 565-569.

Haffner, C., Jarchau, T., Reinhard, M., Hoppe, J., Lohmann, S.M., and Walter, U. (1995). Molecular cloning, structural analysis and functional expression of the proline-rich focal adhesion and microfilament-associated protein VASP. *EMBO J* *14*, 19-27.

Hoffman, L.M., Jensen, C.C., Chaturvedi, A., Yoshigi, M., and Beckerle, M.C. (2012). Stretch-induced actin remodeling requires targeting of zyxin to stress fibers and recruitment of actin regulators. *Mol Biol Cell* *23*, 1846-1859.

Krause, M., Dent, E.W., Bear, J.E., Loureiro, J.J., and Gertler, F.B. (2003). Ena/VASP proteins: regulators of the actin cytoskeleton and cell migration. *Annu Rev Cell Dev Biol* *19*, 541-564.

Lebrand, C., Dent, E.W., Strasser, G.A., Lanier, L.M., Krause, M., Svitkina, T.M., Borisy, G.G., and Gertler, F.B. (2004). Critical role of Ena/VASP proteins for filopodia formation in neurons and in function downstream of netrin-1. *Neuron* *42*, 37-49.

Maruoka, M., Sato, M., Yuan, Y., Ichiba, M., Fujii, R., Ogawa, T., Ishida-Kitagawa, N., Takeya, T., and Watanabe, N. (2012). Abl-1-bridged tyrosine phosphorylation of VASP by Abelson kinase impairs association of VASP to focal adhesions and regulates leukaemic cell adhesion. *Biochem J* *441*, 889-899.

Mejillano, M.R., Kojima, S., Applewhite, D.A., Gertler, F.B., Svitkina, T.M., and Borisy, G.G. (2004). Lamellipodial versus filopodial mode of the actin nanomachinery: pivotal role of the filament barbed end. *Cell* *118*, 363-373.

Moody, J.D., Grange, J., Ascione, M.P., Boothe, D., Bushnell, E., and Hansen, M.D. (2009). A zyxin head-tail interaction regulates zyxin-VASP complex formation. *Biochem Biophys Res Commun* *378*, 625-628.

Niebuhr, K., Ebel, F., Frank, R., Reinhard, M., Domann, E., Carl, U.D., Walter, U., Gertler, F.B., Wehland, J., and Chakraborty, T. (1997). A novel proline-rich motif present in ActA of *Listeria monocytogenes* and cytoskeletal proteins is the ligand for the EVH1 domain, a protein module present in the Ena/VASP family. *EMBO J* *16*, 5433-5444.

Peterson, F.C., Deng, Q., Zettl, M., Prehoda, K.E., Lim, W.A., Way, M., and Volkman, B.F. (2007). Multiple WASP-interacting protein recognition motifs are required for a functional interaction with N-WASP. *J Biol Chem* *282*, 8446-8453.

Reimer, U., Scherer, G., Drewello, M., Kruber, S., Schutkowski, M., and Fischer, G. (1998). Side-chain effects on peptidyl-prolyl cis/trans isomerisation. *J Mol Biol* *279*, 449-460.

Reinhard, M., Halbrugge, M., Scheer, U., Wiegand, C., Jockusch, B.M., and Walter, U. (1992). The 46/50 kDa phosphoprotein VASP purified from human platelets is a novel protein associated with actin filaments and focal contacts. *EMBO J* *11*, 2063-2070.

Rottner, K., Behrendt, B., Small, J.V., and Wehland, J. (1999). VASP dynamics during lamellipodia protrusion. *Nat Cell Biol* *1*, 321-322.

Smith, G.A., Theriot, J.A., and Portnoy, D.A. (1996). The tandem repeat domain in the *Listeria monocytogenes* ActA protein controls the rate of actin-based motility, the

percentage of moving bacteria, and the localization of vasodilator-stimulated phosphoprotein and profilin. *J Cell Biol* *135*, 647-660.

Smith, M.A., Blankman, E., Deakin, N.O., Hoffman, L.M., Jensen, C.C., Turner, C.E., and Beckerle, M.C. (2013). LIM domains target actin regulators paxillin and zyxin to sites of stress fiber strain. *PLoS One* *8*, e69378.

Smith, M.A., Blankman, E., Gardel, M.L., Luettjohann, L., Waterman, C.M., and Beckerle, M.C. (2010). A zyxin-mediated mechanism for actin stress fiber maintenance and repair. *Dev Cell* *19*, 365-376.

Tokuo, H., and Ikebe, M. (2004). Myosin X transports Mena/VASP to the tip of filopodia. *Biochem Biophys Res Commun* *319*, 214-220.

Vetter, I.R., Nowak, C., Nishimoto, T., Kuhlmann, J., and Wittinghofer, A. (1999). Structure of a Ran-binding domain complexed with Ran bound to a GTP analogue: implications for nuclear transport. *Nature* *398*, 39-46.

Volkman, B.F., Prehoda, K.E., Scott, J.A., Peterson, F.C., and Lim, W.A. (2002). Structure of the N-WASP EVH1 domain-WIP complex: insight into the molecular basis of Wiskott-Aldrich Syndrome. *Cell* *111*, 565-576.

Zimmermann, J., Labudde, D., Jarchau, T., Walter, U., Oschkinat, H., and Ball, L.J. (2002). Relaxation, Equilibrium Oligomerization, and Molecular Symmetry of the VASP (336-380) EVH2 Tetramer. *Biochemistry* *41*, 11143-11151.

CHAPTER 5

Complete Determination of the Pin1 Catalytic Domain Thermodynamic Cycle by NMR Lineshape Analysis²

Abstract

The phosphorylation-specific peptidyl-prolyl isomerase Pin1 catalyzes the isomerization of the peptide bond preceding a proline residue between *cis* and *trans* isomers. To best understand the mechanisms of Pin1 regulation, rigorous enzymatic assays of isomerization are required. However, most measures of isomerase activity require significant constraints on substrate sequence and only yield rate constants for the *cis* isomer, k_{cat}^{cis} and apparent Michaelis constants, K_M^{App} . By contrast, NMR lineshape analysis is a powerful tool for determining microscopic rates and populations of each state in a complex binding scheme. The isolated catalytic domain of Pin1 was employed as a first step towards elucidating the reaction scheme of the full-length enzyme. A 24-residue phosphopeptide derived from the amyloid precursor protein intracellular domain (AICD) phosphorylated at Thr668 served as a biologically-relevant Pin1 substrate. Specific ^{13}C labeling at the Pin1-targeted proline residue provided multiple reporters sensitive to individual isomer binding and on-enzyme catalysis. We have performed titration experiments and employed lineshape analysis of phosphopeptide ^{13}C - ^1H constant time HSQC spectra to determine k_{cat}^{cis} , k_{cat}^{trans} , K_D^{cis} , and K_D^{trans} for the catalytic domain of Pin1 acting on this AICD substrate. The on-enzyme equilibrium value of $[\text{E}\cdot\text{trans}]/[\text{E}\cdot\text{cis}] = 3.9$ suggests that the catalytic domain of Pin1 is optimized to operate on this substrate near equilibrium in the cellular context. This highlights the power of lineshape analysis for determining the microscopic parameters of enzyme catalysis, and demonstrates the feasibility of future

² Reprinted with kind permission from Springer, *Journal of Biomolecular NMR*, 2011, volume 51, pages 21-34, "Complete determination of the Pin1 catalytic domain thermodynamic cycle by NMR lineshape analysis" by Alexander I. Greenwood, Monique J. Rogals, Soumya De, Kun Ping Lu, Evgenii L. Kovrigin, and Linda K. Nicholson.

studies of Pin1-PPIase mutants to gain insights on the catalytic mechanism of this important enzyme.

Introduction

Peptidyl-prolyl isomerases, or PPIases, are enzymes that catalyze the isomerization of the peptide bond preceding a proline residue (Fischer and Aumüller, 2003). The peptide bond between the amide nitrogen and the carbonyl carbon of the preceding residue is typically in the *trans* ($\omega = 180$) configuration (Fanghanel, 2003). However, in the case of the peptide bond preceding a proline residue, the *cis* isomer ($\omega = 0$) often exists in equilibrium with *trans* (Fanghanel, 2003). In the absence of stable tertiary structure, such as in short peptides, the population of the *cis* isomer can be between approximately 5% and 40%, depending on sequence (Reimer et al., 1998). Structure or protein-protein interactions can stabilize one isomer preferentially, often leading to nearly either 0% (Ramelot et al., 2000) or 100% *cis* (Sarkar et al., 2011). Prolyl isomerases can be important for facilitating catalysis by isomer-specific enzymes, and are thought to play an important role in facilitating binding by proteins which recognize only one of the isomers. The importance of this activity is highlighted in the example of dephosphorylation of the Ser(P)⁵-Pro⁶ motif in the heptad repeats of the C-terminal domain (CTD) of RNA polymerase II (Meinhart and Cramer, 2004; Xiang et al., 2010). This dephosphorylation is performed by the Proline-directed phosphatase Ssu72 which binds specifically to the lower populated *cis* isomer of the substrate (Werner-Allen et al., 2011; Xiang et al., 2010). Because phosphorylation and dephosphorylation of the CTD occur on the same timescale as transcription (milliseconds to seconds) (Skinner et al., 2004), isomerization by the PPIase Pin1 is necessary to allow Ssu72-mediated dephosphorylation to proceed to completion on the proper timescale. This principle applies similarly to *trans*-specific phosphatases such

as PP2A (Zhou et al., 2000), though the impact of Pin1 activity is presumably most pronounced if there is a substantial population of *cis* isomer to be converted.

Pin1 is the only PPIase in humans that is specific for pSer/pThr-Pro motifs (Lu et al., 1996; Ranganathan et al., 1997). While uncatalyzed inter-conversion between *cis* and *trans* isomers occurs naturally with a half-life on the order of 100 s (Grathwohl and Wüthrich, 1981), the presence of Pin1 can speed this exchange by orders of magnitude into the more biologically relevant timescale of milliseconds. Notably, aberrant function of Pin1 is implicated in cancer (Lu et al., 2006), asthma (Anderson, 2005), and Alzheimer's disease (AD) (Pastorino et al., 2006). Although Pin1 is a much-studied enzyme, we lack a detailed understanding of the actual significance of its isomerase activity towards its most-studied substrates, such as the microtubule-associated protein Tau or the amyloid precursor protein (APP), which are involved in Alzheimer's disease. In the case of APP, Pin1 knockout shifts the proteolytic processing fate of APP towards the amyloidogenic pathway in cell culture and mouse models (Pastorino et al., 2006). This may contribute to Pin1's established protective role against neurodegeneration (Meraz-Rios, 2010; Pastorino et al., 2006). Pin1 binds to and specifically catalyzes isomerization of the pT668-P669 motif in APP *in vitro* (Pastorino et al., 2006), suggesting that the mechanism of Pin1's action on APP processing *in vivo* involves isomerization at this motif (Iijima et al., 2000; Lee et al., 2003). Pin1 is comprised of two domains with similar specificity, a catalytic PPIase domain (hereafter referred to as Pin1-PPIase) and a type IV WW binding domain (Verdecia et al., 2000). While essential for Pin1 function *in vivo* (Lu et al., 2002), the WW domain does not improve catalytic function *in vitro* on phosphopeptide substrates (Eckerdt et al., 2005; Peng et al., 2009; Rippmann et al., 2000). Hence, as an important step toward understanding a key molecular switch involved in the development of AD, focus on the isolated Pin1-PPIase domain avoids substrate competition with the WW

domain and provides the opportunity to obtain a complete description of its catalytic reaction scheme.

Assays of isomerase activity (Fischer et al., 1984; Fischer et al., 1983; Lin and Brandts, 1985) commonly employ an isomer-specific protease such as chymotrypsin, which only cleaves after aromatic residues following a residue preceded by a *trans* peptide bond (Xaa-*trans*-Xaa-Yaa-Xaa, where Yaa is aromatic and Xaa is any amino acid). By coupling the reversible isomerization reaction with the essentially irreversible cleavage of the peptide bond, assays can indirectly measure conversion of *cis* to *trans* by a PPIase by monitoring the cleavage reaction. This is accomplished by incorporating the chromogenic compound p-nitroanilide (pNA) after the cleavage site (most commonly Xaa-Pro-Phe-pNA) and monitoring the change in fluorescence upon release of the pNA. This approach therefore does not allow for much variation in the sequence of the substrate C-terminal to the isomerized proline residue. Furthermore, it can only report on the *cis*-to-*trans* rate constant, k_{cat}^{cis} , and an “apparent” Michaelis constant, K_M^{App} , which is a composite of the binding constants for the *trans* and *cis* conformers. Other problems with this type of assay include the tendency of proteases to degrade the isomerase, and the likely possibility that cleavage of the substrate affects the value of K_M^{App} . Other approaches have employed solvent jumps to perturb the equilibrium of *cis* and *trans* populations of substrates and monitor the return to equilibrium via UV absorption, exploiting the small differences in UV absorption between the *cis* and *trans* isomers (Garcia-Echeverria et al., 1992; Garcia-Echeverria et al., 1993). This, however, imposes similar restriction on substrate sequence because a UV-absorbing residue such as pNA must be located close to the isomerized peptide bond.

NMR provides direct observation of *cis* and *trans* isomers, which due to their slow timescale of interconversion can be identified as distinct resonances. NMR is

therefore another popular tool used for the study of prolyl isomerization, and had in fact been used to measure intrinsic uncatalyzed isomerization in short peptides prior to the discovery of prolyl isomerases (Grathwohl and Wüthrich, 1981). Unlike most other approaches, NMR experiments have the ability to measure isomerization at chemical equilibrium, removing the need to perturb the *cis-trans* equilibrium and take time-resolved datasets. CPMG (Korzhnev and Kay, 2008) or R1 ρ (Massi et al., 2004) experiments can measure the catalyzed rate of exchange as well as the rates and populations of on-enzyme motions. EXSY (Landrieu et al., 2000) and ROESY (Pastorino et al., 2006) experiments have been used to measure the rate of interconversion between two slowly-exchanging states. However, even in routine HSQC (Mulder et al., 1996) spectra, the supreme sensitivity of NMR line shapes to the kinetics and equilibria of individual reaction steps in a complex multi-state scheme is apparent. For complex systems in which multiple states are at equilibrium, NMR lineshape analysis provides a powerful tool with which to determine the microscopic kinetic rates and equilibrium constants connecting the different states in the reaction scheme, complementing these techniques.

The detailed analysis of NMR line shapes is a well-established but underutilized tool for examining protein interactions and motions that occur within the microsecond to millisecond timescale (Gunther and Schaffhausen, 2002; Kern et al., 1995; Kovrigin and Loria, 2006). The processes of ligand binding and release, conformational exchange, and enzymatic turnover can all occur on this timescale (Mittermaier and Kay, 2009a). While classically applied to 1D NMR spectra, lineshape analysis is easily applied to 2D spectra by peak slice extraction. NMR lineshape broadening and changes in chemical shift in both dimensions of a series of HSQC spectra can yield information about kinetics, populations, and unobservable chemical shifts on a residue-specific basis (Gunther and Schaffhausen, 2002). Because

lineshape analysis uses data taken at multiple concentrations of interacting proteins, it is especially applicable to complex models with three, four, or more states (Gunther and Schaffhausen, 2002). Software has been developed to fit lineshape data to multiple, arbitrarily complex models, allowing easy comparisons between models (<http://lineshapekin.net/>, <http://biophysicslab.net/>). Simultaneously fitting data from multiple peaks can allow a global understanding of complex physical processes to emerge. In addition to ligand binding and protein dynamics (Craven et al., 1996; Johnson et al., 1998), lineshape analysis is applicable to the study of catalytic mechanisms and enzyme function, such as that of PPIases (Kern et al., 1995). The advantages of NMR lineshape analysis over standard biochemical isomerase assays lie in the ability to use the natural substrate sequence and the convenience of performing experiments at chemical equilibrium.

Here we present the complete characterization of the reaction scheme of Pin1-PPIase acting on the pT668-P669 motif in APP using NMR lineshape analysis. A specifically isotopically labeled (^{13}C - and ^{15}N) APP-derived phosphopeptide (pAPP659-682, corresponding to residues 659-682 of APP phosphorylated at T668) was titrated with unlabeled Pin1-PPIase, and the induced line broadening was fit to a four-state model (Figure 5.1A). NMR titration experiments using ^{15}N -labeled Pin1-PPIase and unlabeled pAPP659-682 allowed the measurement of the apparent dissociation constant K_D^{App} for the binding reaction, which was used as a constraint in the lineshape analysis. This K_D^{App} was in close agreement with that measured for full-length Pin1, indicating that the isolated Pin1-PPIase domain accurately represents the function of the intact enzyme under these conditions. Using lineshape analysis, the microscopic rates $k_{\text{cat}}^{\text{cis}}$ and $k_{\text{cat}}^{\text{trans}}$ of catalysis as well as isomer-specific dissociation constants K_D^{cis} and K_D^{trans} were determined. Moreover, ^1H - ^1H ROESY exchange experiments were employed to measure the overall rate of exchange k_{ex} for both Pin1-

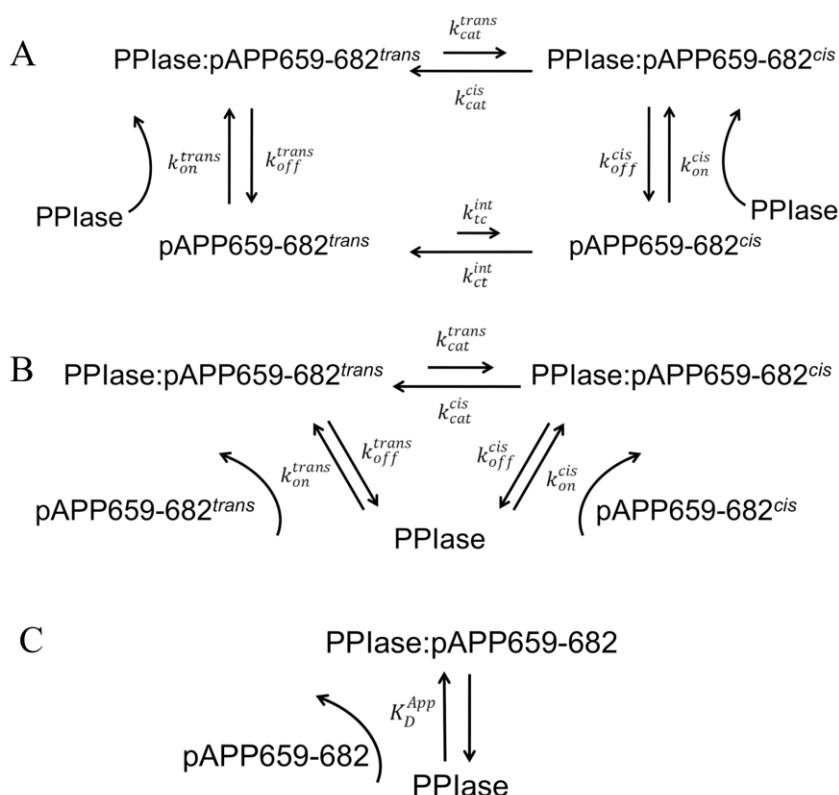


Figure 5.1: Models used to interpret NMR data. (A) Four state model for lineshape fitting of ^{13}C -pAPP659-682 peptide isomerization data. This model describes four states: the *cis* and *trans* isomers of the peptide in the free state, and the *cis* and *trans* isomers bound to the enzyme. (B) Three state model of PPlase catalysis for PPlase-perspective data. This model describes Pin1-PPlase catalysis as a three-state process in which the PPlase can bind to either the *cis* or *trans* isomer of the pAPP659-682 peptide. (C) Two-state approximation for PPlase-perspective titration data. Interpretation of peak positions with this model requires the approximation that exchange between the two bound states in the three-state model occurs on the fast chemical shift timescale. In this model the relative populations are described by a single parameter, the apparent dissociation constant K_D^{App} .

PPIase and full-length Pin1, providing independent validation of the lineshape-derived fitted parameters and further supporting the accurate representation of Pin1 catalytic function by the isolated PPIase domain. Interestingly, the on-enzyme equilibrium of *cis* and *trans* substrate was found to be skewed slightly in favor of *trans*, suggesting that Pin1 may be optimized to operate on this substrate slightly off-equilibrium.

Materials and Methods

Protein expression and purification

A pET vector [GE Health Sciences] imparting kanamycin resistance was used for recombinant Pin1-PPIase expression. This vector encodes a protein consisting of an N-terminal His tag and a TEV cut site followed by the PPIase domain of Pin1 (residues 46-163). Protein was expressed in BL21 star *E. Coli* [Invitrogen] cells grown in 1 L of either LB [BD] or M9 minimal media (using 19 mM $^{15}\text{NH}_4\text{Cl}$ [Isotec]) with 50 $\mu\text{g}/\text{ml}$ kanamycin [IBI Scientific]. Cultures were grown at 37°C to an O.D.₆₀₀ ~0.6, and expression was induced with 1 mM IPTG [CalBioChem] at 15°C for ~20 hours. Cells were then pelleted and resuspended in lysis buffer (50 mM Tris-Hcl [Mallinckrodt Baker], 200 mM NaCl [Mallinckrodt Baker], 10 mM Imidazole [Alfa Aesar], pH 8.0, plus 100 μl protease inhibitor [Sigma], 1 mM DTT [Gold Biotechnology]). Cells were then lysed by freezing and thawing on ice, adding 1 mg/ml lysozyme [EMD], and sonicating (10 cycles). Cells were then centrifuged at 23,000 g and the supernatant was filtered with a 0.8- μm syringe filter [Corning]. Filtrate was then applied to a nickel-NTA column [Qiagen] and washed with 20 bed volumes wash buffer (50 mM Tris-Hcl, 200 mM NaCl, 18 mM Imidazole, pH 8.0). Protein was then eluted with elution buffer (50 mM Tris-Hcl, 150 mM NaCl, 300 mM Imidazole, pH 8.0) and dialyzed into cleavage buffer (50 mM Tris-Hcl, pH 8.0). Recombinant His-tagged TEV protease was then added and the Pin1-PPIase was cleaved from the His-tag overnight at 4°C. The His-tagged TEV was then removed by

putting the cleavage reaction through a second Nickel-NTA column, and the flow-through containing pure Pin1-PPIase was dialyzed into NMR buffer (10 mM HEPES [Fisher, sodium salt], 1 mM DTT, pH 6.9). NMR samples also included 5 mM NaN_3 [Fisher], 1 mM TCEP [Thermo Scientific], and 7% D_2O [Cambridge Isotope Laboratories]. Protein was concentrated with VivaSpin-20 5000 MWC centrifugal concentrators [GE]. The concentration of Pin1-PPIase was measured by the UV absorbance spectrum, using the theoretical extinction coefficient at 280 nm of $7210 \text{ cm}^{-1}\text{M}^{-1}$. Protein purity was verified by SDS-PAGE. The pH of buffers and samples was adjusted using HCl [Mallinckrodt Baker] and NaOH [Sigma]. All peptides were synthesized using solid-phase F-moc chemistry at the Tufts University Core Facility, purified, and delivered as a lyophilized powder. Peptides were dissolved in NMR buffer (plus NaN_3 , TCEP and D_2O), de-salted using a PD MiniTrap gravity column [GE], and their pH adjusted with NaOH before use.

NMR experiments/Data processing

NMR experiments were performed at 25°C on a Varian Inova 600 MHz spectrometer equipped with a $\{\text{H,C,N}\}$ Z-axis gradient probe. Spectra were processed and analyzed using the software tools nmrPipe (Delaglio et al., 1995), nmrDraw (Delaglio et al., 1995), and Sparky (Goddard, 2008). Free induction decays were apodized using an exponential function to preserve the natural lorentzian lineshape, except for the ROESY data for which a phase-shifted sine bell function was used, and zero filled prior to Fourier transformation. Peak heights and positions were measured using the peak detection modules of nmrDraw or Sparky, respectively.

In titration experiments to measure K_D^{APP} , 12 mM pAPP659-682 was added to 0.25 mM ^{15}N -labeled Pin1-PPIase, and the peptide was reverse titrated from $\sim 12 \text{ mM}$ to $\sim 0.8 \text{ mM}$ by diluting with ^{15}N -labeled Pin1-PPIase. Titration points were taken at peptide concentrations of 12, 7, 4, 2, 0.8, and 0 mM. The concentration of peptide was

measured by UV absorbance based on the theoretical extinction coefficient of 1,209 $\text{cm}^{-1}\text{M}^{-1}$ at 280 nm. At each concentration, a two-dimensional ^{15}N - ^1H fast HSQC spectrum (Mulder et al., 1996) was taken with a spectral width of 1.7 kHz (8 kHz) in t_1 (t_2), and a total of 512 (2048) complex data points. A total of 40 scans were acquired per FID with a 1.0 s delay, for a total time per spectrum of 7 hrs.

For lineshape analysis titration experiments, ~1.0 mM unlabeled Pin1-PPIase was added to 0.7 mM labeled peptide and the protein was reverse titrated from 1.0 mM to 0.06 mM by diluting with labeled peptide. Titration points were taken at enzyme concentrations of 1, 0.5, 0.25, 0.1, 0.06, and 0 mM. At each concentration, a two-dimensional ^{13}C - ^1H constant-time (constant time delay of 27 ms) HSQC spectrum (Vuister and Bax, 1992) was taken with a spectral width of 5.5 kHz (8 kHz) in t_1 (t_2), and a total of 256 (2048) complex data points. A total of 88 scans were acquired per FID with a with a repetition delay of 1.0 s, for a total time per spectrum of 7.5 hrs. Constant-time spectra were taken to prevent splitting in the carbon dimension. Wrapping the alpha and delta peaks in the ^{13}C dimension allowed for a smaller window with still well-resolved peaks. The ^{13}C time domain was extended to 512 points by mirror-image linear prediction prior to zero filling.

For rate measurements, 3 mM of peptide was dissolved in NMR buffer and a catalytic amount of Pin1-PPIase (50 μM) was added. The rate of interconversion between the *cis* and *trans* isomers was measured by taking a series of ROESY (Bax and Davis, 1985) spectra with varying mixing times. The rate measurement was taken with mixing times of 0, 0.01, 0.02, 0.04, 0.06 0.08, 0.10, 0.15, and 0.20 s. Spectral widths used were 6 kHz in both dimensions, using a total of 192 complex data points in t_1 and 2048 in t_2 . A total of 52 scans per FID were acquired with a recycle delay of 1.0 s, for a total acquisition time of 64 hrs.

Data fitting

ROESY peak heights for autopeaks and crosspeaks corresponding to the amide proton of E670 were obtained using Sparky processing software after baseline correction using a Gaussian fit (Goddard, 2008). Peak heights were fit to the two-state solution to the Bloch-McConnell equations (Cavanagh, 2007; McConnell, 1958) by least-squares minimization using the Solver function in Microsoft Excel. Fixed parameters included the transverse relaxation constants for the *cis* and *trans* isomers, $R_{2,0}^{trans}$ and $R_{2,0}^{cis}$ determined independently by running the ROESY experiment without enzyme present, and the ratio of *trans* isomer to *cis* isomer, K_{eq} , determined independently by comparing peak volumes of the two isomers. The *cis* autopeak was broadened significantly relative to the *trans* autopeak upon addition of Pin1-PPIase due to the high rate of isomerization. To accommodate this, the data was fit using an additional fitted parameter, I_{tc}^0 , which scales the intensity of the *trans*-to-*cis* cross-peak. Other fitted parameters included the initial intensities of autopeaks, I_{tt}^0 and I_{cc}^0 , and the overall rate of isomerization, k_{ex} . Errors were determined by Monte Carlo analysis, using the noise of the spectrum as experimental error and fitting in Matlab 2010a.

Lineshape fitting was performed using the *BiophysicsLab* Matlab package (Kovrigin, E.L., manuscript in preparation, <http://biophysicslab.net>). *BiophysicsLab* fits data extracted as 1D slices from Sparky (Goddard, 2008) using a custom Python extension *BiophysicsLab 1DNMR*. ^1H -dimension slices from *cis* and *trans* peaks of the ^{13}C -labeled phosphopeptide were extracted separately and normalized by the area under each peak to correct for broadening in the ^{13}C dimension. *Cis* and *trans* datasets were then added together (weighting appropriately) before lineshape fitting. Data was fit to the four-state reaction scheme in Figure 5.1, which considers both the free and bound states of both isomers.

Fitted parameters included the on-enzyme equilibrium constant (K_{eq}^{bound}), the on-enzyme catalysis rate from *trans*-to-*cis* (k_{cat}^{trans}), and the chemical shifts of the proline resonances in the bound peptide (ν_{bound}^{trans} and ν_{bound}^{cis}). Constrained parameters included the apparent dissociation constant (K_D^{App}), the equilibrium constant for the *cis* and *trans* isomers of the free peptide (K_{eq}), the intrinsic (uncatalyzed) rate from *trans*-to-*cis* (k_{tc}^{int}) obtained by measuring isomer-specific binding kinetics (unpublished data), the chemical shifts (ν_{free}^{trans} and ν_{free}^{cis}) and linewidths ($R_{2,0}^{free}$) of the proline resonances in the free peptide, and the small ^1H - ^1H J-couplings between proline ring protons (J_{HH}^i). Because the parameters K_{eq} , ν_{bound}^{trans} , ν_{bound}^{cis} and $R_{2,0}^{free}$ are intrinsic to the free peptide, and easily measured using only the apo spectrum, these parameters were fit once from the apo spectrum and held constant during lineshape fitting. The numerous couplings between proline protons, J_{HH}^i , are available in the literature (Aliev and Courtier-Murias, 2007) and thus held constant. The parameters K_D^{App} and k_{tc}^{int} were not deemed to be reliably extractable parameters from the lineshape titration data, and so were obtained using independent experiments (enzyme-perspective titration, below, and binding kinetics, data not shown). Likewise, the contributions to the apparent transverse relaxation rates of resonances from the bound peptide not due to exchange ($R_{2,0}^{bound}$) and the reverse binding rate constants k_{off}^{cis} and k_{off}^{trans} were not deemed to be reliably extractable parameters, so rather than fitting for them they were constrained and systematically varied to assess the impact of their values on the results and quality of the fit, as discussed in results and discussion as well as the appendix (Appendix Table 5.1).

BiophysicsLab fits titration lineshape data with the Bloch-McConnell equations in the following way: the population column vector \mathbf{P} (equation 5.1A), which describes the populations of the four states (p_i ; free *cis*, free *trans*, bound *cis* and bound *trans*), is calculated for each spectrum using the thermodynamic parameters

K_D^{App} , K_{eq} , and K_{eq}^{bound} , and the total enzyme/peptide concentrations at each titration point (Appendix Equations 5.1-5.3). The rate matrix, which describes the equilibrium rate equations for the four species, is then calculated for each spectrum using the calculated population of free Pin1-PPIase ($PPIase^{free}$) (equation 5.1B). The first-order rates for binding and isomerization are featured in the diagonal and off-diagonal elements of the rate matrix. The chemical shifts (ν_i) of each of the four states appear as the diagonal elements of a square matrix (equation 5.1C, term 2). Likewise, the apparent transverse relaxation rates of resonances not due to exchange ($R_{2,0}^i$) appear in a second matrix (equation 5.1C, term 1), and the frequency variable ν appears in a third (equation 5.1D). The simulated spectrum is given by equation 5.1E in the absence of three-bond proton coupling. To account for the small scalar coupling between proline ring protons, the final simulated spectrum was expressed as a sum of lorentzians that took the form of equation 5.1E with various small offsets in ν according to the scalar coupling constants reported in the literature (Aliev and Courtier-Murias, 2007) (Appendix equations 5.4 and 5.5 and Appendix Table 5.2). This classical approach is justified if scalar couplings are small compared to natural linewidths and exchange rates, as they are here (discussed in detail in Appendix).

$$\mathbf{P} = \begin{pmatrix} p_1 \\ p_2 \\ p_3 \\ p_4 \end{pmatrix} = \begin{pmatrix} [pAPP659-682^{cis}] \\ [pAPP659-682^{trans}] \\ [PPIase : pAPP659-682^{cis}] \\ [PPIase : pAPP659-682^{trans}] \end{pmatrix} \quad (5.1A)$$

$$\mathbf{k} = \begin{pmatrix} -(k_{ct}^{int} + k_{on}^{cis} \cdot PPIase^{free}) & k_{tc}^{int} & k_{off}^{cis} & 0 \\ k_{ct}^{int} & -(k_{tc}^{int} + k_{on}^{trans} \cdot PPIase^{free}) & 0 & k_{off}^{trans} \\ k_{on}^{cis} \cdot PPIase^{free} & 0 & -(k_{cat}^{cis} + k_{off}^{cis}) & k_{cat}^{trans} \\ 0 & k_{on}^{trans} \cdot PPIase^{free} & k_{cat}^{cis} & -(k_{cat}^{trans} + k_{off}^{trans}) \end{pmatrix} \quad (5.1B)$$

$$\mathbf{M}_1 = \begin{pmatrix} R_{2,0}^1 & 0 & 0 & 0 \\ 0 & R_{2,0}^2 & 0 & 0 \\ 0 & 0 & R_{2,0}^3 & 0 \\ 0 & 0 & 0 & R_{2,0}^4 \end{pmatrix} - 2\pi i \begin{pmatrix} \nu_1 & 0 & 0 & 0 \\ 0 & \nu_2 & 0 & 0 \\ 0 & 0 & \nu_3 & 0 \\ 0 & 0 & 0 & \nu_4 \end{pmatrix} - \mathbf{k} \quad (5.1C)$$

$$\mathbf{M}_2 = 2\pi i \nu \begin{pmatrix} 1 & 0 & 0 & 0 \\ 0 & 1 & 0 & 0 \\ 0 & 0 & 1 & 0 \\ 0 & 0 & 0 & 1 \end{pmatrix} \quad (5.1D)$$

$$S_1(\nu) = \text{SF} \cdot \text{Re} \left(\left([1 \quad 1] (\mathbf{M}_1 + \mathbf{M}_2)^{-1} \mathbf{P} \right) \right) \quad (5.1E)$$

Fitting was performed using the truncated Newton interior-point method (Kim et al., 2007) in Matlab 2010a. The quality of the fit was assessed by calculating the sum of squares of residuals, which are normalized by the square of the RMS noise of each spectrum. Fit results were insensitive to the starting values of fit parameters, indicating that in all cases a true minimum was reached. As errors we report the variations in the fitted parameters from varying K_D^{App} within its standard deviation of measurement of 0.3 mM. Uncertainty in K_D^{App} was deemed the largest single source of uncertainty in the fit, as varying other constrained parameters or the experimental data itself within their uncertainties did not impact the fit as much (Appendix Table 5.1).

Results and Discussion

Measurement of K_D^{App} by NMR titration experiments

The Pin1-PPIase/pAPP659-682 interaction from the substrate perspective is represented by a four-state binding scheme (Figure 5.1A) that is described by seven independent rate, equilibrium, or binding constants. In order to minimize the number of fitted parameters in the linshape analysis, the overall apparent binding constant (K_D^{App}) of Pin1-PPIase and pAPP659-682 was measured using a chemical shift

perturbation approach in an independent experiment. Since the binding of Pin1-PPIase to the pAPP659-682 peptide is very weak ($K_D^{App} \sim 1$ mM), it was not possible to reliably measure the binding constant from substrate-perspective titration data due to the limited solubility of Pin1-PPIase. Therefore, the apparent affinity was measured from the perspective of the ^{15}N -labeled Pin1-PPIase domain. Pin1-PPIase exchanges between three states (free, *cis*-bound and *trans*-bound) during catalysis (Figure 5.1B). However, approximation of the Pin1-PPIase interaction with the peptide substrate as a two-state (free and bound) exchange process with an equivalent K_D^{App} (Figure 5.1C) is reasonable if exchange between the bound *cis* and bound *trans* states is fast on the chemical shift timescale. A series of ^{15}N - ^1H HSQC spectra of 0.25 mM ^{15}N -labeled Pin1-PPIase was acquired while titrating with unlabeled pAPP659-682 peptide (soluble up to at least 12 mM). Backbone amide resonances moved progressively during the titration and followed a single trajectory rather than splitting into two peaks (Figure 5.2), justifying the two-state approximation (Figure 5.1C). The chemical shifts of selected residues were fit to the equation for fast exchange ($k_{on} + k_{off} \gg \Delta\omega$) between two states:

$$\Delta\omega = \Delta\omega^{max} \frac{K_D^{App} + [P] + [L] - \sqrt{(K_D^{App} + [P] + [L])^2 - 4[P][L]}}{2[P]} \quad (5.2)$$

where [P] refers to the PPIase enzyme concentration, [L] refers to the pAPP659-682 peptide concentration, and $\Delta\omega$ is the composite chemical shift perturbation which is given by (Ayed et al., 2001; Mulder et al., 1999)

$$\Delta\omega = \sqrt{(\omega_H - \omega_H^{Apo})^2 + (0.154 \cdot (\omega_N - \omega_N^{Apo}))^2} \quad (5.3)$$

Residues that provided the best fits were in close agreement with each other, yielding a K_D^{App} of 1.3 ± 0.3 mM, where error is the standard deviation across 10 individually fit peak walks (Figure 5.3A). A global fit of the same 10 residues also yielded an

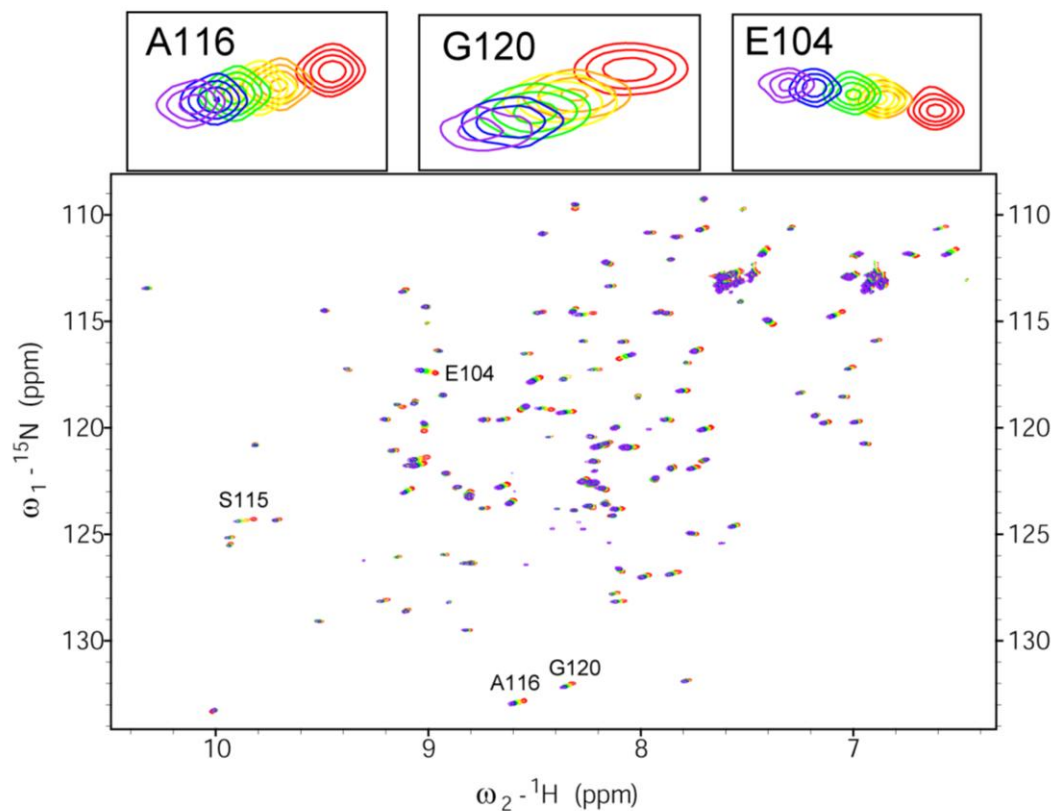


Figure 5.2: Chemical shift perturbation of ^{15}N -labeled Pin1-PPIase upon titration with unlabeled pAPP659-682 peptide. Overlay of ^{15}N - ^1H HSQC spectra of 0.25 mM Pin1-PPIase with varying amounts of unlabeled pAPP659-682 peptide, from 0 mM (red) to 12 mM (purple). Expanded regions (*above*) show example peak trajectories used in the determination of K_D^{App} .

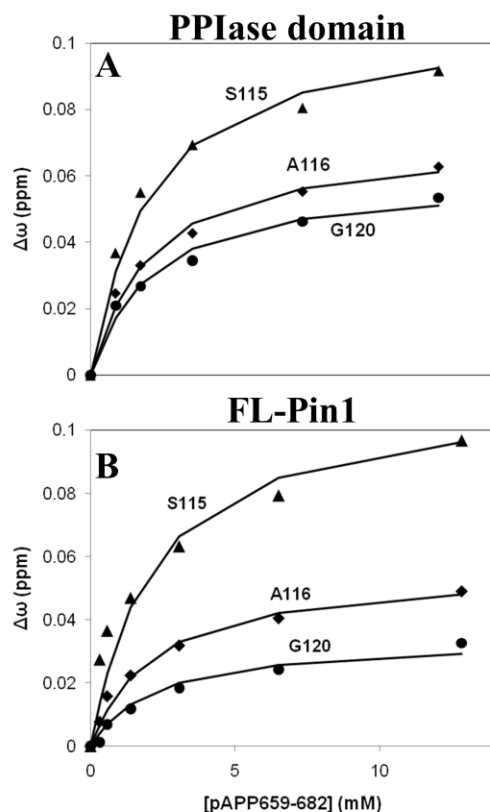


Figure 5.3: Overall binding constant of Pin1 for pAPP659-682 is approximately independent of the presence of the WW domain. To measure the apparent ligand binding affinity, K_D^{App} , ^{15}N -labeled PPIase domain (A) or full-length Pin1 (B) were titrated with the APP-derived phosphopeptide pAPP659-682 and a series of 2D ^{15}N – ^1H HSQC spectra were acquired. The chemical shift perturbation, $\Delta\omega$ (see main text), is plotted for a subset of residues that were used to determine K_D^{App} for each protein.

identical K_D^{App} of 1.3 mM. This dissociation constant represents a weighted sum of the binding affinities for each isomer, *cis* and *trans*, of the substrate peptide:

$$K_D^{App} = \frac{K_{eq} + 1}{\frac{K_{eq}}{K_D^{trans}} + \frac{1}{K_D^{cis}}} \quad (5.4)$$

where $K_{eq} = 13.6 \pm 0.7$ is the ratio of free *trans* isomer to free *cis* isomer, as determined from the ratio of [*trans* peak/*cis* peak] volumes in a ^{13}C - ^1H HSQC spectrum of pAPP659-682 (error is standard deviation across three sets of peaks). The K_D^{App} of 1.3 mM provides a useful constraint on the fitted parameters K_D^{trans} and K_D^{cis} accessible from lineshape analysis as described below.

In order to assess the pertinence of using the isolated PPIase domain as a model to study Pin1 activity, this analysis was repeated with labeled full-length Pin1 (Figure 5.3B). In this case, individual fitting of 7 residues yielded a $K_D^{App, PPIase}$ of 2.2 ± 1.3 mM, while a global fit yielded $K_D^{App, PPIase} = 1.5$ mM. Because the corresponding values in full-length-Pin1 and isolated PPIase are within error of each other, as well as the close correspondence of the globally fit values, we concluded that Pin1-PPIase binding to pAPP659-682 is essentially independent of the presence of the WW domain under the experimental conditions used.

Lineshape analysis yields kinetic rates and equilibrium constant for Pin1-PPIase isomerization of pAPP659-682

The kinetic rates and equilibrium constants describing catalysis by the Pin1 PPIase domain acting on the pT668-P669 motif were next extracted from the lineshapes of nuclei on the pAPP659-682 phosphopeptide substrate. Although measuring dynamics from the perspective of a saturated enzyme provides a wealth of information about enzyme function and mechanisms, the acquired data can be ambiguous to interpret. Enzyme-perspective dynamics can represent substrate turnover, but they can also represent numerous other exchange processes, related or

not related to catalysis (Bosco et al., 2010). Furthermore, depending on the catalytic mechanism and the timescale of substrate binding, resonances from enzyme nuclei may not be sensitive to the actual process of substrate turnover. For these reasons, we sought to measure catalysis by the Pin1 PPIase domain primarily by considering the lineshapes of nuclei on the substrate, which exchange between four states (free *cis*, free *trans*, bound *cis* and bound *trans*, Figure 5.1A). This approach provides the most direct measure of the actual catalytic activity, although it does not by itself provide information about the various residues and motions in the enzyme that contribute to catalysis as enzyme-perspective analysis can (Labeikovsky et al., 2007). We utilized a specifically labeled phosphopeptide, identical to pAPP659-682 but ^{13}C and ^{15}N labeled at Pro669 (^{13}C -pAPP659-682). A constant-time ^1H - ^{13}C HSQC of ^{13}C -pAPP659-682 contains peaks corresponding to the alpha proton as well as the two beta, two gamma, and two delta protons of the proline ring (Figure 5.4). Each proton yielded two peaks, a large peak corresponding to the *trans* isomer and a smaller peak corresponding to the *cis* isomer. With the exception of the gamma protons, which have overlap in their *trans* isomer peaks, and the delta protons, which have overlap in their *cis* isomer peaks, these peaks are well-resolved from each other. The generally large chemical shift differences between the *cis* and *trans* isomer resonances (e.g. ~0.5 ppm in the ^1H dimension for the alpha proton) ensure that their linewidths are particularly sensitive to catalyzed exchange between the two states on the second-to-millisecond timescale. Furthermore, the presence of five sets of well-resolved peaks associated with the major *trans* population ($\text{H}\alpha$, $\text{H}\beta 1$, $\text{H}\beta 2$, $\text{H}\delta 1$, $\text{H}\delta 2$) allows for a global analysis, which can yield a much more reliable fit than analysis of a single pair of resonances.

The four-state binding scheme for the Pin1-PPIase/pAPP659-682 interaction (Figure 5.1A) is described by three independent equilibrium or binding constants (the ratio of the *trans* to *cis* isomers of the free peptide, $K_{eq} = k_{et}^{\text{int}} / k_{tc}^{\text{int}}$, the on-enzyme

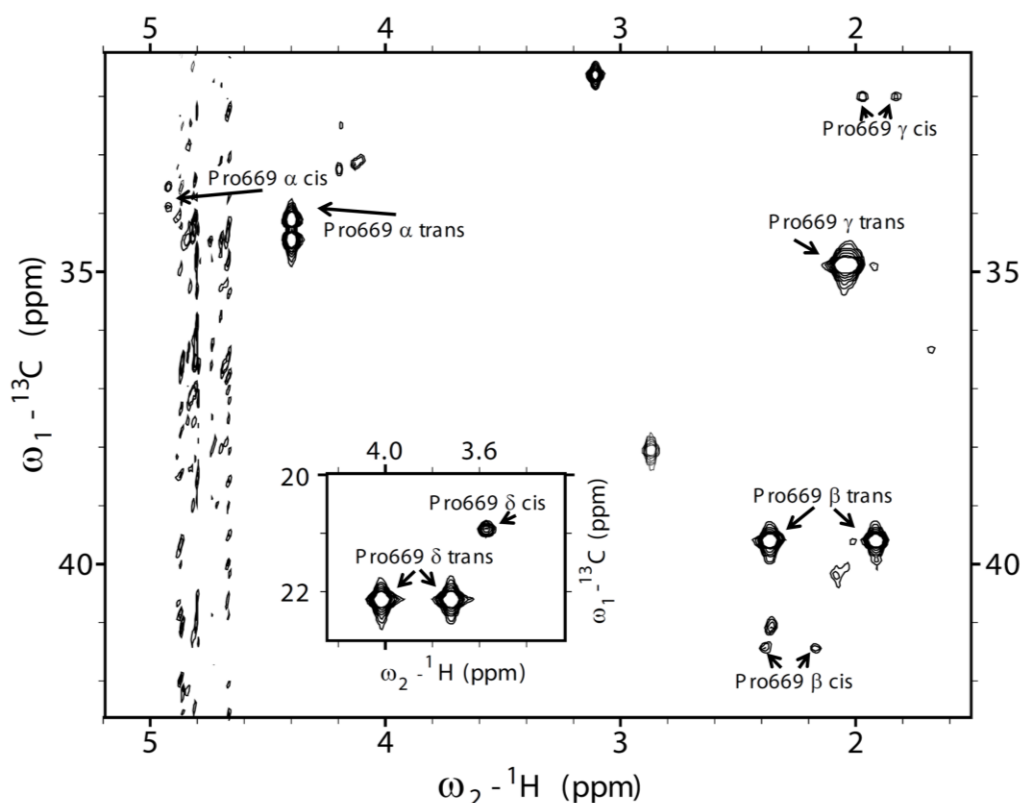


Figure 5.4: ^{13}C - ^1H constant-time HSQC spectrum of specifically labeled ^{13}C -pAPP659-682 peptide. A ^{13}C - ^1H constant-time HSQC (constant time delay of 27 ms) of the APP-derived phosphopeptide ^{13}C -pAPP659-682, specifically ^{13}C labeled on Proline 669, yields a spectrum with peaks corresponding to the proline sidechain protons in both the *trans* and *cis* conformations. Both negative (alpha, delta protons) and positive (gamma, beta protons) peaks are shown in black. The alpha proton peaks are split in the carbon dimension due to coupling with the ^{13}C -labeled carbonyl carbon. The *trans* peaks of the gamma protons were found to overlap, and therefore were not considered in the lineshape analysis. (*inset*) Delta proton peaks.

equilibrium constant, $K_{eq}^{bound} = k_{cat}^{cis} / k_{cat}^{trans}$, and the overall apparent binding constant K_D^{App} , as defined in Equation 5.4) as well as four independent rate constants (the uncatalyzed and catalyzed conversion rates from *cis*-to-*trans*, k_{ct}^{int} and k_{cat}^{cis} , and off rates for the *cis* and *trans* isomers, k_{off}^{cis} and k_{off}^{trans}). In order to determine these microscopic rates and equilibria, lineshape analysis was performed on a series of constant-time ^{13}C - ^1H HSQC spectra of ^{13}C -pAPP659-682 with varying concentrations of unlabeled Pin1-PPIase. Resonances corresponding to the *trans* isomer typically showed a small upfield shift and modest, progressive broadening (Figure 5.5). In all cases, the peaks corresponding to the *cis* isomer broadened substantially upon addition of even low (60 μM) concentrations of enzyme. This can be expected because, in the limit of slow exchange, exchange broadening preferentially affects the minor exchanging component as it has a shorter lifetime (faster rate constant) (Wang and Palmer Iii, 2003). Because of this, essentially only the apo peak positions for *cis* peaks impacted the fit. Constant-time HSQC spectra were utilized to eliminate splitting in the carbon dimension, and to provide resolution of peaks that would otherwise be overlapped in the ^1H dimension. However, use of constant-time ^{13}C evolution precluded lineshape analysis in this dimension, since this mode of evolution provides no encoding of exchange processes into the ^{13}C lineshapes.

Proton dimension peak slices were extracted using the *BiophysicsLab* Sparky extension (Kovrigin, E.L., <http://biophysicslab.net>). To allow simultaneous visualization and analysis of data from both the *trans* and *cis* peaks, peak slices from each isomer of a given nucleus were added together in Matlab to generate a single 1D ^1H spectrum containing both isomer peaks. The resulting 1D ^1H spectra were then fit to a four-state model that considered the bound *trans* and bound *cis* states as well as apo *trans* and *cis* states (Figure 5.1A). The on-enzyme apparent transverse relaxation rate in the absence of exchange ($R_{2,0}^{bound}$) was constrained to be 20 Hz, the average

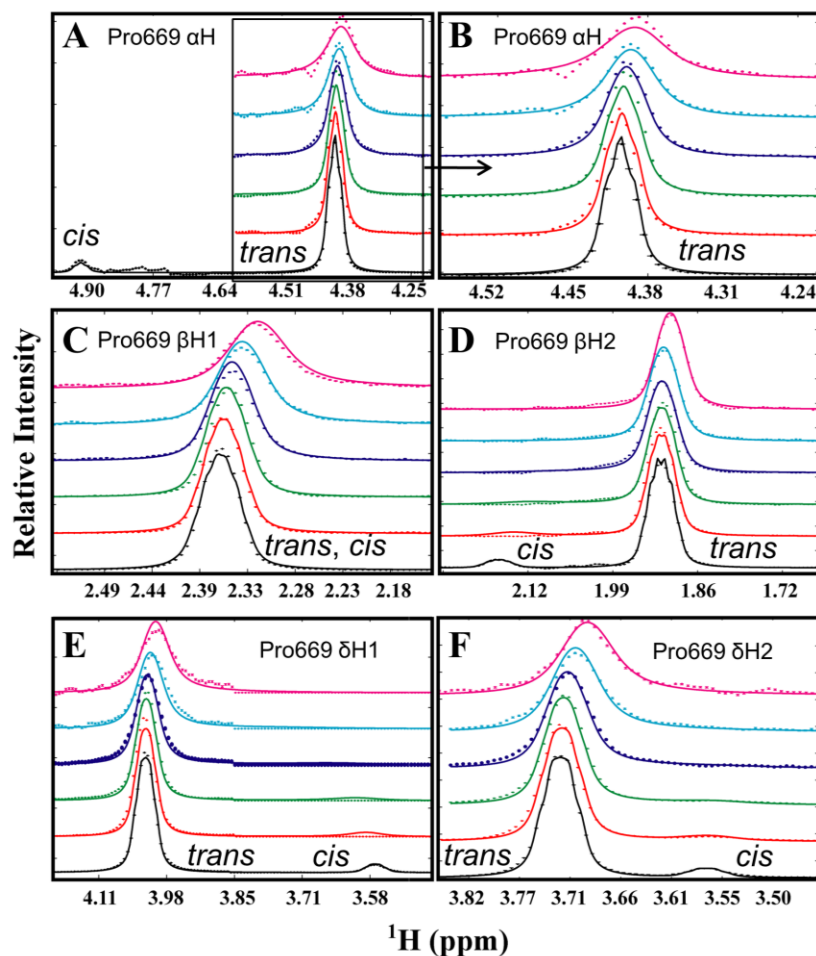


Figure 5.5: NMR lineshape fitting of ^{13}C -pAPP659-682 peptide titration data. Individual ^1H lineshapes for five well-resolved ^{13}C -bonded protons of Pro669 (A-F) were globally fit using lineshape analysis. Stack plots show extracted 1D slices (frequency axis expressed in ppm) from 2D ^{13}C - ^1H constant-time HSQC spectra of 0.7 mM ^{13}C -pAPP659-682 peptide with varying concentrations of unlabeled Pin1-PPIase, from 0 mM (black dots) to 1 mM (magenta dots). The corresponding best-fit globally analyzed lineshapes are shown as solid lines in matching colors. Close proximity of *cis*-Pro669 αH to the water resonance detracted from its inclusion in the stack plot (A); lineshapes of *trans*-Pro669 αH are shown in more detail (B).

value for aliphatic protons in the enzyme. The theoretical value of the transverse relaxation rate for a ^{13}C -attached proton in a 16 kDa complex was also calculated to be 17 Hz using Stokes' law and Figure 1.6 in (Cavanagh, 2007). Because varying this constrained parameter within a range of ± 4 Hz did not impact the result or quality of the fit substantially (Appendix Table 5.1), this approach was deemed valid. Because in general these ^1H lineshapes exhibited small splitting due to J-coupling between the proline ring protons, each peak was modeled as a superposition of lorentzians, using the literature scalar coupling values between the ring protons of L-proline as reported by (Aliev and Courtier-Murias, 2007) (detailed in Appendix). In order to obtain consistent results, it was necessary to simultaneously consider all five groups of peaks in a global fit. The obtained rate, equilibrium, and dissociation constants are presented in the top section of Table 5.1, while constrained global parameters and nucleus-specific parameters are presented in the bottom section.

Table 5.1: Summary of fitted and constrained parameters

Fit parameters	on-enzyme <i>trans/cis</i>	K_D^{trans} (mM)	K_D^{cis} (mM)	on-enzyme k_{ex} (s ⁻¹)	
	3.3 ± 0.5	1.6 ± 0.4	0.4 ± 0.1	1100 ± 90	
Constrained parameters	free <i>trans/cis</i> ^a	K_D^{App} (mM) ^b	Uncatalyzed k_{ex} (s ⁻¹) ^c	k_{off}^{cis} (s ⁻¹) ^d	k_{off}^{trans} (s ⁻¹) ^d
	13.6 ± 0.7	1.3 ± 0.3	0.0085 ± 0.0008	≥ 4,000	≥ 20,000
Nucleus-specific parameters	Proline Protons	$\Delta\omega$ <i>trans</i> (ppm)	$\Delta\omega$ <i>cis</i> (ppm)	$R_{2,0}^{free}$ (s ⁻¹)	J_{HH} (rad/s)
	H α	-0.073	-0.197	75.5	46.9
	H β 1	-0.079	-0.477	87.7	77.0
	H β 2	-0.036	-0.434	109.4	73.9
	H δ 1	-0.022	0.357	99.4	61.1
	H δ 2	-0.044	-0.143	95.1	65.2

a Determined from peak volumes

b Determined from NMR titration of enzyme

c Determined from binding kinetics (data not shown)

d Assuming a diffusion-limited on-rate of $\geq 10^7 \text{ M}^{-1}\text{s}^{-1}$

The value obtained for the on-enzyme rate of exchange, $k_{ex}^{bound} = k_{cat}^{cis} + k_{cat}^{trans}$, was $1500 \pm 100 \text{ s}^{-1}$, in very close agreement with the rate of conformational exchange during catalysis of a model peptide ($1200 \pm 200 \text{ s}^{-1}$) as detected by Labeikovsky *et. al.* (Labeikovsky *et al.*, 2007). Furthermore, since that study showed similar motions in the free enzyme, this measurement seems to suggest that the rates of Pin1 catalysis are dictated by intrinsic motions that are largely independent of the actual substrate. The ratio of bound *trans* to bound *cis* K_{eq}^{bound} was found to be 3.9 ± 0.8 , which may indicate a role for the enzyme in restoring equilibrium to this substrate when it is skewed slightly towards the *cis* isomer, as discussed later. Determination of this ratio allows for the separation of the apparent K_D^{App} into the isomer-specific binding constants $K_D^{trans} = 1.5 \pm 0.4 \text{ mM}$ and $K_D^{cis} = 0.4 \pm 0.1 \text{ mM}$, using equation 5.4 and the definition $K_{eq}^{bound} = k_{cat}^{cis} / k_{cat}^{trans}$. Errors were obtained by propagating the errors in K_D^{App} , K_{eq}^{bound} and K_{eq} .

The dissociation rates k_{off}^{cis} and k_{off}^{trans} were found to have only a small effect on the fit unless they were constrained to be below $1,000 \text{ s}^{-1}$, which reduced the quality of the fit (Appendix Table 5.1). This observation suggests that k_{off}^{cis} and k_{off}^{trans} are sufficiently fast as to have no significant impact on lineshapes. This interpretation is consistent with the enzyme-perspective data, which indicated fast exchange. Assuming diffusion-limited on-rates of greater than $10^7 \text{ M}^{-1}\text{s}^{-1}$, we can only bracket k_{off}^{cis} and k_{off}^{trans} as greater than $4,000 \text{ s}^{-1}$ and $20,000 \text{ s}^{-1}$, respectively.

The best global fit of the data yielded rather large chemical shift changes for the bound *cis* populations of the beta protons and one of the delta protons, on the order of 0.4 ppm. While not unusual for chemical shift changes due to protein-ligand interactions, these were significantly larger than those for the *trans* peaks. This may reflect a distinct environment for the *cis* isomer in the active site of the enzyme, possibly involving closer interactions with the proline ring than for the *trans* isomer. It should be noted that in the fitting these three chemical shift changes diverged to even

larger values when left unconstrained, and that the values presented reflect the upper or lower allowed limits in the fit. Loosening the limits, however, did not result in a substantially improved fit. Therefore, the reported bound chemical shifts for the *cis* isomer, while approximate, clearly indicate a significant change in chemical environment upon binding to the active site.

In order to construct the energy diagram of Pin1-PPIase catalysis, free energies for each of the four states in the model were calculated using the equations

$$\Delta G^{bind} = k_B T \cdot \ln(K_D) \quad (5.5A)$$

$$\Delta G^{cis} - \Delta G^{trans} = k_B T \cdot \ln(K_{eq}) \quad (5.5B)$$

where ΔG^{bind} is the Gibbs free energy of binding for each isomer, k_B is the Boltzmann constant, T is temperature, K_D is the dissociation constant for each isomer,

$\Delta G^{cis} - \Delta G^{trans}$ is the difference between the Gibbs free energies of the *cis* and *trans* isomers, and K_{eq} is the ratio of free *trans* and *cis* populations. Activation energies were calculated using the Eyring equation:

$$\Delta G^i = k_B T \cdot \ln\left(\frac{k_B T}{h \cdot k^i}\right) \quad (5.6)$$

where ΔG^i refers to the activation barrier (catalyzed or uncatalyzed) for either the *cis* (i=ct) or *trans* (i=tc) isomer, h is Planck's constant, and k^i is the measured rate of exchange (catalyzed or uncatalyzed) between *cis* and *trans* (i=ct) or between *trans* and *cis* (i=tc). The values obtained for the peptide bond torsion barrier on (55.4 kJ/mol) and off (84.8 kJ/mol) the enzyme are in good agreement with published measurements and estimates for these values (Kofron et al., 1991; Park et al., 1992; Schutkowski et al., 1998).

Measurement of overall cis/trans exchange by ROESY

As a validation of the best-fit parameters, the catalyzed rate of exchange between the *cis* and *trans* isomers was measured by ^1H - ^1H ROESY experiments. A catalytic amount of PPIase (50 μM) was added to a 3 mM sample of unlabeled

pAPP659-682 and ^1H - ^1H ROESY spectra were taken with a series of mixing times. In the absence of Pin1, the *cis* and *trans* conformations of the amide backbone resonance of E670 are resolved and do not detectably exchange in a ROESY spectrum. Upon addition of Pin1, chemical exchange crosspeaks appear and vary in intensity as a function of mixing time. The intensities of auto-peaks (*cis* and *trans*, $I_{cc}(t)$ and $I_{tt}(t)$) and cross-peaks (*trans*-to-*cis* and *cis*-to-*trans*, $I_{tc}(t)$ and $I_{ct}(t)$) were obtained and fit to the two-state solution of the Bloch-McConnell equations (Cavanagh, 2007; McConnell, 1958) to extract out the rate of isomerization (Figure 5.6A). All four curves for cross- and auto-peaks were simultaneously fit to obtain rates. The value of $k_{ex} = k_{cis \rightarrow trans} + k_{trans \rightarrow cis} = 41 \pm 1 \text{ s}^{-1}$ was obtained and found to be in excellent agreement with the value of 47 s^{-1} predicted by the measured microscopic rates, using the reversible Michaelis-Menten equation

$$k_{ex} = \left(\frac{k_{cat}^{trans}}{K_D^{trans}} + \frac{k_{cat}^{cis}}{K_D^{cis}} \right) \frac{[E]^{tot}}{1 + \frac{[trans]}{K_D^{trans}} + \frac{[cis]}{K_D^{cis}}} \quad (5.7)$$

When this analysis was repeated with full-length Pin1 (Figure 5.6B), a value of $k_{ex} = 28 \pm 1 \text{ s}^{-1}$ was obtained. Although this is modestly lower than the value for the isolated PPIase domain, we concluded that there is no drastic difference in catalysis of pAPP659-682 by Pin1-PPIase and full-length Pin1 under the conditions of the experiment, validating our approach of focusing on the isolated catalytic domain.

A complete description of the Pin1-PPIase thermodynamic cycle for catalysis of a biological substrate

Taken together, the results obtained here provide a complete kinetic and thermodynamic description of the Pin1-PPIase cycle for isomerization of a phosphopeptide corresponding to the Pin1-targeted motif in the intracellular domain of

APP. The kinetic rates for each individual step and the corresponding equilibrium constants have been determined (Figure 5.1A, Table 5.1). A diagram mapping the corresponding relative free energies of each state (Figure 5.7) illustrates that the modest binding energies for each isomer (19.2 kJ and 16.1 kJ for the *cis* and *trans* isomers, respectively), combined with the more favorable binding to the *syn* transition state (49 kJ/mol, or 11.6 kcal/mol) result in a lowering of the activation barrier by 29.4 kJ (7.0 kcal/mol) relative to the uncatalyzed reaction. This enzymatic reduction of the N-C' torsion barrier is comparable to that reported for other PPIase enzymes such as FKBP and CypA (Dugave and Demange, 2003; Fischer et al., 1993; Kofron et al., 1991; Lu et al., 2007; Park et al., 1992). Overall, these results provide the microscopic constants associated with the multi-state thermodynamic cycle of the Pin1 catalytic domain, and demonstrate that these parameters that quantitatively describe the activity of Pin1 on this important biological target are similar to those for other well-studied PPIase enzymes acting on their biological substrates.

Implications of K_{int} for function of Pin1

The internal equilibrium constant, K_{int} , of an enzyme is defined as the ratio of bound substrate to bound product at equilibrium ($K_{\text{int}} = ([ES]_{\text{eq}} / [EP]_{\text{eq}})$). The catalytic efficiency of an enzyme is highly dependent on the relationship between the value of K_{int} and the conditions under which the enzyme operates. For an enzyme that operates near equilibrium of its substrates and products, the optimal value of K_{int} is 1 (Burbaum et al., 1989). However, for an enzyme that operates far from equilibrium, the optimal value of K_{int} is correspondingly skewed. Specifically, if the ratio of substrate to product is much lower than the equilibrium value ($[S]/[P] \ll [S]_{\text{eq}}/[P]_{\text{eq}}$) the optimal value of K_{int} is correspondingly *increased* ($K_{\text{int}} \gg 1$). There is still a limited understanding of the role of Pin1-catalyzed isomerization of many of its substrates,

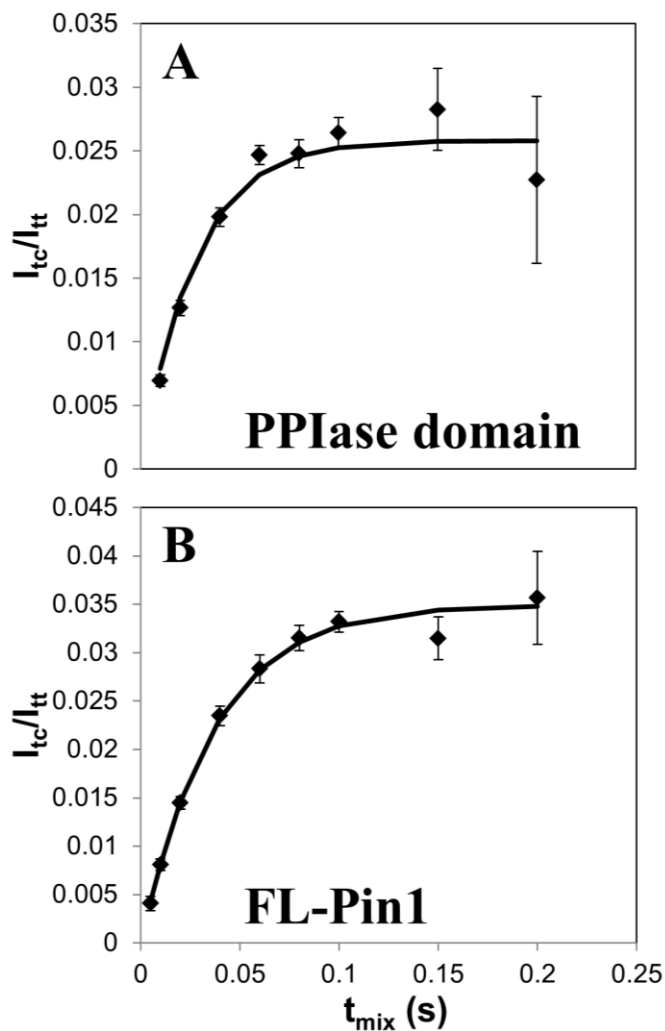


Figure 5.6: ROESY measurement of Pin1-PPIase isomerization rate. In order to measure isomerization rates, a series of ^1H - ^1H ROESY spectra of 3.0 mM pAPP659-682 were taken in the presence of 50 μM PPIase (A) or full-length Pin1 (B). Shown are the normalized cross-peak build-up curves I_{tc}/I_{tt} as a function of mixing time t_{mix} . The rate of isomerization was determined by fitting auto- and cross-peaks, yielding a $k_{ex} = k_{cis \rightarrow trans} + k_{trans \rightarrow cis}$ of $41 \pm 1 \text{ s}^{-1}$ for the PPIase domain and $28 \pm 1 \text{ s}^{-1}$ for full-length Pin1.

such as the AICD of APP (Pastorino et al., 2006). An important factor when considering a mechanism of Pin1 function is the value of K_{int} . For example, if Pin1 exhibits a significantly skewed K_{int} for the pAPP659-682 it may indicate that Pin1 is optimized to operate far from equilibrium in its isomerization of this substrate. This in turn would have implications for the role of isomerization in the biological system, i.e. whether Pin1 serves to restore equilibrium to a population of substrates abnormally enriched for the *cis* isomer or the *trans* isomer. The measured value of K_{int} for the pAPP659-682/Pin1-PPIase complex is 3.9, which may suggest Pin1 is optimized to restore equilibrium to the AICD under conditions where it is slightly skewed towards the *cis* isomer. Pin1 has evolved under selective pressure from multiple substrates (Lu and Zhou, 2007), so it should not be assumed that Pin1 is optimized for its catalysis of the AICD; however, this result is suggestive because evidence exists that implicates the *cis* isomer of the pT668-P669 motif in the AICD in amyloidogenic processing of APP (Iijima et al., 2000; Lee et al., 2003; Ramelot and Nicholson, 2001), and Pin1 protects against this (Pastorino et al., 2006). Future work on other substrates such as the heptad motifs in the CTD of RNA Polymerase II (Buratowski, 2003) should provide insights into the significance of the value of K_{int} .

Concluding Remarks

During the past twenty years, the power of NMR spectroscopy for elucidating the detailed motions of proteins has dramatically increased, with decisive contributions from Lewis Kay and his research group (Grishaev et al., 2008; Hansen et al., 2008a; Hansen et al., 2008b; Religa et al., 2010; Sprangers and Kay, 2007; Vallurupalli et al., 2008). Particularly important is the development of methods to detect and characterize microsecond to millisecond timescale motions via CPMG (Hansen et al., 2008a) or $R_{1\rho}$ (Massi et al., 2004) relaxation experiments that yield

dispersion profiles that can be fit to reveal rates, populations and chemical shifts associated with exchange processes. These methods have opened important windows into motions that occur on the timescale of many biological processes, and have greatly enhanced our understanding of relationships between internal protein motions and function (Mittermaier and Kay, 2009b). While the interpretation of relaxation dispersion profiles has been extended to three-state (Sugase et al., 2007) and four state (Li et al., 2008) exchange processes, the complexity of the exchange reaction remains the major limitation of these methods. Here we have applied classic lineshape analysis as a complementary approach for measuring exchange processes ($k_{ex} < 10^5 \text{ s}^{-1}$) that offers the advantage of being based on the convenient and sensitive HSQC experiment (Mulder et al., 1996).

This study highlights the ability of NMR lineshape analysis to provide a quantitative description of functional motions during catalysis for the four-state reaction scheme of Pin1-PPIase acting on a biological substrate involved in the pathogenesis of Alzheimer's disease. Lineshape analysis of the ^{13}C -Pro-labeled substrate yielded individual kinetic rates, equilibrium constants, and an overall catalytic rate that was independently verified using ROESY exchange spectroscopy. Importantly, since ^{13}C -labeled proline yields a very characteristic spectrum with many well-resolved alpha, beta, delta, and gamma proton peaks, this labeling strategy coupled with lineshape analysis is applicable to the study of any prolyl isomerase and any peptide substrate. Our results support the interpretation of CPMG-derived chemical exchange occurring in and near the active site of Pin1-PPIase saturated with an optimized peptide substrate as on-enzyme isomerization of the substrate (Labeikovsky et al., 2007). These results further suggest that, since similar on-enzyme exchange rates were observed for distinctly different substrates, the intrinsic motions of Pin1-PPIase pre-determine the approximate timescale of this exchange and

substrate-specific variations in overall catalytic rate are governed by their relative affinities. Of particular interest for future lineshape analysis studies is the characterization of specific Pin1-PPIase mutants to gain an in-depth understanding of the Pin1 catalytic mechanism.

REFERENCES

- Aliev, A.E., and Courtier-Murias, D. (2007). Conformational analysis of L-prolines in water. *J Phys Chem B* *111*, 14034-14042.
- Anderson, P. (2005). Pin1: a proline isomerase that makes you wheeze? *Nature Immunology* *6*, 1211-1212.
- Ayed, A., Mulder, F.A., Yi, G.S., Lu, Y., Kay, L.E., and Arrowsmith, C.H. (2001). Latent and active p53 are identical in conformation. *Nat Struct Biol* *8*, 756-760.
- Bax, A.D., and Davis, D.G. (1985). Practical aspects of two-dimensional transverse NOE spectroscopy. *J. Magn. Reson* *63*, 207-213.
- Bosco, D.A., Eisenmesser, E.Z., Clarkson, M.W., Wolf-Watz, M., Labeikovsky, W., Millet, O., and Kern, D. (2010). Dissecting the microscopic steps of the cyclophilin A enzymatic cycle on the biological HIV-1 capsid substrate by NMR. *J Mol Biol* *403*, 723-738.
- Buratowski, S. (2003). The CTD code. *Nat Struct Biol* *10*, 679-680.
- Burbaum, J.J., Raines, R.T., Alber, W.J., and Knowles, J.R. (1989). Evolutionary optimization of the catalytic effectiveness of an enzyme. *Biochemistry* *28*, 9293-9305.
- Cavanagh, J., Fairbrother, W.J., Palmer A.G., Rance, M., Skelton, N.J. (2007). *Protein NMR spectroscopy: principles and practice*, Second edn (Academic Pr).
- Craven, C.J., Whitehead, B., Jones, S.K., Thulin, E., Blackburn, G.M., and Waltho, J.P. (1996). Complexes formed between calmodulin and the antagonists J-8 and TFP in solution. *Biochemistry* *35*, 10287-10299.
- Delaglio, F., Grzesiek, S., Vuister, G.W., Zhu, G., Pfeifer, J., and Bax, A. (1995). NMRPipe: a multidimensional spectral processing system based on UNIX pipes. *J Biomol NMR* *6*, 277-293.
- Dugave, C., and Demange, L. (2003). Cis-trans isomerization of organic molecules and biomolecules: implications and applications. *Chem Rev* *103*, 2475-2532.
- Eckerdt, F., Yuan, J., Saxena, K., Martin, B., Kappel, S., Lindenau, C., Kramer, A., Naumann, S., Daum, S., and Fischer, G. (2005). Polo-like kinase 1-mediated phosphorylation stabilizes Pin1 by inhibiting its ubiquitination in human cells. *Journal of Biological Chemistry* *280*, 36575.
- Fanghanel, J. (2003). Enzymatic catalysis of the peptidyl-prolyl bond rotation: are transition state formation and enzyme dynamics directly linked? *Angew Chem Int Ed Engl* *42*, 490-492.
- Fischer, G., and Aumüller, T. (2003). Regulation of peptide bond cis/trans isomerization by enzyme catalysis and its implication in physiological processes. *Reviews of physiology, biochemistry and pharmacology*, 148:105-150.
- Fischer, G., Bang, H., Berger, E., and Schellenberger, A. (1984). Conformational specificity of chymotrypsin toward proline-containing substrates. *Biochimica et Biophysica Acta* *791*, 87-97.
- Fischer, G., Heins, J., and Barth, A. (1983). The conformation around the peptide bond between the P1-and P2-positions is important for catalytic activity of some proline-specific proteases. *Biochimica et Biophysica Acta* *742*, 452-462.
- Fischer, S., Michnick, S., and Karplus, M. (1993). A mechanism for rotamase catalysis by the FK506 binding protein (FKBP). *Biochemistry* *32*, 13830-13837.

Garcia-Echeverria, C., Kofron, J.L., Kuzmic, P., Kishore, V., and Rich, D.H. (1992). Continuous fluorimetric direct (uncoupled) assay for peptidyl prolyl cis-trans isomerases. *Journal of the American Chemical Society* *114*, 2758-2759.

Garcia-Echeverria, C., Kofron, J.L., Kuzmic, P., and Rich, D.H. (1993). A continuous spectrophotometric direct assay for peptidyl prolyl cis-trans isomerases. *Biochemical and Biophysical Research Communications* *191*, 70-75.

Goddard, T.D., Kneller, D.G. (2008). Sparky 3, University of California, San Francisco.

Grathwohl, C., and Wüthrich, K. (1981). NMR studies of the rates of proline cis-trans isomerization in oligopeptides. *Biopolymers* *20*, 2623-2633.

Grishaev, A., Tugarinov, V., Kay, L.E., Trehwella, J., and Bax, A. (2008). Refined solution structure of the 82-kDa enzyme malate synthase G from joint NMR and synchrotron SAXS restraints. *Journal of Biomolecular NMR* *40*, 95-106.

Gunther, U.L., and Schaffhausen, B. (2002). NMRKIN: simulating line shapes from two-dimensional spectra of proteins upon ligand binding. *J Biomol NMR* *22*, 201-209.

Hansen, D.F., Vallurupalli, P., and Kay, L.E. (2008a). An improved ¹⁵N relaxation dispersion experiment for the measurement of millisecond time-scale dynamics in proteins. *The Journal of Physical Chemistry B* *112*, 5898-5904.

Hansen, D.F., Vallurupalli, P., Lundström, P., Neudecker, P., and Kay, L.E. (2008b). Probing Chemical Shifts of Invisible States of Proteins with Relaxation Dispersion NMR Spectroscopy: How Well Can We Do? *Journal of the American Chemical Society* *130*, 2667-2675.

Iijima, K., Ando, K., Takeda, S., Satoh, Y., Seki, T., Itohara, S., Greengard, P., Kirino, Y., Nairn, A.C., and Suzuki, T. (2000). Neuron Specific Phosphorylation of Alzheimer's Amyloid Precursor Protein by Cyclin Dependent Kinase 5. *Journal of neurochemistry* *75*, 1085-1091.

Johnson, P.E., Creagh, A.L., Brun, E., Joe, K., Tomme, P., Haynes, C.A., and McIntosh, L.P. (1998). Calcium binding by the N-terminal cellulose-binding domain from *Cellulomonas fimi* -1, 4-glucanase CenC. *Biochemistry* *37*, 12772-12781.

Kern, D., Kern, G., Scherer, G., Fischer, G., and Drakenberg, T. (1995). Kinetic analysis of cyclophilin-catalyzed prolyl cis/trans isomerization by dynamic NMR spectroscopy. *Biochemistry* *34*, 13594-13602.

Kim, S.J., Koh, K., Lustig, M., Boyd, S., and Gorinevsky, D. (2007). An interior-point method for large-scale l1-regularized least squares. *Selected Topics in Signal Processing, IEEE Journal of* *1*, 606-617.

Kofron, J.L., Kuzmic, P., Kishore, V., Colon-Bonilla, E., and Rich, D.H. (1991). Determination of kinetic constants for peptidyl prolyl cis-trans isomerases by an improved spectrophotometric assay. *Biochemistry* *30*, 6127-6134.

Korzhnev, D.M., and Kay, L.E. (2008). Probing invisible, low-populated States of protein molecules by relaxation dispersion NMR spectroscopy: an application to protein folding. *Acc Chem Res* *41*, 442-451.

Kovrigin, E.L., and Loria, J.P. (2006). Enzyme dynamics along the reaction coordinate: critical role of a conserved residue. *Biochemistry* *45*, 2636-2647.

Labeikovsky, W., Eisenmesser, E.Z., Bosco, D.A., and Kern, D. (2007). Structure and dynamics of pin1 during catalysis by NMR. *J Mol Biol* *367*, 1370-1381.

Landrieu, I., De Veylder, L., Fruchart, J.S., Odaert, B., Casteels, P., Portetelle, D., Van Montagu, M., Inzé, D., and Lippens, G. (2000). The *Arabidopsis thaliana* PIN1At

Gene Encodes a Single-domain Phosphorylation-dependent Peptidyl Prolylcis/trans Isomerase. *Journal of Biological Chemistry* 275, 10577.

Lee, M.S., Kao, S.C., Lemere, C.A., Xia, W., Tseng, H.C., Zhou, Y., Neve, R., Ahljanian, M.K., and Tsai, L.H. (2003). APP processing is regulated by cytoplasmic phosphorylation. *J Cell Biol* 163, 83-95.

Li, P., Martins, I.R., Amarasinghe, G.K., and Rosen, M.K. (2008). Internal dynamics control activation and activity of the autoinhibited Vav DH domain. *Nat Struct Mol Biol* 15, 613-618.

Lin, L.N., and Brandts, J.F. (1985). Isomer-specific proteolysis of model substrates: influence that the location of the proline residue exerts on cis trans specificity. *Biochemistry* 24, 6533-6538.

Lu, K.P., Finn, G., Lee, T.H., and Nicholson, L.K. (2007). Prolyl cis-trans isomerization as a molecular timer. *Nat Chem Biol* 3, 619-629.

Lu, K.P., Hanes, S.D., and Hunter, T. (1996). A human peptidyl-prolyl isomerase essential for regulation of mitosis. *Nature* 380, 544-547.

Lu, K.P., Suizu, F., Zhou, X.Z., Finn, G., Lam, P., and Wulf, G. (2006). Targeting carcinogenesis: a role for the prolyl isomerase Pin1? *Mol Carcinog* 45, 397-402.

Lu, K.P., and Zhou, X.Z. (2007). The prolyl isomerase PIN1: a pivotal new twist in phosphorylation signalling and disease. *Nat Rev Mol Cell Biol* 8, 904-916.

Lu, P.J., Zhou, X.Z., Liou, Y.C., Noel, J.P., and Lu, K.P. (2002). Critical role of WW domain phosphorylation in regulating phosphoserine binding activity and Pin1 function. *Journal of Biological Chemistry* 277, 2381.

Massi, F., Johnson, E., Wang, C., Rance, M., and Palmer, A.G., 3rd (2004). NMR R1 rho rotating-frame relaxation with weak radio frequency fields. *J Am Chem Soc* 126, 2247-2256.

McConnell, H.M. (1958). Reaction rates by nuclear magnetic resonance. *The Journal of Chemical Physics* 28, 430.

Meinhart, A., and Cramer, P. (2004). Recognition of RNA polymerase II carboxy-terminal domain by 3'-RNA-processing factors. *Nature* 430, 223-226.

Meraz-Rios, M.A.L.-D.L., K.I.; Campos-Pena, V.; De Anda-Hernandez, M.A.; Mena-Lopez, R. (2010). Tau oligomers and aggregates in Alzheimer's disease. *J Neurochemistry* 112, 1353-1367.

Mittermaier, A.K., and Kay, L.E. (2009a). Observing biological dynamics at atomic resolution using NMR. *Trends Biochem Sci* 34, 601-611.

Mittermaier, A.K., and Kay, L.E. (2009b). Observing biological dynamics at atomic resolution using NMR. *Trends in biochemical sciences* 34, 601-611.

Mulder, F.A., Schipper, D., Bott, R., and Boelens, R. (1999). Altered flexibility in the substrate-binding site of related native and engineered high-alkaline *Bacillus subtilis*ins. *J Mol Biol* 292, 111-123.

Mulder, F.A.A., Spronk, C.A.E.M., Slijper, M., Kaptein, R., and Boelens, R. (1996). Improved HSQC experiments for the observation of exchange broadened signals. *Journal of Biomolecular NMR* 8, 223-228.

Park, S.T., Aldape, R.A., Futer, O., DeCenzo, M.T., and Livingston, D.J. (1992). PPIase catalysis by human FK506-binding protein proceeds through a conformational twist mechanism. *J Biol Chem* 267, 3316-3324.

Pastorino, L., Sun, A., Lu, P.J., Zhou, X.Z., Balastik, M., Finn, G., Wulf, G., Lim, J., Li, S.H., Li, X., *et al.* (2006). The prolyl isomerase Pin1 regulates amyloid precursor

protein processing and amyloid-beta production. *Nature* **440**, 528-534.

Peng, J.W., Wilson, B.D., and Namanja, A.T. (2009). Mapping the dynamics of ligand reorganization via ¹³CH₃ and ¹³CH₂ relaxation dispersion at natural abundance. *Journal of Biomolecular NMR* **45**, 171-183.

Ramelot, T.A., Gentile, L.N., and Nicholson, L.K. (2000). Transient structure of the amyloid precursor protein cytoplasmic tail indicates preordering of structure for binding to cytosolic factors. *Biochemistry* **39**, 2714-2725.

Ramelot, T.A., and Nicholson, L.K. (2001). Phosphorylation-induced structural changes in the amyloid precursor protein cytoplasmic tail detected by NMR. *J Mol Biol* **307**, 871-884.

Ranganathan, R., Lu, K.P., Hunter, T., and Noel, J.P. (1997). Structural and functional analysis of the mitotic rotamase Pin1 suggests substrate recognition is phosphorylation dependent. *Cell* **89**, 875-886.

Reimer, U., Scherer, G., Drewello, M., Kruber, S., Schutkowski, M., and Fischer, G. (1998). Side-chain effects on peptidyl-prolyl cis/trans isomerisation. *J Mol Biol* **279**, 449-460.

Religa, T.L., Sprangers, R., and Kay, L.E. (2010). Dynamic regulation of archaeal proteasome gate opening as studied by TROSY NMR. *Science* **328**, 98.

Rippmann, J.F., Hobbie, S., Daiber, C., Guilliard, B., Bauer, M., Birk, J., Nar, H., Garin-Chesa, P., Rettig, W.J., and Schnapp, A. (2000). Phosphorylation-dependent proline isomerization catalyzed by Pin1 is essential for tumor cell survival and entry into mitosis. *Cell growth & differentiation: the molecular biology journal of the American Association for Cancer Research* **11**, 409.

Sarkar, P., Saleh, T., Tzeng, S.R., Birge, R.B., and Kalodimos, C.G. (2011). Structural basis for regulation of the Crk signaling protein by a proline switch. *Nat Chem Biol* **7**, 51-57.

Schutkowski, M., Bernhardt, A., Zhou, X.Z., Shen, M., Reimer, U., Rahfeld, J.U., Lu, K.P., and Fischer, G. (1998). Role of phosphorylation in determining the backbone dynamics of the serine/threonine-proline motif and Pin1 substrate recognition. *Biochemistry* **37**, 5566-5575.

Skinner, G.M., Baumann, C.G., Quinn, D.M., Molloy, J.E., and Hoggett, J.G. (2004). Promoter binding, initiation, and elongation by bacteriophage T7 RNA polymerase. A single-molecule view of the transcription cycle. *J Biol Chem* **279**, 3239-3244.

Sprangers, R., and Kay, L.E. (2007). Quantitative dynamics and binding studies of the 20S proteasome by NMR. *Nature* **445**, 618-622.

Sugase, K., Dyson, H.J., and Wright, P.E. (2007). Mechanism of coupled folding and binding of an intrinsically disordered protein. *Nature* **447**, 1021-1025.

Vallurupalli, P., Hansen, D.F., and Kay, L.E. (2008). Structures of invisible, excited protein states by relaxation dispersion NMR spectroscopy. *Proceedings of the National Academy of Sciences* **105**, 11766.

Verdecia, M.A., Bowman, M.E., Lu, K.P., Hunter, T., and Noel, J.P. (2000). Structural basis for phosphoserine-proline recognition by group IV WW domains. *Nat Struct Biol* **7**, 639-643.

Vuister, G.W., and Bax, A. (1992). Resolution enhancement and spectral editing of uniform ¹³C-enriched proteins by homonuclear broadband ¹³C decoupling. *Journal of Magnetic Resonance* **98**, 428-435.

Wang, C., and Palmer III, A.G. (2003). Solution NMR methods for quantitative

identification of chemical exchange in ^{15}N labeled proteins. *Magnetic Resonance in Chemistry* 41, 866-876.

Werner-Allen, J.W., Lee, C.J., Liu, P., Nicely, N.I., Wang, S., Greenleaf, A.L., and Zhou, P. (2011). cis-Proline-mediated Ser(P)5 Dephosphorylation by the RNA Polymerase II C-terminal Domain Phosphatase Ssu72. *J Biol Chem* 286, 5717-5726.

Xiang, K., Nagaike, T., Xiang, S., Kilic, T., Beh, M.M., Manley, J.L., and Tong, L. (2010). Crystal structure of the human symplekin-Ssu72-CTD phosphopeptide complex. *Nature* 467, 729-733.

Zhou, X.Z., Kops, O., Werner, A., Lu, P.J., Shen, M., Stoller, G., Kullertz, G., Stark, M., Fischer, G., and Lu, K.P. (2000). Pin1-dependent prolyl isomerization regulates dephosphorylation of Cdc25C and tau proteins. *Mol Cell* 6, 873-883.

CHAPTER 6

Perspectives, Additional Observations, and Future Plans

Role of Isomerization in VASP Binding Interactions

In Chapter 2, we demonstrated that the interaction between the VASP-EVH1 domain and (W/F)PPPP motifs is specific for the *trans* isomer of the (W/F)-P peptide bond. Furthermore, we showed that the prolyl isomerase cyclophilin A was able to accelerate binding between VASP-EVH1 and such motifs. Tetrameric VASP may exhibit very tight binding through avidity to the tandem repeat motifs of zyxin, lamellipodin, and ActA. IRAK1 tetramerizes in response to IL-1R and TLR signaling, raising the possibility that the VASP/IRAK1 interaction is regulated by IRAK1 tetramerization. An intriguing implication of our work was that, if the interaction between VASP and IRAK1 is enhanced by avidity, then VASP will preferentially select IRAK1 tetramers that adopt the *trans* peptide bond for each of the four monomers. As this only occurs for rather minor fraction (%*trans*⁴, or 11%) of the total IRAK1 tetramers, this would predict an increased importance for an isomerase such as cyclophilin A to accelerate VASP binding.

These two predictions, that tetramerization of IRAK1 can regulate its interaction with VASP, and that isomerization would then be a major rate-limiting step in this binding interaction, can be tested with purified components *in vitro*. Full length His-tagged VASP expresses well in *E. coli*, though in our hands usage of B121 Rosetta cells and cobalt resin are important. Furthermore, we have cloned expression vectors encoding fusion constructs designed to produce either dimer or tetramer IRAK1-UD. These constructs have N-terminal 6X His tags followed by a TEV protease cleavage site and either the sequence

GHMGGRMKQLEDKIEELLSKIYHLENEIARLKKLIGERGGSA (GCN4_pIL,

dimer) or the sequence GRMKQIEDKLEEILSKLYHIENELARIKKLLGER (GCN4_pLI, tetramer), followed by the UD of IRAK1 (residues 102-222). These GCN4 sequences are known to form leucine zippers of defined oligomeric states (Harbury et al., 1993). In our hands, it is necessary to purify these fusion proteins using a denaturing prep (described for zyxin⁴¹⁻¹⁴⁰ in Chapter 4) for purity as well as to prevent degradation.

In our hands, we have not been able to detect binding of these fusion constructs to VASP by fluorescence spectroscopy under dilute (< 10 μ M) conditions. However, multiple controls remain to be performed. The sequences of the fusion constructs may require a flexible linker in between the IRAK1 sequence and the GCN4 sequence to oligomerize properly. We have not been able to obtain unambiguous evidence for these constructs forming dimers and tetramers, either by cross-linking experiments or by analytical ultracentrifugation (AUC). Unless their oligomeric state is confirmed, it will be difficult to interpret even a positive result of tight binding, so this is an important goal.

Because both VASP and these IRAK1-UD fusion proteins contain multiple tryptophan residues, tryptophan fluorescence titration data will require large baseline subtractions. Likewise, given the difference in tryptophan fluorescence signal for the *cis* and *trans* isomers of the W₁₆₈-P₁₆₉ peptide bond observed in Chapter 2, fluorescence binding kinetics data would be difficult to interpret. Therefore, if the issues in the previous paragraph are resolved, it may be worthwhile to perform surface plasmon resonance (SPR) rather than tryptophan fluorescence to measure binding affinities and rates.

Role of Phosphorylation of VASP Binding Partners

In Chapter 3, we have shown that phosphoserines flanking VASP-binding motifs can have a similar effect as negatively charged amino acids in increasing the affinity of sequences for VASP-EVH1. In our example, the VASP-binding motif in the UD of IRAK1, the motif is flanked by two serines. While studies have identified one of these serines (S173) as being phosphorylated in response to TLR stimulation (Tun-Kyi et al., 2011), it is unknown whether the other (S166) is phosphorylated at all. Given the extensive phosphorylation of the IRAK1-UD in response to IRAK1 activation (Kollewe et al., 2004), it is reasonable to expect that S166 is phosphorylated. However, future experiments should be performed to ascertain this. This may require raising an antibody against this modification, as S166 is contained within a sequence of IRAK1 that is not very amenable to mass spectrometry analysis (personal communication: Greg Finn, Harvard University). The question further remains of how important phosphorylation of IRAK1 is for it to interact with VASP. To address this, it will be informative to test whether mutating these serines to alanine impairs the ability of IRAK1 to co-IP with VASP in cell culture. It will be particularly interesting whether or not TLR stimulation enhances this interaction, as we predict, and whether or not mutation of the serine residues abolishes this enhancement. We have produced a double mutant S166A/S173A IRAK1 expression construct and are pursuing these experiments currently.

Our results further suggest that the interaction of VASP with the proteins lamellipodin and palladin likewise may be regulated by phosphorylation. While it would be trivial for us or others to test whether phosphorylated peptides derived from these proteins bind VASP-EVH1 tighter than their non-phosphorylated counterparts *in vitro*, the most pressing question is what the role of phosphorylation of these proteins is in the cellular context. Given that the VASP-binding sites in lamellipodin are phosphorylated in response to Erk2 signaling and during mitosis

(<http://www.phosphosite.org/>) (Asano et al., 2011; Carlson et al., 2011; Hornbeck et al., 2004; Olsen et al., 2010), it would be interesting to test whether mutating residues T874 and S933 of lamellipodin influence lamellipodial dynamics in either of these contexts.

Secondary Binding Site in EVH1 Domain

In Chapters 3 and 4, we have identified and performed a preliminary characterization of a secondary binding surface on the EVH1 domain of VASP that weakly interacts with the same FPPPP motif that is recognized by the primary binding site. We have shown that this site is employed in the interaction between VASP-EVH1 and the proline-rich region of zyxin, which contains four such FPPPP motifs. Remarkably, when zyxin is in excess, the fourth and second FPPPP motifs simultaneously bind VASP-EVH1 in two orientations, either with the second motif in the primary site and the fourth in the secondary site, or visa-versa. Furthermore, the Y39D mutation of EVH1, meant to mimic Abl-induced phosphorylation of VASP-EVH1 (Maruoka et al., 2012), appears to abolish this secondary interaction.

Future work should include more complete characterization of the possible binding orientations between VASP-EVH1 and the proline-rich region of zyxin. We mutated motif M3 (F104A) because it appeared to bind weakly relative to the other motifs, but it nonetheless must be considered in the complete picture. Likewise, we mutated motif M1 (F71A) somewhat arbitrarily, motivated simply to reduce the complexity of the interaction. It will be important to test whether motifs M1 and M4, or M1 and M2, can similarly bind simultaneously on the two faces of VASP-EVH1.

It is possible that this secondary interaction serves to strengthen VASP binding to zyxin, and that phosphorylation of Y39 is a mechanism to selectively weaken VASP binding to zyxin but not other proteins that do not bind in this manner.

Alternately, this secondary interaction may not contribute significantly to the affinity of VASP-EVH1 for zyxin. To address this, future experiments should include precise quantification of the affinity of zyxin for wild-type and Y39D VASP-EVH1, possibly using fluorescence anisotropy or SPR. However, given the highly complex multi-state interaction between these proteins, care must be taken to account for the different possible stoichiometries and binding orientations in such an experiment. Furthermore, because the LIM domains of zyxin also contribute to binding to VASP (Moody et al., 2009), usage of the full-length sequences of VASP and zyxin may be warranted. Importantly, the use of tetrameric VASP over monomeric EVH1 may well bias the interaction towards a 1:4 stoichiometry, rendering the secondary binding site unimportant.

Given that the proteins lamellipodin and ActA similarly contain multiple FPPPP motifs, it is reasonable to ask whether VASP-EVH1 binds these proteins in a similar manner. The longer length of the proline-rich sequences in these proteins may make NMR a less attractive technique to address this. It may be sufficient to simply monitor global binding of wild-type and Y39D VASP to infer whether the secondary site is employed.

In characterizing this secondary binding site, we only report chemical shift perturbations, which cannot substitute for an atomic-resolution structure. Given the possible conservation of this binding site in the EVH1 domains of multiple protein families, it makes sense to pursue an NMR or crystal structure. It may be relatively straightforward to obtain a structure of VASP-EVH1 with a zyxin sequence bound in this site. By producing a fusion protein with the sequence of zyxin residues 85-123 joined via a short flexible linker to the C-terminus of VASP-EVH1, it should be possible to obtain a solution structure of the complex, in analogy to the method used in (Volkman et al., 2002). This would provide the added benefit of producing the first

VASP-EVH1/peptide complex structure, as only a structure of the EVH1 domain of Mena has been solved with a peptide bound.

Novel Zinc-Binding Sequence in IRAK1-UD

During the course of characterizing the VASP-binding sequence in the UD of IRAK1, we observed that the *cis* and *trans* side-chain peaks of W200 decreased in intensity over time and were replaced by new peaks with distinct chemical shifts. This was reversible by addition of 5 mM TCEP, suggesting that the chemical shift change was due to a disulfide linkage forming between the flanking cysteine residues C199 and C203. The addition of a small amount of protease inhibitor cocktail in DMSO, which promotes disulfide bond formation, may have contributed to this. Interestingly, disulfide formation caused the *cis/trans* ratio to shift significantly, from 25% *cis* reduced to as much as 77% *cis* when oxidized, assuming from relative peak positions that the new major population was the *cis* isomer. This assumption is supported by a report (Shi et al., 2006) showing that short proline-containing peptides substantially increase their population of *cis* upon cyclization by disulfides when the number of residues between the two cysteines is either five or three, as in our sequence (₁₉₉CWPLC₂₀₃).

Zinc has been shown to inhibit IRAK1 kinase activity (Wellinghausen et al., 1997). Based on the conservation of either histidine or cysteine residues at IRAK1 positions 199, 203, and 210 in mammals, we wondered whether IRAK1 directly binds zinc with these residues. Furthermore we speculated that the tendency of these cysteine residues to disulfide bond reflected a conformation preordered to bind zinc. This would predict that IRAK1 binding to zinc would be specific for the *cis* isomer, or preferentially stabilize the *cis* isomer. To test this, we measured the intrinsic tryptophan fluorescence from W200 while zinc was added to IRAK1-UD. We found

that IRAK1-UD indeed binds zinc, with an affinity between 5-30 nM at pH 7.5. Furthermore, adding zinc to IRAK1-UD caused a slow change in fluorescence signal that was accelerated by cyclophilin A, confirming the expectation that zinc binding would display some isomer specificity. We showed that the mutations C199S, P201V, C203S, and H210F all decreased binding, and that the double mutant C199S/C203S completely abolished it (Appendix Figure 6.1).

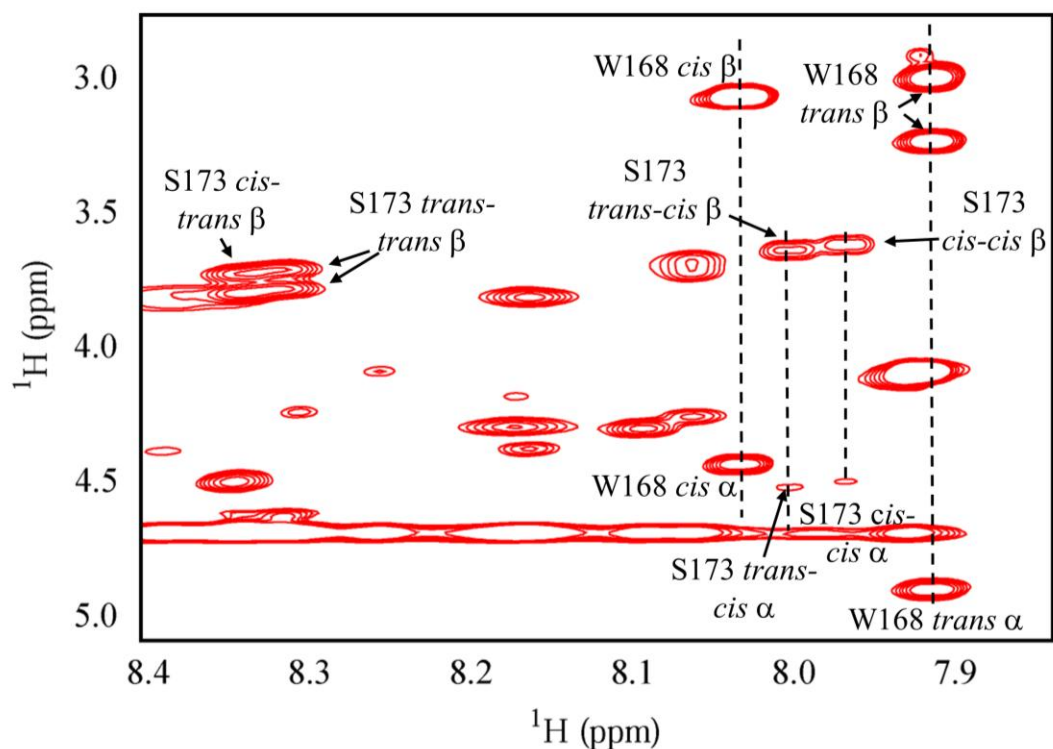
We attempted to use NMR spectroscopy to characterize this interaction with zinc using a short peptide with the sequence KPFCWPLCEISRGTHNFK-amide. This sequence contained N- and C-terminal lysine residues to increase solubility, because a peptide with the similar wt sequence (₁₉₆FPFCWPLCEISRGTHNFS₂₁₃) was insoluble at neutral pH. We were able to obtain ¹H-¹H TOCSY of this peptide bound to zinc at pH 8.0. Zinc binding appeared to induce hydrogen bond formation, based on zinc-induced protection of some backbone amide protons. However, the aliphatic region of the spectrum indicated that the H210 peaks did not respond to the presence of zinc, and that by contrast the extreme N-terminus seemed to be highly sensitive to it. We took this to mean that the N-terminal lysine or extreme N-terminus was preventing H210 from coordinating zinc, possibly by forming some secondary interaction with E204.

These zinc-binding peptide experiments were hampered by the limited solubility of the peptide in the presence of excess zinc. They were similarly hampered by the low affinity of the peptide for zinc at acidic pH, which is necessary to observe backbone amide peaks. The limited solubility of the peptide, as well as the apparent discrepancy between the peptide and the full-length sequence regarding the importance of H210 in binding, argue for design of an additional peptide. In addition, future experiments should include testing for binding of other metals, possibly of physiological relevance or for minimizing aggregation in order to perform NMR.

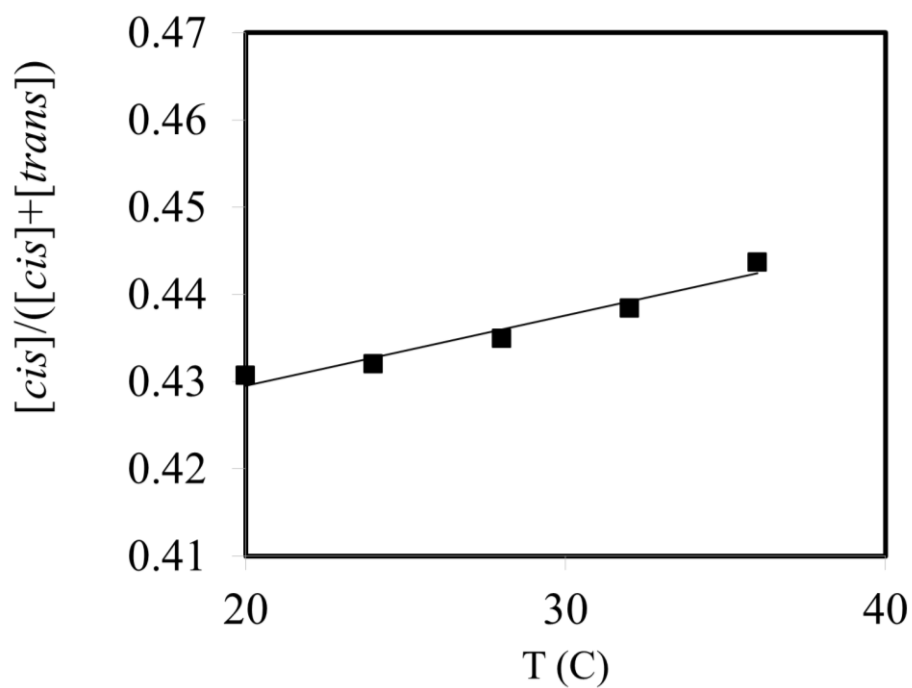
REFERENCES

- Asano, E., Maeda, M., Hasegawa, H., Ito, S., Hyodo, T., Yuan, H., Takahashi, M., Hamaguchi, M., and Senga, T. (2011). Role of palladin phosphorylation by extracellular signal-regulated kinase in cell migration. *PLoS One* 6, e29338.
- Carlson, S.M., Chouinard, C.R., Labadorf, A., Lam, C.J., Schmelzle, K., Fraenkel, E., and White, F.M. (2011). Large-scale discovery of ERK2 substrates identifies ERK-mediated transcriptional regulation by ETV3. *Sci Signal* 4, rs11.
- Harbury, P.B., Zhang, T., Kim, P.S., and Alber, T. (1993). A switch between two-, three-, and four-stranded coiled coils in GCN4 leucine zipper mutants. *Science* 262, 1401-1407.
- Hornbeck, P.V., Chabra, I., Kornhauser, J.M., Skrzypek, E., and Zhang, B. (2004). PhosphoSite: A bioinformatics resource dedicated to physiological protein phosphorylation. *Proteomics* 4, 1551-1561.
- Kollewe, C., Mackensen, A.C., Neumann, D., Knop, J., Cao, P., Li, S., Wesche, H., and Martin, M.U. (2004). Sequential autophosphorylation steps in the interleukin-1 receptor-associated kinase-1 regulate its availability as an adapter in interleukin-1 signaling. *J Biol Chem* 279, 5227-5236.
- Maruoka, M., Sato, M., Yuan, Y., Ichiba, M., Fujii, R., Ogawa, T., Ishida-Kitagawa, N., Takeya, T., and Watanabe, N. (2012). Abl-1-bridged tyrosine phosphorylation of VASP by Abelson kinase impairs association of VASP to focal adhesions and regulates leukaemic cell adhesion. *Biochem J* 441, 889-899.
- Moody, J.D., Grange, J., Ascione, M.P., Boothe, D., Bushnell, E., and Hansen, M.D. (2009). A zyxin head-tail interaction regulates zyxin-VASP complex formation. *Biochem Biophys Res Commun* 378, 625-628.
- Olsen, J.V., Vermeulen, M., Santamaria, A., Kumar, C., Miller, M.L., Jensen, L.J., Gnad, F., Cox, J., Jensen, T.S., Nigg, E.A., *et al.* (2010). Quantitative phosphoproteomics reveals widespread full phosphorylation site occupancy during mitosis. *Sci Signal* 3, ra3.
- Shi, T., Spain, S.M., and Rabenstein, D.L. (2006). A striking periodicity of the cis/trans isomerization of proline imide bonds in cyclic disulfide-bridged peptides. *Angew Chem Int Ed Engl* 45, 1780-1783.
- Tun-Kyi, A., Finn, G., Greenwood, A., Nowak, M., Lee, T.H., Asara, J.M., Tsokos, G.C., Fitzgerald, K., Israel, E., Li, X., *et al.* (2011). Essential role for the prolyl isomerase Pin1 in Toll-like receptor signaling and type I interferon-mediated immunity. *Nat Immunol* 12, 733-741.
- Volkman, B.F., Prehoda, K.E., Scott, J.A., Peterson, F.C., and Lim, W.A. (2002). Structure of the N-WASP EVH1 domain-WIP complex: insight into the molecular basis of Wiskott-Aldrich Syndrome. *Cell* 111, 565-576.
- Wellinghausen, N., Martin, M., and Rink, L. (1997). Zinc inhibits interleukin-1-dependent T cell stimulation. *Eur J Immunol* 27, 2529-2535.

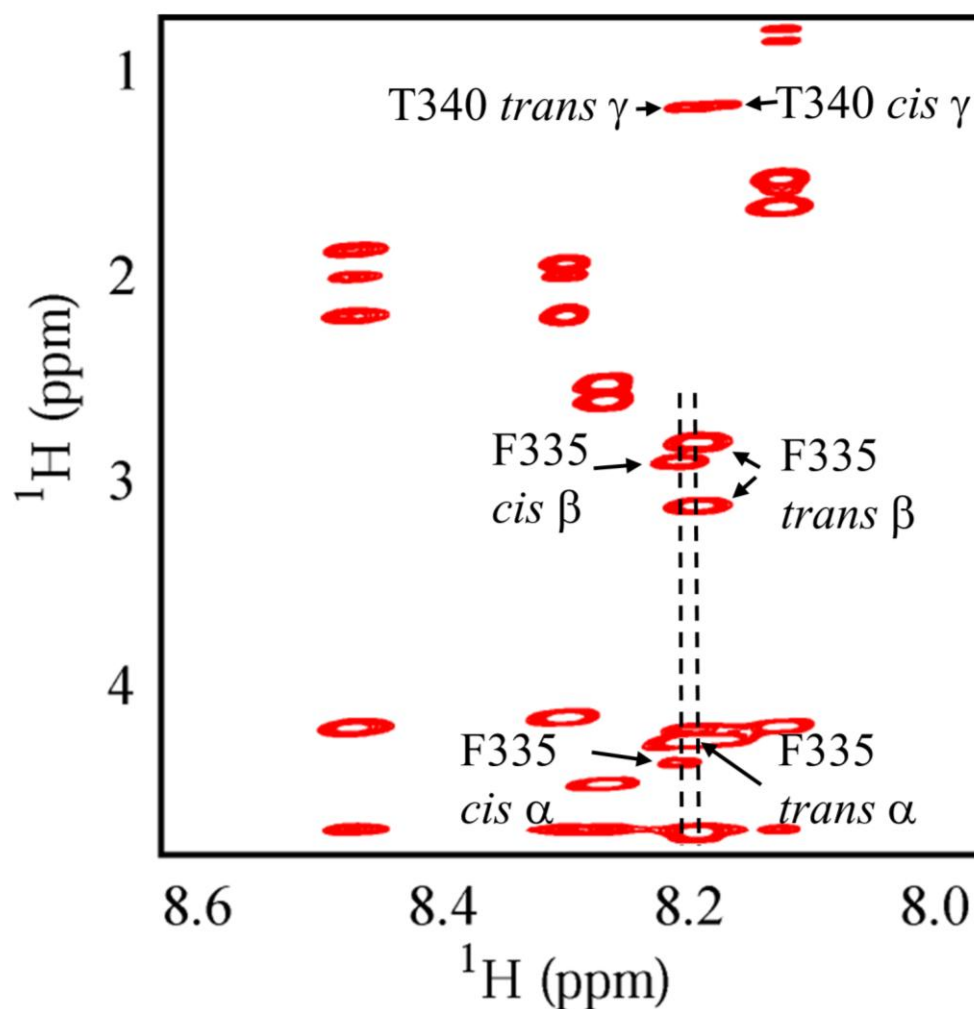
APPENDIX



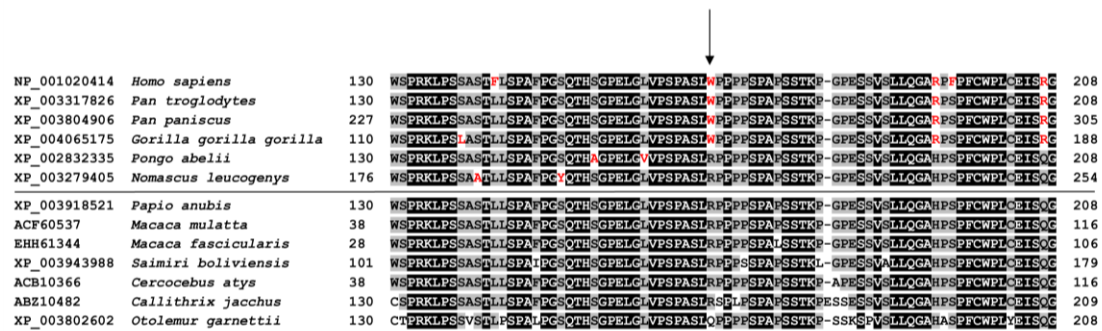
Appendix Figure 2.1: ^1H - ^1H TOCSY showing *cis* and *trans* isomers of W168-P169 and S173-P174 peptide bonds in IRAK1¹⁶²⁻¹⁸⁰. Lines are drawn through TOCSY strips showing the resolved α and β proton peaks for the *cis* and *trans* isomers of W168. The NH chemical shift of S173 is sensitive to the isomer states of both W168-P169 and S173-P174, leading to four distinct strips for S173. Lines are drawn through the two strips corresponding to the *cis* isomer of S173-P174 on the right, and the β peaks of the *trans* isomer of S173-P174 are indicated to the left. Peaks are labeled with the isomer state of W168-P169 designated first, and if applicable, the isomer state of S173-P174 second. Isomer populations of the S173-P174 peptide bond were determined by volumes of the β peaks of S173.



Appendix Figure 2.2: Temperature dependence of population of *cis* isomer of IRAK1-UD. The population of *cis* isomer was determined from the diagonal peaks of the W168 sidechain in ^1H - ^1H TOCSY spectra of the peptide IRAK1¹⁶²⁻¹⁸⁰. The slight temperature dependence was fit to a straight line and this was used to determine the individual isomerization rates k_{CT} and k_{TC} from the observed k_{obs} measured in the fluorescence temperature series, in order to fit to equation 2.7.

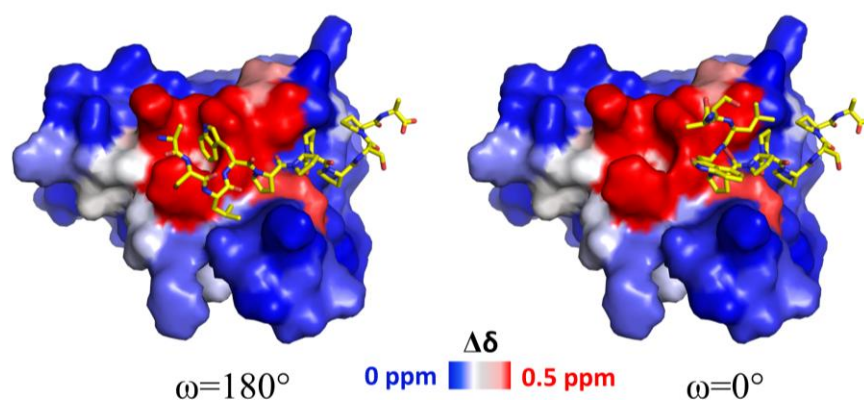


Appendix Figure 2.3: ^1H - ^1H TOCSY showing *cis* and *trans* isomers of F335-P336 peptide bond in ActA³³³⁻³⁴⁴. Dashed lines are shown corresponding to the F335 NH chemical shifts of the *cis* and *trans* isomers of F335-P336. The NH chemical shift of T340 is also split due to its sensitivity to the F335-P336 peptide bond, so its γ peaks are specified.

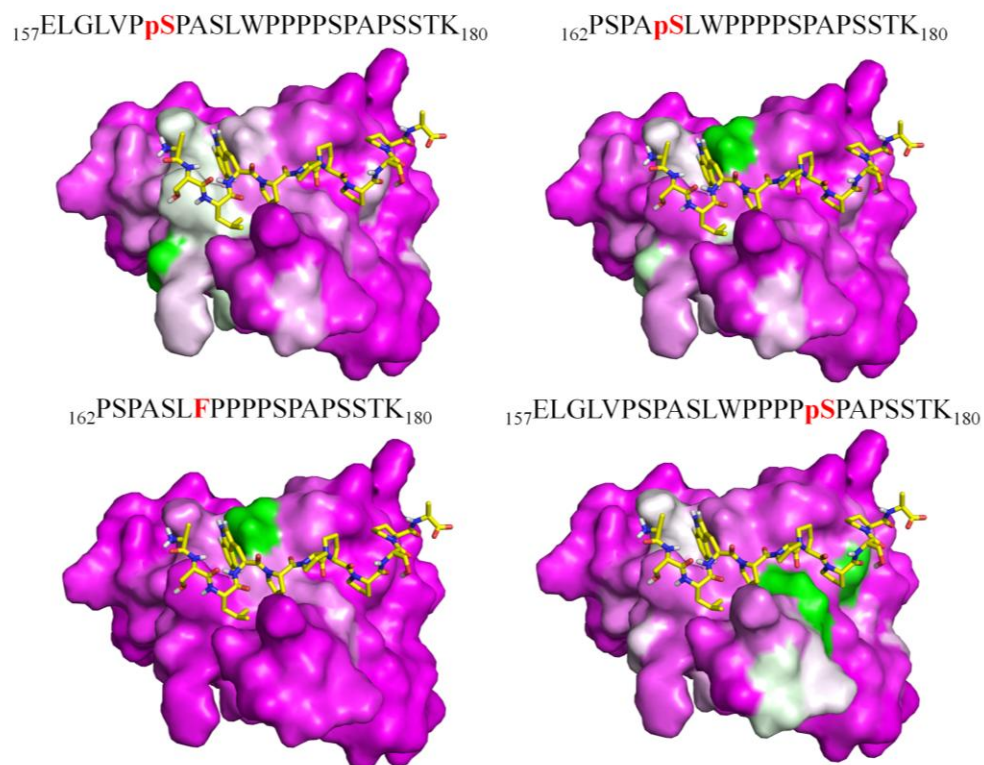


NP_001020414	<i>Homo sapiens</i>	130	WSPRKLPSSASGTLSPAFCGQTHSGPELGVPSPASIRFPPFSPAFSSTKP-GPSSVSLQGARFPFCWPLCEISG	208
XP_003317826	<i>Pan troglodytes</i>	130	WSPRKLPSSASGTLSPAFCGQTHSGPELGVPSPASIRFPPFSPAFSSTKP-GPSSVSLQGARFPFCWPLCEISG	208
XP_003804906	<i>Pan paniscus</i>	227	WSPRKLPSSASGTLSPAFCGQTHSGPELGVPSPASIRFPPFSPAFSSTKP-GPSSVSLQGARFPFCWPLCEISG	305
XP_004065175	<i>Gorilla gorilla gorilla</i>	110	WSPRKLPSSASGTLSPAFCGQTHSGPELGVPSPASIRFPPFSPAFSSTKP-GPSSVSLQGARFPFCWPLCEISG	188
XP_002832335	<i>Pongo abelii</i>	130	WSPRKLPSSASGTLSPAFCGQTHSGPELGVPSPASIRFPPFSPAFSSTKP-GPSSVSLQGARFPFCWPLCEISG	208
XP_003279405	<i>Nomascus leucogenys</i>	176	WSPRKLPSSASGTLSPAFCGQTHSGPELGVPSPASIRFPPFSPAFSSTKP-GPSSVSLQGARFPFCWPLCEISG	254
XP_003918521	<i>Papio anubis</i>	130	WSPRKLPSSASGTLSPAFCGQTHSGPELGVPSPASIRFPPFSPAFSSTKP-GPSSVSLQGARFPFCWPLCEISG	208
ACF60537	<i>Macaca mulatta</i>	38	WSPRKLPSSASGTLSPAFCGQTHSGPELGVPSPASIRFPPFSPAFSSTKP-GPSSVSLQGARFPFCWPLCEISG	116
EHH61344	<i>Macaca fascicularis</i>	28	WSPRKLPSSASGTLSPAFCGQTHSGPELGVPSPASIRFPPFSPAFSSTKP-GPSSVSLQGARFPFCWPLCEISG	106
XP_003943988	<i>Saimiri boliviensis</i>	101	WSPRKLPSSASGTLSPAFCGQTHSGPELGVPSPASIRFPPFSPAFSSTKL-GPSSVSLQGARFPFCWPLCEISG	179
ACB10366	<i>Cercocebus atys</i>	38	WSPRKLPSSASGTLSPAFCGQTHSGPELGVPSPASIRFPPFSPAFSSTKP-APPSSVSLQGARFPFCWPLCEISG	116
ABZ10482	<i>Callithrix jacchus</i>	130	CSPRKLPSSASGTLSPAFCGQTHSGPELGVPSPASIRFPPFSPAFSSTKPSSSSVSLQGARFPFCWPLCEISG	209
XP_003802602	<i>Otolemur garnettii</i>	130	CTPRKLPSSASGTLSPAFCGQTHSGPELGVPSPASIRFPPFSPAFSSTKP-SSKSPVSLQGARFPFCWPLCEISG	208

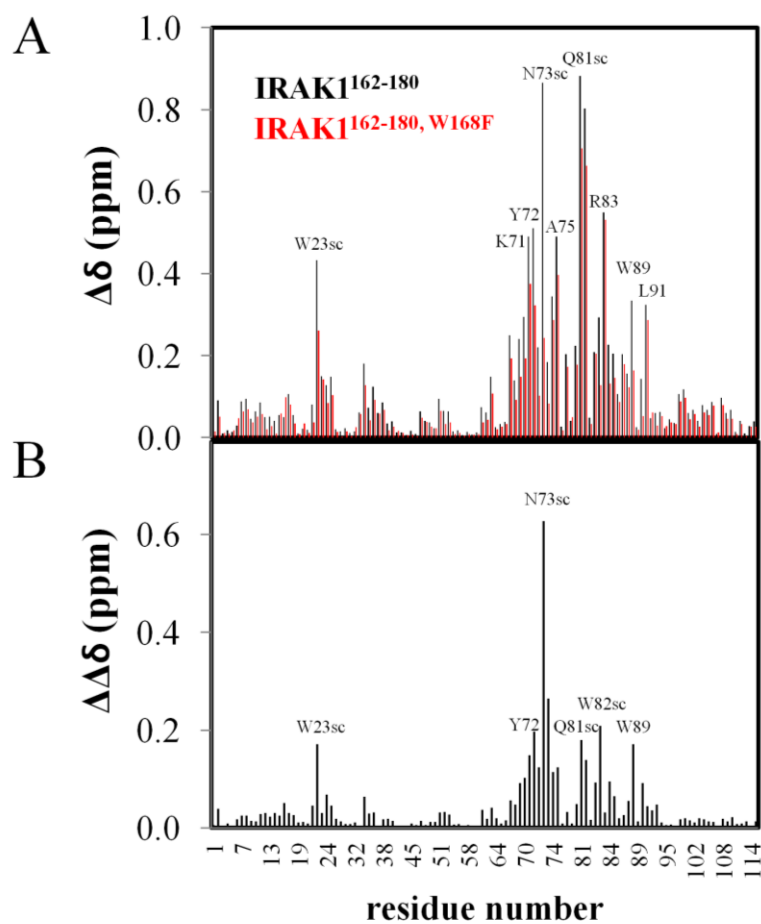
Appendix Figure 2.4: Alignment of IRAK1 residues 130-208 in primates shows that W168 is a very recent mutation. In this alignment, apes (above) are separated from monkeys and prosimians by a horizontal line. Black background indicates an absolutely conserved residue, whereas grey background indicates the major allele of a residue not absolutely conserved. Red letters represent amino acids corresponding to new mutations that appear in apes. W168 is one of five such amino acids in humans for this 78-residue stretch of IRAK1.



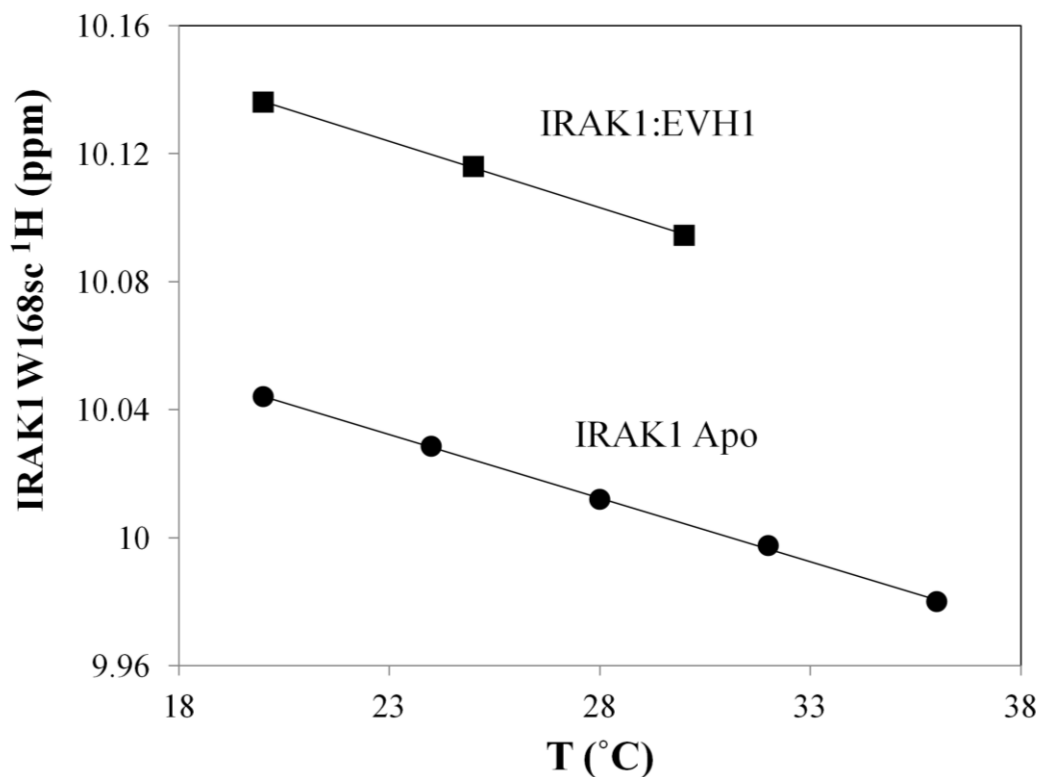
Appendix Figure 2.5: Structural model rationalizing isomer specificity of IRAK1-UD/EVH1 interaction. A representation of the solution structure of the VASP-EVH1 domain (PDB ID code 1EGX (Ball et al., 2000)) with IRAK1 peptide residues modeled into the binding site, with W168-169 in either the *cis* (right) or *trans* (left) state. The surface representation of the EVH1 domain is colored according to chemical shift perturbation of the IRAK1¹⁶²⁻¹⁸⁰ titration.



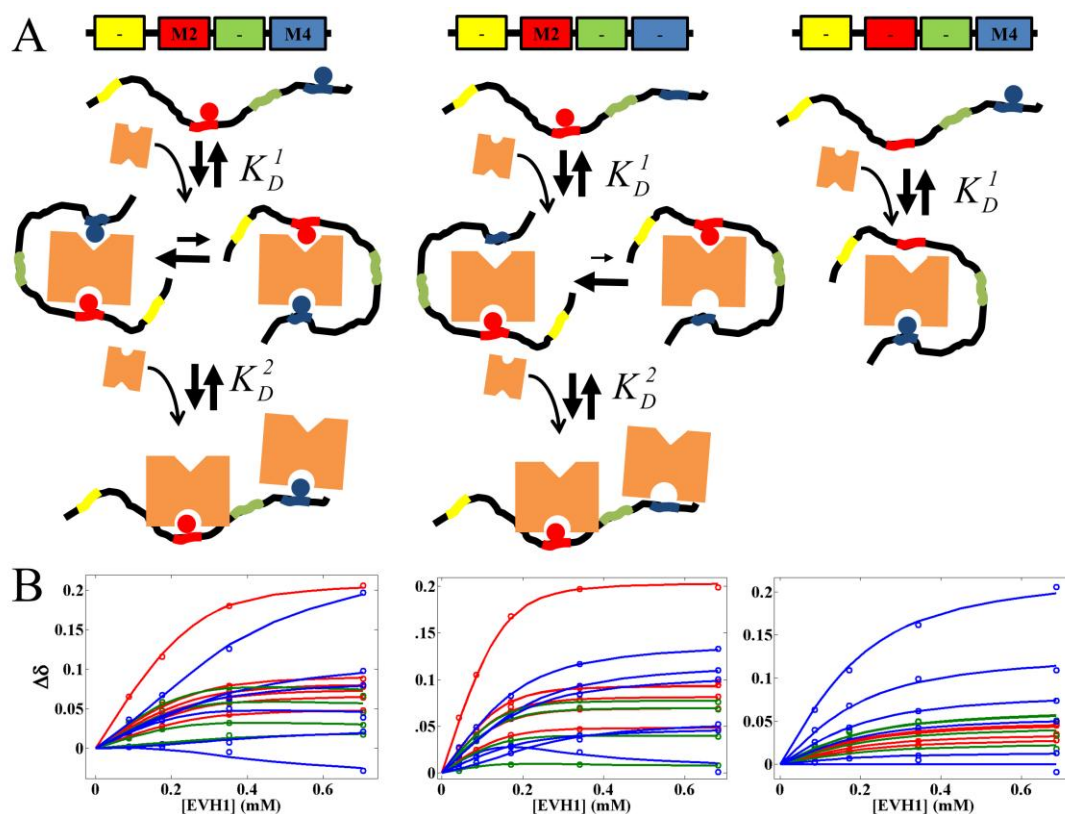
Appendix Figure 3.1: Chemical shift perturbation difference analysis indicates a single binding orientation of EVH1/IRAK1 complex. The differences in bound ^{15}N EVH1 chemical shifts between the IRAK1¹⁶²⁻¹⁸⁰ titration and the IRAK1^{162-180, W168F}, IRAK1^{157-180, pS163}, IRAK1^{162-180, pS166}, and IRAK1^{157-180, pS173} titrations were mapped to the EVH1 structure. The perturbation differences correspond well with the model's positions of the S166, W168, and S173 side chains, supporting the model and supporting a single binding orientation for the peptide. (magenta=no difference, green=highest difference)



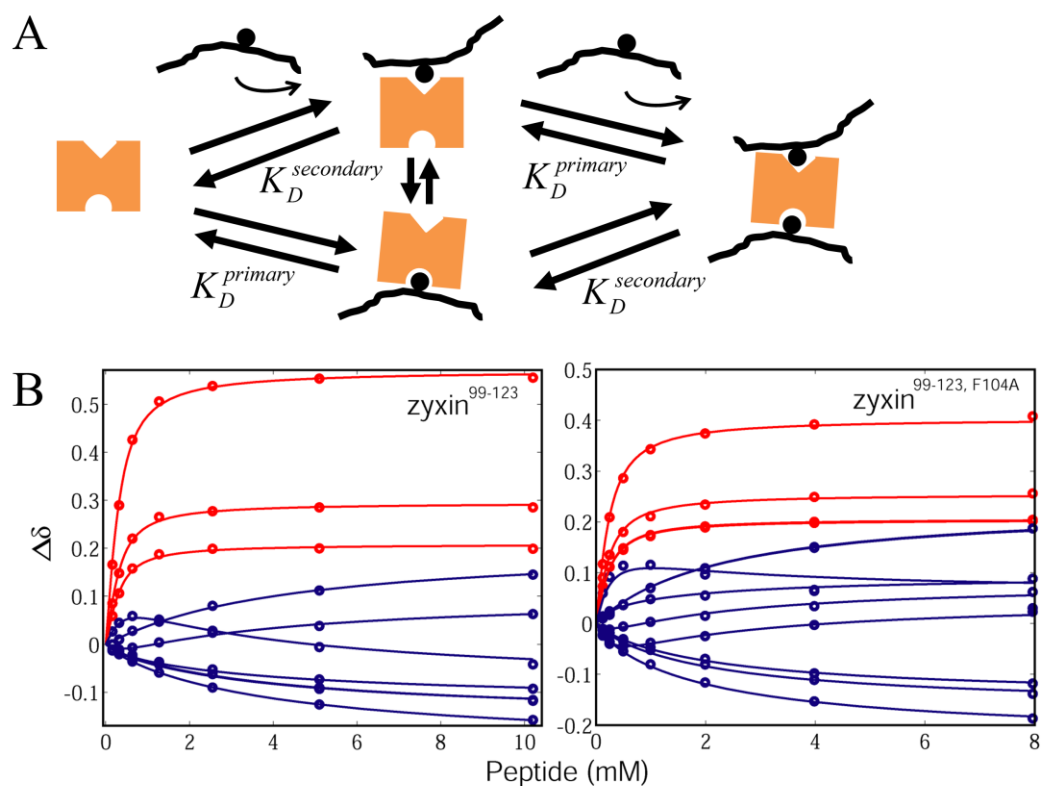
Appendix Figure 3.2: ^{15}N -EVH1 chemical shift perturbation profiles of IRAK1¹⁶²⁻¹⁸⁰ and IRAK1^{162-180, W168F}. (A) The chemical shift perturbation profiles ($\Delta\delta$) of ^{15}N EVH1 bound to either IRAK1¹⁶²⁻¹⁸⁰ (black) or IRAK1^{162-180, W168F} (red). (B) Chemical shift perturbation differences ($\Delta\Delta\delta$) between the ^{15}N EVH1 IRAK1¹⁶²⁻¹⁸⁰ and IRAK1^{162-180, W168F} titration data.



Appendix Figure 3.3: Temperature dependence of IRAK1 W168 sidechain chemical shift indicates no hydrogen bond with VASP-EVH1. The ^1H chemical shift of the indole sidechain amide peak of IRAK1¹⁶²⁻¹⁸⁰ is plotted as a function of temperature in the presence (top) and absence (bottom) of excess EVH1 domain. The slope of the curve is identical in each case, indicating there is no hydrogen bond formed between the EVH1 domain and the sidechain of W168.



Appendix Figure 4.1: Fitting ^{15}N zyxin⁴¹⁻¹⁴⁰/EVH1 binding curves. (A) Models used to fit ^{15}N zyxin⁴¹⁻¹⁴⁰/EVH1 titration data. While the F71A/F104A and F71A/F104A/F114A mutants were modeled to bind EVH1 domain (orange) in both 1:1 and 1:2 stoichiometries, the F71A/F104A/F93A mutant was modeled to only bind EVH1 domain in a 1:1 complex. Rounded and triangular indentations in the orange EVH1 domain represent the primary and secondary binding sites, respectively. (B) Fitting of binding data. Symbols represent chemical shift differences in ppm, as differences either in the ^1H dimension or in the ^{15}N dimension but scaled by the factor 0.154. Lines represent fits to the data. Colors (red, green, or blue) represent the motif the data is derived from, either the second, third, or fourth respectively.



Appendix Figure 4.2: Fitting ^{15}N EVH1/zyxin peptide titration data. (A) The model used to fit ^{15}N EVH1/zyxin peptide titration data, which accounts for both primary (rounded indentation) and secondary (triangular indentation) binding sites, and treats each peptide (zyxin⁹⁹⁻¹²³ and zyxin^{99-123, F104A}) as having only one binding site. The EVH1 domain is shown as an orange box and the peptide is shown as a black line. (B) Representative ^{15}N EVH1/zyxin peptide titration data (figures) and fits (lines). Binding curves reflecting the primary binding site are shown in red, and curves representing the secondary binding site are shown in blue. The peptides used in each titration are indicated.

Appendix Table 4.1: Assignments of zyxin residues 69-126, excluding prolines

Residue					<i>cis</i> peaks			
	N	NH	H α	NOEs	N	NH	H α	NOEs
E69	121.2	8.48	4.19	4.38	121.1	8.52	4.26	4.40
D70	121.7	8.21	4.53	4.18	121.7	8.26	4.56	4.26
F71	122.1	8.05	4.85	4.52	120.3	7.83	4.48	4.56
P72	-							
L73	124.7	8.27	4.61	4.42	124.1	8.35	4.51	3.78
P74	-							
P75	-							
P76	-							
P77	-							
L78	123.3	8.31	4.31	4.41				
A79	126.0	8.35	4.33	4.31				
G80	109.4	8.39	3.97	4.33				
D81	121.1	8.29	4.64	3.98				
G82	109.9	8.42	3.96	4.64				
D83	121.4	8.26	4.61	3.96				
D84	121.4	8.36	4.59	4.61				
A85	125.1	8.23	4.25	4.59				
E86	120.1	8.38	4.21	4.25				
G87	110.4	8.33	3.92	4.21				
A88	124.3	8.11	4.31	3.91				
L89	121.5	8.27	4.35	4.29				
G90	110.0	8.33	3.95	4.34				
G91	109.3	8.16	3.90	*	109.3	8.21	3.96	*
A92	124.0	8.02	4.25	3.90	124.4	8.09	4.31	3.95
F93	120.8	8.13	4.88	4.25	121.2	8.09	4.47	4.31

Appendix Table 4.1 (Continued)

Residue					<i>cis peaks</i>			
	N	NH	H α	NOEs	N	NH	H α	NOEs
P94	-							
P95	-							
P96	-							
P97	-							
P98	-							
P99	-							
I100	122.0	8.22	4.11	4.45				
E101	125.8	8.52	4.27	4.11				
E102	123.4	8.39	4.23	4.25	123.7	8.44	4.33	4.32
S103	117.8	8.20	4.38	4.23	118.2	8.33	4.43	4.32
F104	123.5	8.25	4.91	4.39	124.0	8.28	4.48	4.44
P105	-							
P106	-							
A107	126.3	8.33	4.59	4.44	126.1	8.31	4.50	4.36
P108	-							
L109	123.6	8.35	4.31	4.40				
E110	122.8	8.43	4.27	4.31				
E111	122.5	8.37	4.25	4.27				
E112	123.5	8.38	4.20	4.25				
I113	123.3	8.06	4.09	4.20	123.9	8.15	4.12	4.27
F114	126.5	8.42	4.93	4.08	126.3	8.23	4.64	4.12
P115	-							
S116	118.9	8.42	4.75	4.46	118.2	8.46	4.64	3.89
P117	-							
P118	-							
P119	-							
P120	-							
P121	-							
E122	121.7	8.55	4.24	4.41				
E123	122.5	8.45	4.31	4.23				
E124	123.4	8.50	4.29	4.31				
G125	111.1	8.51	3.99	4.29				
G126	109.8	8.18	4.07	3.99				

(-) indicates proline residues, which do not show peaks in ^{15}N - ^1H HSQC spectra
 (*) indicates that no NOE was observed.

“*Cis peaks*” refers to the isomer of the Phe-Pro peptide bond nearest the residue.

Appendix 5 Equations:

Equilibrium thermodynamic equations for lineshape analysis, where P denotes the protein (PPIase) and L denotes the ligand (pAPP659-682):

$$[P:L] = \frac{1}{2} \left(K_D^{App} + [P^{tot}] + [L^{tot}] - \sqrt{\left(K_D^{App} + [P^{tot}] + [L^{tot}] \right)^2 - 4[P^{tot}][L^{tot}]} \right) \quad (\text{A 5.1})$$

$$[L^{free}] = [L^{tot}] - [P:L] \quad (\text{A 5.2A})$$

$$[P^{free}] = [P^{tot}] - [P:L] \quad (\text{A 5.2B})$$

where $[P:L]$ is the concentration of Pin1-PPIase bound to the pAPP659-682 peptide, K_D^{App} is the apparent dissociation constant, $[P^{tot}]$ is the concentration of total Pin1-PPIase, $[P^{free}]$ is the concentration of free Pin1-PPIase, $[L^{tot}]$ is the concentration of total pAPP659-682 peptide, and $[L^{free}]$ is the concentration of free pAPP659-682 peptide.

$$[L^{trans}] = [L^{free}] \cdot \frac{K_{eq}}{K_{eq} + 1} \quad (\text{A 5.3A})$$

$$[L^{cis}] = [L^{free}] \cdot \frac{1}{K_{eq} + 1} \quad (\text{A 5.3B})$$

$$[P:L^{trans}] = [P:L] \cdot \frac{K_{eq}^{bound}}{K_{eq}^{bound} + 1} \quad (\text{A 5.3C})$$

$$[P:L^{cis}] = [P:L] \cdot \frac{1}{K_{eq}^{bound} + 1} \quad (\text{A 5.3D})$$

where $[L^{trans}]$ is the concentration of free pAPP659-682 peptide in the *trans* conformation, $[L^{cis}]$ is the concentration of free pAPP659-682 peptide in the *cis* conformation, $[P:L^{trans}]$ is the concentration of Pin1-PPIase bound to pAPP659-682

peptide in the *trans* conformation, $[P : L^{cis}]$ is the concentration of Pin1-PPIase bound to pAPP659-682 peptide in the *cis* conformation, K_{eq} is the ratio of the *trans* isomer to the *cis* isomer for free pAPP659-682, and K_{eq}^{bound} is the ratio of the *trans* isomer to the *cis* isomer for the bound complex of Pin1-PPIase and pAPP659-682.

Scalar coupling equations for lineshape analysis:

$$\begin{aligned}
 J_{HH}^1 &= J_{HH}^A + J_{HH}^B + J_{HH}^C + J_{HH}^D \\
 J_{HH}^2 &= -J_{HH}^A + J_{HH}^B + J_{HH}^C + J_{HH}^D \\
 J_{HH}^3 &= J_{HH}^A - J_{HH}^B + J_{HH}^C + J_{HH}^D \\
 J_{HH}^4 &= J_{HH}^A + J_{HH}^B - J_{HH}^C + J_{HH}^D \\
 J_{HH}^5 &= J_{HH}^A + J_{HH}^B + J_{HH}^C - J_{HH}^D \\
 J_{HH}^6 &= -J_{HH}^A - J_{HH}^B + J_{HH}^C + J_{HH}^D \\
 J_{HH}^7 &= -J_{HH}^A + J_{HH}^B - J_{HH}^C + J_{HH}^D \\
 J_{HH}^8 &= -J_{HH}^A + J_{HH}^B + J_{HH}^C - J_{HH}^D
 \end{aligned} \tag{A 5.4}$$

$$S_2(\nu) = \sum_{i=1}^8 [S_1(\nu + J_{HH}^i / 2) + S_1(\nu - J_{HH}^i / 2)] / 16 \tag{A 5.5}$$

where J_{HH}^{A-D} are the four largest scalar coupling constants for each of the five analyzed proton resonances as reported in the literature (Aliev and Courtier-Murias, 2007) and reproduced in Appendix Table 5.2 below, J_{HH}^i are all the possible linear combinations of these coupling constants as defined in equation A5.4, $S_1(\nu)$ is the spectrum in the absence of scalar coupling as defined in equation 5.1E of chapter 5, and $S_2(\nu)$ is the final simulated spectrum in the presence of scalar coupling.

Appendix Table 5.1: Impact of variations in constrained parameters on fit

Constrained parameters					Fit parameters		error
$K_D^{App} (mM)$	$k_{off}^{cis} (s^{-1})$	$k_{off}^{trans} (s^{-1})$	$R_{2,0}^{bound} (Hz)$	K_{eq}	K_{eq}^{bound}	$k_{cat}^{trans} + k_{cat}^{cis} (s^{-1})$	
<u>1.3</u>	<u>4000</u>	<u>20000</u>	<u>20</u>	<u>13.6</u>	<u>3.9</u>	<u>1540</u>	<u>0.0711</u>
1.3	4000	20000	20	12.9	3.9	1560	0.0735
1.3	4000	20000	20	14.3	3.9	1520	0.0692
1.3	4000	20000	16	13.6	3.7	1540	0.0712
1.3	4000	20000	24	13.6	4.1	1530	0.0714
1.3	400	2000	20	13.6	2.6	3620	0.0784
1.3	1000	5000	20	13.6	3.3	2480	0.0723
1.3	40000	200000	20	13.6	4.2	1430	0.0739
1.0	4000	20000	20	13.6	4.8	1440	0.0700
1.6	4000	20000	20	13.6	3.3	1640	0.0720

Variation of constrained parameters in Chapter 5:

Selected constrained parameters were varied within their standard deviations of measurement or within reasonable estimates of their values in order to ascertain the influence of uncertainty in the values of these parameters on the results and quality of the fit. The “best” fit which produced the reported values is on top, with numbers underlined. Constrained parameters which have been perturbed from their values in the best fit are in bold and italics. Note that although decreasing K_D^{App} or K_{eq} from their measured values slightly improved the fit, this was not deemed significant enough to warrant re-evaluating these independently-measured parameters.

Appendix Table 5.2: Scalar coupling values employed in lineshape simulation (Aliev and Courtier-Murias, 2007)[†]

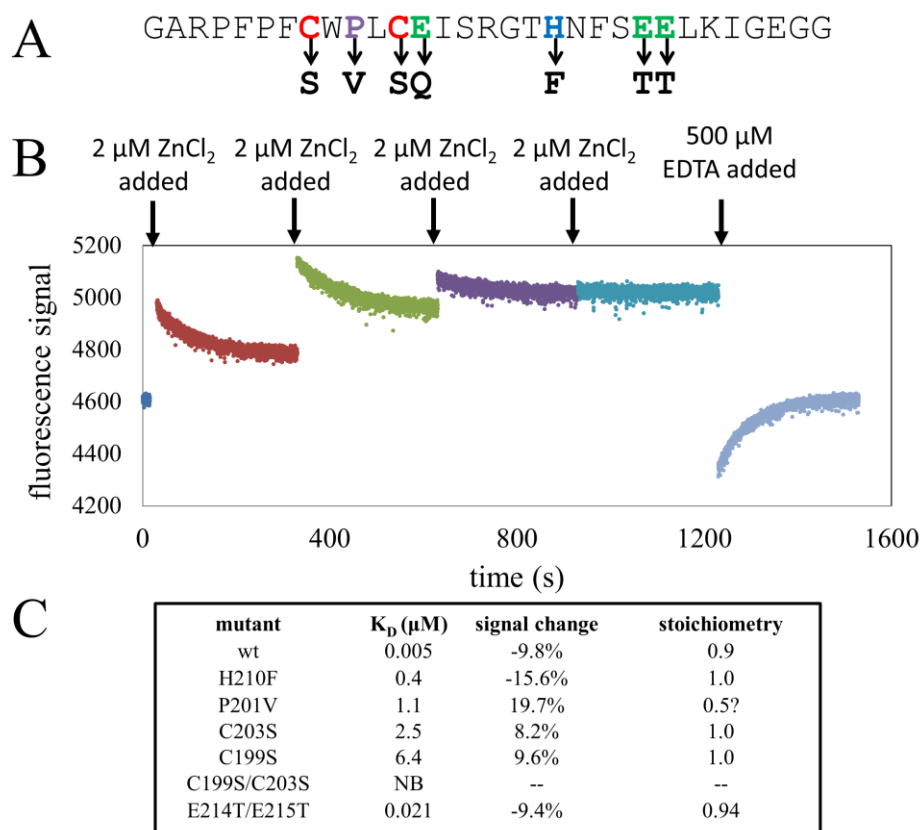
	H α	H β_1	H β_2	H δ_1	H δ_2
J_{HH}^A (Hz)	8.81	-13.3	-13.3	11.59	-11.59
J_{HH}^B (Hz)	6.61	8.81	7.53	7.52	7.61
J_{HH}^C (Hz)	-0.51	7.52	6.78	6.69	6.84
J_{HH}^D (Hz)	-0.39	6.74	6.61	-0.46	0.45

[†]Each column in Appendix Table 5.2 lists the four largest scalar coupling constants J_{HH}^{A-D} to a given nucleus, as given in Table 1 of (Aliev and Courtier-Murias, 2007). These coupling constants were used in equations A5.4 and A5.5 to simulate the final spectrum.

Treatment of scalar coupling in Chapter 5:

The observed ^1H lineshapes exhibited small but noticeable splitting due to J-coupling between the proline ring protons. These were modeled by treating each peak as simply a superposition of 16 lorentzians (equations A5.4, A5.5) using the J-coupling values reported in (Aliev and Courtier-Murias, 2007) (Appendix Table 5.2). The line shape analysis of scalar coupled spin systems requires, generally, a more sophisticated approach (Binsch, 1969; Rao, 1989) than that which is used for uncoupled systems (McConnell, 1958). However, a number of considerations supported use of a conventional classical approach for line shape fitting. First, upon peptide binding to the protein, the coupling pattern does not change (the proline ring remains chemically intact, spin systems do not change and no couplings are lost). Second, the observed coupling constants in the free peptide are in the range of 0.4-13 Hz. Upon addition of Pin1-PPIase the proline resonances broaden to linewidths on the order of FWHH~50 Hz at the highest titration point, where the peptide is still only half-saturated. Thus, if any scalar coupling constants change in the bound state (due

possibly to stabilization of a ring-pucker conformer or fast mixing between *cis* and *trans* isomers) it is still unlikely that this would contribute substantially to the overall lineshape. To the extent that the J-coupling constants do differ in the bound state, this change in overall line shape is absorbed in the $R_{2,0}^{bound}$ parameter, which has very little effect on the fit over a range of ± 4 Hz (Appendix Table 5.1). Third, the determined exchange rates are all fast ($k/J_{HH} > 10$) compared to scalar coupling, which minimizes the error that can arise from a classical approach (Gunther and Schaffhausen, 2002). It is important to note that our simplified approach is only a good approximation due to the combination of factors mentioned above. In the general case of a coupled spin system in exchange, an accurate line shape analysis based on density matrix formalism is required (Binsch, 1969; Kaplan, 1958; Rao, 1989).



Appendix Figure 6.1: Zinc binding to IRAK1-UD. (A) The sequence of IRAK1-UD (G192-G122) shown to bind zinc, with tested mutants shown by arrows pointing from mutated residues. (B) Representative raw tryptophan fluorescence data (IRAK1-UD E214T/E215T mutant) used to characterize zinc binding. Zinc is titrated into the protein and tryptophan fluorescence time courses are collected. Zinc induces a large increase in signal intensity which is followed by a slow decrease, which is accelerated by CypA. EDTA induces a large decrease in signal intensity, followed by a slow increase, which is also accelerated by CypA. (C) Binding parameters obtained by fitting the slow phase of fluorescence data (or fast phase for Cys and Pro mutants) to the bimolecular binding equation, for various IRAK1-UD mutants.

REFERENCES

- Aliev, A.E., and Courtier-Murias, D. (2007). Conformational analysis of L-prolines in water. *J Phys Chem B* *111*, 14034-14042.
- Ball, L.J., Kuhne, R., Hoffmann, B., Hafner, A., Schmieder, P., Volkmer-Engert, R., Hof, M., Wahl, M., Schneider-Mergener, J., Walter, U., *et al.* (2000). Dual epitope recognition by the VASP EVH1 domain modulates polyproline ligand specificity and binding affinity. *EMBO J* *19*, 4903-4914.
- Binsch, G. (1969). A Unified Theory of Exchange Effects on Nuclear Magnetic Resonance Line Shapes. *Journal of the American Chemical Society* *91*, 1304-1309.
- Gunther, U.L., and Schaffhausen, B. (2002). NMRKIN: simulating line shapes from two-dimensional spectra of proteins upon ligand binding. *J Biomol NMR* *22*, 201-209.
- Kaplan, J. (1958). Exchange Broadening in Nuclear Magnetic Resonance. *Journal of Chemical Physics* *28*.
- McConnell, H.M. (1958). Reaction rates by nuclear magnetic resonance. *The Journal of Chemical Physics* *28*, 430.
- Rao, B.D. (1989). Nuclear magnetic resonance line-shape analysis and determination of exchange rates. *Methods Enzymol* *176*, 279-311.